Agile Intelligent Antenna System for Industry 4.0 and Beyond

Abdul Jabbar

Submitted in fulfilment of the requirements for the
Degree of Doctor of Philosophy

James Watt School of Engineering
College of Science and Engineering
University of Glasgow

March 2024

Abstract

The next-generation industrial paradigms such as Industry 4.0 and beyond require ultra-high reliability, extremely low latency, high throughput, and fine-grain spatial differentiation for wireless communication, sensing, and control systems. Traditional industrial wired networks suffer from impediments such as expensive installation and maintenance costs, wear and tear, reduced flexibility, and restricted mobility in dynamic industrial environments. Moreover, the conventional sub-6 GHz industrial, scientific, and medical (ISM) wireless bands such as 2.4 and 5 GHz are not able to fully meet the requirements of high bandwidth, high data rate, and low latency for emerging industrial wireless applications.

To overcome the aforementioned challenges, the utilization of the 60 GHz millimeter-wave (mmWave) license-free ISM band, spanning from 57–71 GHz, is being considered as a potential solution for advancing next-generation industrial wireless communication and sensing applications, as well as for future technologies of beyond fifth-generation (5G) and sixth-generation (6G). This spectrum offers a large bandwidth of 14 GHz and experiences low spectral congestion. However, its effectiveness is hindered by significant path loss and high signal attenuation caused by oxygen absorption, posing additional challenges to design wideband, high-gain, compact, and cost-effective antenna solutions.

This thesis encompasses three antenna design solutions offering high-performance metrics, aimed at next-generation mmWave industrial wireless applications and 6G technologies. The first antenna design is a compact and wideband 64-element planar microstrip array based on a hybrid corporate-series network. The array has the size of 2 cm × 3.5 cm × 0.025 cm and offers -10 dB impedance bandwidth over the entire 57–71 GHz, 1 dB gain bandwidth of 13 GHz from 57–70 GHz, low side lobe levels, and above 70% radiation efficiency in the whole band of interest. The inherent phase shift across the operating frequency in the series-fed antenna elements is leveraged to achieve frequency beamscanning over a scan range of 40° with less than 1 dB scan loss.

The second antenna design is a compact, low-cost, high-gain, and planar 16-element linear array using the corporate feed technique. This design provides squintless high directional beams towards the broadside over 7 GHz of bandwidth (57–64 GHz), and 1 dB gain -bandwidth of more than 3 GHz. This makes it a suitable candidate for industrial fixed wireless access communication scenarios that require large bandwidth and multi-gigabit data rate, such as high-definition video signal transfer. An antenna with a broad 1 dB gain bandwidth can find various

applications across different sectors. Primarily, such an antenna could be utilized in wireless communication systems where reliable and high-speed data transmission is essential. spans across mobile communication networks, enhancing signal strength and coverage for improved data throughput, and seamless connectivity for IIoT applications, enabling efficient data exchange in various settings such as critical industrial automation scenarios. Additionally, in radar systems, a broad 1 dB gain bandwidth antenna could improve target detection and tracking accuracy, enhancing situational awareness in surveillance applications. Overall, the broad frequency coverage provided by the 1 dB gain bandwidth antenna makes it versatile for a wide range of applications requiring robust and reliable wireless communication capabilities.

The third proposed antenna solution is the hallmark of this thesis. A fully programmable electronically beamsteerable dynamic metasurface antenna (DMA) is designed and tested for the first time at 60 GHz band, thereby marking a significant milestone in advanced mmWave beamforming metasurface antennas. The 16-element linear DMA is based on novel digital complementary electric inductive capacitive (CELC) metamaterial elements whose radiation states can be dynamically controlled through a high-speed field programmable gate array (FPGA). The smart DMA can synthesize narrow beams, wide beams as well as multiple beams from a single aperture by generating different digital coding combinations. The proposed DMA is a low-cost and low-power smart beamforming antenna applicable to a diverse range of mmWave communication, sensing, and imaging avenues for smart wireless industries and 6G networks with agile beam-switching having a delay of less than 5 ns.

The proposed DMA boasts striking features, including compact size, meticulously designed PCB, and software control via binary coding from a high-speed FPGA. Operating within the high-frequency mmWave ISM band, it encompasses a diverse range of license-free mmWave applications. The designed DMA achieves key performance metrics, boasting a bandwidth exceeding 2.16 GHz around 60 GHz, a high gain of above 9 dBi for most beamforming codes, and a radiation efficiency surpassing 60%. Additionally, it offers a versatile beam synthesis capability, enabling the generation of narrow pencil beams, wide beams, and multiple beams from a single DMA aperture.

The proposed antenna solutions were fabricated, and tested through an in-house designed measurement setup which is elucidated in this thesis. Eventually, the striking futuristic applications of mmWave antennas, and their associated open research challenges are highlighted.

Declaration

Name: Abdul Jabbar
Registration Number:

I certify that this thesis presented for the examination for a Ph.D. degree at the University of Glasgow is solely my work unless otherwise explicitly stated.

The copyright of this thesis rests with the author. No quotation from it is permitted without full acknowledgment or prior agreement from the author. I declare that this thesis does not include work forming part of a thesis presented successfully for another degree and that this thesis has been produced in accordance with the University of Glasgow's Code of Good Practice in Research.

The Author

Signature: Abdul Jabbar
Date: 12 March 2024

Acknowledgments

First of all, I thank Almighty ALLAH for all his countless blessings, and for giving me the strength and capability to complete my Ph.D. work.

Foremost, I would like to express my immense and sincere gratitude to my supervisor Dr. Masood Ur-Rehman for his encouragement, kindness, patience, and technical guidance throughout this work, which led to a positive impact on my personal and professional skills. I am immensely thankful to my co-supervisor, Prof. Muhammad Imran, for his support, guidance, and mentorship throughout this work. I especially express my profound gratitude and appreciation to Prof. Qammer H. Abbasi for his phenomenal role and steadfast support both technically and personally during my Ph.D. journey. I feel blessed to have this chance to work under such an impactful supervisory committee that steered me to green pastures.

I express my sincere gratefulness to the University of Glasgow and Communication, Sensing, & Imaging (CSI) group for fostering a thriving research culture, and helpful colleagues, with huge diversity but no division. I would like to express my sincere gratitude and appreciation to my colleagues, Jalil Ur-Rehman Kazim, Mahmoud Shawky, and Mostafa Elsyed for their effective and valuable collaborative support during this work.

I would like to take this opportunity to express gratitude to Prof. Zhibo Pang from ABB Corporate Research Center, Sweden, for his kind support and facilitating me to visit ABB. I am highly grateful to Prof. Rashad Ramzan for his mentorship and wholehearted encouragement to pursue my Ph.D. journey.

I am highly grateful and appreciative to my supportive and well-wishing family, particularly my elder brothers, who have consistently motivated and guided me throughout to achieve my goals.

I extend heartfelt appreciation to my wife for her unwavering support and for being a constant source of energy and inspiration throughout my Ph.D. journey.

Most importantly, I am deeply thankful and indebted to my beloved parents, for their tremendous support and endless self-sacrifices which have been invaluable in my pursuit of academic success.

Lastly, I extend acknowledgment to myself, for persevering through various inevitable challenges during my Ph.D. journey and eventually accomplishing a commendable level of success.

Table of Contents

List of Publications

The following papers were published under the ambit of this thesis.

Journal Papers

[1] **Abdul Jabbar**, Muhammad Ali Jamshed, Qammer Abbasi, Muhammad Ali Imran, and Masood Ur-Rehman. "Leveraging the Role of Dynamic Reconfigurable Antennas in Viewpoint of Industry 4.0 and Beyond." *Research,* 6: 0110, 2023. (*doi.org/10.34133/research.0110*).

[2] **Abdul Jabbar**, Qammer H. Abbasi, Nadeem Anjum, Tahera Kalsoom, Naeem Ramzan, Shehzad Ahmed, Piyya Muhammad Rafi-ul-Shan, Oluyemi Peter Falade, Muhammad Ali Imran, and Masood Ur Rehman. "Millimeter-wave smart antenna solutions for URLLC in industry 4.0 and beyond." *Sensors,* 22, no. 7: 2688, 2022. (*doi.org/10.3390/s22072688*).

[3] **Abdul Jabbar**, Jalil Ur-Rehman Kazim, Zhibo Pang, Muhammad Ali Babar Abbasi, Qammer Hussain Abbasi, Muhammad Ali Imran, and Masood Ur Rehman. "A Wideband Frequency Beam-Scanning Antenna Array for Millimeter-Wave Industrial Wireless Sensing Applications." *IEEE Sensors Journal, March 2024. (doi.org/10.1109/JSEN.2024.3370135).*

[4] **Abdul Jabbar**, Mostafa El Syed, Zhibo Pang, Julien Le Kernec, Qammer Abbasi, Muhammad Ali Imran, and Masood Ur-Rehman. “60 GHz Programmable Dynamic Metasurface Antenna (DMA) for Next-Generation Communication, Sensing and Imaging Applications: From Concept to Prototype”, *IEEE Open Journal of Antennas and Propagation, 2024.* (*doi.org/10.1109/OJAP.2024.3386452*).

Conference Papers

[5] **Abdul Jabbar**, Muhammad Ali Imran, Qammer Abbasi, and Masood Ur-Rehman “60 GHz Programmable Dynamic Metasurface Antenna for 6G Avenues, Contactless HealthCare, and Smart Factories.” *IEEE International Symposium on Antennas and Propagation and USNC-URSI Radio Science Meeting (AP-S/URSI),* Florence, Italy, 2024.

[6] **Abdul Jabbar**, Qammer Abbasi, Muhammad Ali Imran, and Masood Ur-Rehman. "Impact of Dielectric Substrate, Feed Connector, and Fabrication Tolerances on the Performance of Planar Millimeter-Wave Antenna Arrays." *IEEE 18th European Conference on Antennas and Propagation (EuCAP),* Glasgow, UK. 2024.

[7] **Abdul Jabbar**, Zhibo Pang, Ghazanfar A. Safdar, Qammer Abbasi, Muhammad Ali Imran, and Masood Ur-Rehman. "A Compact Wideband Millimeter-Wave Beam-Scanning Antenna Array for Industry 4.0 and Beyond Applications." *IEEE International Workshop on Antenna Technology (iWAT),* Aalborg, Denmark, 2023.

[8] **Abdul Jabbar**, Qammer Abbasi, Zhibo Pang, Muhammad Ali Imran, and Masood Ur-Rehman. "High-performance 60 GHz Beamforming Antenna Array For 5G and Beyond Industrial Applications." *IEEE 17th European Conference on Antennas and Propagation (EuCAP)*, Florence, Italy, 2023.

[9] **Abdul Jabbar**, Muhammad Ali Jamshed, Qammer Abbasi, Muhammad Ali Imran, and Masood Ur-Rehman. "60 GHz High Gain Planar Antenna Array for Millimeter-Wave Industrial Applications." *IEEE International Symposium on Antennas and Propagation and USNC-URSI Radio Science Meeting (AP-S/URSI)*, Portland, Oregon, USA, 2023.

[10] **Abdul Jabbar**, Qammer Abbasi, Muhammad Ali Imran, and Masood Ur-Rehman. "Design of Efficient and Wideband 60 GHz Series-Fed Millimeter-Wave Antenna Array for Next-Generation Multi-Gigabit Industrial Applications." *IEEE International Symposium on Antennas and Propagation and USNC-URSI Radio Science Meeting (AP-S/URSI)*, Portland, Oregon, USA, 2023.

[11] **Abdul Jabbar**, Muhammad Ali Jamshed, Mahmoud A. Shawky, Qammer Abbasi, Muhammad Ali Imran, and Masood Ur-Rehman. "Multi-Gigabit Millimeter-Wave Industrial Communication: A Solution for Industry 4.0 and Beyond." *IEEE Global Communications Conference (GLOBECOM)*, Rio de Janeiro, Brazil, 2022.

[12] **Abdul Jabbar**, Qammer Abbasi, Muhammad Ali Imran, and Masood Ur-Rehman. "Design of a 60 GHz microstrip antenna for multi-gigabit industrial communication in the viewpoint of industry 4.0." *IEEE International Workshop on Antenna Technology (iWAT)*, Dublin, Ireland, 2022.

[13] **Abdul Jabbar**, Qammer Abbasi, Muhammad Ali Imran, and Masood Ur-Rehman. "Design of a 60 GHz Antenna for Multi-Gigabit WiGig Communication in Industry 4.0." *IEEE International Symposium on Antennas and Propagation and USNC-URSI Radio Science Meeting (AP-S/URSI)*, Denver, USA, 2022.

Contributions to Collaborative Publications As A Co-author

[1] Jalil ur Rehman Kazim, Ahsen Tahir, James Rains, Tie Jun Cui, **Abdul Jabbar**, Muhammad Ali Jamshed, Masood Ur-Rehman, Akram Alomainy, Muhammad Ali Imran, and Qammer H. Abbasi. "In-Home Monitoring Using Wireless on the Walls for Future HealthCare: Real-World Demonstration." *Advanced Intelligent Systems*, 5, no. 9 (2023): 2300007.

[2] Humayun Zubair Khan, **Abdul Jabbar**, Masood Ur Rehman, Muhammad Ali Imran, and Qammer Abbasi. “Reflective Metasurface for Linear and Circular Polarization Conversion in the X, Ku, and K Bands”, *IEEE Antennas and Wireless Propagation Letters (2024)*.

[3] Mahmoud A. Shawky, **Abdul Jabbar**, Muhammad Usman, Muhammad Imran, Qammer H. Abbasi, Shuja Ansari, and Ahmad Taha. "Efficient blockchain-based group key distribution for secure authentication in VANETs." *IEEE Networking Letters*, 5, no. 1 (2023): 64-68.

[4] Hamayun Zubair, **Abdul Jabbar**, Farooq Tahir, Muhammad Ali Imran, and Qammer Abbasi. "Multi-Band Anisotropic Metasurface: Simultaneous Linear and Circular Polarization for Robust Satellite Communication." *IEEE 18th European Conference on Antennas and Propagation (EuCAP)*, Glasgow, UK. 2024.

[5] Muhammad Zubair, **Abdul Jabbar**, Mobayode O. Akinsolu, Muhammad Ali Imran, Bo Liu, and Qammer H. Abbasi. "Design of Truncated Microstrip Square Patch Antenna for Terahertz Communication." *IEEE International Symposium on Antennas and Propagation and USNC-URSI Radio Science Meeting (AP-S/URSI)*, pp. 1558-1559, 2022.

List of Figures

List of Tables

List of Abbreviations and Acronyms

5G/6G/B5G	5^{th} Generation/6^{th} Generation/Beyond 5G
AGV	Automated Guided Vehicle
AMR	Autonomous Mobile Robot
CELC	Complementary Electric Inductive Capacitive
CSI	Communication, Sensing, and Imaging
DMA	Dynamic Metasurface Antenna
EIRP	Effective Isotropic Radiated Power
eMBB	Enhanced Mobile Broadband
HPBW	Half-power beamwidth
IoT/IIoT	Internet of Things/Industrial Internet of Things
ISAC	Integrated Sensing and Communication
ISM	Industrial, Scientific, and Medical
LWA	Leaky-wave antenna
mGbps	multi-gigabit per second
MIMO/mMIMO	Multiple-Input-Multiple-Output/Massive MIMO
mmWave	Millimeter-wave
MTC	Machine Type Communication
MTL	Microstrip Transmission Line
P2P / P2MP	Point-to-Point / Point-to-Multipoint
PIN	Positive Intrinsic Negative
RF	Radio-frequency
RIS	Reconfigurable Intelligent Surface
Rx	Receiver
SLL	Side-lobe level
URLLC	Ultra-Reliable and Low-Latency
WISN	Wireless Industrial Sensors Network
WLAN	Wireless Local Area Network
WPAN	Wireless Personal Area Network

Chapter 1

Introduction

1.1 Background and Motivation

Wireless communication vastly supersedes the conventional wired communication system in modern industrial settings due to its cost-effectiveness, enhanced flexibility, and impressive scalability networks [1]. Industrial wireless communication, control, and industrial wireless sensing networks (IWSN) have become an integral part of the modern smart factories and cyber-physical systems in industries, thereby paving the way towards Industry 4.0 and Industry 5.0 [2]–[6]. These industrial generations encompass various sophisticated technologies and emerging applications such as intelligent logistics [7], flexible manufacturing [8], image-based real-time error correction and fault detection [9], remote visual monitoring and surveillance, image-guided automated assembly, and high-definition video surveillance [10], [11], autonomous mobile robots (AMRs), and autonomous guided vehicles (AGVs) with collision avoidance cognition , human-machine interaction to realize co-bot kind of environment [12], mass customization and personalization [13], digital twins [14]–[19], and Industrial Internet of Things (IIoT) [2], [5], [20], [21], to name but a few.

Traditional wired networks (such as ethernet IEEE 802.3 standard) suffer from some impediments such as expensive installation and maintenance costs, restricted mobility, reduced sflexibility, and lack of reconfigurability in dynamic industrial environments [22]. Moreover, the legacy sub-6 GHz industrial, scientific, and medical (ISM) wireless bands such as 2.4 and 5 GHz are not able to fully meet the requirements of high bandwidth, high data rate, and low latency for most of the aforementioned industrial applications [4], [23].

To overcome the aforementioned challenges, next-generation industrial paradigms envision embracing advanced technologies like millimeter-wave (mmWave) communication to meet the requirements of bandwidth and Ultra Reliable and Low Latency Communications (URLLC). In this view, 60 GHz mmWave license-free wireless communication is envisaged as a potential enabler for next-generation wireless industrial applications due to remarkable features such as huge available bandwidth (14 GHz from 57–71 GHz), low spectral congestion, high inherent

security due to narrow directional antenna beams, and highly compact antenna size [24], [25]. Furthermore, as the industrial environment is typically indoors, factors like rain fade and other outdoor obstructions are naturally minimized, allowing high-frequency paradigms to operate efficiently within industrial wireless networks.

At the forefront of this perspective, reconfigurable/programmable and high-performance antennas act as the cornerstone of wireless networks. They play a pivotal role in ensuring reliable and efficient connectivity, unlocking the full potential of a wireless industrial paradigm. This necessitates the design of compact, wideband, low-cost, and high-performance mmWave antenna systems. Furthermore, the cutting-edge beamforming mmWave antenna array systems have the potential to elevate industrial wireless communication and sensing capabilities to new heights.

The small footprint of 60 GHz mmWave antennas can be leveraged in wireless smart cameras and vision technologies which can enable various applications like remote visual monitoring, intelligent logistics product tracking, image-guided automated assembly, fault detection, virtual reality/augmented reality (VR/AR), and digital-twins. Moreover, vision capabilities empower robots, machinery, and other industrial automation systems to interact with objects meaningfully and navigate their environments safely, facilitating adaptation to evolving manufacturing conditions and unlocking a plethora of new industrial applications.

In the pursuit of advancing further, the 5G URLLC does not fulfill all the Key Performance Indicators (KPIs) of sophisticated mission-critical industrial wireless applications. To provide satisfactory services to these applications, 6G communication systems demand high energy efficiency, high throughput, high security, extremely low latency, and cognitive agility [26]–[30]. At physical layer (PHY) end, these requirements pose unprecedented challenges in terms of antenna design methodologies and key performance metrics such as wide bandwidth, high gain, low variation in gain across the desired bandwidth, low-cost, ease of integration as well as reprogrammable and reconfigurable antenna properties such as real-time beamsteering through software control.

These groundbreaking research prospects towards high-performance antenna design set the motivation of this thesis, aiming to enhance the performance of next-generation industrial wireless applications.

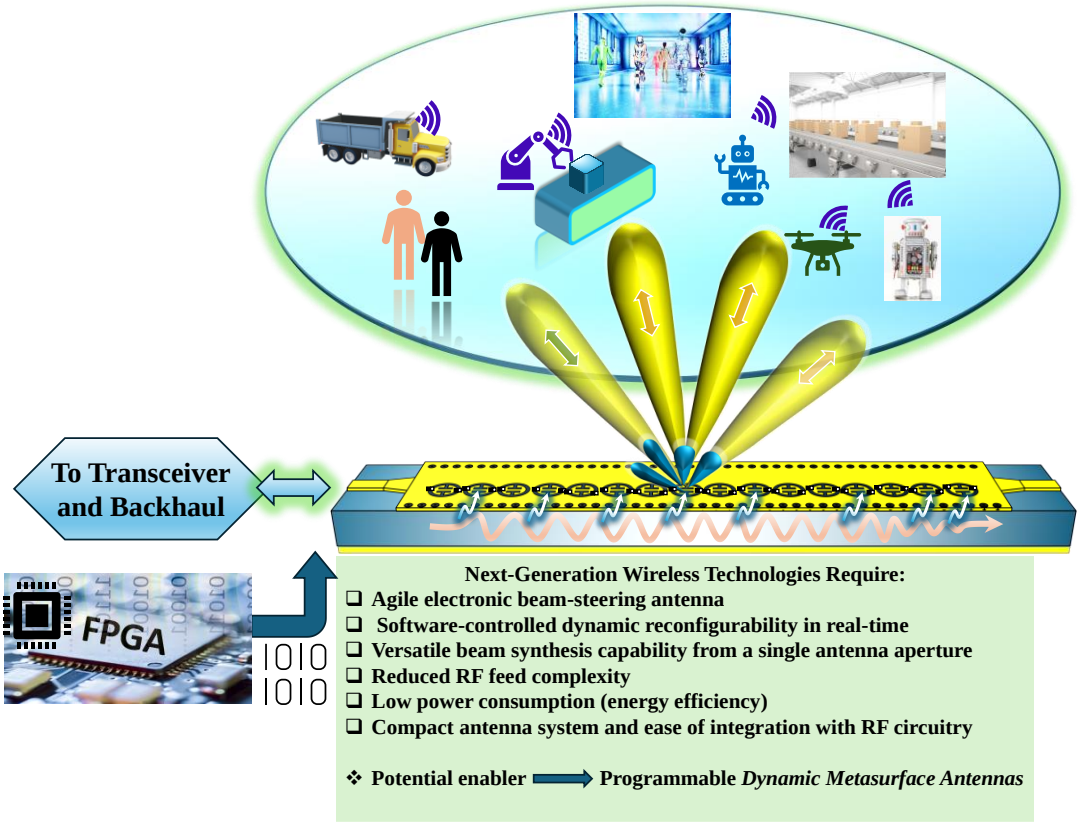

Figure 1.1. A conceptual depiction of advanced beamforming antenna requirement in next generation wireless technologies.

1.2 Problem Description

The problem description is articulated in two main aspects, in view of agile electronic beamsteering antenna domain, and passive beamforming conventional antenna domain. Within the realm of beyond 5G and 6G technologies, as well as the paradigms of Industry 4.0 and 5.0, there is a focus on realizing a dynamically reconfigurable wireless framework. Accomplishing this objective necessitates innovative beamforming antenna solutions with active electronic beamsteering to locate and synchronize antennas between intended transceivers and enabling the exploration of multiple spatial signal paths for seamless connectivity.

Traditional phased array beamforming antenna systems are often associated with exorbitant costs and high energy consumption, which necessitate the requirement of software-controlled electronically beam-steerable antennas with reduced RF feed complexity, low power consumption, and simplified beamforming hardware [31]–[34]. At 60 GHz mmWave band, the design aspect of these smart beamforming antennas poses additional design intricacies and requires immense optimization to achieve an acceptable antenna performance [35]. Moreover,

for mission-critical industrial applications, the extremely low latency at the micro-second or even nano-second level from antenna hardware during beam-switching is required. To address these several critical and essential challenges, the development of high-performing, cost-effective, and energy-efficient novel beamforming antenna system is crucial, as depicted in Figure 1.1.

Furthermore, in terms of conventional passive antenna realm, the efficient and reliable 60 GHz mmWave wireless communication presents a critical challenge in industrial settings, where the need for high data rates and low latency must contend with the limitations of limited propagation distance at 60 GHz. The susceptibility to atmospheric absorption, and thus the path loss has the highest peak around 60 GHz in the electromagnetic spectrum from direct current (DC, i.e., 0 Hz) to 200 GHz, as illustrated in Figure 1.2 (excerpted from [36]). This necessitates the utilization of high-gain directional antenna arrays to mitigate path loss as well as to relax the requirements of high-gain power amplifiers (PAs) at the transmitter end and low noise amplifiers (LNAs) at the receiver end to reduce the overall cost of link budget. Moreover, the pursuit of attaining a wide antenna bandwidth, stable radiation performance, and consistent high gain across a broad spectrum of 60 GHz using low-cost techniques is desirable as well as challenging. Substrate integrated waveguide (SIW)-based slotted leaky-wave antennas (LWA) are often designed around high frequency bands to achieve a wideband and frequency-selective beamforming performance [37]–[45]. However, those antennas are complex to fabricate as they usually involve multitude of vias. Additionally, designing effective slot patterns to attain the desired radiation characteristics poses a critical challenge. Therefore, to reduce the fabrication complexity and cost, and to enhance the antenna reproducibility around 60 GHz, achieving passive beamforming with conventional microstrip planar antenna arrays with high performance is desirable as well as challenging.

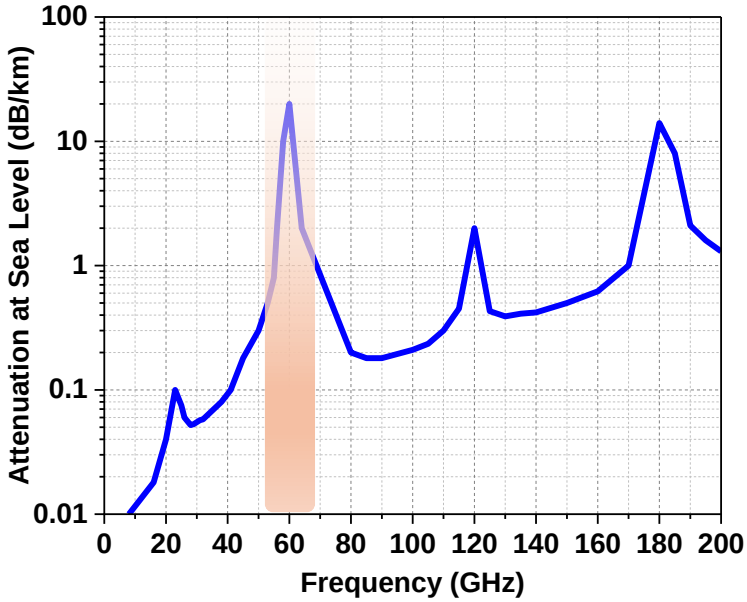

Figure 1.2. The properties of atmospheric absorption of EM waves up to 200 GHz [36].

1.3 Aims and Objectives

The primary aims and objectives of this thesis are as follows:

- Investigation and exploration of contemporary industrial wireless communication framework. To identify potential existing frequency bands and the need for smart antennas at those frequency bands.
- To identify the use cases of industrial wireless communication and sensing applications and propose antenna design solutions related to them.
- Exploration of mmWave antenna designs and challenges, and to devise a low-cost, compact, and reproducible passive beamforming antenna solution around 60 GHz band with high performance. For high data rate and static industrial wireless applications, design of a compact, wideband, and fixed beam antenna array with ease of integration with mmWave equipment.
- Design, fabrication, and prototype testing of a novel programmable beamforming antenna with agile beamsteering capability, low-power consumption and versatile beam synthesis ability for dynamic industrial wireless applications under the ambit of 6G technology.

1.4 Thesis Outline

The rest of this thesis is organized as follows:

Chapter 2 presents the literature review of the industrial revolution journey toward Industry 4.0 and Industry 5.0, industrial wireless networks, operating frequency bands in the industrial wireless networks, the potential of mmWave in next-generation industrial wireless networks, and the related smart antenna solutions.

Chapter 3 describes the design, analysis, and performance of a linear 8-element wideband frequency beamscanning array and subsequently designed 64-element planar beamscanning array. The antenna array performance in terms of bandwidth, gain, sidelobes, beamwidth, and beam-scanning is presented in detail. Prototype fabrication and complete 60 GHz antenna measurements are elucidated. Moreover, the ease of integration and utility of the proposed array with standard 60 GHz RF equipment such as mmWave power sensors, and mmWave evaluation boards is also practically illustrated.

Chapter 4 presents the design, analysis, and performance of a squint-less fixed-beam 16-element wideband antenna array. The antenna array performance in terms of bandwidth, gain, sidelobes, and fixed broadside beam over a wide bandwidth is presented in detail. Prototype fabrication and antenna measurements are demonstrated.

Chapter 5 presents the complete design philosophy of a 60 GHz DMA prototype from the construction of a digital metamaterial element to a complete programmable electronically beam steerable agile DMA array. The complete electronic beamsteering performance is presented and validated through measurements.

Chapter 6 concludes the thesis, and presents futuristic research opportunities and directions.

Chapter 2

Literature Review

2.1 Industry 4.0 and Beyond: A Glimpse!

The Industrial Revolution has come a long way to see the digitalized sophisticated era from the mechanized using steam engines (Industry 1.0), to the division of labor, and mass production using electrical energy to power machines (Industry 2.0), to the third industrial revolution with the advent of advanced computer technology, Information Technology (IT), and automated production processes (Industry 3.0) [46], [47]. Subsequently, a new era of the industrial realm began in 2011 (the fourth industrial revolution or Industry 4.0), bringing about significant changes throughout the manufacturing market [48]. A visualization of the industrial transformational journey is depicted in Figure 2.1.

Industry 4.0 is a paradigm of the cyber-physical world whose philosophy is based on fully automated and digitally connected smart factories for enhanced production and customized user experience [6], [49], [50]. As mentioned above, various key enabling technologies are involved in one way or the other to bring the concept of Industry 4.0 to operation, such as wired as well as wireless technologies, IIoT [3], [51], [52], cloud/fog computing [3], [52], big data [53], digital twins [17], artificial intelligence [54]–[58], smart communication [23], [59]–[61], additive manufacturing [62], [63], advanced robotics [64]–[66] and cyber-physical systems [17], [51]. The main theme of Industry 4.0 revolves around automation and mass customization through machine-to-machine (M2M) without much human intervention.

It is worth mentioning here that Industry 4.0 is not the apex of the modern smart industrial world, rather the visualization and conceptualization of Industry 5.0 are under conception in research. These encompass a more human-centric approach to envision an evolved industrial generation, i.e., Industry 5.0 [67]–[69]. It aims to leverage human creativity in addition to the intelligence of machines [67], [68], [70], [71]., thus promoting a co-botic environment rather than an exclusively robotic one. Therefore, efficient human-machine interaction is a fundamental essence of Industry 5.0.

Yet to the surprise of readers, this is not the end and researchers have put forward the notion of Industry 6.0 [72], [73], details of which are beyond the scope of this thesis. Nevertheless,

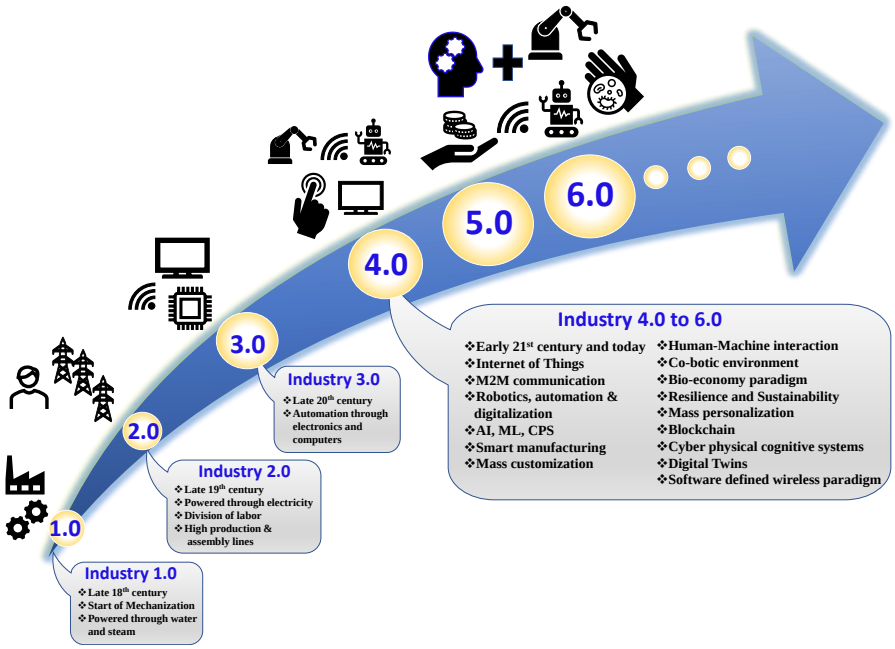

Figure 2.1. A conceptual demonstration of the industrial transformations and futuristic trends.

Industry 4.0 is still undergoing practical realization and has not yet been implemented pervasively. On the technological grounds, most of the PHY-enabling technologies (such as smart antennas) that serve to visualize Industry 4.0 can equally be utilized to pursue Industry 5.0 and beyond. Therefore, in this thesis, we collectively refer to these so-called generations as *Industry 4.0 and beyond.* Some of the key enabling technologies for Industry 4.0 and beyond are presented in Figure 2.2 [48].

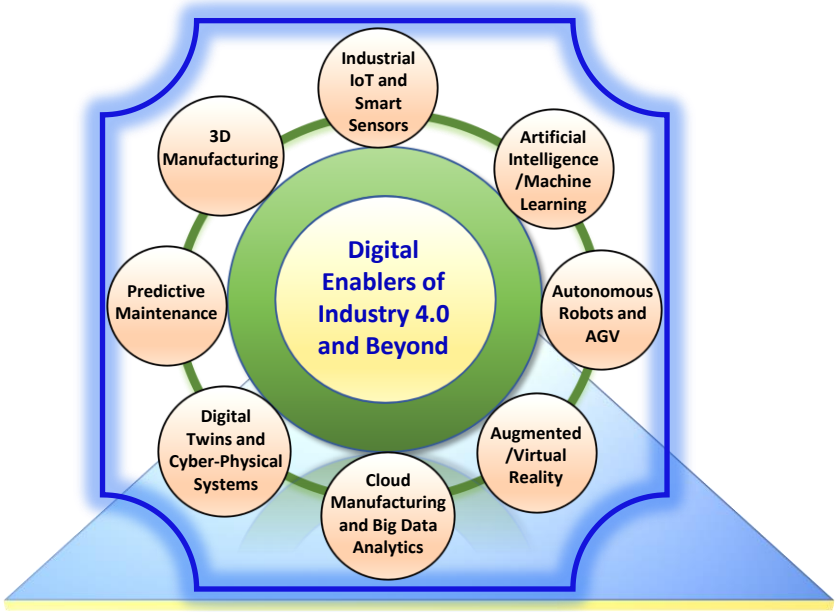

Figure 2.2. Key digital drivers of Industry 4.0 and beyond, excerpted from [48].

2.2 Overview of Wireless Industrial Paradigm

With the widespread pervasiveness of wireless technologies in consumer electronics, there is a growing interest in utilizing standard wireless technologies within industrial settings. In an industrial setting or a smart factory floor, the benefits of using wireless technologies are manifold as the cost and time needed for the installation and maintenance of a large number of wired networks (cables) can be substantially reduced. Moreover, the traditional wired networks (although wired industrial technology is mature such as ethernet IEEE 802.3 and wired fieldbuses) suffer through serious impediments such as restricted mobility, reduced flexibility, and a lack of reconfigurability from the viewpoint of modern industrial application and use case [74]. In light of these challenges, industrial Wireless Local Area Networks (WLANs) and Wireless Personal Area Networks (WPANs) provide flexible and scalable connectivity solutions tailored to the dynamic needs of industrial settings, enabling efficient data exchange and real-time monitoring of operations [75].

The integration of wireless networks within device-level factory automation systems is contingent upon several crucial factors. Primarily, the selection of both the radio transmission systems and protocols must be meticulously chosen to meet the specific requirements of the wireless environment [21]. This consideration holds particular significance as these networks are intended for deployment in harsh industrial environments where various forms of interference can lead to transmission errors. Additionally, the design of high-performance antennas and RF frontends must be carefully evaluated [1], [76]–[80].

In the industrial wireless paradigm, the required quality of service (QoS) and quality of data (QoD) in terms of low latency, high reliability, high throughput, seamless connectivity, and agility are crucial for automation, IIoT and industrial cyber-physical systems (CPS) [17], [81], [82]. With CPS, the physical processes are constantly analyzed and managed in the digital paradigm via a computational process that has a direct impact on real-world manufacturing activities [83], [84]. The feedback from physical processes impacts computational methods in an optimization feedback loop. Moreover, with the use of digital twins, smart manufacturing could utilize digital replicas of the tangible goods produced in an industrial environment [85]. The KPIs and performance requirements of some major use cases of smart manufacturing under the ambit of Industry 4.0, excerpted from [23], [83], [86], and [84] are presented in Figure 2.3.

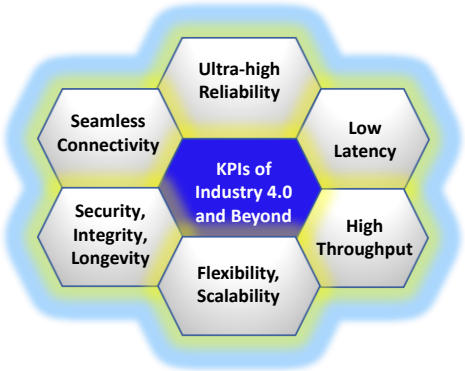

Use Cases	Latency (milli-sec)	Reliability (packet error rate)	Data Rate (bps)	Comm. Range (m)	Device Mobility (m/s)
Monitoring and Control	~20	10^{-5}	Kbps-Mbps	100 m-1 km	<10
Discrete Manufacturing	250 µs - 1 ms	10^{-9}	Kbps-Mbps	<50 m	<10
Augmented Reality	10	10^{-5}	Mbps-Gbps	<100	<3
Process Automation	>50 ms	10^{-5}	Kbps-Mbps	100 m-1 km	<10
Automatic Guided Vehicles	15-20	10^{-6}	Kbps-Mbps	2	<10
Safety Operations	~10	10^{-9}	Kbps-Mbps	<10	<10
Digital Twin	50	10^{-5}	Mbps-Gbps	<1 km	High
Remote Visual Monitoring	10-100	10^{-6}	Mbps-Gbps	Several km	Low
Human-Machine Interaction	<10	10^{-9}	Kbps-Mbps	As Factory Floor	Low

Figure 2.3. KPIs of Industry 4.0 and beyond along with smart manufacturing use cases and PHY wireless communication requirements.

So far, an overview of the industrial wireless landscape and its relevant aspects has been briefly provided. It's important to note that in any wireless communication paradigm, the design and performance of antennas are crucial for ensuring reliable and robust end-to-end connectivity. Therefore, the subsequent focus will be directed toward the requirements and characteristics of antenna designs specifically tailored for industrial wireless applications.

The first and foremost concern in the antenna design revolves around the choice of operating frequency band. Within the scope of this thesis, two significant frequency regions from an industrial wireless communication perspective were thoroughly investigated, viz., sub-6 GHz ISM band and mmWave ISM band. These investigations resulted in two comprehensive publications under the ambit of this thesis. Sub-6 GHz frequency bands in industrial wireless communication and related antenna designs are presented in [87], whereas the potential use cases and smart antenna applications to boost the performance of industrial wireless networks

at 60 GHz mmWave ISM band are extensively covered in [25]. Here, a brief overview of these two frequency bands is presented.

2.3 Sub-6 GHz Industrial Frequency Bands and Wireless Communication

At sub-6 GHz, the communication channel, wave propagation conditions, and hardware capabilities are well studied, and path losses are well managed by a single or few antennas. To avoid sub-6 GHz spectral congestion, and mitigate spectral interference, smart reconfigurable antenna techniques such as frequency reconfigurability, polarization reconfigurability, and especially radiation pattern reconfigurability can be employed to unleash the potential of flexible and smart industrial manufacturing and other applications [88]–[92].

Various wireless communication protocols exist for industrial applications such as IEEE 802.11 (Wi-Fi family) for wireless local area networks (WLAN), IEEE 802.15.1 for wireless personal area networks (WPAN), and IEEE 802.15.4 for low data-rate private area networks (PAN) [78], [83]. Furthermore, the prevalent industrial wireless standards are Wireless HART (Highway Addressable Remote Transducer), ISA100.11a (International Society of Automation), WIA-PA (Wireless Networks for Industrial Automation-Process Automation), WIA-FA (Wireless Networks for Industrial Automation-Factory Automation), WSAN-FA (wireless sensor actuator network for factory automation), WISA (Wireless Interface for Sensors and Actuators), Wi-Fi, Bluetooth, and Zigbee[78]. These standards mainly operate in license-free sub-6 GHz ISM bands, such as 2.4 GHz and 5 GHz. An overview of the adoption of industrial wireless standards, their key features, as well as their similarities and differences are studied in [78], [83] and [93]. Table 2.1 provides a summary of the existing sub-6 GHz wireless protocols that are employed for a variety of applications in Industry 4.0 and beyond.

The sub-6 GHz band is spectrally congested and suffers from various impediments such as spectral interference and low available bandwidth. Industry 4.0 would demand high data rates and high-quality connectivity for various smart applications, such as time-sensitive networking, intelligent logistics, remote visual monitoring, AGVs/AMRs, etc. For these applications, conventional sub-6 GHz bands show high latency and spectral congestion. As a result, the KPIs of Industry 4.0 and beyond may be compromised severely. To mitigate these issues and to achieve high throughput as well as high bandwidth for modern industrial operations, Wi-Fi-6/6E [94]–[97] and Wi-Fi-7 [98]–[103] have been proposed in the literature to boost the network performance even at lower frequency bands.

A brief overview of the potential sub-7 GHz potential technologies, other than legacy sub-

Table 2.1. Existing industrial wireless communication standards at sub-6 and sub-7 bands.

Wireless Standard	**IEEE PHY Prootcol**	**Operating Frequency Band (GHz)**
WirelessHART	802.15.4	2.4
ISA100; WIA-PA	802.15.4	2.4
Zigbee	802.15.4	2.4
WISA/WSAN-FA	802.15.1	2.4
Bluetooth	802.15.1	2.4
WIA-FA	802.11	2.4
Wi-Fi 5	802.11ac	5
Wi-Fi 6	802.11ax	2.4 / 5.15–5.83
Wi-Fi 6E	802.11ax	2.4 / 5.92–7.125
Wi-Fi 7	802.11be	2.4 / 5.92–7.125
5G	FR-1 Band	410 MHz–7.125 GHz

6 GHz ISM bands, for industrial wireless networks is presented below. It is important to mention here that Wi-Fi 6/6E and Wi-Fi 7 ptotocols cover the portion of spectrum between 6 GHz and 7 GHz, therefore it is better to refer these bands as *sub-7 GHz* bands. Any new generation of radio technology always tries to take advantage of the use of new spectrum bands as they become available because the spectrum is analogous to the air that wireless networks breathe. Therefore, the new generation of Wi-Fi accepts the use of the 6 GHz spectrum as an immediate method to provide high network efficiency in 802.11ax (Wi-Fi 6/6E) and to boost peak throughput in 802.11be (Wi-Fi 7). Moreover, next-generation of Wi-Fi such as Wi-Fi 8 has also been put forward in the research [104], [105].

2.3.1 Wi-Fi 6/6E

Wi-Fi 6E is designed where greater bandwidth, low latency, high throughput, and excellent network efficiency are all important considerations and are well-suited for industrial applications. Wi-Fi 6/6E provides functionalities that are implemented in industrial-grade

components. The Wi-Fi 6/6E is backed by OFDMA (orthogonal frequency-division multiple access) which represents a significant advancement in Wi-Fi 6's ability to provide effective communication [94]. Using OFDMA, the communication channel is split up into several resource units, or smaller channels. Different industrial entities may use these subchannels in a variety of bundles. This enables simultaneous data transmission, which reduces the time between packets. Furthermore, as Wi-Fi 6/6E can serve more users in less time, it can achieve substantially reduced latency as well as a more equitable distribution of bandwidth among clients.

Another aspect is that since only a small portion of the channel must be used for each transmission, it can offer a more effective transmission of small data packets. This prevents bandwidth from being wasted [95], [96]. For instance, this enables various industrial entities, such as massive industrial sensor network deployment, AGVs, and conveyor belts, to react to unforeseen situations. Consequently, it can be operated at a faster speed without increasing risk. This also lays the groundwork for addressing in parallel the increasingly common demands for dependable real-time in automation components and data-intensive applications like the transmission of high-definition images and videos for vision-based time sensitive networking (TSN) or remote visual monitoring in factory automation [94], [103]. Additional features included in the Wi-Fi 6 standard are 8 × 8 multi-user (MU) MIMO and the higher modulation scheme such as 1024-Quadrature Amplitude Modulation (QAM), which both increase the nominal data rate and enhance overall industrial WLAN performance [94].

2.3.2 Wi-Fi 7

The IEEE 802.11be standard also marketed as Wi-Fi 7 or Extremely High Throughput (EHT) [106], [107], is a new addition to the Wi-Fi standard that aims to increase the nominal throughput to as much as 46 Gbps through spatial multiplexing and spatial diversity [98], [100]. The PHY layer is improved via double bandwidth to 320 MHz, increased modulation to 4096-QAM, and an increase in the number of spatial streams to 16 × 16 multi-user (MU)-MIMO [101], [103]. To achieve exceptionally high throughput, the EHT PHY provides higher bandwidth, more spatial streams, and a higher modulation method.

For a single PHY link, the maximum throughput can be calculated by using the formula[108] $Max.\,PHY\ data\ rate = \frac{N_{CBPS} \times N_{SD} \times N_{SS} \times R}{T_{SYM}}$.

where N_{CBPS} is the number of coded bits per OFDM symbol (12 bits for 4096-QAM)), N_{SD} is the number of data subcarriers depending on channel bandwidth (3920 for 320 MHz channel),

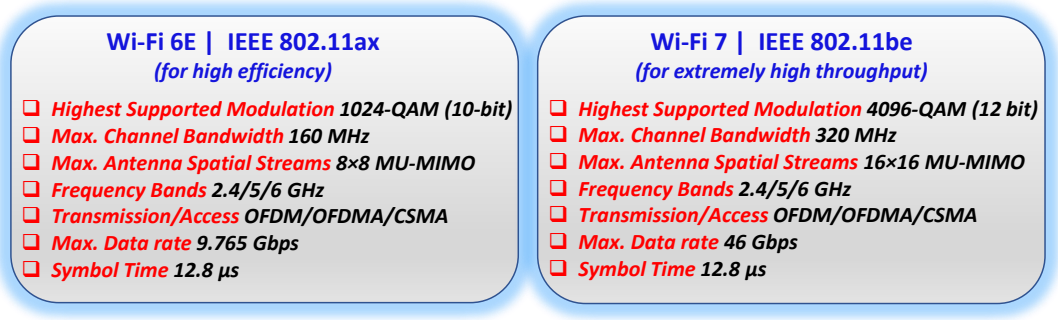

Figure 2.4. A summary of key PHY parameters of Wi-Fi 6 and Wi-Fi 7.

N_{SS} is the number of spatial data streams generated by the antenna (16 for 16 × 16 MIMO), R is the code rate (5/6 for 4096-QAM), and T_{SYM} is the OFDM symbol duration (12.8 12.8 µs) including guard time. For a typical theoretical calculation of the maximum PHY data rate achieved via Wi-Fi 7 link, consider a link using 4096-QAM modulation (N_{CBPS} =12 bits), 320 MHz channel (N_{SD}=3920), 16 × 16 MIMO (N_{SS}=16), CODE RATE OF 5/6 (R=5/6), and short guard interval time of 0.8 µs (T_{SYM} = 12.8+0.8), the maximum achievable link throughput is 49 Gbps [108],[109].

Apart from Standard Ethernet and private 5G technologies, the potential solution for various industrial applications is anticipated to be Wi-Fi 6/6E (IEEE 802.11ax) and Wi-Fi 7 (IEEE 802.11be). The technologies will likely be integrated with advancements for time-sensitive communication, such as the time sensitive networking (TSN) standards outlined by IEEE 802.1, to create a solution in an Industry 4.0 context. Additionally, to ensure fair coexistence with independent APs deployed in the same coverage area and to optimize channel access, the implementation of Distributed-MIMO in 802.11be would necessitate the design of new distributed carrier sense multiple access with collision avoidance (CSMA/CA) mechanisms that are compliant with regulations [107]. These higher-layer techniques would require MIMO antennas with uncorrelated channels, or multi-beam antennas for spatial diversity [110]. A summary of some key PHY parameters of Wi-Fi 6 and Wi-Fi 7 is presented in Figure 2.4**.**

2.4 mmWave Industrial Wireless Paradigm: 60 GHz Spectrum

Traditional sub-6 GHz wireless communication can not fully meet the bandwidth and throughput requirements of modern Industry 4.0 and beyond applications. For instance, high-

Table 2.2. Wireless protocols of 60 GHz mmWave ISM band.

IEEE Standard	Forum Type	Peak data rate (Gbps)	Maximum Bandwidth Combined (GHz)
IEEE 802.11ay	International standard	100	8.64
IEEE 802.11ad	Industry consortium	8	2.16
IEEE 802.15.3c	International standard	5.7	<3
WirelessHD	Industry consortium	4	2
ECMA387	International standard	4.032	2.16

resolution video signals in a smart factory would need to be transmitted over a wireless system that supports new applications, requiring significantly high QoS in terms of reliability, latency, and throughput. To meet these demands, the 60 GHz mmWave ISM band is envisaged as a potential enabler for the next-generation industrial wireless applications [10], [24].

The 60 GHz ISM band offers 14 GHz of contiguous bandwidth from 57–71 GHz. The band is subdivided into 6 channels, each with a bandwidth of 2.16 GHz as shown in Figure 2.5. Different 60 GHz mmWave WLAN and WPAN wireless protocols include IEEE 802.11ad, IEEE 802.11ay, IEEE 802.15.3c, WirelessHD, and ECMA387 [36], [111]–[113]. Besides, some customized industrial protocols, such as WirelessHP, have also been presented in the literature for extremely low latency mmWave industrial applications [1].

The license-free 60 GHz ISM band offers a range of applications across various industries. One prominent application is in wireless communication systems, where this band provides high-speed data transmission suitable for applications requiring ultra-fast connectivity, such as high-definition video streaming, virtual reality, and augmented reality. Additionally, the 60 GHz band is ideal for short-range, high-capacity links, making it suitable for wireless backhaul in dense environments, providing a cost-effective solution for extending network coverage and capacity. Moreover, this band is well-suited for indoor wireless networking applications, enabling gigabit-speed wireless connections for various IIoT sensors. Furthermore, the 60 GHz band finds utility in industrial automation, facilitating reliable and low-latency communication between machinery and control systems, and enhancing efficiency and productivity in manufacturing processes. Overall, the license-free 60 GHz ISM band offers a versatile platform for a wide range of high-speed, short-range wireless communication and sensing applications in next-generation industrial networks [25].

IEEE 802.11ay supports faster and longer-range mGbps communication. This protocol provides ultra-high performance for Point-to-Point (P2P) and Point-to-Multipoint (P2MP)

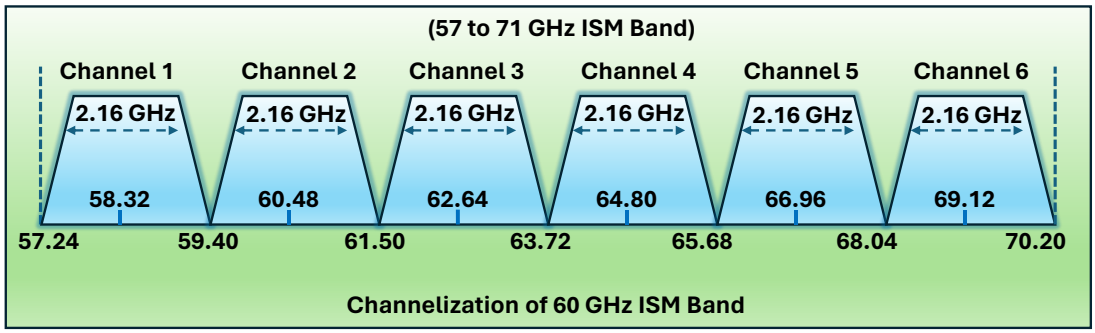

Figure 2.5. Channel division of 60 GHz ISM band.

transmissions, either indoor or outdoor. It is a standalone unlicensed protocol that provides a theoretical peak data rate of up to 100 Gbps [113]. In addition, it provides a bandwidth of 8.64 GHz through channel bonding and channel
aggregation to provide higher bandwidth and data rates [113], [114], and also supports MU-MIMO. From an antenna design perspective, at least 2.16 GHz of bandwidth must be supported by the 60 GHz antenna to occupy at least one channel for high data rates and to realize the potential of the IEEE 802.11ay protocol.

A summary of various 60 GHz protocols is presented in Table 2.2.

2.4.1 Opportunities of mmWave Industrial Wireless Communication

Some of the prime advantages of utilizing the 60 GHz mmWave ISM band and thus antenna designs at this band for industrial applications are presented below.

2.4.1.1 Large Available Bandwidth

The large available bandwidth of the 60 GHz unlicensed band unfolds many applications for Industry 4.0 and beyond. It offers a huge available bandwidth of 14 GHz which is way more than the combined bandwidth of 85 MHz around 2.4 GHz and 500 MHz around 5 GHz ISM bands [35], [115]. Bandwidth-hungry smart industrial applications such as vision-guided robots, ultrahigh definition video and imaging for remote visual monitoring, smart safety instrumented systems, intelligent logistics, and high precision image-guided automated assembly, to name a few [10], [11] are realizable through 60 GHz mmWave networks.

2.4.1.2 Inherent Security and Reduced Interference

The 60 GHz communication is sensitive to blockage due to weak diffraction capability around the objects and high path loss [116]. Moreover, because of array configurations and beamforming, the nature of communication is highly directional. This aspect employed as a fortune from PHY reliability and industrial security point of view. This also helps in avoiding jamming signals due to the high directionality of the transmitter and receiver antenna systems. The problem of jamming detection and mitigation in indoor mmWave industrial applications.

Moreover, due to the highly directional nature of 60 GHz array antennas, mmWave communication primarily functions as noise-limited rather than interference-limited, which paves an opportunity for collaborative robots to communicate and sense at the same time in a smart industrial environment without interference.

2.4.1.3 Efficient Spectrum Reuse and Frequency Diversity

Since mmWave beamforming with large arrays produces highly directional beams, thus the effect of co-channel interference is greatly reduced. To benefit from this inherent feature, MIMO or multi-beam antenna techniques can be employed to re-use the spectrum resource and produce uncorrelated redundance radiation beams. This will provide diversity gain and multiplexing gain, in addition to the array gain [117]. In this way, spatial redundancy and diversity can be efficiently utilized to reuse the spectrum in mmWave industrial communication and control.

2.4.1.4 Antenna Size Reduction and Miniaturized Radios

At the 60 GHz band, the free space wavelength is 5 mm. This paves the way to design highly compact antenna arrays and radio. This enables the utilization of intelligent multiple antennas at terminals, making them easily integrated into different components of industrial automation systems. For instance, miniature radios can be installed in motor bearings, rotating engines, oil pumps, and other hard-to-reach locations.

2.4.1.5 Path Loss Mitigation Through Beamforming Array Antenna Gain

To combat the high path loss issues, 60 GHz communication leverages the beamforming antenna gain with the multitude of antenna elements within a low form factor. As a result, array gain helps to improve signal-to-noise ratio (SNR) to mitigate path loss at 60 GHz. Thanks to the smaller wavelength at 60 GHz, array form factors are much lower as compared to those of

sub-6 GHz designs. Moreover, for the same physical antenna size, mmWave transmissions allow for a better antenna gain to mitigate path loss and improve link budget.

The free space path loss (*PL*) at a free space operating wavelength λ_0 and a distance d between Tx and Rx antennas can be calculated as [118]:

$$PL = 20 \times \log_{10}\left(\frac{4\pi d}{\lambda_0}\right) \tag{2.1}$$

At 60 GHz, the free space PL is 68 dB. Using the Friis equation [36], at the receiver end, the received power P_{Rx} in dB can be calculated as:

$$P_{Rx} = P_{Tx} + \mathrm{G_{Tx}} + G_{Rx} - PL \tag{2.2}$$

Where P_{Tx} is the transmit power from the transmitter, $\mathrm{G_{Tx}}$ is the transmitter antenna gain and G_{Rx} is the receiver antenna gain. For unity antenna gains and $P_{Tx} = 10\ dBm$, the P_{Rx} is estimated to be -58 dBm. However, with 15 dBi beamforming antenna array gain at Tx and Rx ends, ($\mathrm{G_{Tx}} = \mathrm{G_{Rx}} = 15\ dBi$), the received power would be -28 dBm, leading to 30 dB increase in signal strength.

2.5 60 GHz mmWave Antenna Design Techniques

At 60 GHz mmWave ISM band, an efficient antenna design is of paramount importance because of a range of critical factors such as combatting high path loss, compact size, and integration with frontend transceivers. Hence, antenna design must be low-cost, high-performance, compact, and easily integrateable for industrial and other commercial equipment [36], [119]. Various types of antenna designs have been reported at the 60 GHz band, such as on-chip antennas (AoC) and antennas-in-package (AiP) [120], LTCC-based antennas [121], and PCB based antennas [122]–[130].

Silicon based on-chip antennas suffer from high radiation losses and low gain due to low resistivity and high permittivity of silicon substrate [120]. Some techniques such as doping the silicon substrate with additional elements or introducing other materials like silicon-germanium modify the electrical properties of the substrate to mitigate radiation losses and enhance antenna performance [131]. LTCC-based antennas are complex to fabricate, expensive, and usually generate high surface waves because of the high permittivity of LTTC

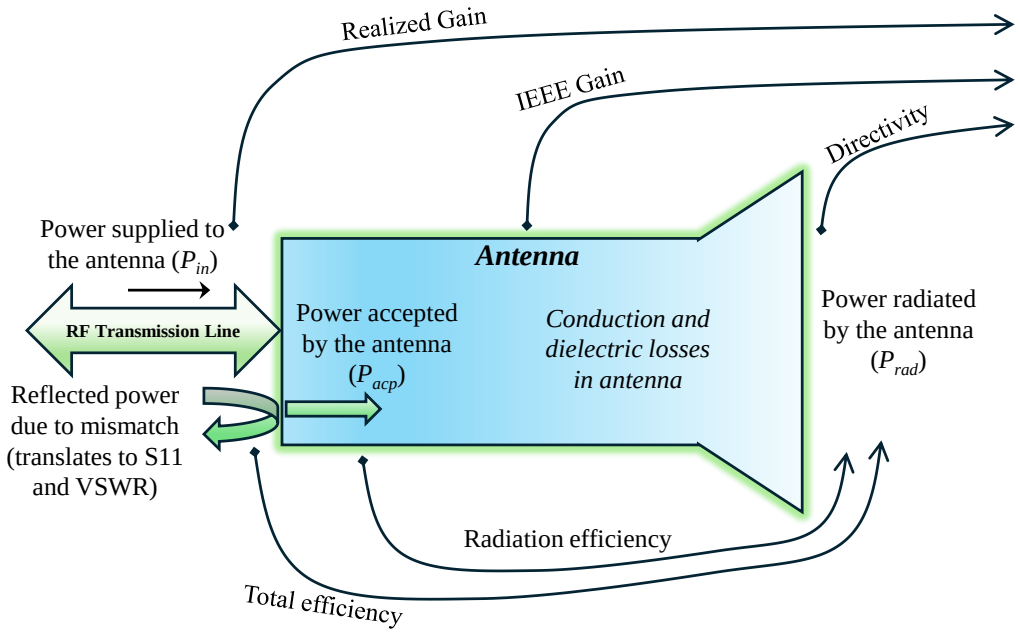

Figure 2.6. Antenna power, gain, and efficiency flowchart.

materials due to which the radiation pattern of the antenna is likely to to degrade and cross-coupling is increased. PCB-based antennas are low-cost, less complex, and provide easy integration with radio transceivers. Therefore, in this thesis, the focus is laid on the PCB-based antenna designs to achieve high-performance.

2.6 Overview of Fundamental Antenna Parameters

For the sake of completion, a brief discussion on crucial antenna performance indicators is presented here. This section may serve as a guideline for understanding fundamental antenna performance indicators.

Consider Figure 2.6, the power provided at the input terminal of the antenna from an RF signal generator/transmitter is denoted by a P_{in}. The antenna will accept some power (P_{acc}) and reflect some power depending on the input matching. From the remaining accepted power, some of the power is dissipated inside the antenna conductor and dielectric. The remaining power is radiated from the antenna (P_{rad}), to generate a certain radiant intensity in a specified/ different direction from the antenna aperture such that $P_{rad} \leq P_{acp} \leq P_{in}$ [132].

2.6.1 Reflection Coefficient and Impedance Bandwidth

The voltage standing wave ratio (VSWR) and reflection coefficient (S11, or Γ) characterize how much power is reflected from the antenna input terminal. Often, a -10 dB level for S11 is considered a benchmark to characterize the input impedance bandwidth of the antenna, and the spectral region where the magnitude of S11 is below -10 dB is referred to -10 dB impedance bandwidth of the antenna.

$$\text{VSWR} = \frac{1 + |S11|}{1 - |\text{S11}|} \tag{2.3}$$

The bandwidth of an antenna is relative to various parameters. Usually, impedance bandwidth refers to the spectral region between higher (f_H) and lower frequency points (f_L) where |S11| ≤ -10 dB. The percentage fractional bandwidth (FBW) is another parameter that is evaluated as:

$$\text{FBW (\%)} = \frac{Bandwidth}{Center\ Frequency} = \left[2 \times \frac{f_H - f_L}{f_H + f_L}\right] \times 100 \tag{2.4}$$

2.6.2 Radiation Efficiency and Total Efficiency

The antenna radiation efficiency is calculated by the ratio of power radiated from the antenna P_{rad} to the power accepted by the antenna P_{acp} as ((2.5).

$$\text{Radiation Efficiency} = \frac{P_{rad}}{P_{acp}} \tag{2.5}$$

The radiation efficiency only accounts for losses in the antenna itself (e.g. conductive or dielectric losses), not taking the input impedance matching into consideration. Therefore, antennas with bad matching can still have a good radiation efficiency.

The total efficiency takes input impedance mismatches into account. It is thus dependent on the network the antenna is connected to.

$$\text{Total Efficiency} = \frac{P_{rad}}{P_{in}} \tag{2.6}$$

2.6.3 Directivity and Realized Gain

The directivity of an antenna is the ratio of the radiation intensity for a given direction to the radiation intensity that would be produced if the radiated power (P_{rad}) were radiated isotropically. The larger the peak directivity of an antenna, the more focused the energy is. Highly directive antennas focus the energy to the desired angle while the radiation intensity in other directions is reduced.

2.6.4 IEEE Gain

The IEEE gain (or simply gain) is the ratio of the radiation intensity in a given direction to the radiation intensity that would be produced if the accepted power (*Pacp*) were radiated isotropically. The difference between gain and directivity is only the reference power by which the radiation intensity is normalized. As the factor between radiated power and accepted power is the radiation efficiency, thus gain equals directivity and efficiency as:

$$\text{IEEE Gain} = \text{Radiaiton Efficiency} \times \text{Directivity} \tag{2.7}$$

2.6.5 Realized Gain

Note that IEEE gain does not take input impedance mismatch losses into account. The realized gain is a parameter that considers these losses as:

$$\text{Realized Gain} = \text{Total Efficiency} \times \text{Directivity} \tag{2.8}$$

The realized gain depends on the input impedance matching. Since mismatch will result in additional losses, the realized gain is smaller than the IEEE gain. The IEEE gain in return is smaller than the directivity due to the radiation efficiency. Only for an ideal lossless antenna and perfect matching can the three parameters be theoretically equal.

2.6.6 Radiation Pattern

The radiation pattern represents the spatial distribution of the electromagnetic field generated by an antenna. The antenna pattern can be expressed as a 3D plot, 2D pattern cuts, or a mathematical function. In this thesis, the array antenna will produce either a fan-shaped

radiation pattern (if the antenna has linear geometry) with a narrow half-power beamwidth (HPBW) in one spatial plane and a wider HPBW in other orthogonal plane. In the case of the planar antenna array, the directional radiation pattern is obtained by having narrow HPBW in both azimuth and elevation planes, applicable to directional mGbps P2P communication links. The HPBW is the angle within which the radiation pattern loses its half power (-3 dB, or 0.5 in linear) on both angular sides relative to the peak power. The sidelobe level (SLL) can be observed directly from the 2D radiation patterns, especially when the pattern is illustrated in normalized form.

2.7 An Overview of State-of-the-Art Reconfigurable Antennas

An antenna itself is a dumb device and is not smart/adaptive/reconfigurable! It simply radiates the energy over a specific area within a specific frequency band based on its design and geometry. However, the behavior of the antenna can be dynamically changed by incorporating auxiliary electronics with it so that an overall antenna system can respond to external software commands and reconfigure its properties and/or radiation profile, to develop a programmable and reconfigurable antenna system. The concept of smart/adaptive antennas covers different types of antenna solutions as available widely in the literature [118]. In this section, keeping the focus on advanced beamforming antenna technologies, an overview of cutting-edge novel *programmable metasurface based beamforming* antennas is presented.

With the proliferation of advanced wireless technologies such as 6G, and the modern Industry 5.0 paradigm, the concept of software-defined/software-controlled paradigm has evolved at full pace. In that view, the concept of digitally coded metasurfaces, such as Reconfigurable Intelligent Surfaces (RIS) got hype and various researchers have worked on hardware as well as signal processing aspects of RIS [31], [33], [133]–[139]. These metasurfaces are envisioned to provide seamless connectivity and enhance channel capacity through external software programs in real time and are anticipated to be applicable to mitigate non-line-of-sight scenarios. Interestingly, the modern industrial wireless paradigm is subject to change its environment from time to time and suffers from severe on-floor blockages, and jamming attacks to mitigate which smart reconfigurable wireless solutions with agile beamforming are crucial [140].

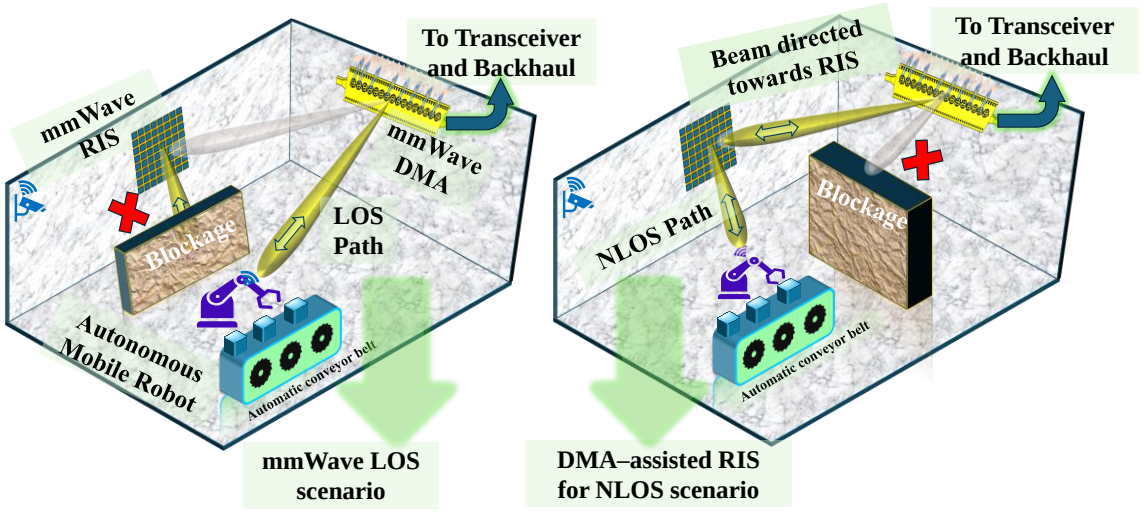

Figure 2.7. An envisioned scenario depicting *DMA–assisted RIS-enabled* software-controlled mmWave wireless paradigm to support 6G and Industry 5.0.

Since RIS is a reflective surface and requires to be excited from an external RF source antenna, therefore an overall bulky network comes into play. Moreover, typically at mmWave frequency bands, directional communication prevails due to small form factor and concept of antenna arrays. Because of this, a RIS has to be fed through directional beamforming antennas with prior knowledge of RIS location. Nevertheless, instead of reflections, the "*radiative type"* metasurfaces have recently gained attention as they possess the benefits of in-plane circuit feed, low profile, dynamic tunability, and seamless integration with the radio-frequency (RF) frontends [87], [141]–[144]. The radiative metasurface apertures truly depict antenna effects, and are referred to as DMA in the literature [143]. DMA is an emerging concept which offers controllable radiation pattern diversity and adaptability from a simplified and compact hardware. The RF excitation mechanism and beamforming mechanism of DMA are extremely simple as compared to costly, complex, and power-hungry conventional phased array antennas [109]. These antennas are also referred to as Reconfigurable Holographic Surfaces (RHS) in the literature [31], [32], [145].

This thesis explores DMAs for novel beamforming technique, their hardware-level designs, fundamental design and performance issues, and the available operating DMA hardware prototypes at different operating frequencies. Upon review, it is learned that very few DMA prototypes are reported in the literature at lower frequencies, such as, X-band (between 8 to 12 GHz) [146]–[148], 23.5 GHz [149], and 27 GHz [150], all using conventional rectangular metamaterial elements.

Moreover, usually DMAs suffer from low radiation efficiency, low gain, and high side lobes if not designed carefully, which is a potential challenge for their utilization in the communication domain. To date, there is no available DMA hardware prototype around higher mmWave bands, such as at 60 GHz or sub-THz region. Considering this challenging antenna design area as an opportunity, we designed a first-ever DMA hardware prototype around 60 GHz which produces programmable and fully controlled agile beams towards a desired direction in real-time, controlled through FPGA. A detailed design philosophy, theory of operation, radiation mechanism, and analysis of 60 GHz DMA will be presented in Chapter 5.

Based on the iterature review related to DMAs and RISs, here, we propose an insight that a DMA should not be considered as a competing device to RIS, rather a DMA might be utilized to complement a RIS to construct an overall robust and fully software-controlled reconfigurable EM wireless paradigm. To depict a typical mmWave use case in this view, a high-level conceptual diagram is shown in Figure 2.7. It demonstrates that typically in an indoor mmWave wireless communication paradigm, a DMA can serve to a user equipment through a direct LOS beam. However, if the LOS path is blocked, then the DMA should direct its beam towards the RIS (through prior knowledge of the position of the RIS), so that RIS could reflect that signal towards the intended user. Moreover, the transmission power level can be adjusted automatically from the DMA to supply a high power beam towards RIS, to maintain seamless connectivity. Often, LOS blockage can be a serious issue to mitigate which RIS is envisaged to play its tole. However, a RIS has to be excited from an external source antenna, and that aspect is neglected. Therefore, from the state-of-the-art literature review and investigations, we propose a *DMA–assisted RIS-enabled* software-controlled wireless paradigm for the next generation of wireless technologies such as 6G and Industry 5.0.

Chapter 3

Design of 57–71 GHz Frequency-Selective Beamforming Antenna Array

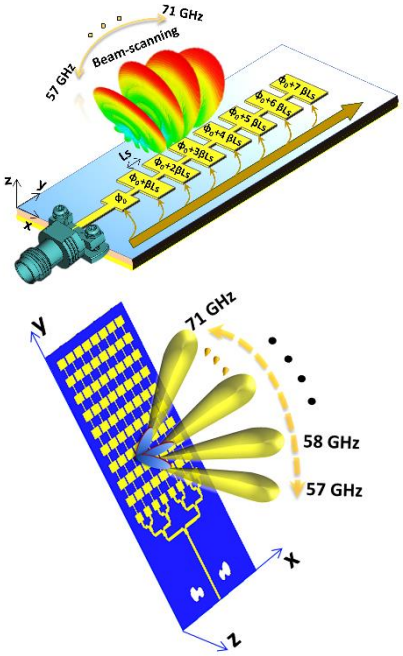

Based on the key performance metrics of the 60 GHz mmWave antennas such as wide impedance bandwidth, broad 1 dB gain bandwidth and low cost repeatable solutions, this chapter provides low cost and high performance 60 GHz antenna solution in view of these requirements. It comprehensively presents the design, analysis, and performance of the proposed wideband 8-element linear array and subsequent 64-element compact planar antenna array with passive frequency-beam scanning capability. The array is designed to cover the entire 57–71 GHz ISM band with frequency-selective passive beamscanning and simpler design geometry to reduce fabrication complexities, and in turn cost. The preliminary simulated design was reported in [151], whereas the complete design methodology, performance analysis, fabrication, measurement results, and tested use cases are published in [152].

Beamforming involves directing the radiation pattern of an antenna array towards a specific directions. Frequency selective beamforming specifically refers to the ability of an antenna array to dynamically adjust its beam direction, based on the frequency of the signal being transmitted or received. In other words, a frequency beamscanning antenna achieves this by scanning its beam across different directions or sectors within the frequency band of interest. This allows it to adaptively scan its beam towards different targets or adjust to changes in the propagation environment across different frequencies. It is worth mentioning here that frequency selevtice beamforming is an inherent property of SIW-based slotted LWAs, which are complex to fabricate due to involvement of vias. However, in this thesis, we implemented passive beamforming technique over a wide bandwidth using the simplest possible series-fed microstrip patch antenna aperture.

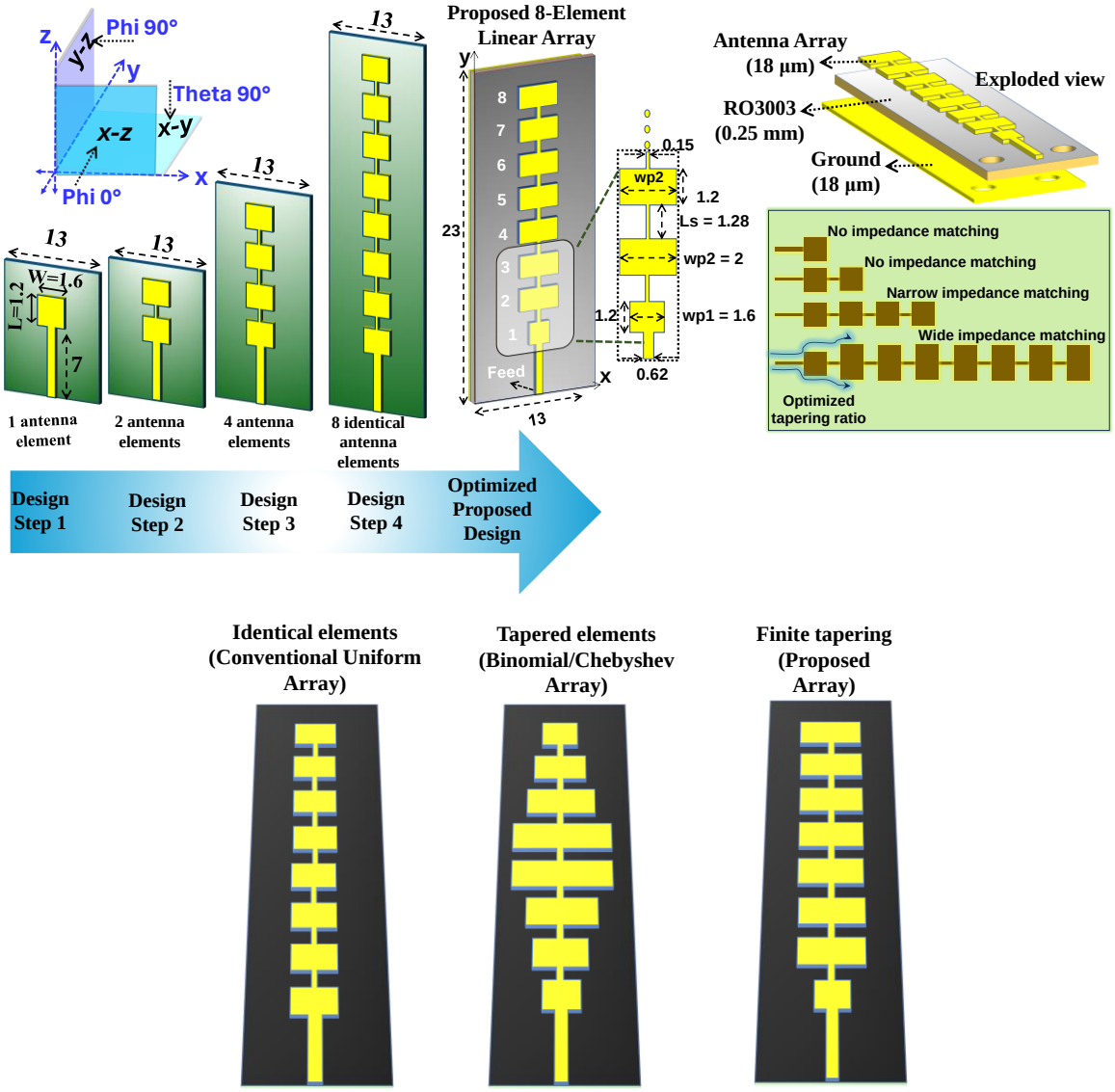

Figure 3.1. Design evolution steps and schematic diagram of the proposed 1 × 8 linear series-fed antenna array (dimensions in millimeters).

3.1 Design of 1 × 8 Linear Antenna Array

3.1.1 Design Methodology

First, the design of the proposed 8-element wideband linear antenna array based on microstrip patch elements is presented. The term linear array corresponds to the arrangement of antenna elements along one direction (i.e., either along the x-axis or y-axis). Patch antennas are inherently narrowband and often various techniques are used to enhance the bandwidth such as cuts/slots in the patch, using additional parasitic patches, or using defective ground

structures [153]–[155]. Another possibility to increase the bandwidth is to increase substrate thickness while lowering the quality factor to get around the narrow bandwidth restriction. However, increased surface waves, increased antenna dimensions, and losses would be the cost. Additionally, the stronger surface waves would alter the antenna radiation pattern and interact with other electronics on the same substrate, and potentially affect the feeding structure of the antenna which is not favorable at the 60 GHz band. In contrast to conventional patch antenna impedance matching approaches, the proposed antenna design avoids all of the aforementioned design complexities.

In the proposed solution, multiple resonances were deliberately introduced in the desired band by using multiple patch elements in series-fed topology. As the RF signal travels in the series array, the loading impedance of each patch element changes (with varying phases), and different resonant modes appear in spectral proximity in a way that they get close to each other. As a result, a wideband -10 dB impedance matching was achieved.

3.1.2 Antenna Design Parameters and Design Evolution Steps

The design evolution steps with optimized dimensions to reach an 8-element series-fed array are shown in Figure 3.1. Initially, the width (W) and length (L) of the microstrip patch element at 60 GHz were calculated using standard patch antenna equations as [156]:

$$W = \frac{c}{2f_r}\sqrt{\frac{2}{\varepsilon_r + 1}} \tag{3.1}$$

$$L = \frac{c}{2f_r\sqrt{\varepsilon_{eff}}} - 2\Delta L \tag{3.2}$$

The effective permittivity and extended length were calculated as:

$$\varepsilon_{eff} = \frac{\varepsilon_r + 1}{2} + \frac{\varepsilon_r - 1}{2}[1 + 12\frac{h}{W}]^{\frac{1}{2}} \tag{3.3}$$

$$\Delta L = 0.412h\frac{(\varepsilon_{eff} + 0.3)(\frac{W}{h} + 0.264)}{(\varepsilon_{eff} - 0.258)(\frac{W}{h} + 0.8)} \tag{3.4}$$

here f_r = center operational frequency, c= speed of light, ε_r = relative permittivity of the substrate, ε_{eff} = effective relative permittivity of the substrate, h = the thickness of the substrate, and ΔL = extended length of the patch that depends on width and height of the substrate.

A thin 0.25 mm Rogers 3003 material was used as a substrate with given dielectric constant of 3, copper conductor layer of 18 microns, and loss tangent of 0.001. Initially, a half-wavelength patch (with a length of 1.2 mm and width of 1.6 mm) corresponding to 62 GHz was designed. A full ground plane is used at the bottom of the substrate to achieve a broadside radiation pattern. A 50 Ω feed line (edge-launched feed) was used to excite the patch.

Contrary to the conventional uniform distribution, binomial distribution, or Chebyshev distribution [157], the tapering of the other 7 patches (patches 2 to 8) was optimized to 2 mm (instead of 1.6 mm width of patch 1), here called as finite tapering. The input impedance of each patch is loaded with the series-fed microstrip transmission line (MTL) and the patch next to it, which varies with operating frequency and affects the overall reflection coefficient, as elucidated through numerical simulations. Moreover, a reasonable theoretical interpretation about the input impedance of a generic 9-element series-fed array is reported in [158]. Moreover, it can be noticed from Figure 3.1 (bottom figure) that the binomial/Chebyshev array distribiutions present higher element size towards the center of the array, which would increase the total array size in case of large planar arrays.

Of the three array distributions (uniform, binomial, and Chebyshev), a uniform amplitude array yields the smallest HPBW (and the highest directivity). It is followed, in order, by the Chebyshev and binomial arrays. In contrast, binomial arrays usually possess the smallest SLL followed, in order, by the Chebyshev and uniform arrays [118]. The proposed array resembles closely to uniform array case except finite tapering of the first patch element.

3.1.3 Parametric Optimization and Analysis

Initially, the impedance of the single patch element was found to be around 210 Ω. The connecting MTL has a thin width of 0.15 mm, which lies within the fabrication limits. As shown in Figure 3.1, by loading the initial patch element to the seven other optimized patches and seven optimized MTLs, the impedance characteristics of each patch element change, including varying phases. This design methodology leads to the emergence of different resonant modes in close spectral proximity, such as at 57.1, 60.04, 62.31, 67.81, and 70.61 GHz in case of the proposed array design. Consequently, the antenna array achieves a broad -10 dB

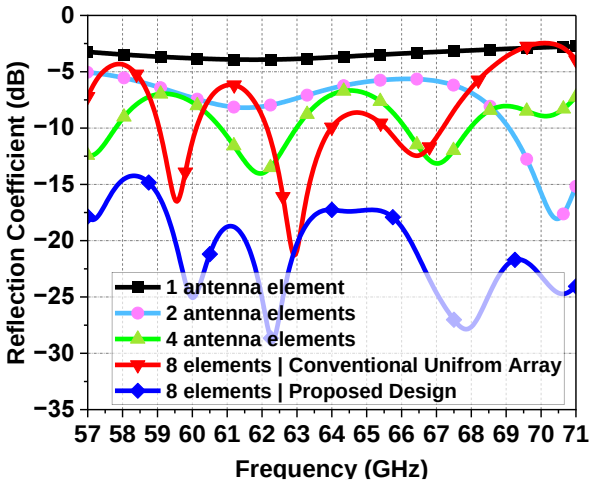

Figure 3.2. Simulated reflection coefficient for different design evolution steps.

impedance matching, while achieving an overall average input impedance of 50 Ω. The series MTL has an optimized width of 0.15 mm (must be within fabrication limits) and a length (*Ls*) of 1.28 mm. For simulations, a full wave electromagnetic solver, Computer Simulation Technology (CST) Microwave Studio was used.

It is evident from Figure 3.2 that with all identical patch elements (i.e., the case of the uniformly distributed array), -10 dB impedance bandwidth is limited with few resonance points. Similarly, as tapering was increased towards the center of the array (i.e., wp_2 = 2.2, 2.4, 2.6 mm which tends to be the case of binomial/Chebyshev distribution), the bandwidth became quite smaller (less than 2 GHz) with reduced flat gain and also leads to increased size of patch elements. However, with the proposed design approach of finite tapering, the entire 57–71 GHz band is covered. The wide achieved bandwidth is due to the combination of finite tapering, fine tuning of interelement distance, as well as optimization of the overall geometric dimensions.

Another aspect of the wide achieved bandwidth of proposed design is that since the wave phenomenon of the series-fed array (as described in section 3.1.4.4) is similar to the travelling wave leaky wave antennas which are usually wideband due to multiple resonance modes inside the antenna aperture, therefore, more number of patch elements were added in the series-fed array topology to mimic the behavior of a travelling wave leaky wave antennas, while still keeping the design to the simplest possible level (without any vias).

The effect of the tapering width (wp_2) of the patch elements and length (*Ls*) of the series-connected MTL on impedance bandwidth is shown in Figure 3.3 and Figure 3.4 respectively. Note that in Figure 3.3, the curves for wp_1=wp_2 correspond to all identical elements including the first patch element, which becomes the case of a conventional uniform distributed array

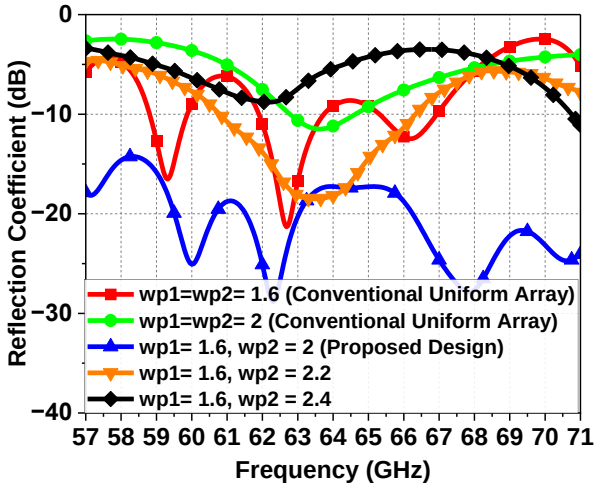

Figure 3.3. Effect of width tapering on -10 dB impedance bandwidth of the proposed 1 × 8 array.

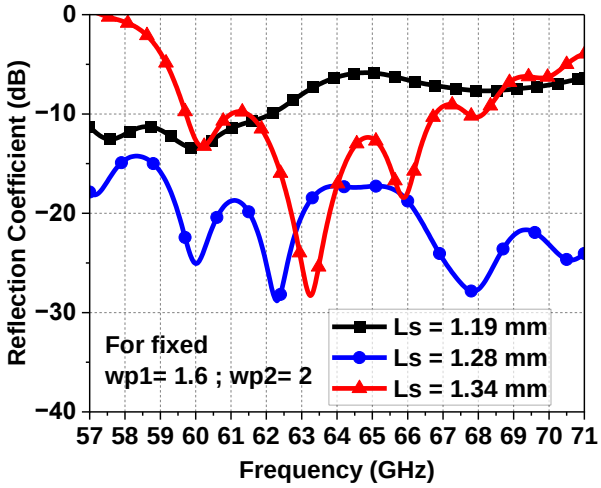

Figure 3.4 Effect of change in the length of series-connecting MTL array of the proposed 1 × 8 array.

and shows limited bandwidth. Moreover, its gain fluctuation is also high in the band of interest. The impact of *Ls* on the reflection coefficient was analyzed by keeping the widths constant as shown in Figure 3.4, and *Ls* was parametrized to various lengths. The optimized *Ls* dimension was set at 1.28 mm (0.256 λ_0 at 60 GHz), which produced the desired result.

Initially, a preliminary design based on Rogers 4003c substrate was published in [151], however, its gain variation was more than 2.5 dB above 67 GHz with less than 80% radiation efficiency. As presented above, the Rogers 3003 substrate with dielectric constant of 3, thickness of 0.25 mm, and dissipation factor (loss tangent) of 0.001 was then employed that manifested high-performance metrics such as wide bandwidth and flat gain with less than 1 dB gain variation in 57–71 GHz [152].

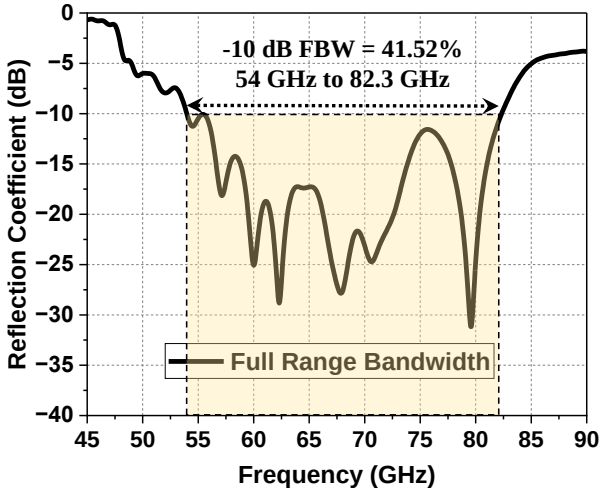

Figure 3.5. Achieved full range reflection coefficient of the proposed 1 × 8 array, revealing 41.52% FBW.

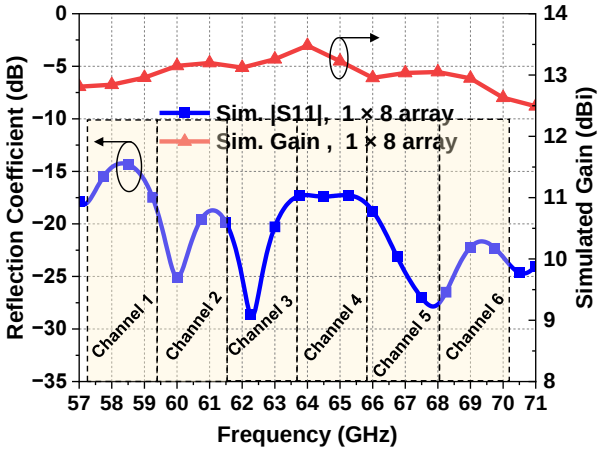

Figure 3.6. Simulated reflection coefficient and realized gain of the proposed 1 × 8 array.

3.1.4 Simulated Results of the Proposed 1 × 8 Linear Array

3.1.4.1 Bandwidth and Realized Gain

The optimized full-range simulated reflection coefficient (-10 dB impedance) of the proposed 1 × 8 linear array is shown in Figure 3.5. The array provides 41.52% FBW from 54–82.3 GHz. However, as our band of interest is 57–71 GHz, therefore all other results are presented in this frequency range. The -10 dB reflection coefficient along with the realized gain covering all 6 channels of 60 GHz ISM band is shown in Figure 3.6. The peak realized gain of 13.48 dBi at 64 GHz is observed, whereas the realized gain is above 12.56 dBi in 57.24–70.20 GHz (all 6 channels of 60 GHz ISM band), thereby providing less than 1 dB gain variation in the entire desired band of interest. In other words, 1 dB gain-bandwidth is 13 GHz which is the hallmark of the proposed antenna array design.

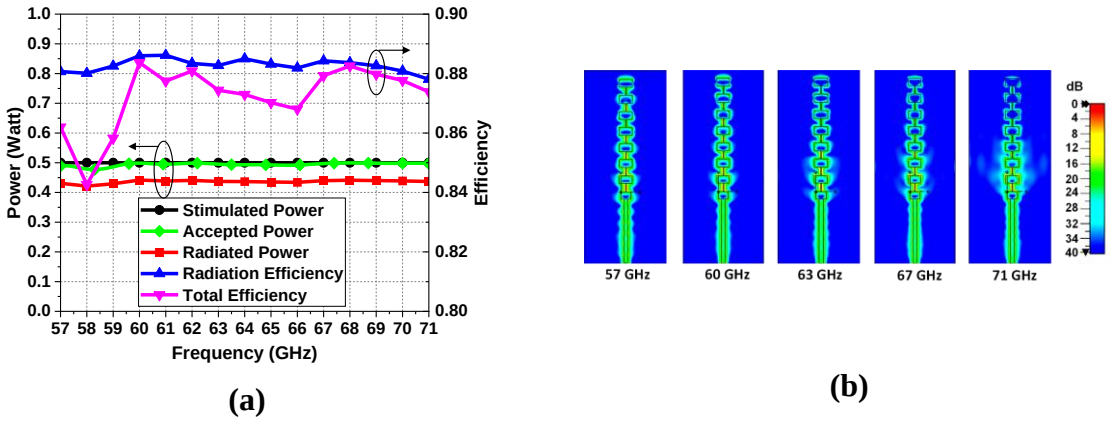

Figure 3.7. (a) Power and efficiency profile. (b) E-field distribution of the proposed 1 × 8 array.

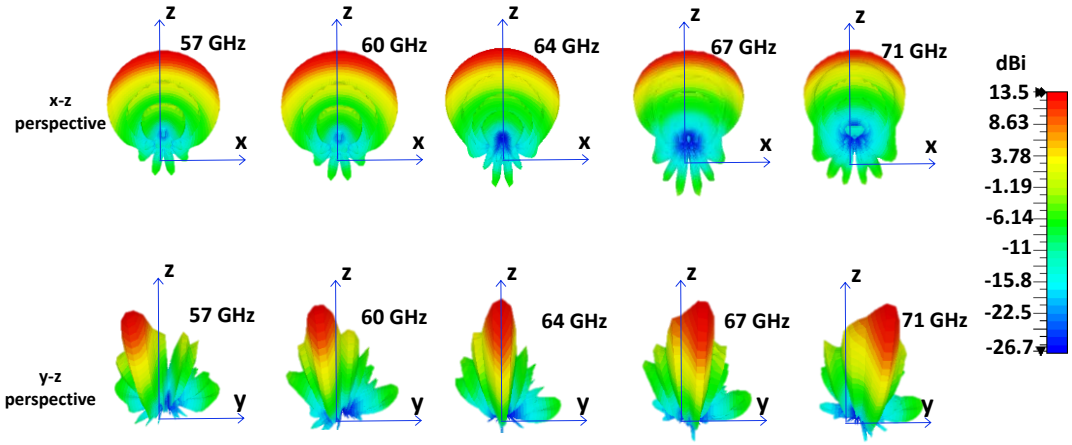

Figure 3.8. 3D simulated radiation patterns of the proposed 1 × 8 array in 57–71 GHz band from two different angular perspectives. (top) co-polar x-z perspective (bottom) co-polar y-z perspective.

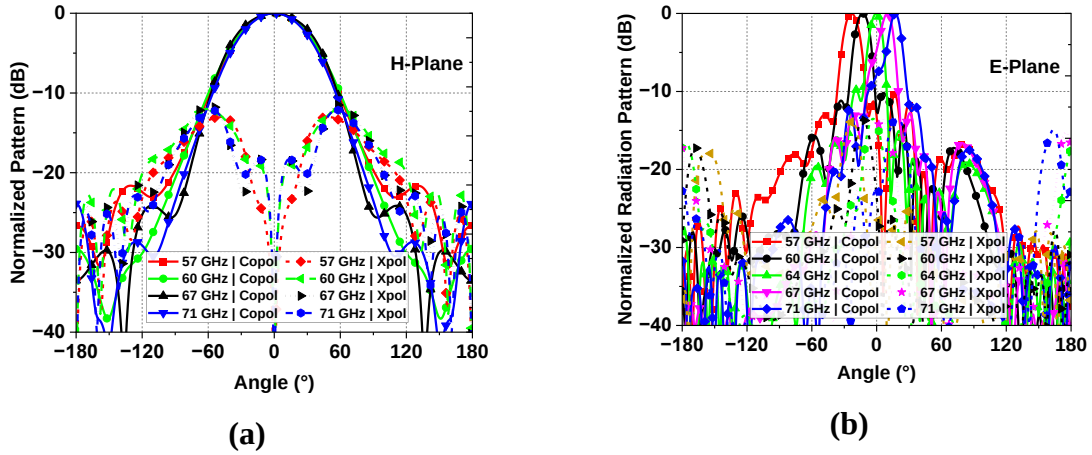

Figure 3.9. 2D rectangular plots of simulated radiation patterns of the proposed 1 × 8 array across 57–71 GHz band. (a) co and x-pol x-z plane/azimuth/phi 0°. (b) co and x-pol y-z plane/elevation/phi 90°.

3.1.4.2 Power Profile and Efficiency

The power profile of the antenna is shown in Figure 3.7(a). For an input-stimulated signal of 0.5 W, the accepted power is above 0.477 W throughout 57–71 GHz. The radiated power varies between 0.421 W to 0.441 W, which results in above 87.81% radiation efficiency and above 84.26% total efficiency in the whole 57–71 GHz band. The E-filed distribution at different operating frequency points is demonstrated in Figure 3.7(b), showing almost uniform field strength till 67 GHz, however note that as the frequency moves to higher end (71 GHz), the field strength is less intense at the end elements and more spurious radiations are produced near the initial elements. This might lead to relatively high SLL and pattern distortion at higher frequency, as revealed in Figure 3.8 (pattern at 71 GHz).

3.1.4.3 Radiation Patterns

The 3D radiation patterns at various frequency points are shown in Figure 3.8 whereas 2D patterns are presented in Figure 3.9. A fan-shaped radiation pattern is observed with a wider HPBW in the x-z -plane (phi 0°) ranging between 63.44° to 77° across the 57-71 GHz band. Narrow HPBW is achieved in the y-z plane (phi 90°) ranging between 12° to 14°. This is due to the linear geometry of the array in which the radiation pattern is squeezed along the direction of elements while expanding in the orthogonal direction. The array is broadside at 64 GHz. The SLLs are below -10 dB in both planes. Note that beyond 67 GHz, the beamwidth appears to be increased somehow, that can be seen especially in 3D pattern. However, this is due to the shoulder effect of the series fed array. In other words, the SLL is increased on one side which appears to be like a small fan-shaped pattern in y-z plane.

The array is linearly polarized. A linear polarized antenna typically exhibits lower cross-polarization levels, as verified by Figure 3.9 (a) and (b). It indicates that the array can provide better discrimination between the desired signal and unwanted signals with different polarization. Moreover, the linear polarized antennas may experience reduced multipath interference compared to circular polarized antennas. This polarization purity is particularly beneficial in environments with strong reflective surfaces, such as harsh industrial environments. Nevertheless, this is quite application-specific. For instance, a polarization mismatch between vertical linear and horizontal linear antennas would lead to loss of signal. In that case, circular polarization (CP) is helpful as it would only cause a 3 dB loss in power

but not the whole signal. However, left-hand CP and right-hand CP would again cause a complete loss in the signal.

The fan beam pattern has applications in P2MP connectivity in various indoor mmWave wireless industrial applications which include IIoT, sensing and monitoring industrial processes for data collection and proactive analysis, predictive maintenance, asset tracking, and collision avoidance [159]–[162], as well as efficient energy transport over 60 GHz for IWSN [163].

3.1.4.4 Frequency Beamscanning Analysis

The antenna's main beam can be scanned either electronically or in a passive way. Frequency beamscanning is a type of passive beamscanning in which the direction of the main beam varies with the change in operating frequency due to the analog phase shifts that apply the same phase shift for signals at different frequencies. When the signal bandwidth is large, the fixed antenna spacing in the series-fed topology induces frequency-dependent phase shifts across the array, causing the frequency-dependent beam-scanning phenomenon, as conceptually illustrated in Figure 3.10. The phase variation along the series-fed elements at each operating frequency acts as ϕ, $\phi+\beta Ls$, $\phi+2\beta Ls$,… , $\phi(n-1)\beta Ls$, where ϕ is the reference phase at the first element, and n is a total number of elements of the array. In fact, βLs is the electrical length that adds a phase shift along the direction of the array. Here, $\beta=2\pi/\lambda_g$ is the phase constant of the propagation wave and is a frequency-dependent parameter. It indicates how the phase of the wave changes as it travels through a medium. Ls represents the length of the MTL between two patch elements over which the wave propagates.

For each operating frequency, the parameter β alters, leading to a change in the total accumulated phase across the antenna aperture at that frequency. Thus, the total phase shift along the y-coordinate (where elements are arranged in series) is contributed from the phase accumulation "βLs" of the wave propagation which results in the frequency beam-scanning phenomenon. The u-v heat maps in Figure 3.11 demonstrate that the main beam shifts in the elevation plane with the change in operating frequency. Such wideband beamscanning antenna performance is desirable for various IIoT applications as well as wideband mmWave frequency scanning radars, as depicted in Figure 3.12.

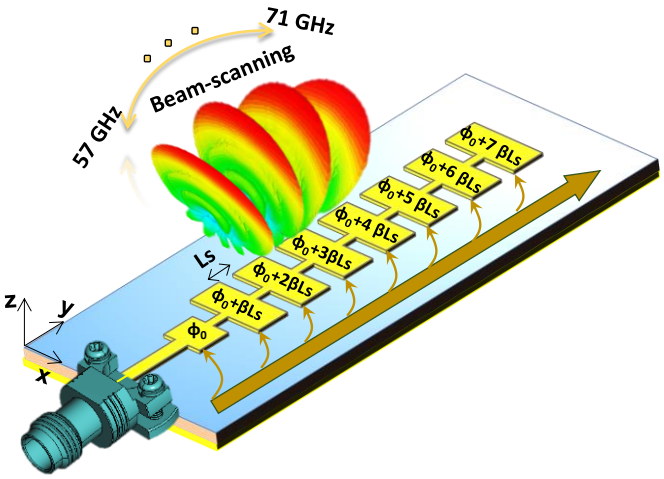

Figure 3.10. Illustration of the wave formation across the antenna aperture. The total phase shift along the y-coordinate is contributed by the phase accumulation βLs of the guided wave propagation. The varying net phase relative to the operating frequency results.

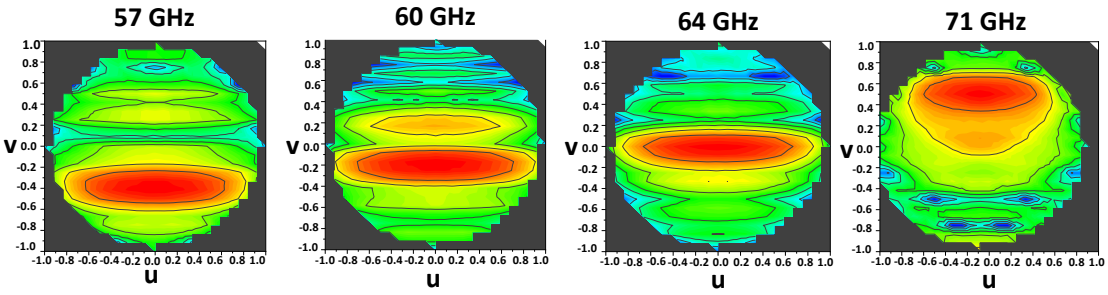

Figure 3.11. Demonstration of frequency beamscanning of the proposed 1 × 8 array (extracted from CST Microwave Studio and post-processed in OriginPro software).

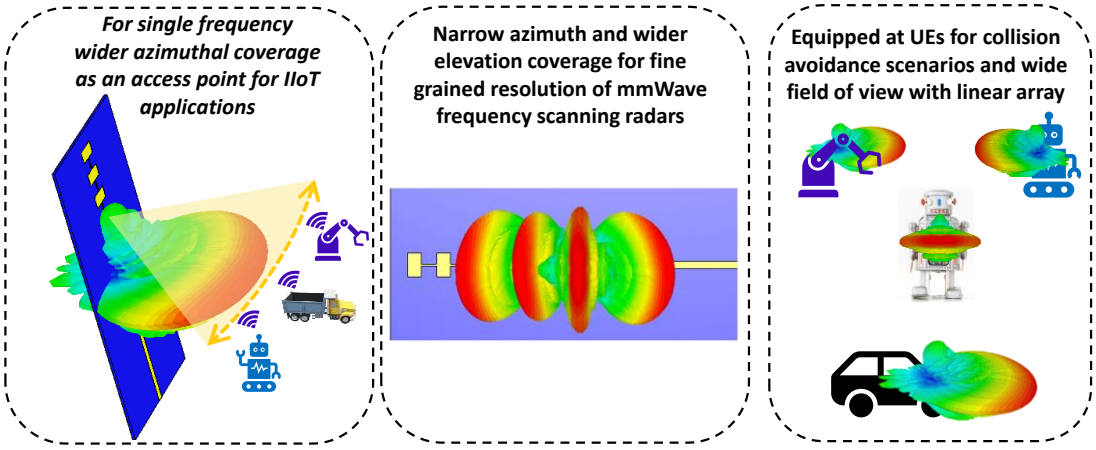

Figure 3.12. Application scenarios of the linear antenna array with fan beams.

3.2 Design of 64-Element (8 × 8) Planar Array

3.2.1 Design Methodology

As described in Chapter 1, the atmospheric absorption and EM wave attenuation are the highest around the 60 GHz band, therefore high-gain directional antenna beams are often required to mitigate path loss. The high gain of the antenna array translates into a reduction of the transmit power needed for a given link performance and enhances SNR at the receiver end. Thus, in a harsh industrial environment, the high-gain antenna array at 60 GHz is crucial to mitigate path loss and facilitates reliable connectivity over a distance of tens of meters.

The feed network for an antenna array can either be designed using a corporate feed (also called a parallel feed), or a series-feed network as implemented in the above sections. In a corporate feed network, the main RF signal is symmetrically divided into two or more required paths such that each radiating element is excited with the same phase, as shown in Figure 3.13(a). In a series-fed array configuration, one of the array elements is directly provided with RF energy from the source, while the other antenna elements are excited indirectly through a series transmission line, as shown in Figure 3.13(b). Both of these arrangements lead to a linear array leading to two limitations: first iswith the gain is not increased after a certain array size, and second is that the array size becomes too large in one dimension. In this work, to design a compact and high-gain array, a hybrid parallel-series array topology is utilized as demonstrated in Figure 3.13(c). An 8-channel equal power divider is designed and integrated with eight of the above-described linear sub-arrays at each output port of the divider, as shown in Figure 3.14(a).

Each proposed 8-element (1 × 8) linear array serves as a sub-array to design a compact 64-element (8 × 8) planar array. To avoid grating lobes (multiple maxima), the inter-element separation should not exceed half wavelength, whereas to avoid aliasing and misplaced nulls, the interelement spacing should be less than or equal to $\lambda/2$. Thus, the gap between the consecutive antenna elements is optimized and finally kept at $0.48\ \lambda_0$ (where λ_0 is the free space wavelength at 60 GHz).

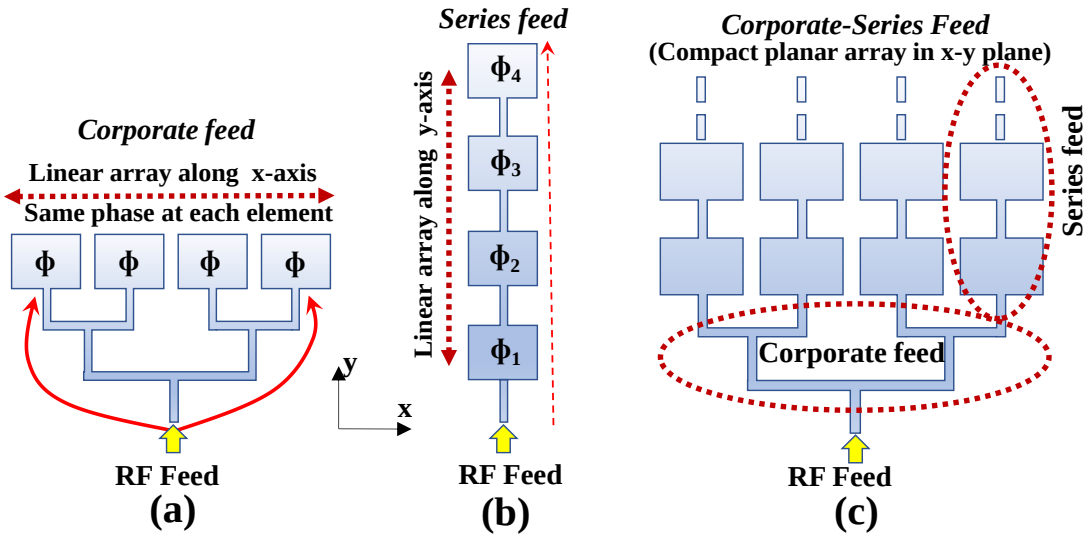

Figure 3.13. Conceptual depiction of different types of feed mechanisms for antenna arrays. (a) corporate feed. (b) series feed. (c) hybrid or corporate-series-feed.

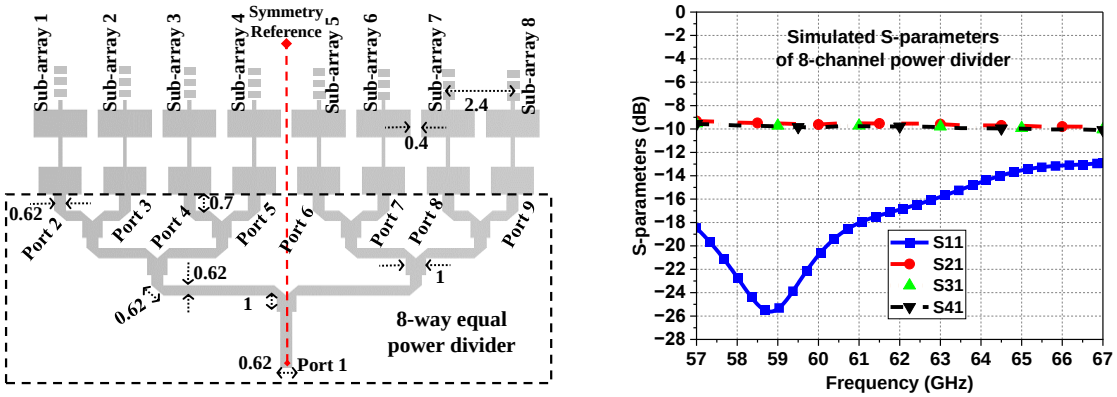

Figure 3.14. (a) Schematic of 8-way equal power divider to excite 8 linear sub-arrays in a parallel-series topology (dimensions in mm). (b) Scattering parameters of the power divider.

3.2.2 Simulated Results and Analysis of 8 × 8 Array

The consistency in the magnitude and phase of the transmission coefficients of a power divider is crucial for the reliable transmission of data packets for accurate delivery of signals to the nodes of industrial access networks [164]. The RF power divider should have low insertion loss, and maximum power should be available at each output port (i.e., at each input of the sub-array antenna) with equal magnitude and phase. Note that in the case of an 8-way equal power divider, 1/8 of the total power (equivalent to -9.03 dB) should ideally be available to each outport port (port 2 to port 9 as labeled in Figure 3.14(a)).

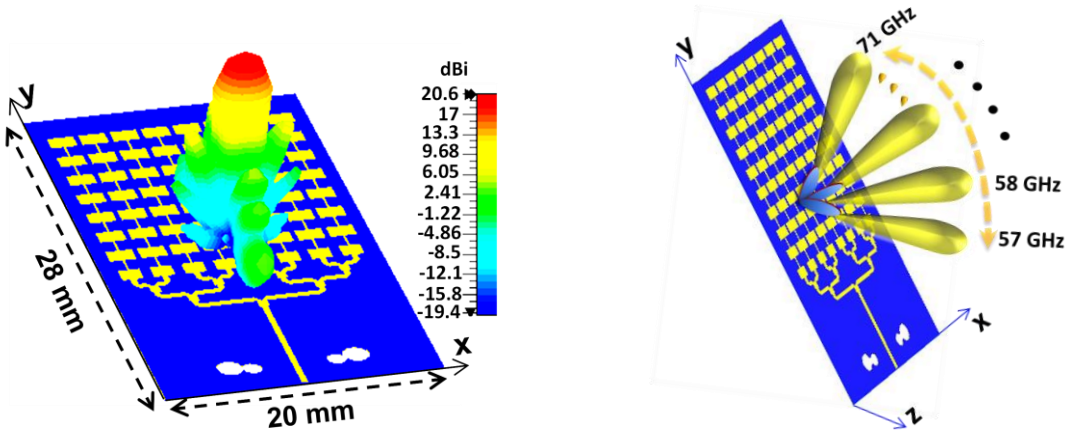

Figure 3.15. 3-D simulated design of the proposed planar array with broadside beam at 64 GHz.

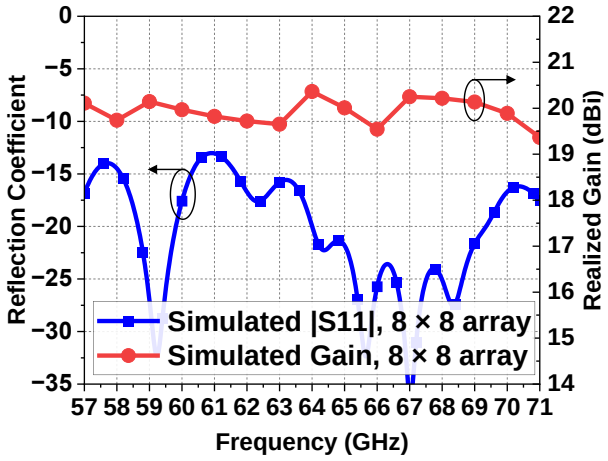

Figure 3.16. Simulated reflection coefficient and realized gain of the proposed 8 × 8 array.

The scattering parameters of the power divider are shown in Figure 3.14(b). The transmission coefficient (|S21|, or insertion loss of the power divider) is within -9.6 to -10.1 dB. The reflection coefficient (|S11|) is lower than -10 dB within the desired band of interest.

The 3-D schematic view of the proposed 64-element (8 × 8) array is shown in Figure 3.15. The simulated reflection coefficient and realized gain are shown in Figure 3.16. The planar array provides a peak simulated realized gain of 20.79 dBi at 64.5 GHz, whereas the simulated realized gain is above 19.65 dBi in the 57–70.5 GHz band, revealing high gain flatness over a wide band of interest. The 2-D radiation patterns in the x-z and y-z planes are shown in Figure 3.17 (a) and (b) respectively. High-gain directional radiation patterns with narrow beamwidth in both azimuth and elevation planes are achieved. Within 57–70.5 GHz, the simulated HPBW varies between 10.87° to 13.14° in the azimuth plane and 7.86° to 10.98° in the elevation plane.

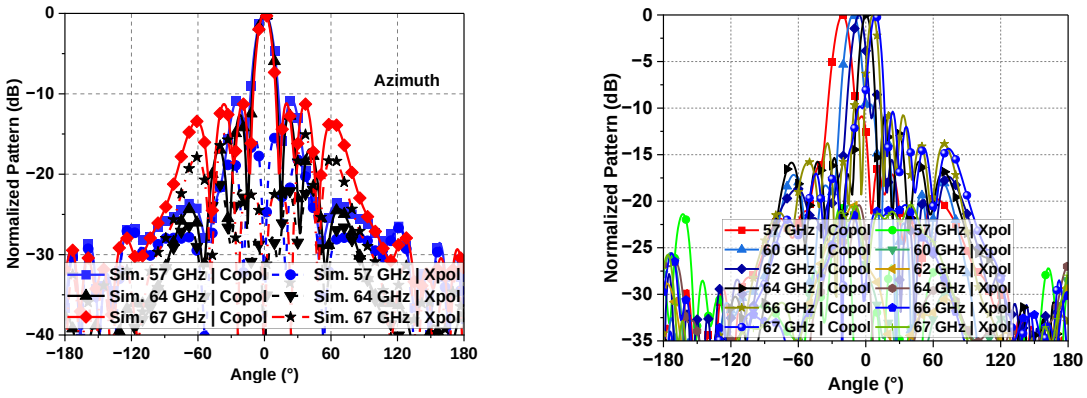

(a) (b)

Figure 3.17. Simulated normalized radiation patterns of 8 × 8 array at various operating frequency points. (a) in the azimuth (x-z) plane. (b) in the elevation (y-z) plane.

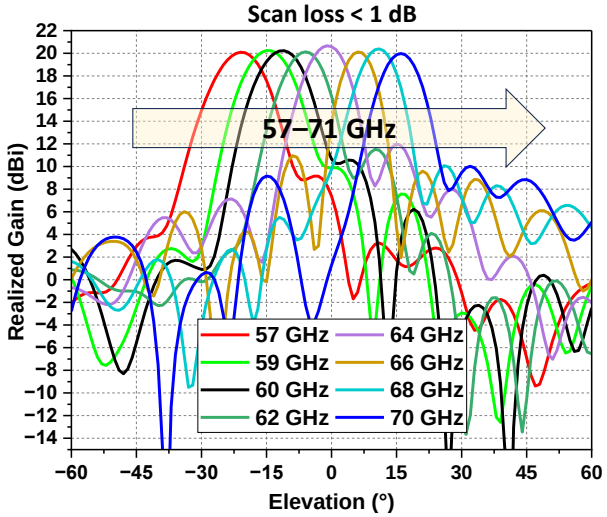

Figure 3.18. The un-normalzied absolute realized gain pattern in the y-z plane showing frequency beamscanning with scan loss is below 1 dB across 57–71 GHz.

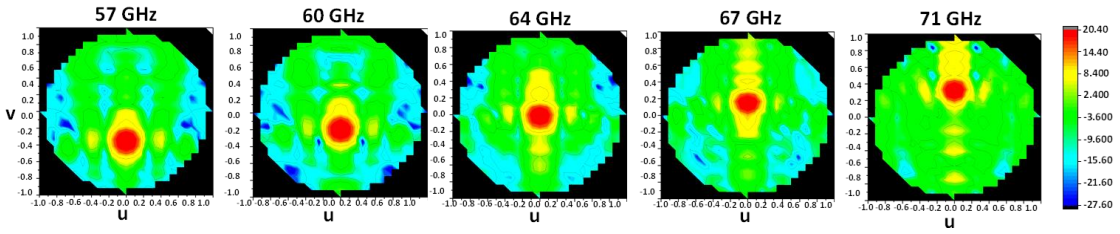

Figure 3.19. Demonstration of frequency beamscanning through heat maps (extracted from CST Microwave Studio and post-processed in OriginPro software).

The SLLs are below -10 dB, and the x-pol levels in the direction of the main beam are below -20 dB. The radiation efficiency of the 8 × 8 array is above 83 % in the 57–71 GHz band. The scan loss across frequency-beam scanning is less than 1 dB in the whole band of interest, as illustrated in Figure 3.18. The heat maps presented in Figure 3.19 provide a clear visualization of frequency beamscanning in the elevation plane.

3.3 Prototype Fabrication and Measurement Results

The fabricated prototypes of the proposed 1 × 8 and 8 × 8 arrays are shown in Figure 3.20. The size of the 8 × 8 array including the power divider is 20 mm (4 λ_0) × 28 mm (5.6 λ_0) × 0.25 mm (0.05λ_0), where λ_0 is free space wavelength at 60 GHz. The fabrication was made using the LPKF ProMat S103 milling machine. For RF feed, a 1.85 mm standard solderless connector was used which provides mode-free operation in the V-band. At mmWave bands, soldering can add additional losses and can lead to changes in the desired resonance frequencies if done imperfectly, therefore solderless connectors are preferable for practical measurements. Moreover, since 1.85 mm RF connectors are expensive, therefore the reusability feature of solderless connectors makes them a cost-effective solution. The dimensions of the connector are presented in Appendix C.

3.3.1 Measurement of Reflection Coefficient

The reflection coefficient was measured on the *Agilent E8361A* vector network analyzer (VNA) as shown in Figure 3.21. Here, it is instructive to mention that we utilized 1.85 mm standard RF equipment in our measurement setup, which supports a maximum frequency of 67 GHz. Consequently, the measured results onwards are presented here within the 57–67 GHz range. The VNA is calibrated before reflection coefficient measurements. The measured reflection coefficients for both arrays are shown in Figure 3.21. Note that the connector might lead to a higher reflection coefficient, however, the resonance trend is quite similar to that without the connector. The measured reflection coefficient shows a -10 dB level covering the entire 57–67 GHz band. The deviations observed in the measured |S11| are due to many practical reasons, amongst which fabrication tolerance is prominent.

3.3.2 Measurements of Realized Gain and Efficiency

An over-the-air (OTA) antenna measurement setup was prepared in an open space of an indoor lab environment to measure far-field radiation patterns and gain, as shown in Figure 3.22. A complete anechoic chamber is not needed for 60 GHz measurements due to directional characteristics and high path loss at this band. Note that this feature stands out as a key advantage of mmWave bands, contributing to the inherent security of critical mmWave industrial communication. A standard gain V-band horn antenna was used as a transmitter (Tx), whereas the proposed array under test (AUT/Rx antenna) was mounted on a 360°

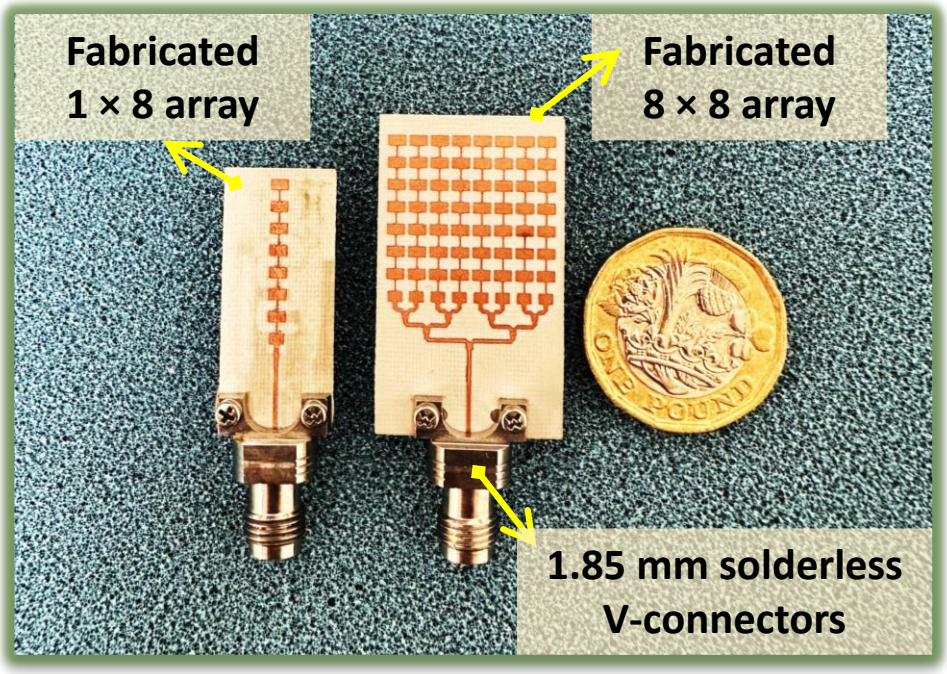

Figure 3.20. Fabricated prototypes of linear and planar antenna arrays.

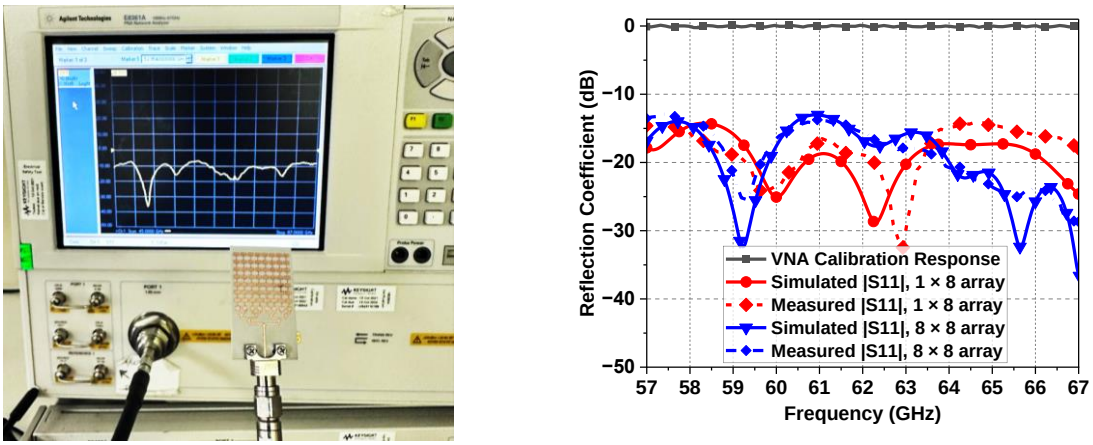

Figure 3.21. Measured S11 of linear and planar arrays along with measurement setup using E8361A VNA.

rotator/turntable. The turntable is attached to a PI motor controller and the rotation was automated using LabVIEW with a precise angular resolution of 1° step.

The distance between the Tx and Rx antennas was set as 29 cm (for 1 × 8 array) and 62 cm (for 8 × 8 array) to satisfy the far-field condition. Since we aim to design a wideband high-gain compact array, therefore onwards the measured patterns of the 8 × 8 array are shown. Nevertheless, the measured gain and radiation patterns of the 1 × 8 array were observed in good

agreement with the simulations, validated by measured S11 and gain as in Figure 3.21 and Figure 3.24(a) respectively. The measurement setup of 1 × 8 array is shown in Appendix A.

The gain was measured using the relative gain comparison method [118]. Two sets of measurements were performed at each frequency at a single direction of maximum power with a 1 GHz step in the 57–67 band and S21 was measured on VNA. In one set, S21 was measured using two identical horn antennas ($S_{21_{horn}}$), whereas, in the other set, one of the horns was replaced with the proposed array ($S_{21_{array(dB)}}$). At each test frequency, the gain (in dB scale) was calculated by $G_{array_{(dB)}} = G_{horn_{(dB)}} + S_{21_{array(dB)}} - S_{21_{horn(dB)}}$, where G_{array} is the measured gain of the array at a fixed frequency and G_{horn} is the known gain of the standard gain horn antenna at that frequency. A detailed derivation of this formula is provided in Figure 3.23. The measured gain, directivity, and radiation efficiency of the proposed 8 × 8 array are shown in Figure 3.24(b). The peak measured gain is 20.12 dBi at 64 GHz. The measured gain is above 19.23 dBi throughout the band of interest, thereby providing a measured 1 dB gain bandwidth of more than 13 GHz.

The calculated radiation efficiency was found using the measured gain as:

$$Calulated\ Efficiency\ = \frac{Measured\ Gain}{Simulated\ Directivity} \tag{3.5}$$

. The peak aperture efficiency of 8 × 8 array is 61.79% at 57 GHz. Aperture efficiency is a measure of how effectively the antenna's physical area is used. At each operating frequency (or corresponding free-space wavelength λ), the aperture efficiency was calculated using measured gain and effective physical area ($W \times L$) of 8 × 8 array, excluding power divider as:

$$Aperture\ Efficiency\ = \frac{Gain_{measured} \times \lambda^2}{4\pi \times W \times L} \tag{3.6}$$

From Figure 3.24(b), note that the aperture efficiency drops as the frequency increases. Using (3.6), this can be juistified as the physical size (W and L) of the array is fixed, and gain is also flat across the frequency band, therefore the only dominant factor controlling the aperture efficiency is the wavelength which is in direct relation with the aperture efficienc . Since the wavelength decreases with the increase in frequency, therefore the aperture efficiency is decreasing as the operating frequency is increased.

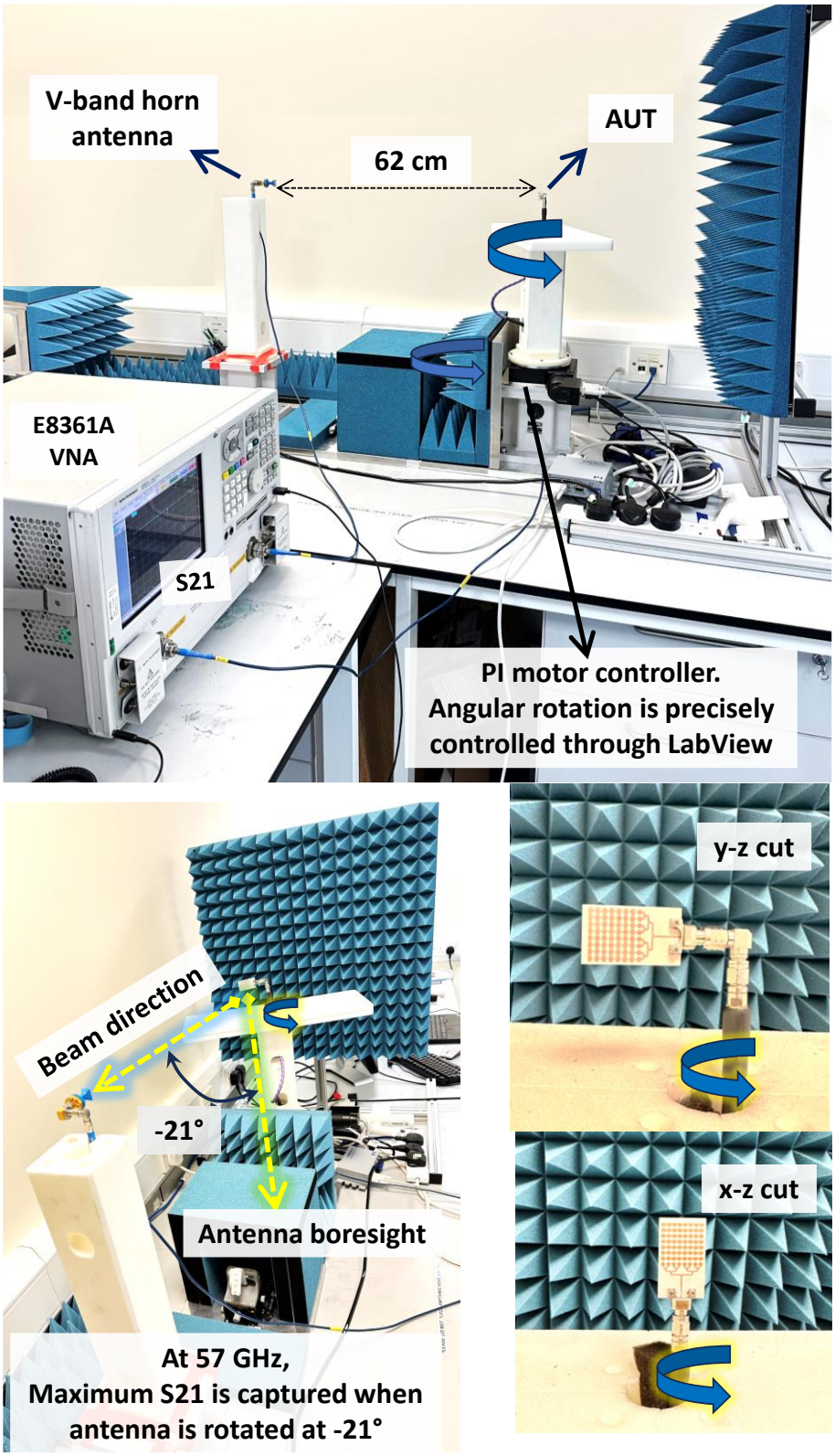

Figure 3.22. OTA mmWave radiation pattern and gain measurement setup.

Gain Measurement Through Gain-Comparison Method

Friis Equation

$$P_R = P_T + G_T + G_R - P_L \quad \textit{dB Scale}$$

P_{AUT} = Received power by antenna under test
P_{Horn} = Received power by standard gain Horn antenna
P_T = Transmit power
G_T = Gain of Transmitting Antenna
G_{AUT} = Gain of Antenna Under Test (G_{AUT})
G_{Horn} = Gain of standard gain horn antenna (known gain)
PL = Pathloss

(Using standard gain horn antenna)

$$P_{Horn} = P_T + G_T + G_{Horn} - P_L \longrightarrow (1)$$

$Note\ that: P_{HORN} - P_T = S21_{Horn}\ (dB)\ on\ VNA$

(Using AUT)

$$P_{AUT} = P_T + G_T + G_{AUT} - P_L \longrightarrow (2)$$

$Note\ that: P_{AUT} - P_T = S21_{AUT}(dB)\ on\ VNA$

Insert value of G_T from equation (1) in equation (2), and solve (2) for P_{AUT}

$$P_{AUT} = P_T + (P_{Horn} - P_T - G_{Horn} + P_L) + G_{AUT} - P_L$$

$$(P_{AUT} - P_T) = (P_{Horn} - P_T) - G_{Horn} + \cancel{P_L} + G_{AUT} - \cancel{P_L}$$

$= S21_{AUT}$ $= S21_{Horn}$

$$G_{AUT}\ (dBi) = G_{Horn}\ (dBi) + S21_{AUT}(dB) - S21_{Horn}(dB)$$

Figure 3.23. Mathematical derivation to calculate the gain from the gain comparison method.

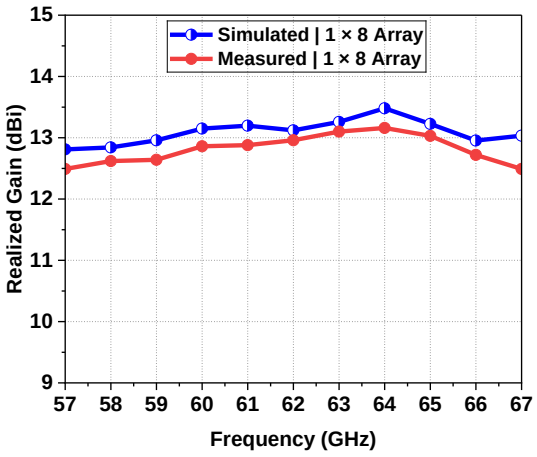

(a)

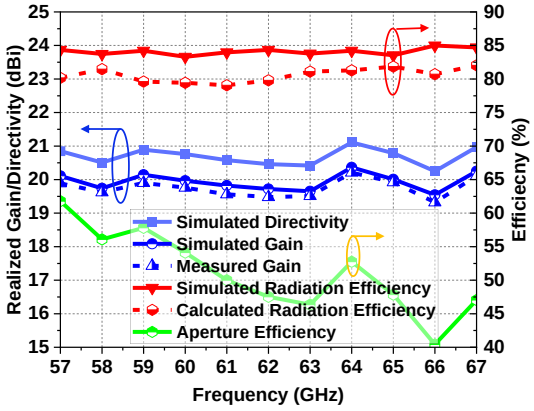

(b)

Figure 3.24. (a) Measured gain of 1 × 8 array. (b) Measured gain, calculated radiation efficiency, and aperture efficiency of 8 × 8 array.

3.3.3 Measurements of Radiation Pattern

The radiation patterns were measured in both azimuth and elevation planes in 1° resolution from -90° to +90°. The measured radiation patterns in the x-z plane (as phi 0° of simulated reference) at 57, 64, and 67 GHz are shown in Figure 3.25, which matches quite well with the simulated results. The SLLs are below -10 dB and x-pol levels are below -30 dB in the direction of the main lobe.

The measured radiation pattern in the elevation (y-z) plane in the 57-67 GHz range was measured by rotating the array as well as horn to 90° as demonstrated in Figure 3.22. The elevation plane is the principal plane of beam-scanning because the elements' arrangement is along the y-axis. Measured radiation patterns in the elevation plane are shown in Figure 3.26. The measured HPBW ranges between 8.1° to 10.8° from 57–67 GHz in the y-z plane. SLL is less than -10 dB and x-pol levels are below -20 dB.

Another visualization of the measured frequency beam-scanning performance of the proposed 8 × 8 array in the elevation plane in polar form as well as with the direction of 3D beams is demonstrated in Figure 3.27.

3.3.4 Comparison of the Proposed Antenna With State-of-the-Art

The performance comparison of the proposed array design with other closely related antenna arrays at the 60 GHz band available in the literature is presented in Table 3.1. It can be noticed that the proposed array outperforms various other designs in terms of high-performance indicators such as wide impedance BW, and high flat gain while maintaining a compact size.

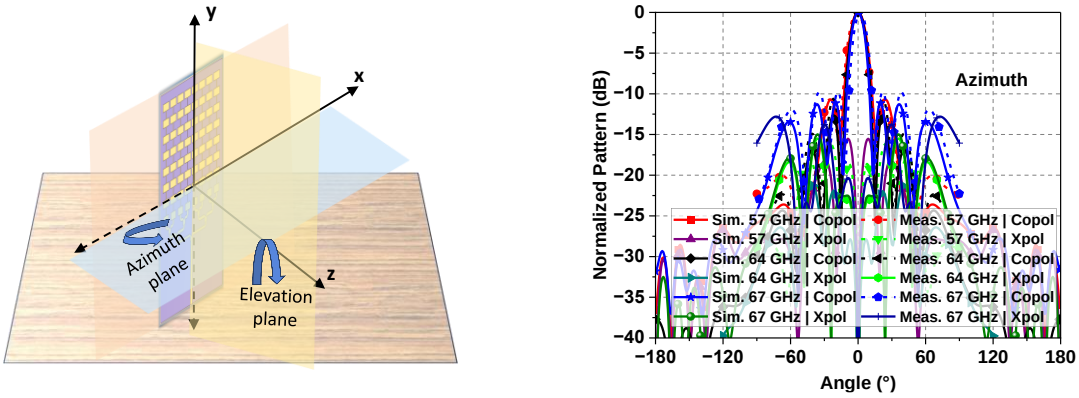

Figure 3.25. Measured radiation patterns of 8 × 8 array at 57, 64, and 67 GHz in azimuth plane.

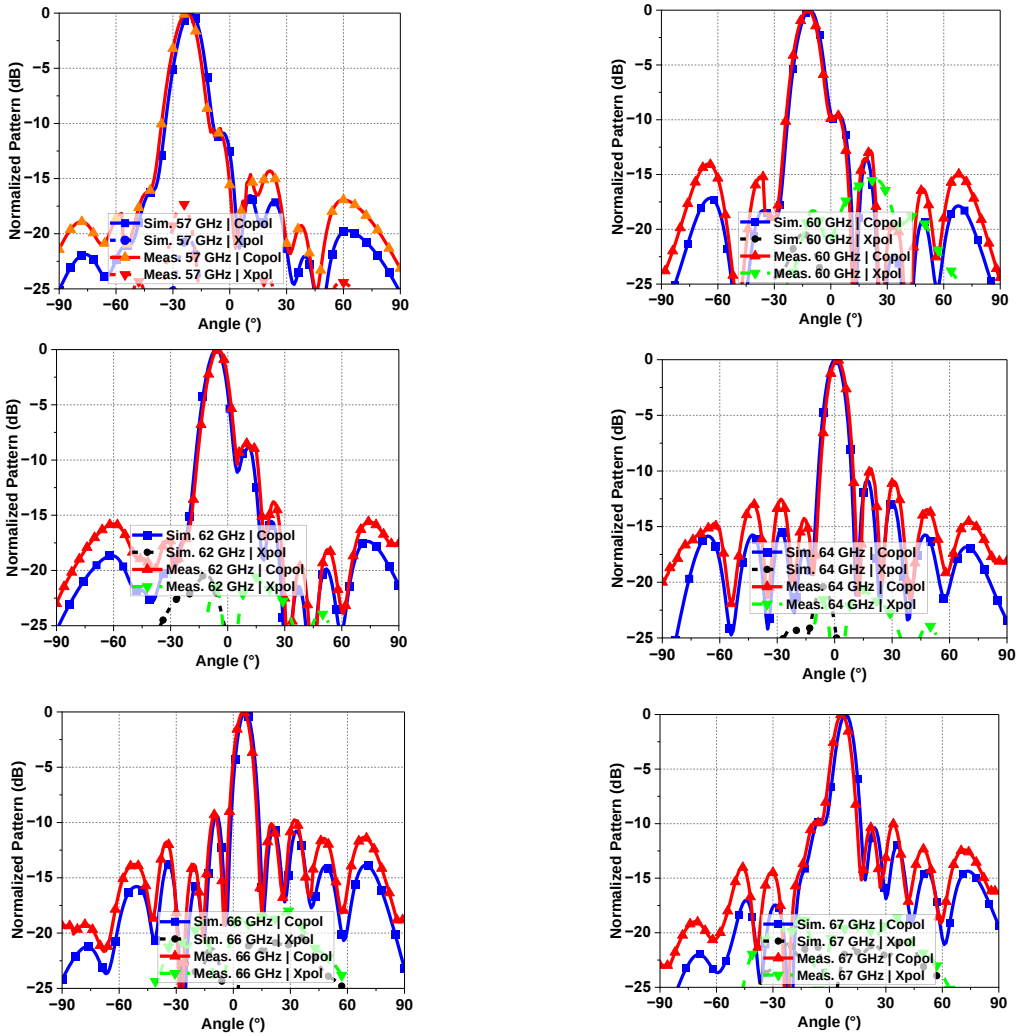

Figure 3.26. Measured radiation patterns of 8 × 8 array at 57, 60, 62, 64, 66, and 67 GHz in elevation plane.

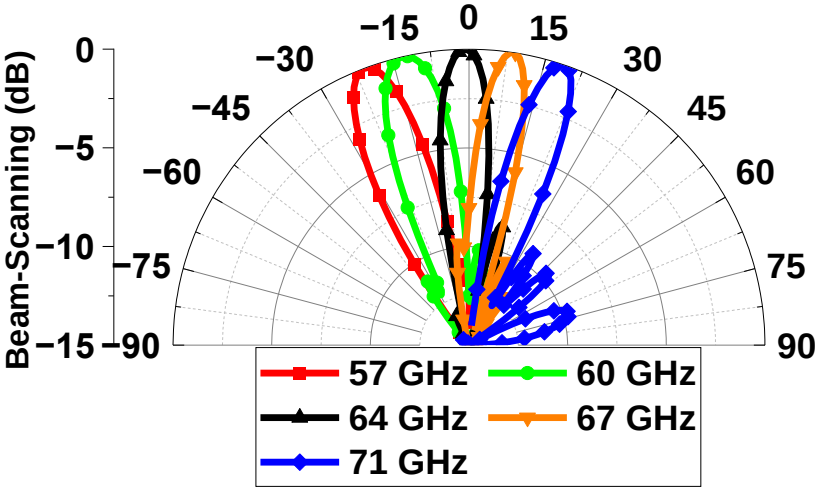

(a)

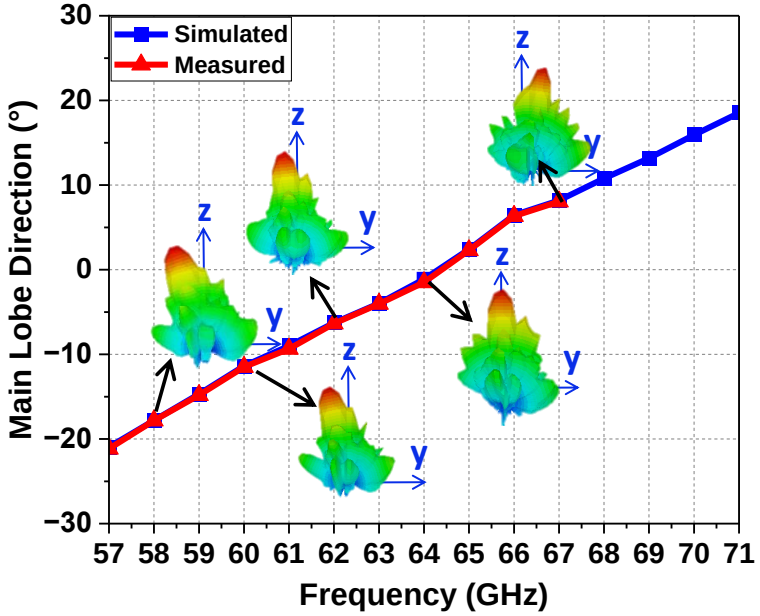

(b)

Figure 3.27. (a) Measured frequency beam-scanning performance of 8 × 8 array in y-z plane (up to 67 GHz) demonstrated in polar form. (b) 3D pattern visualization with the main lobe direction. The blue curve shows the simulated result.

Table 3.1. Performance comparison of the proposed antenna design with other related designs in the literature.

Ref.	Array Geometry	-10 dB BW (FBW %)	Peak Gain (dBi)/ Gain Variation in 57-71 GHz	Beam-scanning (Scanning Range)	Size (mm) (W × L × H) (*λ=5mm at 60 GHz)	Comments
[42]	SIW planar leaky wave slot array 1 × 8	55–65 (16.66 %)	14.5 (> 3 dB)	Yes -72° to +48°	23 × 38 × 0.38 (4.6λ×7.6λ×0.076)	• High fabrication complexity • Gian variation is above 3 dB • Bandwidth is limited
[122]	Planar SIW slot array 12 × 12	59.3–61.8 (4.12 %)	22 (> 3 dB)	No	NA × NA × 0.51 (*λ ×*λ× 0.102λ)	• High fabrication complexity • Gian variation is above 3 dB • Limited bandwidth
[165]	SIW multilayer PCB 1 × 4	50.79–70.85 (33 %)	11.9 (> 3 dB)	No	22 × 25 × 1.05 (4.4λ×5λ×0.21λ)	• High fabrication complexity • Gian variation is above 3 dB
[129]	Microstrip dipoles 1 × 4	57–64 (10.69 %)	16.5 (> 3 dB)	No	18.5 × 30 × 0.25 (3.7λ×6λ× 0.05λ)	• Low fabrication complexity • Gian variation is above 3 dB • Limited bandwidth
[166]	Parallel-series fed microstrip patch array 8 × 4	58–60.5 (4.22%)	18 (Not given)	No	35 × 35 × 0.1 (7λ×7λ× 0.02λ)	• Low fabrication complexity • Very limited bandwidth • Low radiation efficiency
[157]	Series-fed microstrip patch array 2 × 10	58.5–62 (4.2%)	16.4 (> 3 dB)	Partial, at two angles only. -20° and +20	× 30 × 0.0.51 (3.7λ×6λ× 0.102λ)	• Low fabrication complexity • Very limited bandwidth
This Work [151], [167]	**Series-fed linear array 1 × 8**	**54–82.3 (41.52%, sim.) 54–67 (Meas. presented)**	**13.48 (< 1 dB)**	**Yes -23° to +17°**	**13 × 23 × 0.25 (2.6λ×4.6λ×0.05λ)**	• Low fabrication complexity • Wide bandwidth • High gain with 1 dB gain bandwidth > 13 GHz
	Parallel-series planar array 8 × 8	**49.28–73 (38.79%, sim. 49.28–67 (meas. presented)**	**20.36 (< 1dB)**	**Yes -21° to +19°**	**20 × 28 × 0.25 (4λ×5.6λ×0.05λ)**	

3.4 Potential Application Scenarios of the Proposed 8 × 8 Antenna Array

The narrow directional beams of the planar array are applicable for P2P mGbps communications links and high-resolution radar scanning. The proposed antenna can be used with a wideband frequency 57–71 GHz frequency controller radar system for sensing/scanning purposes, as demonstrated conceptually in Figure 3.28. As the main beam tilts with the variation in frequency, this may be not desirable for wideband communication scenarios where the beam should be pointing towards the same direction over a wide beam, nevertheless, a highly directional narrow-band CW signal can be produced to test various V-band communication test scenarios. However, frequency beamscanning is a cost-effective passive beamforming solution that applies to various industrial sensing and imaging applications, such as industrial automation and robotics applications by enabling precise sensing in manufacturing environments, warehouse operations, AGVs/AMRs for tasks such as material handling, inventory management, and surveillance. Moreover, based on the physical orientation of the proposed antenna, application-specific horizontal or vertical tracking can be achieved.

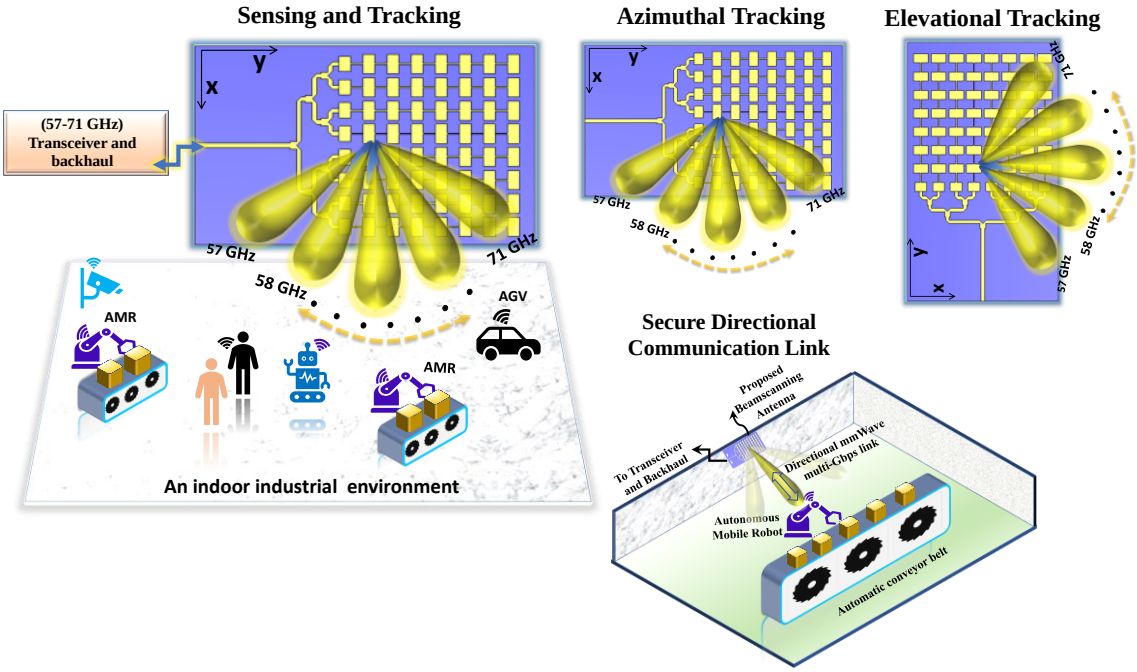

Figure 3.28. Potential application scenarios of the proposed mmWave beamscanning antenna array.

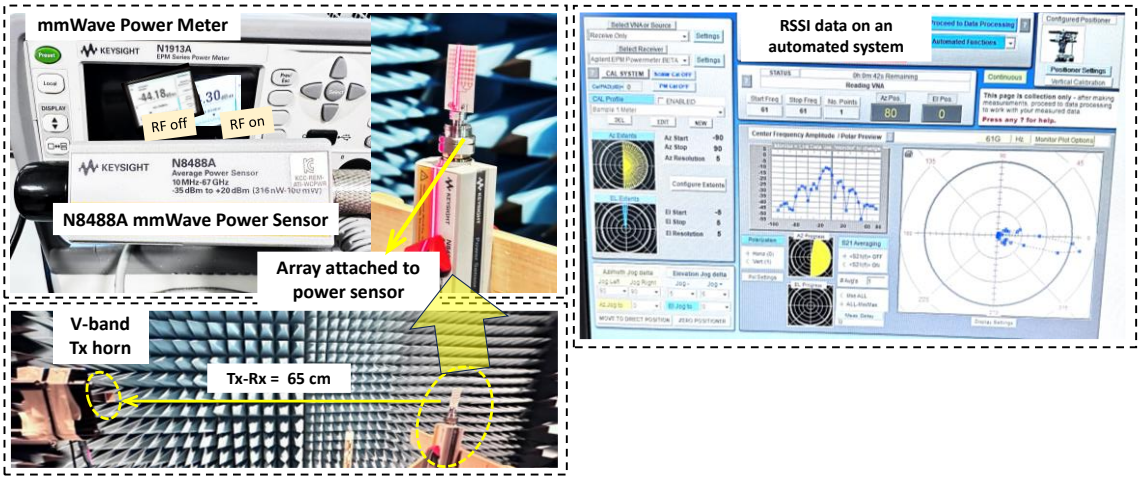

Figure 3.29. RSSI testing using the proposed antenna with Keysight's N8488A mmWave power sensor. Demonstration of establishing a 60 GHz wireless link using the proposed antenna array with Analog Devices EK1HMC6350 evaluation board. (a) end-to-end signal transfer using 1.85 mm coaxial cable (b) 60 GHz wireless signal transfer using the proposed antenna array. (c) effect of hand blockage.

3.5 Practical Demonstrations of the Direct Integration of the Proposed Antenna with Standard mmWave Equipment

The commercially available standard V-band antennas (such as standard gain horn antennas) are often extremely expensive as well as bulky. The proposed antenna array in this work offers a tremendously low-cost, compact, and reproducible alternative solution to costly commercially available V-band antennas. Moreover, the proposed array offers comparable and satisfactory performance in terms of gain and bandwidth, with wide area coverage (in case of linear 1 × 8 array) as well as directional narrow beams (in case of 8 × 8 array). The seamless integration with 1.85 mm standard mmWave equipment is easily attainable due to the design of the edge-launch microstrip feed. Here, we briefly demonstrate two practical test cases of the proposed array for 60 GHz sensing and communication applications.

3.5.1 RF Sniffing for RSSI

To test the usability and RF sensing performance of the proposed 60 GHz array prototype, we conducted RF sniffing to capture the received signal strength indicator (RSSI). RSSI is an important parameter in the sensing domain to characterize the environment and extract meaningful information from it. The test setup is shown in Figure 3.29. The measurement was performed in the mmWave lab facility of Institute of Electronics, Communications & Information Technology (ECIT), Queen's University, Belfast.

The proposed array was attached with Keysight's N8488A mmWave power sensor. The output of the power sensor was connected to the N1913A mmWave power meter. A CW RF signal was generated using a mmWave signal generator at different frequencies and a horn antenna was used as Tx at a 65 cm distance, and RSSI was analyzed at the Rx end. The dynamic range of about 30 dB was achieved without using any power amplifier. At 60 GHz for instance, the peak received power level was -14.30 dBm, whereas it was below -44.18 dBm when RF was switched off from the RF generator. Such RSSI-based measurements can be employed to analyze radio propagation scenarios, implement channel sounding techniques, characterize the RF performance in terms of transmitted Effective Isotropic Radiated Power (EIRP), as well as to model the path loss of different types of indoor industrial environments within 60 GHz band.

3.5.2 Establishing a 60 GHz Wireless Link Using Proposed Array With Analog Devices EK1HMC6350 Evaluation Board

Owing to the directional features of 60 GHz antennas and numerous sensing and detection applications as well as joint communication and sensing for autonomous vehicle scenarios using signal processing evaluation platforms have been demonstrated earlier [168]–[171]. However, expensive mmWave V-band horn antennas were used to establish a working setup.

The proposed antenna array provides an off-the-shelf and low-cost solution to test various sensing scenarios using 60 GHz signal processing and evaluation platforms. Here, we briefly demonstrate a direct integration of our proposed array with Analog Devices EK1HMC6350 evaluation kit to establish a 60 GHz mmWave link. The evaluation boards were provided by ABB Corportae Research Center, Vasteras, Sweden. The experimental setup is demonstrated in Figure 3.30. It includes an HMC6300 chipset with the Tx module and an HMC6301 with the Rx module, a USB interface, and graphical user interface (GUI) software to program the Tx and Rx chipsets by writing to the device registers. Two evaluation boards were used for separate Tx and Rx chipsets being half-duplex systems.

To test the setup, a 1 MHz FM signal was supplied to the evaluation board which is upconverted in the 57 to 64 GHz range. The transmitter was locked at 60 GHz through Tx and Rx GUIs. First, a 1.85mm standard coaxial cable was attached between the Tx and Rx boards to ensure the proper working of boards and signal retrieval, as illustrated in Figure 3.30(a). Then, the coaxial cable was replaced by the proposed 8 × 8 planar arrays to confirm the 60 GHz wireless link. A 4-channel oscilloscope was used to observe the transmitted and received

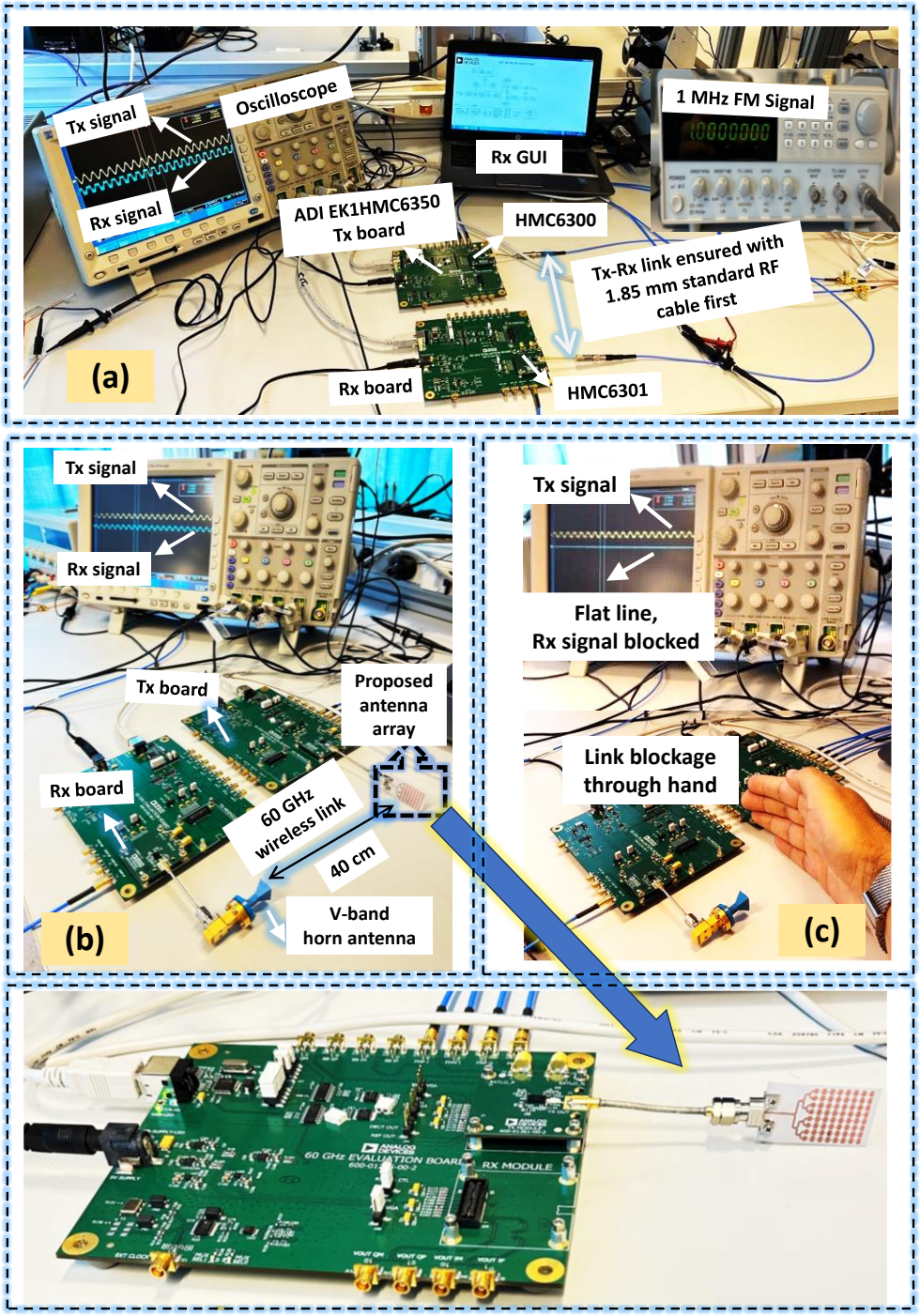

Figure 3.30. Demonstration of establishing a 60 GHz wireless link using the proposed antenna array with Analog Devices EK1HMC6350 evaluation board. (a) end-to-end signal transfer using 1.85 mm coaxial cable (b) 60 GHz wireless signal transfer using the proposed antenna array. (c) effect of hand blockage.

signal waveforms. The transmitted waveform was successfully received. We conducted a Tx-Rx link test using two identical 8 × 8 arrays, one at the Tx side and the other at the Rx side.

For verification, we replaced one of the arrays with a commercial V-band horn antenna, as shown in Figure 3.30(b). The received waveform was similar in both instances. Such demonstration platform when used with digital baseband processing can be used to analyze bit error rates, error vector magnitude, as well as other link budget analyses. Moreover, as illustrated in Figure 3.30(c). the received signal is blocked (flat line on the oscilloscope) when LOS is blocked by placing a hand in between the Tx and Rx antennas. This type of blocking effect provides an efficient signature in the 60 GHz sensing domain and can be employed for 60 GHz activity monitoring and sensing in indoor environments.

As a summary, this chapter extensively described the construction and analysis of the antenna array manifesting beam tilt operation with frequency along abroad frequency spectrum from 57–71 GHz. In the next chapter, the design of a fixed beam wideband antenna array will be discussed.

Chapter 4

Design of a Fixed Beam Wideband Millimeter-Wave Antenna Array

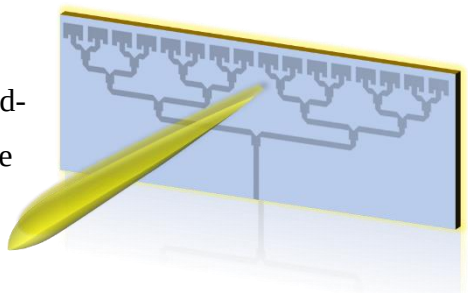

In this chapter, the design and performance of a fixed-beam wideband corporate-fed linear antenna array are presented. Unlike beam tilt/squint) phenomenon across the operating frequency (i.e., frequency dependent beamscanning) in the previous design of Chapter 3, here the main beam remains fixed towards the broadside in the whole band of interest. The fixed beam over a wide mmWave bandwidth is a potential solution for extremely high data rate communication scenarios, such as high definition video transfer . The content of this chapter is published in [172].

4.1 Antenna Array Design

The proposed antenna is designed on a Rogers 4003C substrate. The choice of RO4003 in this design is due to high reigidity of the substrate. It has dielectric constant of 3.55, thickness of 0.2 mm, dissipation factor of 0.0027, and copper thickness of 0.035 mm. A comparison between different substrate choices and their impact will be presented at the end of this chapter. Here, first a conventional rectangular microstrip patch antenna is used as a basic radiator because of its low profile and planar geometry. The bottom side of the antenna has a full copper layer acting as a ground plane, because of broadside intended beams. For impedance matching, inset cuts with optimized dimensions were introduced in the patch. The entire antenna array and feed network are designed and optimized to match 50 Ω impedance.

After the design of a single resonating antenna element around 60 GHz, a 2-way power divider was designed as a starting point for array construction. Then the same array was scaled-up to construct a higher-order array configuration. A 16-way parallel equal power divider was designed for the 16-element array. The gap (inter-element spacing) between consecutive antenna elements was optimized to be 2.04 mm to achieve a better tradeoff in gain and SLLs (0.77 λ_g, or 0.41 λ_0 where λ_g and λ_0 are the guided and free space wavelengths respectively at 60 GHz). The junction lengths of the power divider lines were optimized at 0.73 mm to match the impedance of 50 Ω line width (0.45 mm).

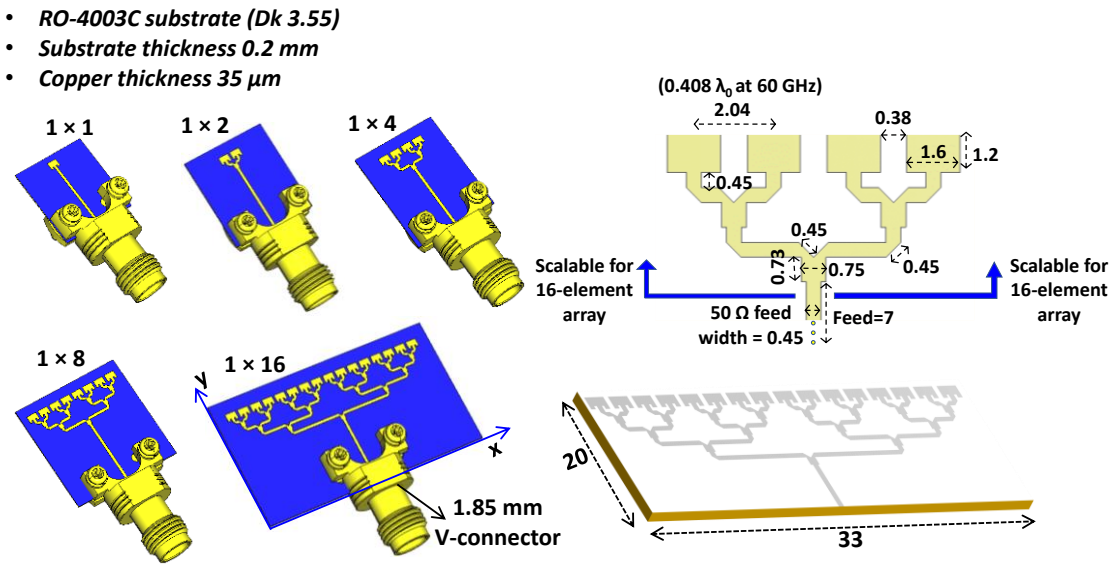

Figure 4.1. Geometry of proposed array antennas with realistic connector model. Optimized dimensions of proposed feed network in millimeter. Following the same dimensions, 2, 4, 8, and 16-element arrays are designed.

At each junction (where the array splits into two), a 50 Ω line produces a parallel impedance effect and results in a virtual 25 Ω impedance point (i.e., $50 \times 50/(50 + 50)$. The quarter wave transmission line segments with an optimized width of 0.75 mm were used to match 25 Ω with 50 Ω. The 90° sharp corners as well as junction points of the feed network were chamfered with the chamfering dimension of 0.45 mm. The chamfered transitions are used for the smooth flow of the current and to reduce possible spurious radiations from the sharp edges of the feed network. The array is symmetrical around the y-axis. The complete design steps, antenna schematic, and optimized antenna dimensions are shown in Figure 4.1.

4.2 Simulation Results and Analysis

For the single-element antenna design, time domain (TD) as well as frequency domain (FD) simulations were performed on CST Microwave Studio. The simulated reflection coefficient of the single element (TD) provides a bandwidth of more than 2.16 GHz (61.77–64.4 GHz) as shown in Figure 4.2(a). The TD and FD reflection coefficients show slightly shifted resonances. The realistic connector model was also co-simulated in TD solver with the patch antenna. Onwards, all of the simulated results are in TD solver. The antenna is fed through an edge-launched 1.85 mm standard connector and its effect is simulated as presented in Figure 4.2(a).

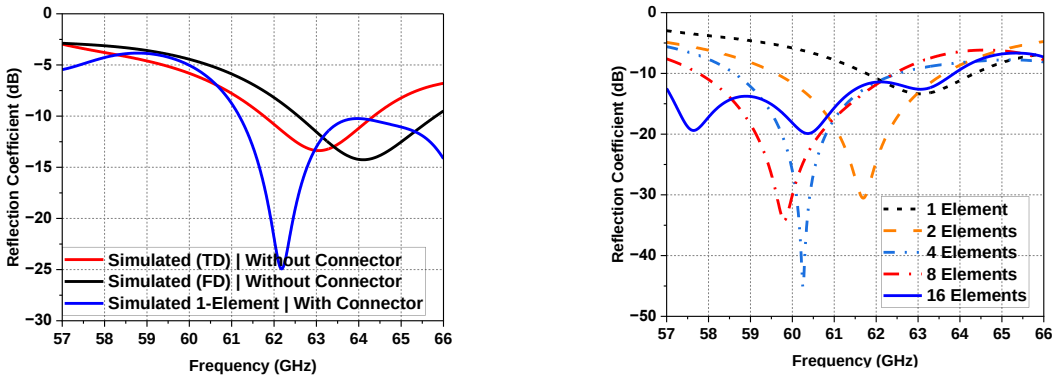

(a) (b)

Figure 4.2.(a). Simulated reflection coefficient of single-element antenna. (b) Simulated reflection coefficients of 2, 4, 8, and 16-element array designs.

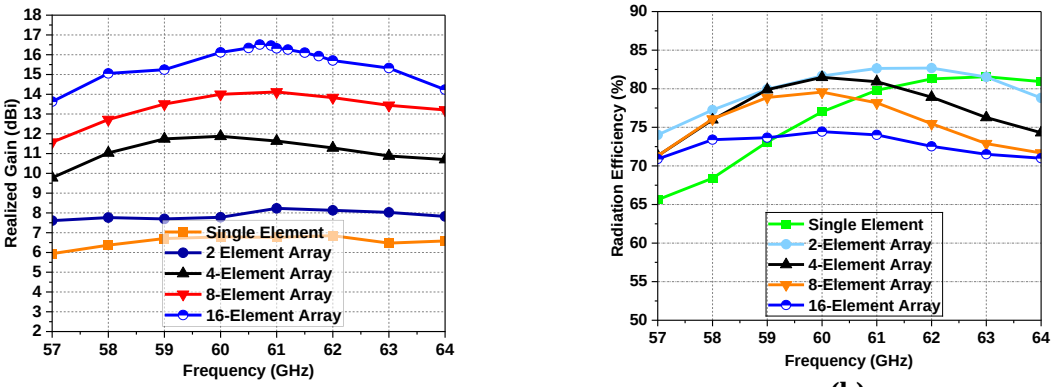

(a) **(b)**

Figure 4.3. (a) Simulated realized gain (b) radiation efficiency of 2, 4, 8, and 16-element array designs.

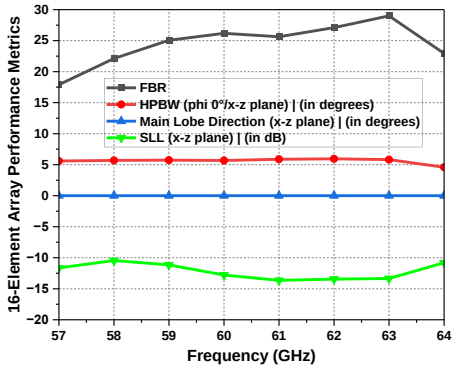

Figure 4.4. FBR, SLL, MLD, and HPBW of the 16-element array.

The reflection coefficient of a single element with the inclusion of RF connector showed shift in resonace frequency at 62.18 GHz, with -10 dB impedance bandwidth of 3 GHz (from 61.18 GHz to 64.2 GHz).

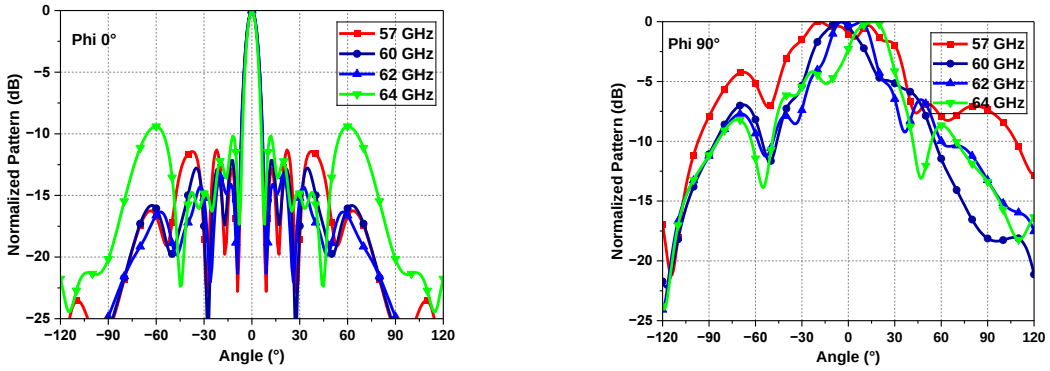

Figure 4.5 (a)2D radiation pattern of 16-element array in (a) x-z/ Phi 0°plane. (b) y-z/Phi 90° plane.

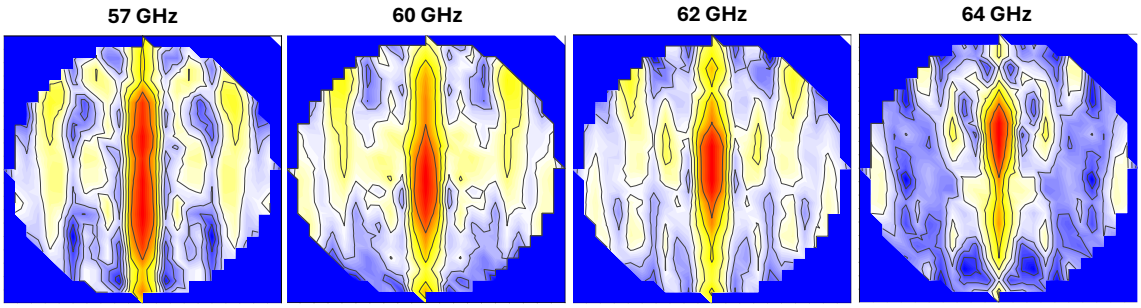

Figure 4.6. U-V heat maps demonstrate fixed broadside beams across 57–64 GHz (extracted from CST Microwave Studio and post-processed in OriginPro software).

The simulated reflection coefficients of antenna arrays with different numbers of elements are shown in Figure 4.2(b). The -10 dB impedance bandwidth for 2, 4, 8, and 16-element arrays ranges between 59.61–63.62 GHz, 58.62–62.53 GHz, 57.77–62.43, and 57–64 GHz respectively. The 16-element array provides the -10 dB impedance bandwidth ranging between 55 to 63.85 GHz.

The simulated peak realized gain values for 2, 4, 8, and 16-element arrays are 8.23, 11.63, 14.11 and 16.5 dBi respectively within 57–64 GHz, as shown in Figure 4.3(a). The peak gain of 16-element array is 16.5 dBi at 60.7 GHz. Its realized gain is greater than 15 dBi between 58 to 63.8 GHz. The 1 dB gain-bandwidth is 3.77 GHz (between 59.13–62.9 GHz). The radiation efficiency for all array antennas is above 70% in the covered bandwidth as shown Figure 4.3(b). As depicted in Figure 4.4, for 16-element array high front-to-back ratio (FBR) of above 20 dB, narrow HPBW in azimuth plane around 6°, and SLLs below -12 dB are achieved within 57–64 GHz. The main lobe direction (MLD) is towards broadside till 63 GHz without squint effect, although beam starts tilting at 64 GHz.

The radiation patterns of the 16-element array in x-z (Phi 0°) and y-z (Phi 90°) planes are presented in Figure 4.5 (a) and (b) respectively. Highly directional narrow beams are achieved in the principal plane of interest, i.e., x-z plane. The main beam is towards the broadside at all frequency points till 63 GHz, however at 64 GHz it has tilt due to high SLL as demonstrated by heat maps in Figure 4.6. This shows that although -10 dB impedance bandwidth (|S11|) is up till 64 GHz, however *pattern bandwidth* (radiation pattern, SLL etc) is limited to 63 GHz.

4.3 Prototype Fabrication and Measured Results

The fabricated prototypes of single-element and 16-element array along with reflection coefficient measurement setup using E8361A VNA are shown in Figure 4.7. Measured reflection coefficients are presented in Figure 4.8, and match well with the simulated results. The deviations are primarily due to the fabrication tolerance. The radiation pattern measurement setup is shown in Figure 4.9. The measurement procedure is same as described in Chapter 3, Section 3.3.3. The radiation patterns trend matches well with the simulated results. The difference between measured and simulated gain is mainly due to lossy connector and power drop across the divider due to fabrication tolerances.

Some deviations in the measured results at the angles beyond ±40° are due to 2° anguler steps during pattern measurement which can be improved using 1° step, for instance. However, LOS peak mateches with the simulated result to a great extent.

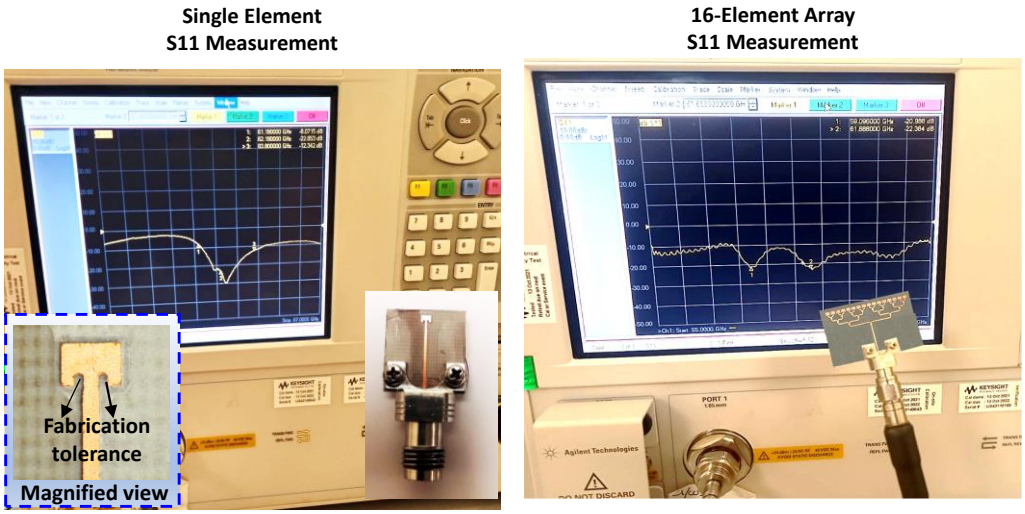

Figure 4.7. Reflection coefficient measurmenet setup of the fabricated prototypes.

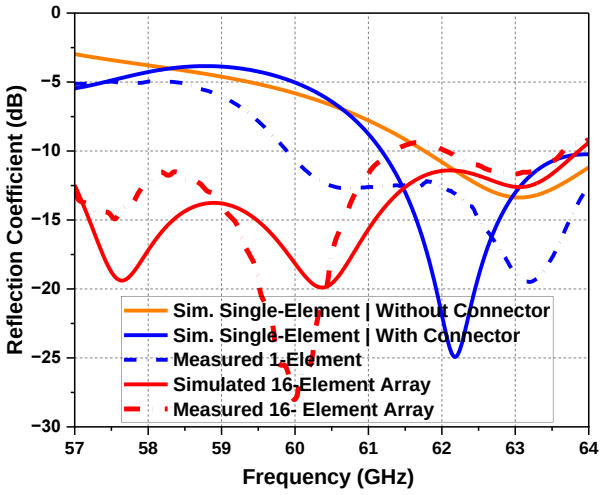

Figure 4.8. Measured reflection coefficient of the 16-element array and single element antenna.

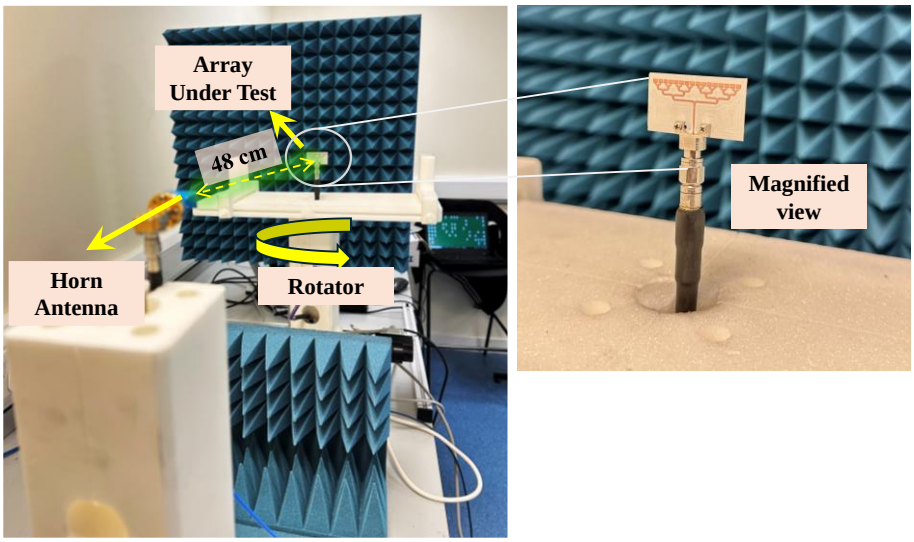

Figure 4.9. Radiation pattern and gain measurement setup for 60 GHz antenna array.

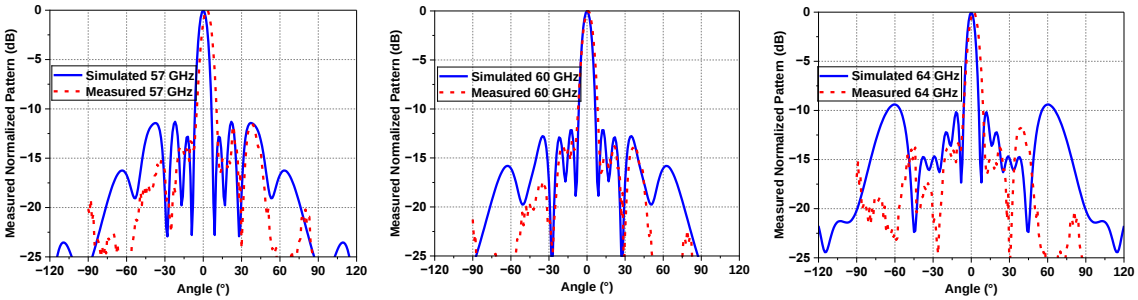

Figure 4.10. Measured radiation patterns at 57, 60, and 64 GHz in x-z plane.

Table 4.1. Performance comparison of the proposed antenna array design with some of the other closely related 60 GHz antennas in the literature.

Ref.	-10 dB imp. BW (GHz)	Peak gain (dBi)	Array topology	Radiation Efficiency (%)	Size array (mm × mm)
[122]	59.3–61.8	22	Complex 12-way SIW array	68	Not reported
[123]	54.6–71.2	16	4 × 4	NA	14 × 16
[124]	55–68	15.6	4 × 4	67	20 × 20
[125]	59.2–60.4	20.6	32 (4 × 8)	78	17 × 22.5
[126]	57–62.8	11.6	1 × 2	85	20.64 × 20
[127]	57.5–60.7	18	4 × 4	NA	18.5 × 30
[128]	58–61.3	13	2 × 2	NA	10.5 × 10.5
This Work [172]	**55–64**	**16.5**	**1 × 16**	**>70**	**20×33**

A performance comparison of the proposed array with other planar antenna arrays at 60 GHz is presented in Table 4.1. The proposed antenna reveals high-performance in terms of wide impedance bandwidth, high peak gain, compact size, and repeatability of the design.

4.4 Applications of the Proposed Fixed Beam, High Gain, Wideband Array

Fixed beam wideband 60 GHz array antennas have become crucial elements in many wireless communication systems, providing numerous applications and advantages. An important use case is in the field of high-speed wireless networks, namely in indoor settings where there are large numbers of users requiring strong and reliable access. These antennas enable the transmission of data at multi-gigabit per second rates over short distances, making them well-suited for applications such as ultra-fast internet access, high-definition video streaming, and AR/VR experiences [10], [25]. Furthermore, in developing smart indoor networks, and wireless bakchaul, stationary beam wideband 60 GHz array antennas facilitate uninterrupted connection among numerous devices, facilitating instantaneous data transfer [173]. These antennas are designed to optimise the use of the spectrum and reduce interference, resulting in improved network performance and reliability [35].

Fixed beam wideband 60 GHz array antennas have multiple uses, including indoor wireless networks as well as P2P and P2MP wireless backhaul lines. These antennas are essential

components of crucial infrastructure for providing connectivity to end-users, acting as a link between fiber-optic backbone networks and user equipment [174]–[176] . These antennas utilise the broad range of frequencies available at 60 GHz to facilitate the transmission of large amounts of data over relatively short to medium distances [36]. This provides a cost-effective alternative to expensive fibre optic installations in industrial, urban and suburban sectors. Moreover, the fixed beam characteristic of these antennas offers intrinsic security advantages by restricting the broadcast beam to specified directions, thus reducing the possibility of eavesdropping and unauthorised access [10], [24], [177].

High-speed, large-capacity wireless communication systems have become an indispensable infrastructure in all fields as a driving force for building a smart society. The proposed array provides 7 GHz of continuous bandwidth from 57–64 GHz which can provide mGbps data rate communication links in emerging indoor smart industrial applications as well as outdoor infrastructure. In this view, a conceptual depiction of a use case of the proposed fixed beam wideband antenna array is depicted in Figure x., where the 60 GHz fixed beam wideband antenna array can be used to provide P2P mGbps data rate coverage, as conceptually depicted in Figure 4.11.

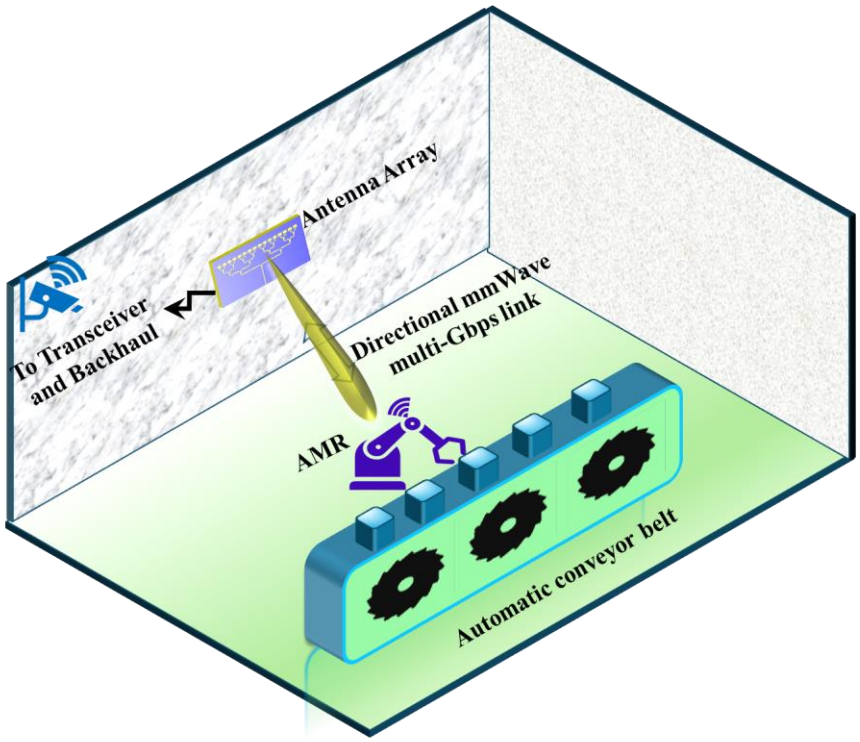

Figure 4.11. Applicaion scenario of a fixed beam antenna for mGbps data rate.

4.5 Some Practical Design Considerations During mmWave Antenna Design

During the work conducted in Chapter 3 and Chapter 4, various mmWave antenna design investigations were carried out, such as impact of dielectric substrate, RF feed connector and practical fabrication As a part of this thesis contribution, we published a detailed analysis of these design considerations on planar mmWave antenna arrays in [178]. This section is presented in light of those investigations.

4.5.1 Impact of Dielectric Substrate

We investigated the performance analyses of an 8-element wideband series-fed microstrip array using three widely used dielectric substrate materials to design mmWave planar antennas, viz., Rogers (RO) 3003, RO5880, and RO4003C. The design of the three 1 × 8 linear arrays is shown in Figure 4.12 and the design methodology is same as described above in section 3.1. All three substrates have identical copper thicknesses of 17.5 μm and approximately similar standard available thicknesses for a fair performance comparison. The selected substrate thickness (*H*) and dielectric constants (ε_r) of these materials are as: RO3003 with ε_r of 3, *H* of 0.25 mm, and dissipation factor of 0.001; RO5880 with ε_r of 2.2, *H* of 0.252 mm, and dissipation factor of 0.0004; and RO4003C with ε_r of 3.55 and *H* of 0.203 mm, and dissipation factor of 0.0027. The arrays are excited using edge-launched 50 Ω microstrip feed.

The width of the antenna array is set to 13 mm for all cases to accommodate the footprint of the connector. The width of the feed (w_f) line was matched to 50 Ω (Z_0), calculated using $wf = \frac{7.48 \times H}{e^{Z_0 \frac{\epsilon_r + 1.41}{87}}} - (1.25 \times mt)$ [118] and was further fine tuned. As the ε_r values of RO3003 (ε_r=3) and RO4003C (ε_r=3.55) are not largely different, we optimized the design with feed width only and kept other dimensions of the patch elements and MTL identical for these two cases. The only difference between these two is in the substrate thickness and width of the feed line whose value depends on the dielectric constant and the substrate thickness. However, the same dimensions did not work in the desired band of interest (57–71 GHz) as the variation in ε_r of RO5880 (ε_r=2.2) becomes significant. Thus, as shown in Figure 4.12, the overall dimensions are optimized through simulations to achieve wide impedance matching in the desired band.

The reflection coefficient (|S11|) for the three presented designs is shown in Figure 4.13(a). All three array designs are optimized to achieve |S11| less than -10 over the band of interest with multiple resonances at slightly different frequency points. The proposed arrays cover -10

dB impedance bandwidth of more than 25% (around 60 GHz band) covering the entire 57–71 GHz ISM band. The array designed on RO4003 shows relatively higher reflections between 59 GHz and 60 GHz (but still below -10 dB). Note that as the frequency goes above 67 GHz, the reflection coefficient also goes high for RO4003C and RO5880 arrays. However, the reflection coefficient of the RO3003 array is less than -15 dB throughout, and specifically less than -20 dB between 66 GHz to 71 GHz. Hence, at a higher frequency region, RO3003 showed consistent RF performance with better impedance matching.

The radiation efficiency profile is shown in Figure 4.13(b). The radiation efficiency of the array with RO4003C is less than 80 % and varies between 73.95% at 71 GHz to the peak value of 78.64% at 63 GHz, although its |S11| is less than -10 dB in the band of interest. For RO3003, the radiation efficiency varied between 87.81% at 71 GHz to the peak value of 88.62% at 61 GHz, which indicates consistent good performance over the whole band of interest. The radiation efficiency was found to be highest for the RO5880 array which varied between 89.02% at 71 GHz to the peak value of 90.04% at 63 GHz. The high efficiency for RO5880 is mainly due to the relatively low loss dissipation factor and lower dielectric constant of RO5880. Moreover, the higher losses in case of RO4003C substrate are also maninyl due to its high conductor and dielectric losses as compared to other two dielectric substrates, as shown in Figure 4.13(c) and (d).

The total efficiency for all three arrays is higher at those points where |S11| is lower (i.e., good impedance matching), whereas it is lower at the points where |S11| (reflection) is higher (i.e., near -10 dB). Note that above 67 GHz, the total efficiency is the highest for the RO3003 array as compared to the other two arrays, because of its good impedance matching in that band. It is noteworthy that it is the total efficiency that translates directly into the realized gain of an antenna.

The realized gain for the three antenna arrays is shown in Figure 4.14(a). It is noteworthy that the variation in the gain is high for RO5880 and RO4003C substrates and the gain drops rapidly beyond 67 GHz. From 57–66 GHz, RO4003 array showed a gain variation of 0.97 dB with a peak realized gain of 13.32 dBi at 60.5 GHz. However, after 66 GHz the gain dropped to a value of 7.89 dBi at 71 GHz. Thus, in the whole 57–71 GHz, the variation in gain is about 5.42 dB for the array designed on RO4003C. The peak realized gain for RO5880 array is 14.88 dBi at 59 GHz, whereas the minimum gain in the band of interest is 9.55 dBi at 71 GHz. The gain dropped by more than 3 dB beyond 66 GHz for RO5880 array.

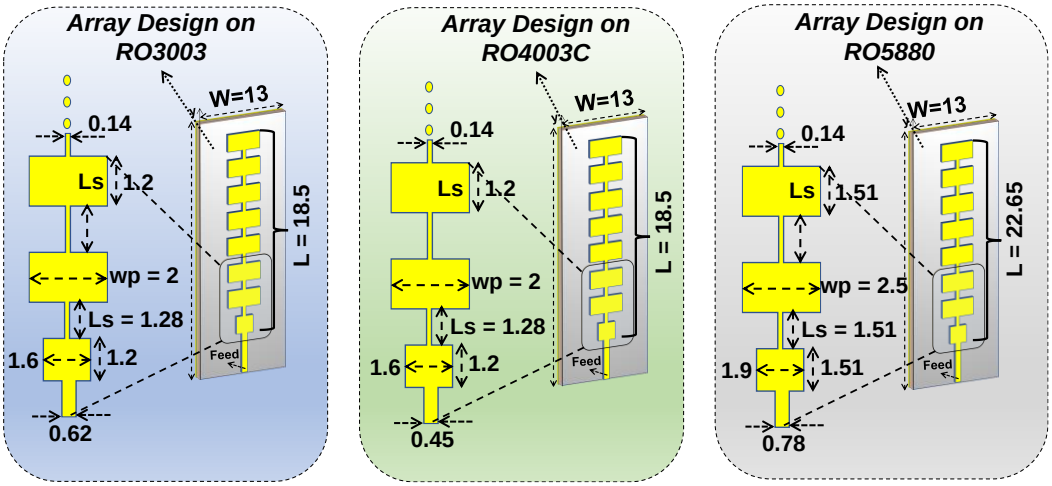

Figure 4.12. Design and optimized geometry of the 1 × 8 series-fed array antennas using three different dielectric substrate materials (dimensions in mm).

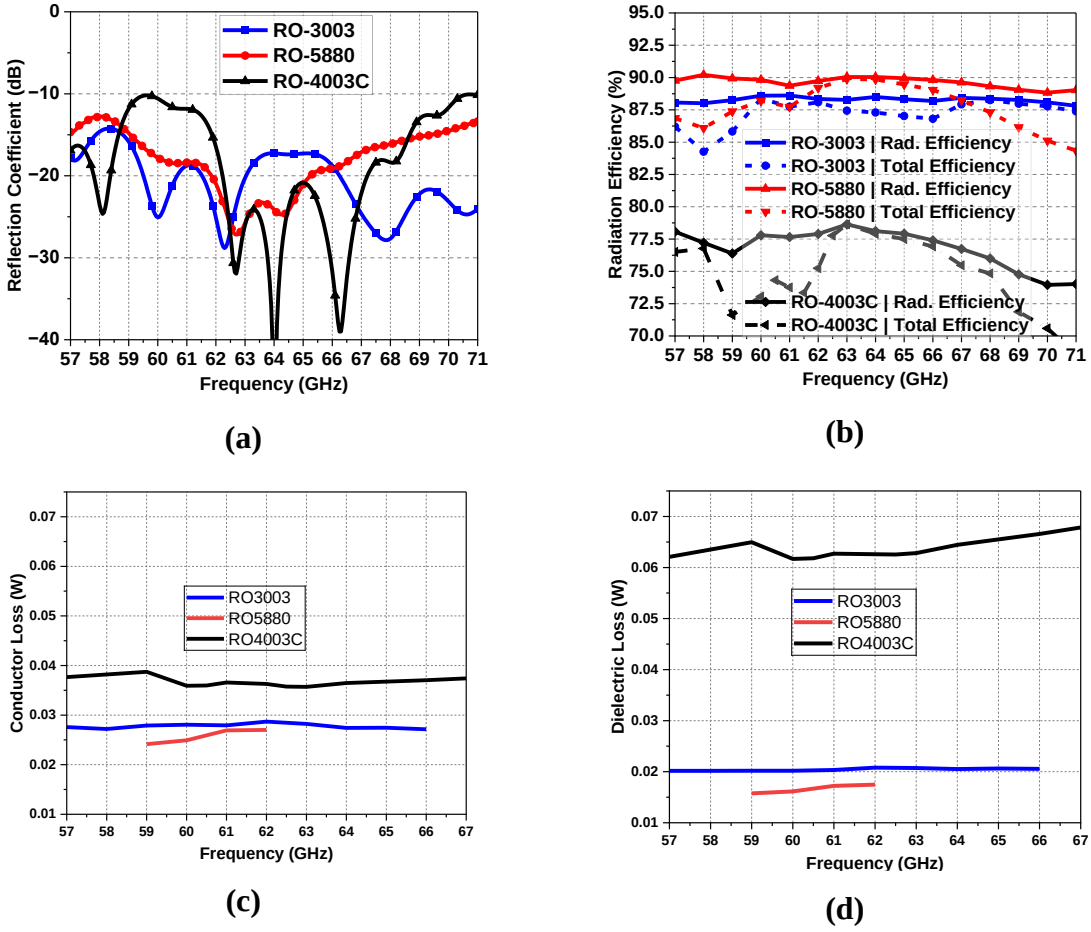

Figure 4.13. Simulated results for 1 × 8 array designs using three different substrates (RO3003, RO5880, and RO4003C). (a) Reflection coefficient. (b) Radiation efficiency and total efficiency. (c) Conductor loss for different substrates. (d) Dielectric loss for different substrates.

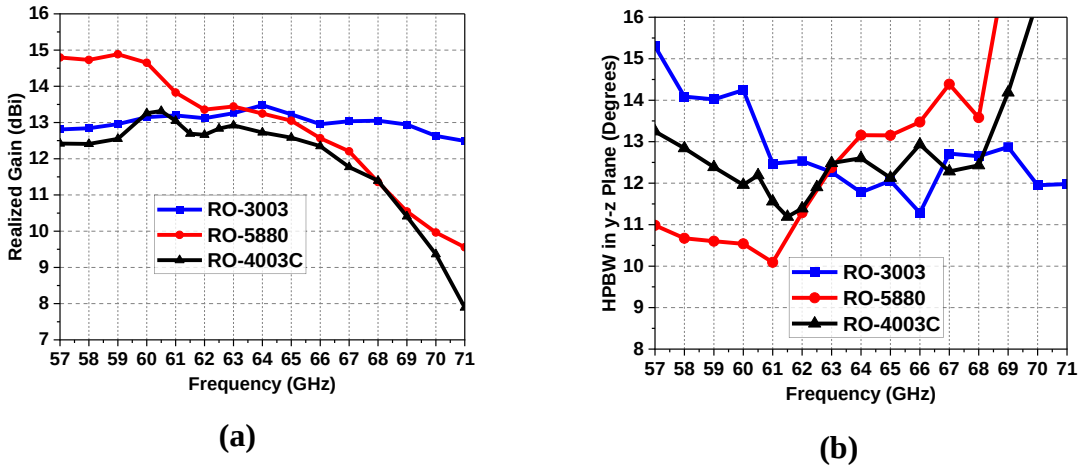

Figure 4.14. Simulated results for 1 × 8 array designs using three different substrates (RO3003, RO5880, and RO4003C). (a) Realized gain. (b) HPBW.

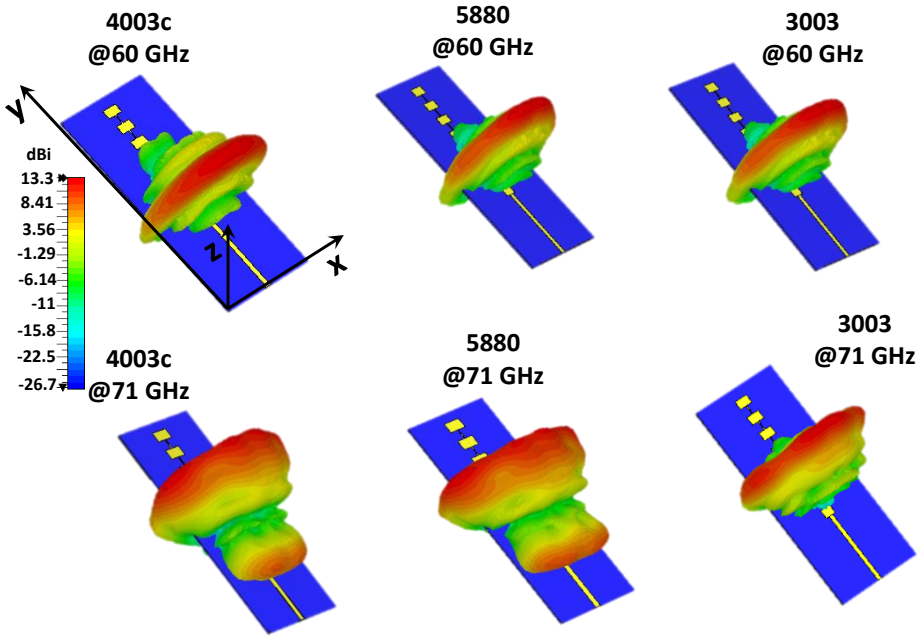

Figure 4.15. Simulated 3-D radiation patterns at 60 GHz and 71 GHz for 1 × 8 array designs using RO3003, RO5880, and RO4003C.

Relative to the peak gain in 57–71 GHz band, the RO4003C array showed a 1 dB gain bandwidth of 9 GHz, and a 3 dB gain bandwidth of 12 GHz. For the RO5880 array, 1 dB gain bandwidth is 4.5 dB, whereas its 3 dB gain bandwidth is about 10.5 GHz.

The array designed on RO3003 showed the best gain performance with a peak realized gain of 13.48 dBi at 64 GHz, and a minimum realized gain of 12.49 dBi at 71 GHz. Thus, less than 1 dB gain variation is observed in the entire 57–71 GHz (i.e., its 1 dB gain bandwidth is 14 GHz). This depicts the high RF performance consistency of RO3003 substrate even at higher

frequencies. Note that low gain variations (within 1 dB) over a wide desired bandwidth are highly desirable at mmWave bands to combat high path loss (although it is quite challenging to achieve). The HPBWs in y-z plane are presented in Figure 4.14(b).

The 3-D radiation patterns of three array prototypes at 60 GHz and 71 GHz are shown in Figure 4.15. It can be noted that beyond 67 GHz, the arrays designed on RO4003C and RO5880 show high SLL, and the radiation pattern is distorted. However, with RO3003, the SLL is below -9 dB till 71 GHz. This can be related to stable current distribution with higher radiation performance and better than -20 dB reflection coefficient of RO3003 substrate beyond 67 GHz, as depicted already in Figure 4.13. Moreover, as a whole, the SLL performance of RO5880 and RO3003 arrays are better than those of the RO4003C array. The average metal loss for RO4003C and RO3003 array designs in 57-67 GHz is 0.036 W and 0.027 W respectively, whereas the average dielectric loss for RO4003C and RO3003 array designs is 0.020 W and 0.063 W respectively. These losses depict the impact on the efficiency and gain performance.

In summary, it is worth mentioning here that RO5880 is a soft material which is sometimes difficult to fabricate antennas at high frequency, however it can provide high radiation efficiency at some desired bands. RO3003 is relatively roboust than RO5880, but still considered soft, and provides consistent RF performance especially at higher frequencies such as around 60 GHz and around 77 GHz automotive radar applications. Nevertheless, although relatively presents high radiation losses, the structural robustness and durability of RO4003 is high and better as compared to RO3003 and RO5800 substrates, which may be considered beneficial for some applications.

4.5.2 Impact of RF Connector

It is instructive to mention here that while designing the mmWave antennas, it is essential to account for the precise dimensions and footprint of the connector to prevent any incompatibility while integrating it with an antenna. First of all, the thickness of the substrate is in direct relation to the width of the input feed line, therefore it is crucial to select the substrate thickness carefully to ensure that the microstrip feed width remains smaller than the dimensions of the dielectric clearance around the RF pin of the connector. Failing to do so could potentially lead to a short circuit between the feed line and the metallic body of the connector, resulting in the loss of RF signal to the antenna ground. Although some tapering of feed width can be considered to avoid this in the case of thicker substrates, however, it might adversely affect the

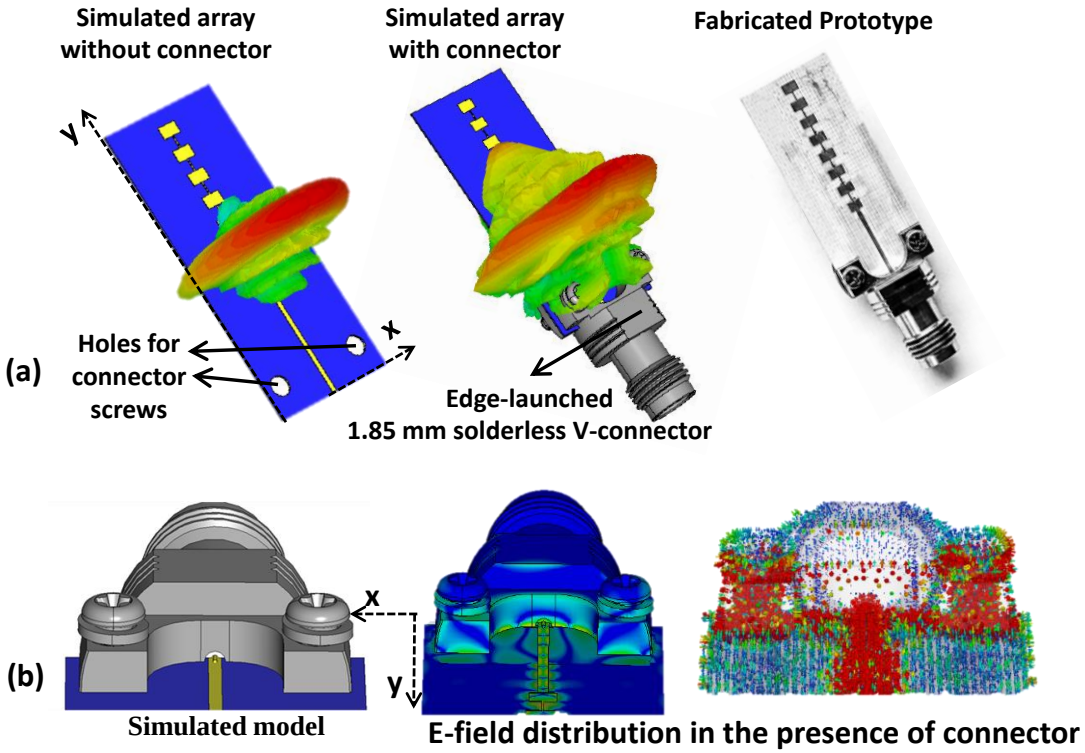

Figure 4.16. (a) Schematic view of the proposed simulated array on R03003 substrate with and without RF connector at 64 GHz illustrating impact on the radiation pattern. (b) E-field distribution in the presence of connector.

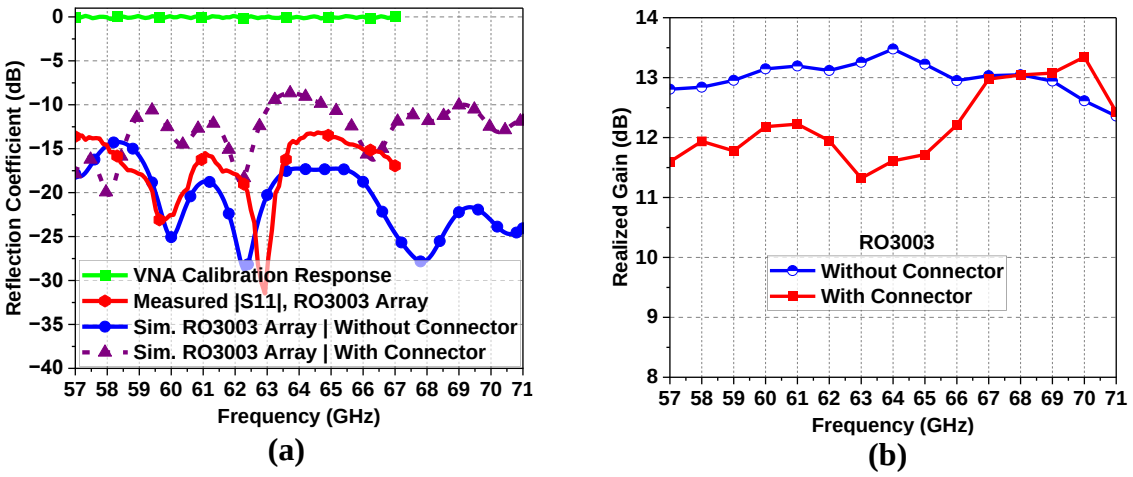

Figure 4.17. (a) Measured reflection coefficient of the 1 × 8 array designed on RO3003 substrate illustrating connector effect. (b) Effect of connector on realized gain.

.

impedance matching. In this work, the connector's dielectric clearance is 0.98 mm, whereas the 50 Ω feed width is 0.62 mm for a 0.25 mm thick substrate, which lies inside the connector's dielectric clearance region.

The 3D model of the 1.85 mm standard connector was co-simulated with an antenna array as demonstrated in Figure 4.16(a). The width of the connector is about 12 mm, therefore the

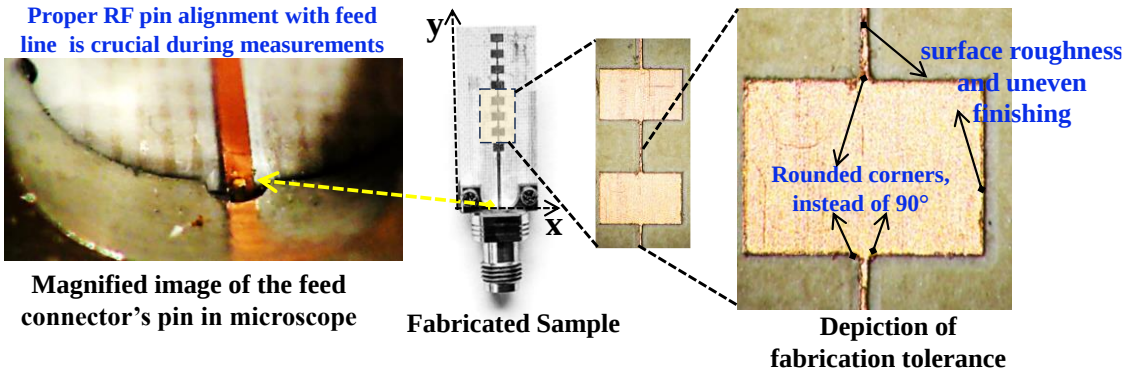

Figure 4.18. Practical demonstration of the fabrication tolerance and RF feed pin alignment.

substrate's width was set to be 13 mm to accommodate the connector. In simulations, the array was excited by feeding the dielectric part of the connector with a waveguide port. Moreover, the connector can distort the radiation pattern and increase SLL as can be noted from 3D pattern and E-field distribution in the presence of connector in Figure 4.16(a) and (b). The impact of inclusion of connector on reflection coefficient and realized gain is shown in Figure 4.17(a) and (b) respectively. With connector, relatively higher reflections and reduced gain (within 1dB mostly and at some frequency regions upto 2 dB) are observed. To minimize the impact of the connector on radiation pattern distortion, it is wise to use a longer feed line to have an adequate distance from the antenna aperture, as designed in this work.

4.5.3 Impact of Fabrication Tolerance

A magnified image of the fabricated prototype is shown in Figure 4.18. Note that in simulations, the MTLs and patches are designed with ideal 90° corners, however during the practical fabrication process, the corners are rounded/bent and the copper surface might be rough. Such fabrication tolerance affects the antenna performance and results in measurement discrepancies at mmWave bands, as depicted by slightly deviated measured |S11|. Moreover, since the RF pin (diameter 0.17 mm) is very tiny, it should accurately touch the microstrip feed line and must not be misaligned, otherwise the desired results might not be obtained.

In Chapter 3 and this chapter, the frequency-selective beamscanning and fixed beam wideband 60 GHz antenna array designs are presented respectively, using conventional antenna array technique, but with high performance metrics. In order to achieve advanced electronic beamsteering performance for next-generation wireless technologies, the next chapter will discuss the complete design and performance of an innovative electronic beamsteerable metasurface antenna with radiation pattern reconfiguration capability.

Chapter 5

60 GHz Programmable Dynamic Metasurface Antenna (DMA) for Agile Beamforming

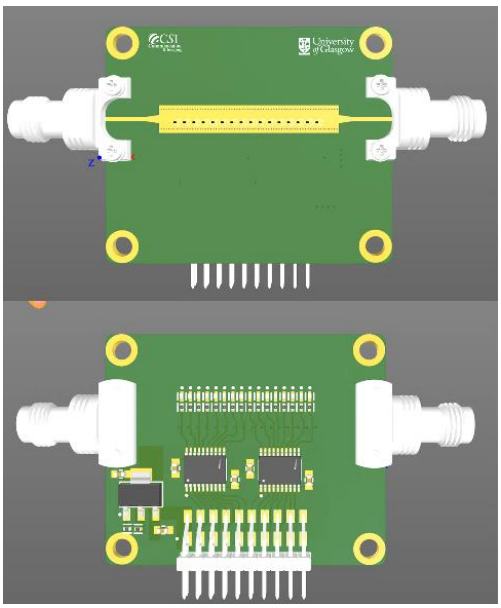

In Chapters 3 and 4, we introduced antenna solutions built on traditional microstrip arrays with improved performance characteristics. However, these designs lacked the capability of fixed frequency beamsteering. To address this limitation and achieve agile fixed frequency electronic beamsteering, the metasurface technology and its unique properties were employed. This allowed to develop an innovative intelligent antenna system, offering exceptional flexibility and adaptability in terms of radiation pattern reconfigurability. From this perspective, our review paper [109] examines the exploration of *dynamic metasurface antennas* and elucidates their role in creating reconfigurable solutions for industrial and other wireless environments.

DMA is a groundbreaking advancement in beamforming antenna technology, offering unprecedented flexibility and adaptability [143]. By leveraging programmable metasurface structures, these antennas can dynamically control electromagnetic waves, enabling agile beamforming, radiation pattern synthesis, polarization control, and frequency agility. This transformative capability opens doors to a multitude of applications across next-generation wireless technologies, from communication systems to imaging and sensing technologies. With the potential to revolutionize wireless communication, sensing and imaging networks, DMAs stand at the forefront of cutting-edge research and innovation. A complete hardware prototype of a 60 GHz mmWave DMA is designed and tested in this work. A comprehensive paper comprising this work has been published in [179], whereas a short insight is reported in [180].

5.1 Introduction to DMA

The remarkable properties of metamaterials to manipulate electromagnetic (EM) waves have yielded a variety of exotic phenomena and gained significant interest in a variety of domains. Their effective parameters can be tailored when used within planar structures, also known as metasurfaces, to accomplish a specific transformation of transmitted, received, or incident EM waves. The next-generation (beyond 5G and 6G) wireless technologies are envisioned to adapt to dynamic conditions through intelligent and software-reconfigurable paradigms to maintain the quality of service and seamless connectivity. Therefore, much of the attention has been paid to the dynamically tunable metasurfaces whose operational status can be electronically reconfigured, such as reconfigurable intelligent surfaces (RIS) and coded reflect/transmit metasurface arrays [133], [134], [136]–[138], [181]. Mainly, the dynamic coded surfaces work on the principle of reflections and are required to be fed through an external source antenna which renders the whole network quite bulky [182]–[184]. A comprehensive review of reflective digitally coded metasurfaces is presented in [135]. Nevertheless, instead of reflections, the transmitting metasurfaces (converting in-plane wave to over the air radiation) have recently gained attention as they possess the benefits of in-plane circuit feed, low profile, dynamic tunability, and seamless integration with the radio-frequency (RF) frontends[143].

Dynamic metasurface antenna is an emerging concept which offers controllable radiation pattern diversity and adaptability from a simplified and compact hardware platform [143]. Some other nomenclatures are also used in literature, such as Reconfigurable Holographic Surfaces [31]–[33], [185]. Predominantly, these metasurface antennas make use of polarizable dipole metamaterial elements of the sub-wavelength size that can dynamically reconfigure their radiation pattern using a single channel, thereby providing efficient control over steerable beams [186]–[188].

A conceptual representation of the waveguide-fed one-dimensional (1-D) DMA is shown in Figure 5.1. The metamaterial elements couple with a portion of the guided mode that propagates inside the waveguide and radiates it into the free space using the variety of modalities, such as semiconductor components such as positive-intrinsic-negative (PIN) diodes, varactor diodes as well as liquid crystals. In this work, we used PIN diodes integrated with each meta-atom, to independently control the coupling and non-coupling states of each meta-element through a digital binary coding sequence generated from a programmable FPGA.

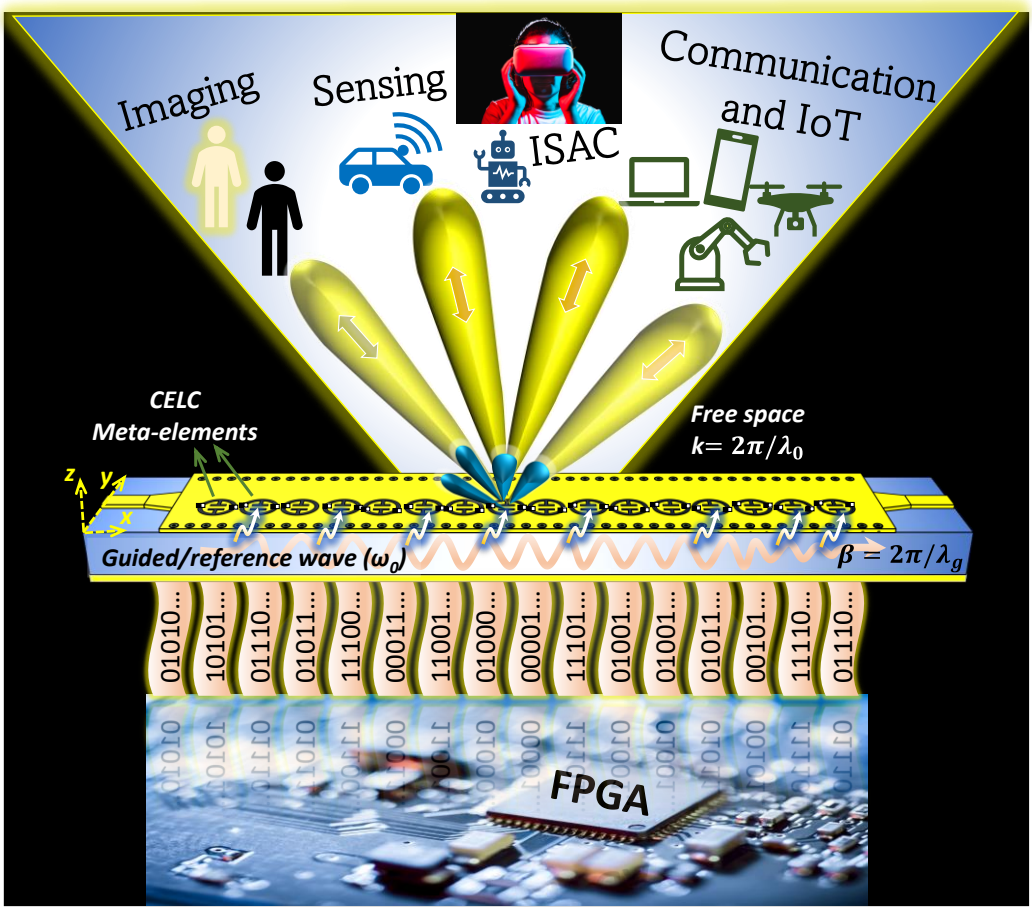

Figure 5.1. A conceptual depiction of a DMA integrated with a software-programmable FPGA. The excitation states "0" and "1" of the meta-elements are independently controlled according to the applied 1-bit digital coding sequence through embedded PIN diodes, resulting in real-time agile electronic beam-steering.

Not only does this transformational feature improve signal quality and beam pattern, but it also allows adaptive beamforming, and pattern diversity, making these antennas desirable for next-generation mmWave communication, sensing, and imaging (CSI) applications [31], [137], [143], [189], [190].

A DMA is based on metamaterial elements consuming substantially less power and offers low-cost than conventional phased array antenna systems because it eliminates the need for complex and lossy corporate feed systems, as well as active phase shifters and amplifiers. Furthermore, a metamaterial element's resonance can be dynamically tuned using above mentioned electronic components with low power requirements and without the need for complex active circuitry [188]. The remarkable features such as smaller size, lower cost, easy integration, and feed mechanism through planar waveguide apertures, reduced hardware complexity, and lower power consumption make DMA an interesting and viable choice for the next-generation of smart wireless networks [33], [109], [141], [143], [185].

The dynamic metasurface apertures have been employed for imaging and sensing applications [139], [189]–[193]. Moreover, owing to their promising potential, recently some of their other EM aspects have been demonstrated such as channel estimation [194], communication model [195], and analysis using a discrete dipole framework [196]. Although much research interest has been laid in recent years towards sensing and imaging applications of DMAs, however, a promising higher mmWave hardware-level design of DMA to serve as a high-performance beam-steering antenna array for the wireless communication domain is highly desirable and is still in its infancy. Quite a few DMA prototypes have been reported for the communication domain around X-band (8 to 12 GHz) [146]–[148], 23.5 GHz [149], and 27 GHz [150] using conventional rectangular CELC resonators. Nevertheless, owing to very small dimensions at higher mmWave bands, the DMA design along with integrated RF feed and controllable hardware becomes immensely challenging. More specifically, the design and experimental verification of DMAs at higher mmWave bands (around 60 GHz) and sub-THz bands is a critical next step in unlocking their potential for 6G communication and is still in the early phases of research, as explicitly envisioned in [143].

5.2 Design Methodology of the Proposed DMA

In general, a DMA primarily consists of numerous resonating metamaterial elements placed periodically in a planar waveguide structure. DMA can be one dimensional linear array (1-D array), where elements are arranged along one of the axes, for instance along x-axis as in this work, or two dimensional planar array (2-D array) where elements are arranged along x and y axes. We divide the design phases of a DMA into two main steps. First, the design of a planar SIW structure which will be used to excite the CELC metamaterial element. This is because the CELC resonator is a magnetic dipole and thus magnetic field (H-wave) is required to excite it, whereas the planar SIW structure readily provides TE_{mn} modes, which are H-waves. The TE modes refer to the transverse electric mode in the dominant mode of propagation. The second step is the design of the CELC resonator at the desired frequency band and integrating it into the waveguide aperture. The pattern reconfigurability can then be achieved by forming a multitude of meta-elements and incorporating passive electronic components, such as PIN diodes in this work, with each CELC resonator along with an appropriate biasing network to achieve beam-steering.

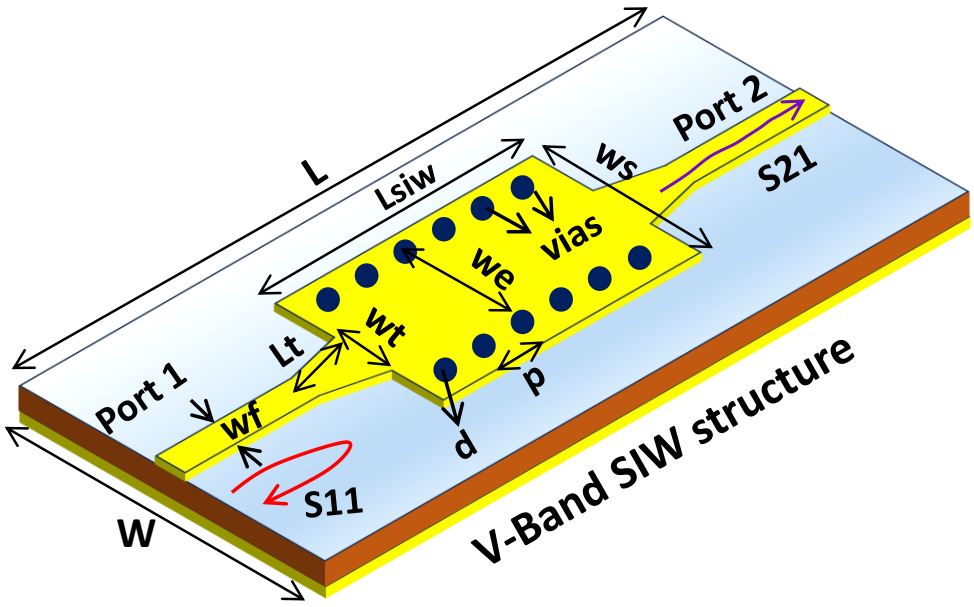

Figure 5.2. Schematic design of V-band SIW structure. (dimensions in mm). L=20.32, W=15, wf=0.62, Ls = 4.16, ws = 4.16, we = 3.05, wt = 1.25, Lt = 2.16, d = 0.2, p = 0.4, Lsiw = 4 for DMA element and Lsiw = 27.36 for DMA.

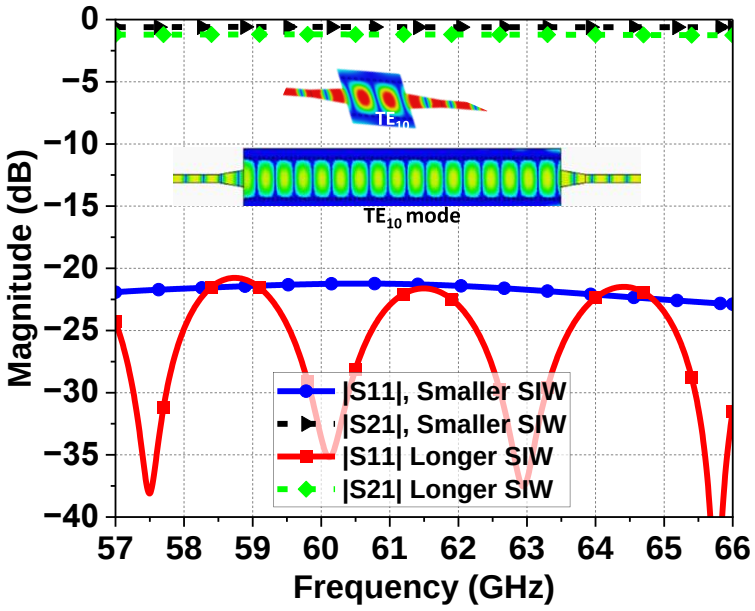

Figure 5.3. Reflection and transmission magnitude of designed SIW structure.

SIW is a highly adaptable and effective transmission structure that is extensively utilised in microwave and mmWave applications [41]. SIW is capable of supporting multiple modes of

propagation, each with unique properties and benefits. The TE_{10} mode is the primary mode in SIW, similar to the basic mode in rectangular waveguides. In this mode, the electric field is perpendicular to the direction of propagation. This mode has little loss and dispersion, rendering it well-suited for high-frequency applications [118]. In contrast to conventional rectangular waveguides, SIWs do not possess the requisite symmetry to sustain transverse magnetic TM modes due to RF wall created by via fence, which entail a magnetic field perpendicular to the direction of transmission [118]. The lack of TM modes in SIW setups is due to the limitations imposed by integrating the waveguide vias into a dielectric substrate. This integration restricts the required fluctuation of the magnetic field across the waveguide's cross-section. Consequently, SIW structures generally depend on TE modes for signal propagation, which restricts their modal features in comparison to conventional waveguides [41]. However, fortunately for DMA design, the TE modes (e.g., TE_{10}) are desirable as these are magnetic waves which are sufficient to excite CELC magnetic dipole metamaterial elements [186].

5.2.1 Design of V-Band SIW Structure

The SIW structure was designed using Rogers 3003 substrate, with a dielectric constant of 3, thickness of 0.25 mm, and copper cladding of 17.5 μm, as shown in Figure 5.2. An electroplated wall of vias is designed carefully to achieve high transmission (S21) and low reflection coefficient (S11) around the 60 GHz band. The diameter of vias (d) is set as 0.2 mm (0.04 λ_0) and the distance (pitch) between any two consecutive vias (p) is set as 0.4 mm (0.08 λ_0) to minimize the leakage losses (here λ_0 is the free space wavelength at 60 GHz) [197]. We designed the SIW structure to operate at the first dominant TE_{10} mode. In an SIW structure, the TE_{10} mode is the fundamental mode of operation. It represents the lowest-order mode with a cutoff frequency typically defined by the dimensions of the waveguide and the properties of the substrate material. The TE_{10} mode is widely utilized in SIW structures for various microwave and mmWave applications due to its simplicity and ease of analysis [118]. The cutoff frequency of the dominant mode and effective width of SIW is calculated as [198]:

$$f_{c_{(TE_{10})}} = \frac{c}{2\varepsilon_r w_{eq}} \tag{5.1}$$

$$w_{eq} = w_{siw} - \frac{d^2}{0.95\,p} \tag{5.2}$$

where c is the speed of light, w_{siw} is the distance between two rows of vias, and w_{eq} is the effective width of SIW which is a function of the pitch length and the diameter of vias. These dimensions were then further optimized in an electromagnetic solver to achieve high S21 and low S11 parameters to make sure that the SIW structure itself should not radiate.

A 50 Ω microstrip feed line having a width of 0.62 mm is designed and a tapered transition from microstrip to SIW is optimized with the proposed width of 1.25 mm to ensure better reflection and transmission performance. The edge-fed SIW makes the design extremely easy for measurements as well as to integrate it with other RF radio circuitry, such as with mmWave power sensors for RF sniffing.

The simulated magnitude of the reflection coefficient (|S11|) and transmission coefficient (|S21|) of the SIW structure is presented in Figure 5.3. Once carefully designed, the length of SIW does not significantly affect the reflection coefficient while insertion loss is merely added for longer structure (i.e., |S21| can be reduced due to resistive and dielectric losses of the longer substrate), thus it can be scaled down in length to excite a single CELC resonator, as required. For single CELC resonator excitation, SIW length (L_{siw}) is 4 mm, whereas to accommodate 16 CELC resonators, the overall L_{siw} is 27.36 mm. The |S21| (transmission coefficient, or insertion loss) is better than –1.19 dB for longer SIW and -0.6 dB for shorter SIW, whereas |S11| is below -21 dB in both cases in the desired band of interest, covering the entire 57-66 GHz ISM band. The phase distribution in the structure is uniform and the E-field distribution of the SIW structure illustrates TE_{10} mode confined with the SIW structure, as shown in the inset of Figure 5.3.

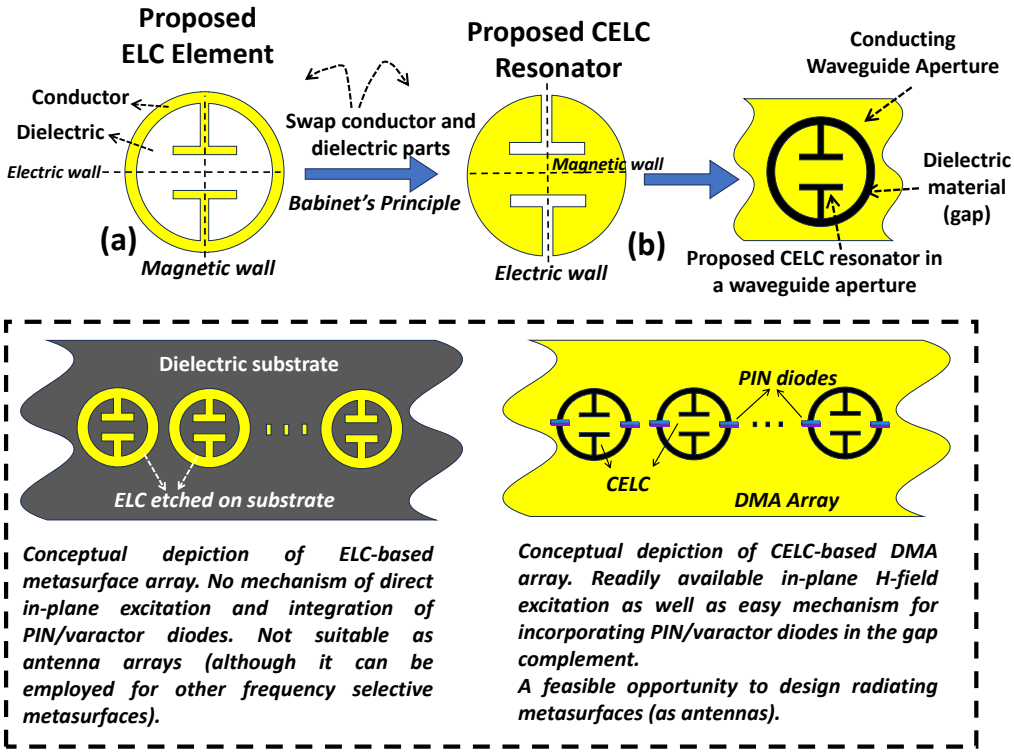

Figure 5.4. Design philosophy and schematic of the proposed CELC metamaterial unit element.

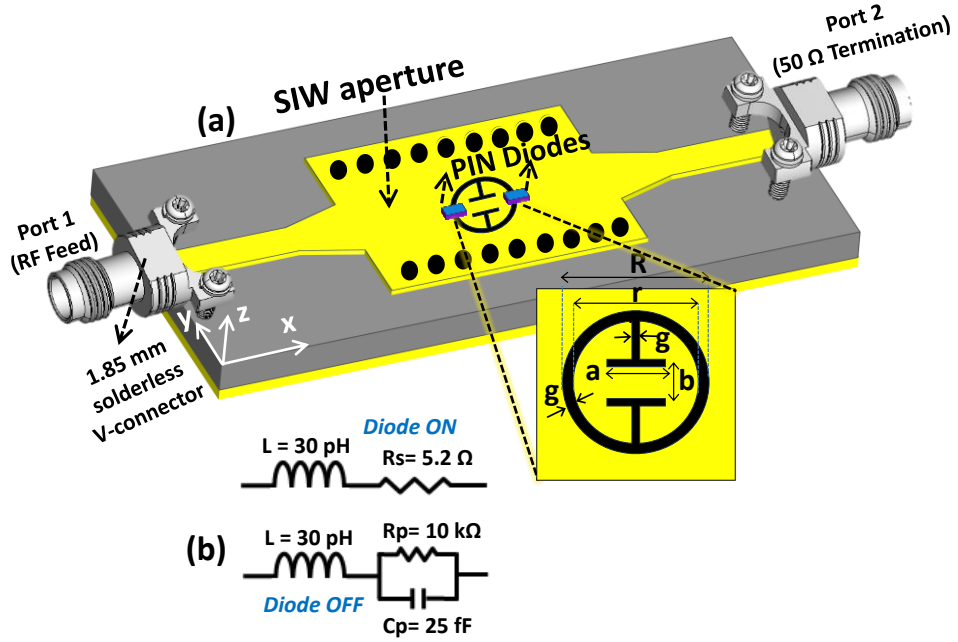

Figure 5.5. (a) Schematic design of the proposed SIW-fed DMA element. Only the top layer antenna part is depicted in this figure. (R = 1.1, r = 0.9, g = 0.1, a = 0.3, b = 0.2). Dimensions are in mm. (b) Circuit model of PIN diode.

5.2.2 Design of the Proposed 60 GHz CELC Metamaterial Unit Element

The design philosophy of a DMA element is demonstrated in Figure 5.4. Consider first the proposed design of an ELC element in Figure 5.4(a). The structure consists of a conducting ring with two mutually perpendicular strips at two positions to create a small capacitive gap between them which responds to an electric field (E-field). The ELC elements radiate poorly when embedded in a conducting plane and therefore are not a feasible choice for radiating metasurfaces (i.e., antenna arrays). Having said that, the proposed ELC resonator can be employed to design frequency-selective metasurfaces for other applications, which is not the scope of this work. On the other hand, their complement metamaterial elements (i.e., CELC) with an effective magnetic response provide better radiation characteristics [188]. According to Babinet's principle [199], the dual/complement of an ELC element (i.e., CELC) is a pure magnetic resonant structure that couples strongly to the magnetic field (H-field) [187], [200]. The proposed CELC resonator is designed by interchanging the conductor and dielectric parts of the ELC, thereby swapping electric and magnetic walls, as shown in Figure 5.4(b). Note that the geometry of the proposed CELC is different than that of the conventional rectangular CELC element. The enhanced performance comparison of the proposed CELC is discussed in the later Section 5.5.3.

The design and geometry of the CELC element are a crucial part of the DMA design and primarily dictate the spectral region of operation. While some intuition may be used during the design stage of a DMA, the characteristics of the element are not individually modified through a single dimension. Instead, an extensive optimization approach based on full-wave numerical simulations is required to achieve the desired radiation features. The design involves careful optimization of the geometry and sub-wavelength size to achieve its resonance response at a desired frequency. The dimensions of the inset cuts are optimized to resonate around 60.5 GHz and play a crucial role in the efficient radiation performance of the CELC element. The diameter of the CELC element is 0.9 mm ($\lambda_0/5.55$). A circular slot with a diameter of 1.1 mm is etched in the SIW aperture to place the designed CELC resonator. The position of CELC is horizontally equidistant from both ports for symmetry, while the vertical offset was optimized at 0.5 mm from the center for better DMA performance. The radial gap between the SIW aperture and CELC is 0.1 mm for mode coupling and loading the PIN diodes effectively. The DMA is fed from port 1, while port 2 is used to dampen the residual energy in the structure and avoid standing waves. The proposed schematic of the DMA element is shown in Figure 5.5.

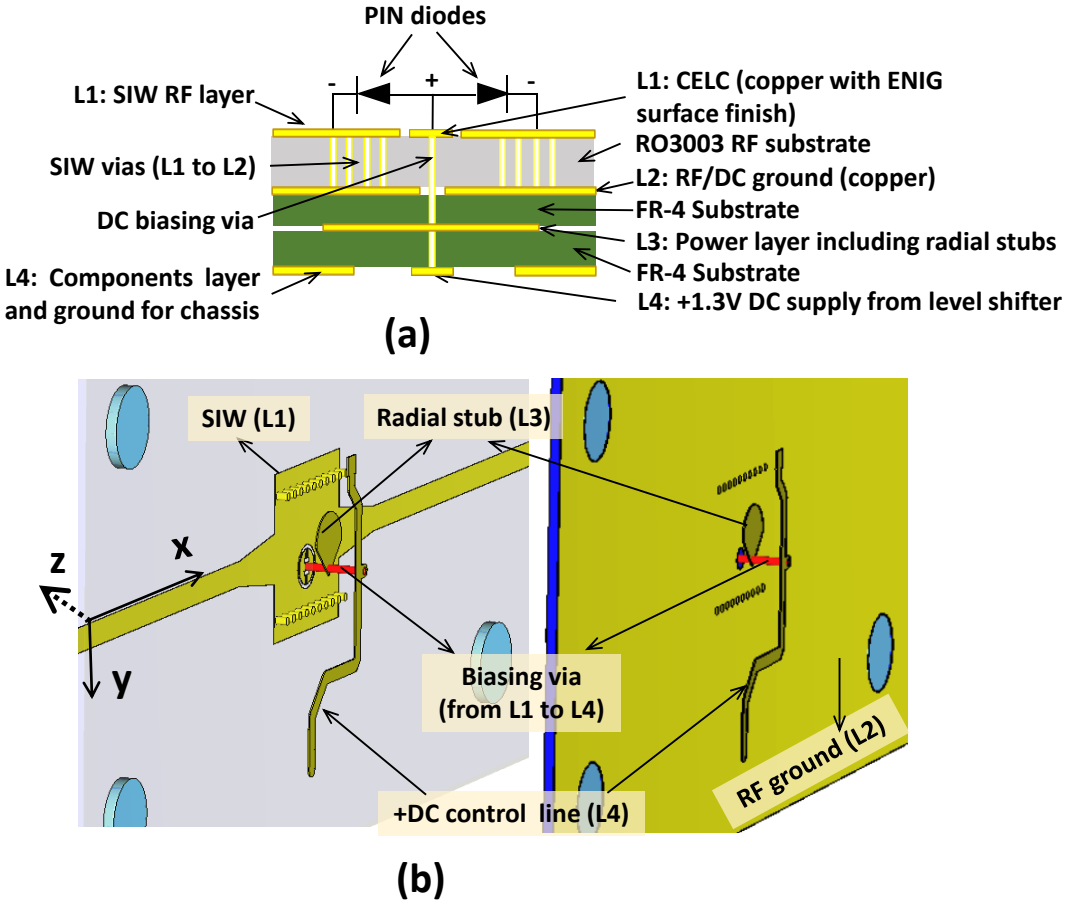

Figure 5.6. (a) Cross-sectional 4-layer PCB stack up view (b) A realistic schematic model of the single DMA element including biasing network for accurate simulations. (left) without RF ground shown (i.e., L2). (right) with RF ground (L2) shown.

5.2.3 Tunability of CELC Meta-Element and Biasing Scheme

The tunability of the CELC resonator is achieved by controlling the switching state of the loaded PIN diodes (MADP-000907-14020W) [201] on the capacitive gap between the CELC and SIW aperture. In simulations, the PIN diode was modelled as an equivalent lumped element circuit as shown in Figure 5.5(b). For the forward biased state (diode on), a series combination of L = 30 pH and Rs = 5.2 Ω was used, whereas for the reversed biased state (diode off), a combination of L = 30 pH with Cp = 25 fF and Rp = 10 kΩ was used (as from data sheet [201]).

The cross-sectional view of the printed circuit board (PCB) layer stack of the DMA consists of 4 layers, as presented in Figure 5.6(a). The top layer (L1) comprises CELC meta-element and SIW conductor, layer 2 (L2) includes RF ground, layer 3 (L3) is exclusively prepared for +DC power and radial stubs, while layer 4 (L4) consists of biasing lines, DC ground area, and components (such as voltage regulator integrated circuits (ICs), coupling capacitors to reduce

switching noise, and light-emitting diodes (LEDs) for debugging and beamforming visualization. Further detail about layer stack-up is provided in Section V-A.

The PIN diodes are biased with a positive DC voltage at the center of the CELC resonator through a metalized via of 0.2 mm diameter, extending from the center of the CELC (L1) to the DC control line at the bottom (L4). The choice of the center point of CELC for biasing via is because it indicated near zero E-field distribution in the numerical simulations, therefore its impact on the radiation pattern and the guided wave is minimal while biasing. The DC and RF share a common ground layer and the DC negative terminal can be connected to the external metallic body of the feed connector during practical antenna measurements. To separate the DC line from RF, an open-ended radial stub of quarter-wavelength (at 60 GHz) radius was designed with biasing via at L3. Therefore, by generating a virtual short circuit for RF current, this sectoral radial stub effectively blocks RF from reaching the DC source. These methods minimize the additional loss produced by the biassing network, which often occurs in reconfigurable reflect arrays. The realistic schematic model of a single DMA element including PIN diodes and DC biasing network (i.e., biasing via, radial stub and DC control line) is illustrated in Figure 5.6(b), whose realistic simulated results are presented in Section 5.6.

5.3 Radiation Mechanism of DMA and Theory of Operation

The biasing state of the PIN diode decides the radiating (coupling) or non-radiating (non-coupling) state of the CELC resonator. When the diode is forward-biased, the CELC resonator is effectively shorted with SIW aperture and thus becomes a part of the SIW structure. As a result, its resonance and radiation characteristics are lost. On the other hand, when the PIN diode is reverse-biased, the CELC resonator is effectively isolated from the SIW structure and becomes analogous to an open circuit with respect to the SIW aperture. Consequently, the CELC resonator couples the portion of the waveguide mode to the radiation mode and exhibits radiation characteristics. In this way, a 1-bit “digital element” with either radiating (“1”) or non-radiating (“0”) state forms the basis of a DMA.

Note that in this mode of operation, the diode-off state leads to the CELC element-on state, and the diode-on leads to the CELC element-off state. Therefore, the overall DMA design in the radiation state consumes much less power as compared to the conventional power-hungry phased array systems [185], [32]. Eventually, the binary digital coding combinations (“0s” and “1s”) when applied to a number of CELC resonators in an array topology form the basis of a

digital programmable metasurface antenna array for fixed frequency electronic beam-steering, controlled externally through FPGA.

5.4 Dispersive Characteristics and Left-Handed Metamaterial Properties Of The Proposed CELC Meta-Element

There has been a lot of interest in artificially engineered materials with effective negative permittivity (ENG), effective negative refractive index (NRI), and negative group velocity (NGV) after the concept was theorized by Veselago [202]. These media, also known as left-handed metamaterials, exhibit unique electromagnetic features that are not observed in naturally occurring materials, such as the reversal of Snell's Law, Doppler's effect, and the Vavilov-Cerenkov effect (radiation produced by a fast-moving particle as it travels through a medium) and unusual focusing properties [203], [204]. What distinguishes the resulting media is that the effective permittivity, effective refractive index, and group velocity can attain negative values around the resonant frequency band with high dispersion characteristics (known as anomalous dispersion) which are not observed in conventional materials.

The proposed CELC element in the radiation state exhibits dispersive properties of the DMA structure which are elucidated here. These dispersive characteristics depend on a strong absorption spectrum around the resonance and can be extracted from the S-parameters of the structure. The transmission phase around the resonance further elucidates the resonance phenomenon. The double phase slope reversal within the absorption resonance band exhibits anomalous dispersion characteristics of the DMA element during its radiation state, as shown in Figure 5.7. The anomalous dispersive phase is attributed to negative group delay (τ_g), negative group refractive index (ng), negative group velocity (vg), and negative slope of the refractive index (n) within the resonance band. The concept of group delay is closely related to group velocity and provides a way to describe the velocity of propagation of electromagnetic wave packets [205]. For a well-behaved wave packet, it is the time delay that the signal envelope experiences as it travels through a medium of specified length. It is related to the negative of the angular frequency (ω) derivative of the transmission phase (ϕ_{s21}) as:

$$\tau_g = -\frac{d\phi_{s21}}{d\omega} \tag{5.3}$$

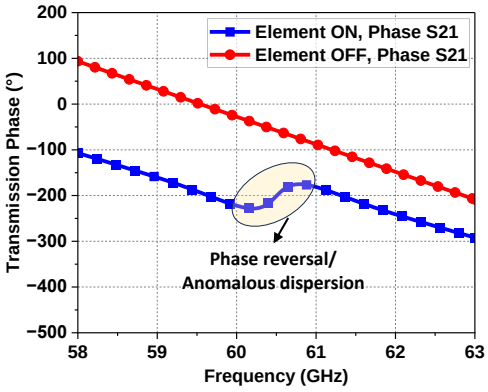

Figure 5.7. Transmission phase of the proposed DMA element in radiating (element-on/ "1") and non-radiating (element-off/ "0") states.

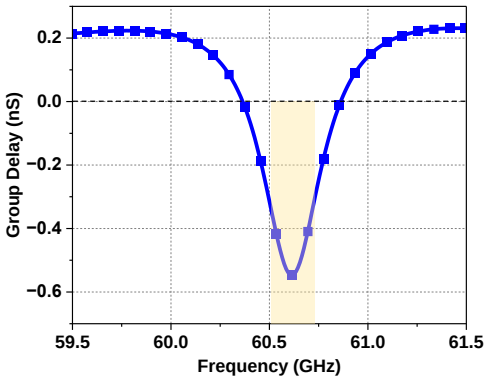

Figure 5.8. Group delay of the radiating CELC meta-element.

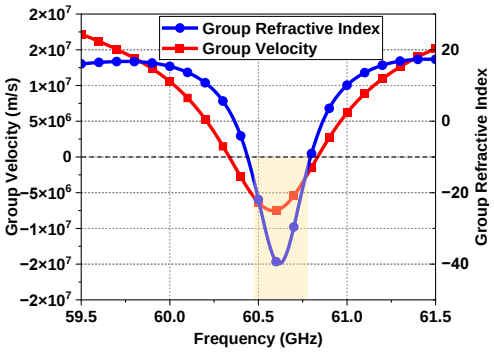

Figure 5.9. Group velocity and group index of the radiating CELC meta-element.

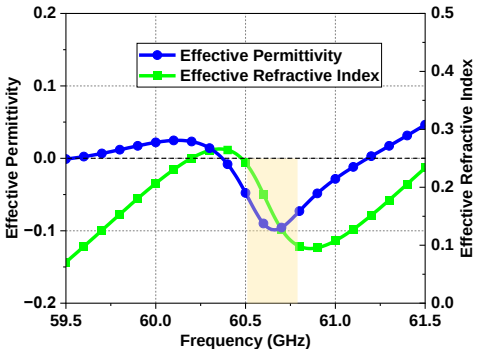

Figure 5.10. Effective refractive index and effective permittivity of the radiating CELC.

It can be observed from Figure 5.7 that the slope of the S21 phase is positive around the resonance, which according to (5.3) leads to a negative group delay.

The negative of the radiating CELC element around its resonant frequency is shown in Figure 5.8 which is of the order -0.53 ns. The group velocity and group refractive index are related as:

$$v_g = \frac{c}{n(\omega) + \omega(\frac{dn}{d\omega})} \tag{5.4}$$

The whole term in the denominator refers to the group refractive index. According to (5.4), the decreasing value of the refractive index with frequency (i.e., negative slope) leads to the negative group velocity and hence the negative group index (*ng*). It can be noted from Figure 5.9 that around the resonance band of the radiating CELC element, the group velocity and group index are negative. This is in agreement with ((5.4) by noting that the slope of the

effective refractive index around the resonance band is negative, as shown in Figure 5.10. Moreover, as demonstrated in Figure 5.10, the effective permittivity is also negative around 60.5 GHz. These characteristics exhibited by the proposed CELC element satisfy the properties of an ENG left-handed metamaterial medium [203].

5.5 Simulated Results and Analysis of Single DMA Element

5.5.1 S-Parameter Analysis in Radiating And Non-Radiating States

The magnitude of S11 and S21 of the proposed DMA element in on and off states is shown in Figure 5.11. When the PIN diode is off, the CELC couples to the waveguide mode and absorbs energy which is then radiated. The element-on state of the CELC shows strong Lorentzian-like resonance at 60.5 GHz characterized by |S21| dip of -15 dB. Note that around the resonance band where S21 drops, the CELC element being an open circuit resonator offers high impedance to the input side and therefore S11 might degrade. However, being an antenna property, it is always preferable to maintain |S11| to be less than -10 dB to maximize the accepted power and minimize standing waves. In the proposed design, |S11| of the DMA element in the radiating state is less than -10 dB around the resonance band. When the PIN diode is on, CELC behaves as a short circuit and virtually becomes part of the SIW structure. Consequently, its resonance effect is lost, and its impedance is matched to that of the SIW structure therefore maximum energy flows towards port 2, thereby presenting |S21| > -1.5 dB and |S11|< -15 dB. It is important to note that a single CELC element manifests a high Q-factor and narrow bandwidth of operation, however, with array configuration, the overall operating bandwidth is enhanced by resonance combination of multiple CELC meta-elements.

It is instructive to mention here that the proposed DMA element prototype without loading the PIN diode acts as an ideal DMA element with an open circuit CELC resonator that will always be a radiating case around 60.68 GHz, due to coupling with waveguide mode through the open circuit capacitive gap. Here we present the effect of loading PIN diodes with the CELC element as well as the effect of biasing network to assert the most realistic simulation results. Hence, the simulation results for four different design cases are presented to test a single DMA element as follows:

1) Open circuit DMA element, without biasing and without diodes, which represents the most ideal case to analyze the resonance behavior of CELC while reducing the simulation time.

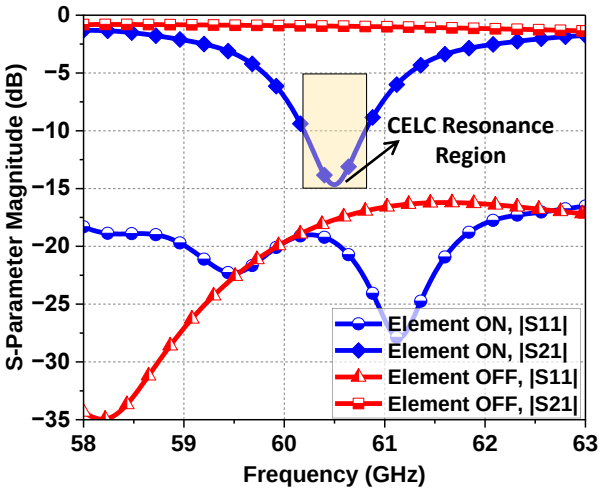

Figure 5.11. Magnitude response of S11 and S21 of the proposed DMA element in radiating (element ON) and non-radiating (element OFF) states.

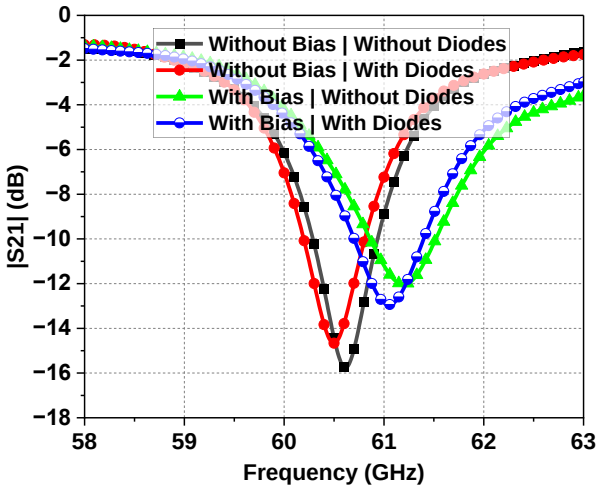

Figure 5.12. |S11| and |S21| of the proposed single DMA element in radiating (element ON) and non-radiating (element OFF) states.

2) Design with loaded PIN diodes but without a biasing network.

3) Inclusion of biasing network but without PIN diodes.

4) DMA with complete biasing network as well as loaded reverse-biased PIN diodes.

The impact of the above-mentioned four design cases on the resonant frequency (|S21| shift) is presented in Figure 5.12. It can be noted that the resonance frequency shifts from 60.6 GHz to 61 GHz when the biasing network is included in the model. This blue shift is due to the addition of parallel inductance of the biasing via with inherent inductance of the CELC meta-element. Note that the net inductance decreases in a parallel combination ($\omega_0 = \frac{1}{\sqrt{LC}}$) and thereby the resonance frequency increases. Similarly, the loaded diodes cause a slight redshift

in the resonance frequency due to the possible addition of small parasitic capacitance of PIN diodes (as mentioned in the datasheet [201] that extremely small parasitics might exist) in the off state. Note that the net capacitance increases in a parallel circuit combination. Typically, the resonance band radiated power and realized gain showed minimal impact from the inclusion of a biasing network and PIN diodes. This ensures the effective and careful design considerations employed in the proposed 60 GHz DMA element, which would serve as a building block of a large DMA array.

5.5.2 Radiated Power, Realized Gain, and Radiation Efficiency of DMA Element

The power profile of the DMA element in on and off states is shown in Figure 5.13. For an input power of 0.5 W and accepted power of 0.47 W, the peak radiated power of DMA in the radiating state is 0.36 W at 60.68 GHz for open circuit CELC (i.e., without embedding PIN diodes and bias network). With the inclusion of a bias network and PIN diodes, the peak radiated power of 0.33 W is observed at 61 GHz with the accepted power level of 0.45. Thus, the radiation efficiency of the DMA element is above 73%. Note that we used two PIN diodes to fully suppress the CELC radiation in the element-off state.

It is analyzed from numerical simulations that although one diode works well in a reverse biased state and the efficiency as well as gain can increase a little bit, however, it is the element-off state that is important to consider for DMA design to fully suppress the resonance effect of the CELC meta-element for effective 1-bit performance. When using a single forward-biased diode, the meta-element is not fully suppressed as shown in Figure 5.13(a). With two diodes, the radiation is highly suppressed in a diode-on state, which is desirable. Furthermore, the two diodes maintain the element's symmetry which prevents the asymmetrical current flow and thus the distortion of the radiation pattern. As shown in Figure 5.13(b), the radiated power of the proposed DMA in the element-off state is below 0.05 W when both PIN diodes are in on state.

The peak realized gain (realized gain takes into account the input impedance mismatch loss as well as dielectric and conductor losses) of DMA in radiating state is 7.59 dBi at 60.68 GHz for open circuit CELC, and 7.07 dBi at 61 GHz with bias network and off-state PIN diodes. The gain in the non-radiating state is below -5 dBi, as shown in Figure 5.14. Note that more than 11 dB difference in radiated power and gain is observed in element-on and -off states, which reveals the excellent performance of the proposed DMA element.

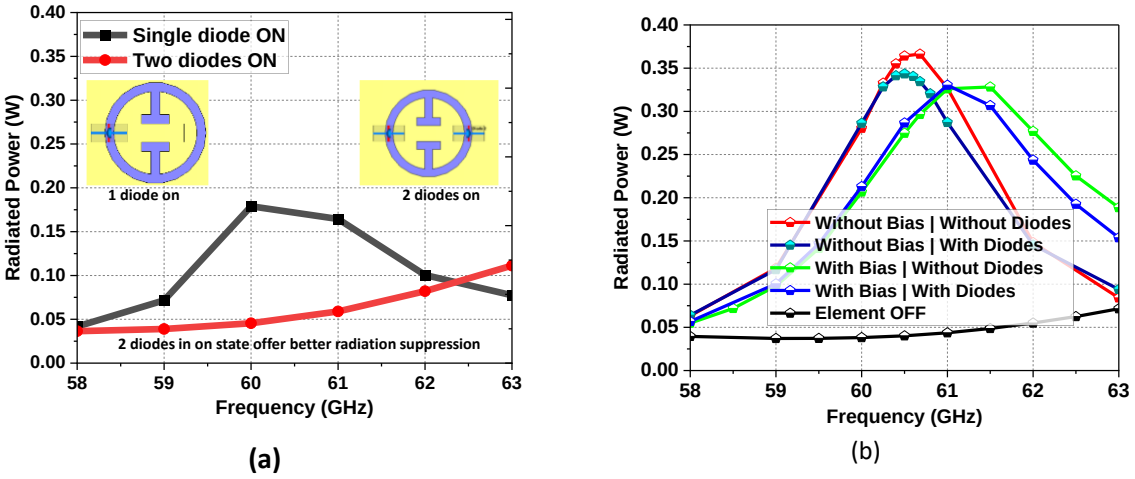

Figure 5.13. (a) Radiated power with single and two diode case (didoe on). (b) Radiated power of the proposed DMA element in on and off states (with two didoes off, onwards all are two didoe cases).

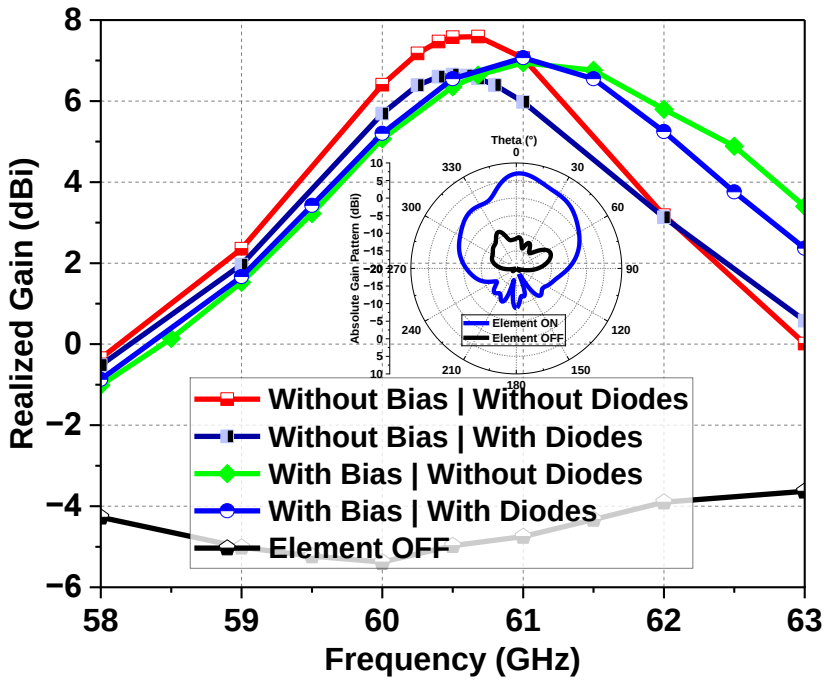

Figure 5.14. Realized gain of the proposed DMA element in on and off states.

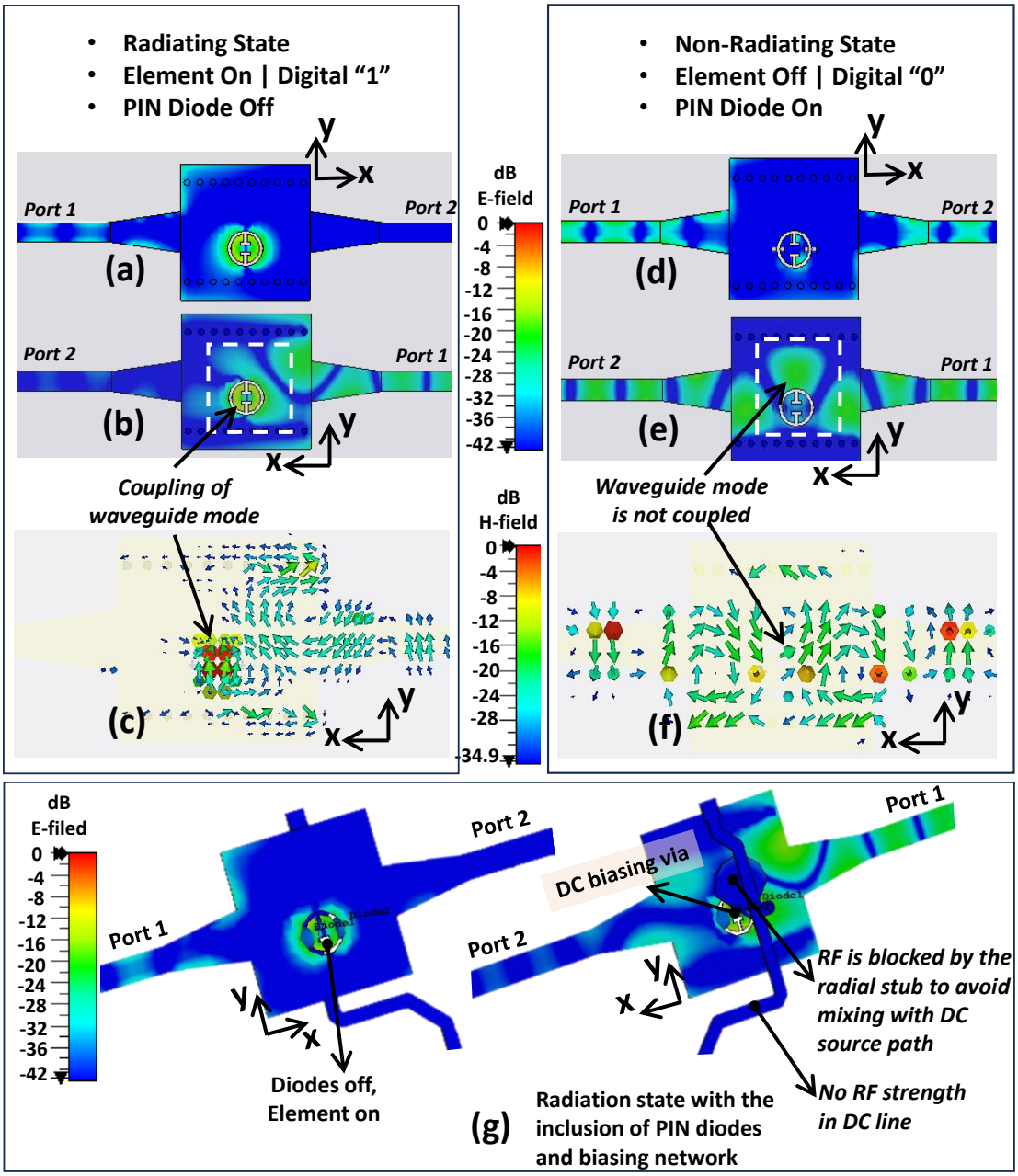

Figure 5.15. E- and H-field distribution of DMA element at 60.5 GHz. (a) E-field top view in radiating state. (b) E-field bottom view in radiating state. (c) H-field bottom view in radiating state. (d) E-field top view in a non-radiating state. (e) E-field bottom view in a non-radiating state. (f) H-field bottom view in a non-radiating state. (g) Simulations of the realistic schematic model of the DMA element as shown in Figure 5.6(b) reveal that radial stub effectively isolates RF from the DC source, and the field strength is the least towards the DC control line.

The radiation mechanism is further illustrated in Figure 5.15 through field distribution. As shown in Figure 5.15 (a and b), when PIN diodes are off, the CELC element couples with the waveguide mode at its resonant frequency of 60.5 GHz and radiates well with a strong E-field. Conversely, when PIN diodes are on, the CELC is shorted with the SIW structure, hence the

energy travels towards port 2 (without coupling) with negligible radiated field intensity around it, as illustrated in Figure 5.15 (d, e). Similarly, H-field intensity in radiating and non-radiating states are shown in Figure 5.15(c) and Figure 5.15(f), respectively. The effect of radial stub and biasing via has minimal effect on the performance of DMA, as illustrated in Figure 5.15(g).

5.5.3 Performance Comparison Between Proposed and Conventional Rectangular CELC Meta-Elements

The rectangular-shaped CELC element has been used extensively in a variety of dynamic metasurface apertures, as well as in recent DMAs [31], [142], [143], [143], [147], [186], [188], [192], [206]–[208]. In this section, a simulated performance comparison of the proposed CELC element and the conventional rectangular CELC based single DMA elemnt is presented. The dimensions of the rectangular CELC were also optimized to resonate around 60 GHz band, as shown in Figure 5.16. Rest of the SIW design was kept same. The simulated results for only ideal radiating state are shown for the sake of completion.

The transmission coefficient revealing the resonance frequency for both cases, realized gain, radiated power, and radiation efficiency are shown in Figure 5.17(a), (b), (c) and (d) respectively. It is obvious that the resonance enhance,ment is prominent in case of the proposed CELC. Moreover, gain and radiated power are also higher as compared to that of the convemttional rectangular CELC element. This is mainly due to the large circular shaped aperture area of the proposed CELC as compared to the rectangular shaped geometry.

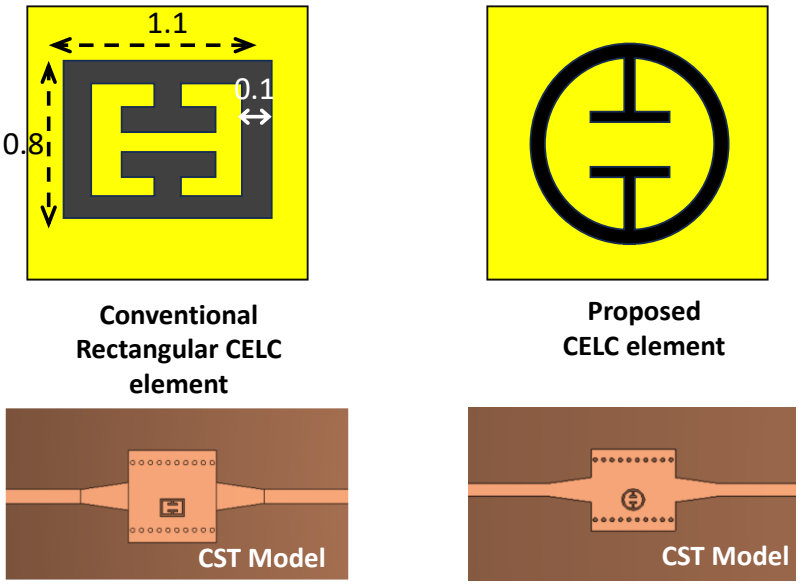

Figure 5.16. Geometry of the proposed and conventional rectanguar CELC metamaterial elements.

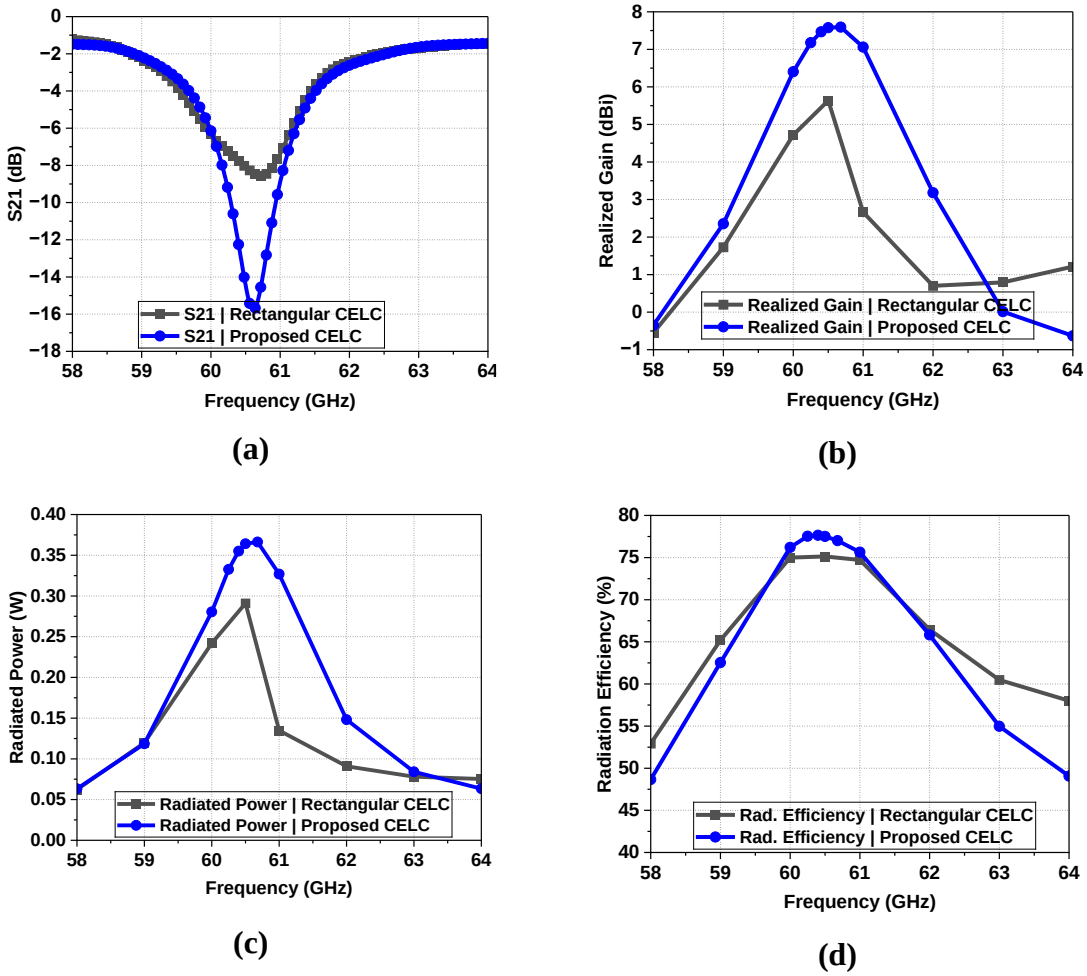

Figure 5.17. Simulated results of the proposed vs rectangular CELC based single DMA element in radiation state. (a) |S21|, (b) Realized gain. (c) Radiated power. (d) Radiation efficiency.

5.6 Polarizability and Array Factor

Having a subwavelength dimension, the CELC resonator can be modelled as a polarizable magnetic dipole that couples with the waveguide mode to radiate EM energy. The induced dipole moment (m) in the presence of an in-plane magnetic field (H_i) is related to the polarizability (α) of the CELC resonator as [188], [209]:

$$m = H_i \alpha \tag{5.5}$$

Polarizability is a measure of how readily an external electric field may polarize a CELC resonator. Since the CELC resonator manifests typical Lorentzian-like resonance in its

radiation state (as shown by |S21| dip of Figure 5.11), therefore its polarizability can be modelled according to Lorentzian dispersion as:

$$\alpha = \frac{F\omega^2}{(\omega_0^2 - \omega^2 + j\omega\Gamma)} \tag{5.6}$$

where ω is the excitation angular frequency, ω_0 is the resonant frequency which is associated with the fundamental geometrical features of each CELC resonator as $\omega_0 = \frac{1}{\sqrt{LC}}$, F is the coupling factor/oscillator strength, and Γ is the damping factor ($\Gamma = \frac{\omega_0}{2Q}$) due to resistive effect of the structure, where Q is the quality factor of the resonator ($Q = \frac{\sqrt{LC}}{R}$). According to (5.5) and (5.6), the field radiated from the CELC resonator has an amplitude and phase determined by the in-plane EM wave multiplied by the polarizability of the CELC resonator.

As the SIW is excited in dominant TE_{10} mode, therefore the transverse component of the magnetic field at the position of a given metamaterial element causes the predominant excitation which has sinusoidal variation as a function of the distance along the propagation direction. As the EM wave propagates along the x-axis in the designed case, the in-plane transverse magnetic field component along the y-direction is expressed as:

$$\boldsymbol{H_i} = H_0 e^{-j\beta x_i}\boldsymbol{y} \tag{5.7}$$

where H_0 is the initial magnetic field fed into the SIW structure, β is the effective waveguide propagation constant in SIW (which can be given as $\beta = \frac{\omega}{v_g} = \frac{n_g\omega}{c}$) and x_i is the position of the ith element in case of a DMA. The far-field pattern of a CELC resonator at a distance r is given by the far-field magnetic field vector $\boldsymbol{H_{rad}}$ as:

$$\boldsymbol{H_{rad}} = \frac{\omega^2 m}{4\pi r} cos\theta [e^{-jkr+j\omega t}]\widehat{\boldsymbol{\theta}} \tag{5.8}$$

In (5.8), r is the approximated magnitude of the difference between the location of the radiation source and the observation point at a far-field distance, $\widehat{\boldsymbol{\theta}}$ is the unit vector in the direction of the radiated wave indicating the direction of the magnetic field, and ($k = \frac{2\pi}{\lambda_0}$) is the free-space wave number. Note that the radiation pattern of a single DMA element (as shown in the inset

of Figure 5.14) follows the cosine function as dictated by (5.8), where its intensity is towards the broadside (i.e., towards 0°) with maximum intensity (cos 0°=1) and diminishes around 90°. Considering that the elements do not strongly perturb the waveguide mode and do not interact with each other, the azimuth far-field radiation pattern of the *1-D DMA* of *N* dipole elements in a desired direction (ϕ) from the superposition of the field radiated by each CELC radiator as:

$$\boldsymbol{H_{rad}} = -H_0 \frac{\omega^2}{4\pi r} e^{-jkr} cos\theta \sum_{1}^{N} \alpha_i(\omega)\, e^{-jx_i(\beta + ksin\phi)} \widehat{\boldsymbol{\theta}} \qquad (5.9)$$

Here $cos\theta \sum_1^N \alpha_i(\omega)\, e^{-jx_i(\beta+ksin\phi)}$ is the array factor of 1-D DMA. Being a 1-D array, the in-plane wave has the dependence on $e^{-jkxsin\phi}$ factor, ϕ is the angle of propagation normal to the surface of array aperture, and $\widehat{\boldsymbol{\theta}}$ shows directional wave vector. The terms in ((5.9) account for the dipole strength, angular frequency, distance from the array to the observation point, the angular dependence of the radiation pattern, and the spatial distribution of magnetic dipole elements along the array. The array factor is a function of the geometry of the array and the excitation phase.

The angular resonance frequency ω_0 is fundamentally related to the inductance and capacitance of the CELC element and can be controlled either through the geometry of the CELC element, modifying the local dielectric environment, or by integrating electronic components such as PIN diodes (as in this work) with each meta-element. The overall phase accumulation in the guided wave introduces the phase variation required to produce directed beams by exciting CELC elements along the aperture. It is an interesting phenomenon that varying the separation distance and/or the phase β between the elements is achieved by the on-and-off scheme of PIN diodes and the characteristics of the total field and the beam shapes (beamwidth and number of lobes) of the array are dynamically controlled. In this way, dynamic reconfigurability of radiation patterns is achieved with extremely low power requirements and without the need for complex active circuitry.

5.7 DMA Array Design and Simulated Results

5.7.1 PCB Layer Stack Up of the Proposed DMA

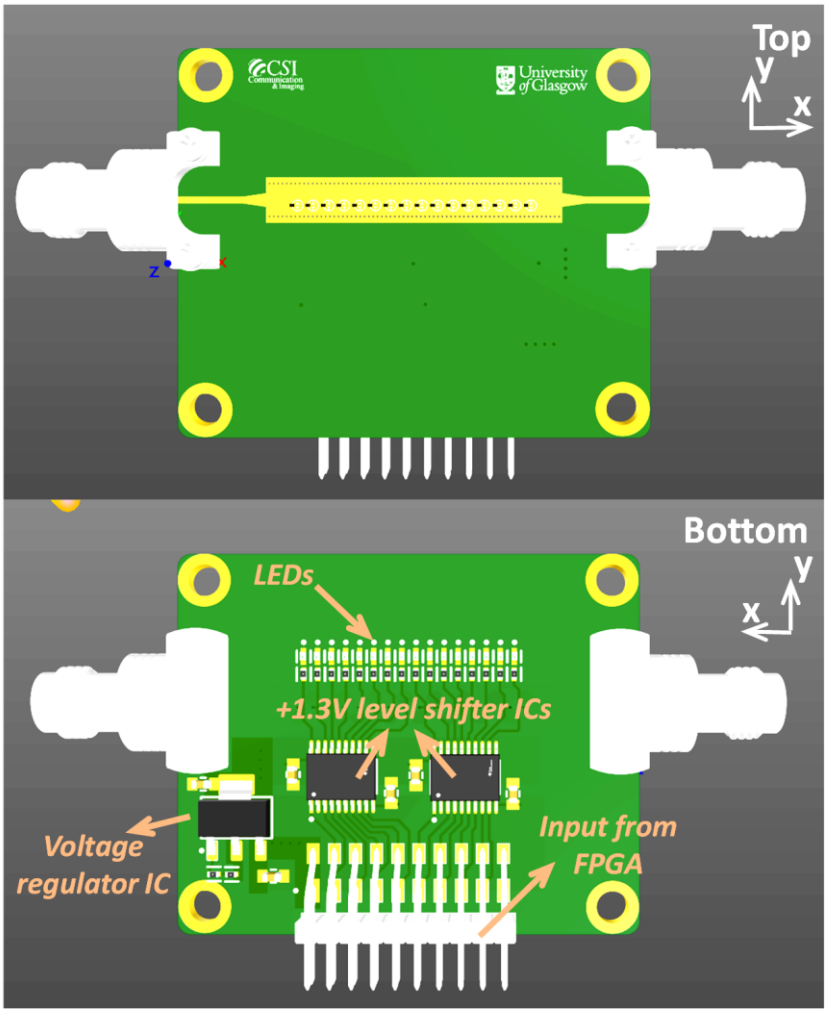

(a)

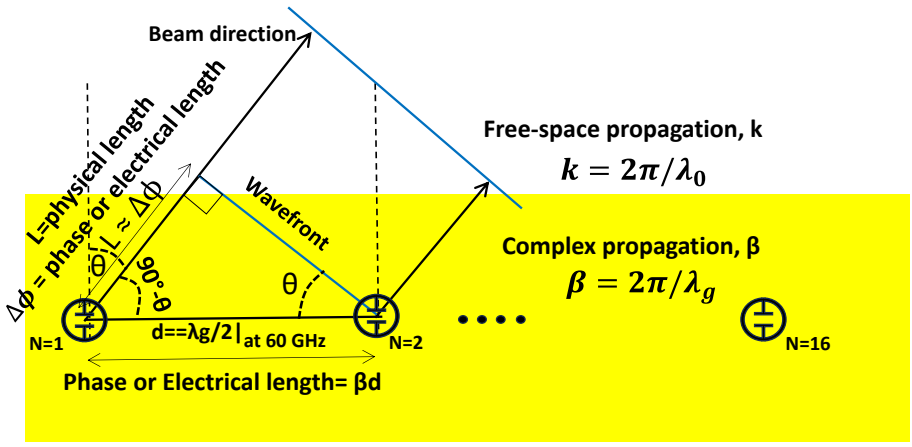

(b)

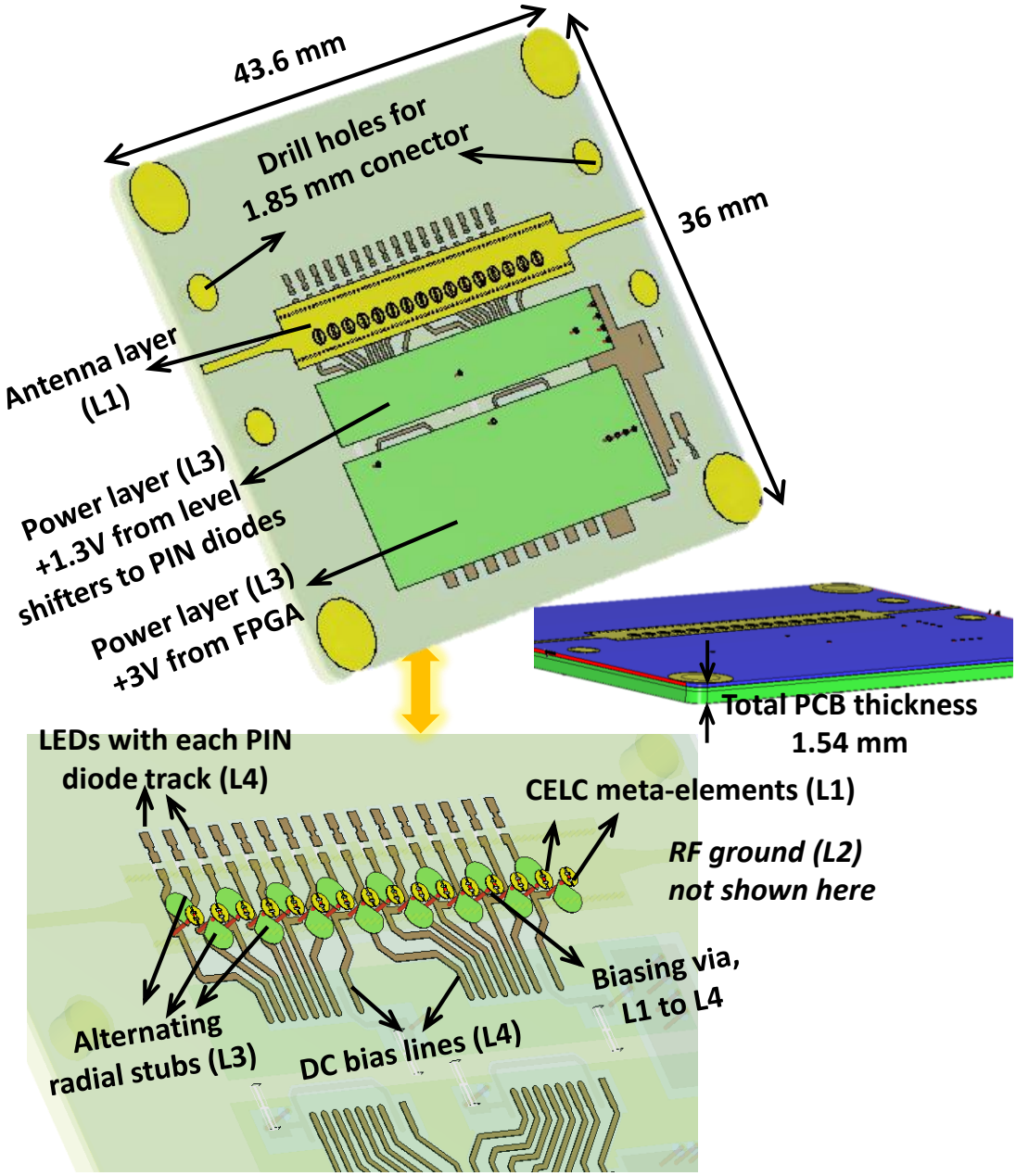

Figure 5.18. (a) Schematic view of the proposed 60 GHz 1-D DMA PCB. (b) The schematic diagram for DMA beam-steering. (c) Exploded schematic view of 4-layer PCB of DMA with DC biasing network revealed.

The PCB view of the proposed DMA designed in Altium is shown in Figure 5.18(a) and the perspective view of the interlayer schematic of the 4-layer PCB depicting the biasing scheme is shown in Figure 5.18(c). The DMA comprises 16 CELC meta-elements, thus encompassing 32 PIN diodes. The dimensions of the SIW structure are the same as those used to excite a single DMA element, except that the length of the SIW aperture is increased to 27.36 mm to

accommodate 16 meta-elements (see Figure 5.2). The S-parameters of the elongated SIW structure are already shown in Figure 5.3. The inter-element gap is 1.44 mm, which is equivalent to $\lambda_g/2$ or $\lambda_0/3.47$ at 60 GHz to avoid mutual coupling. This gap was fine tuned to achieve better SLL and gain performance and is close to Nyquist limit. Note that, for imaging applications the inter-element gap is not fine tuned to Nyquist limit, and rather can be more densed [210]. However, from wireless communication perspective, element spacing at Nyquist limit is desirable [148].

The radial stubs (at L3) connected to each biasing via are oriented in alternating directions to fit within the confined area. Moreover, L3 is exclusively designed to route control lines of PIN diodes. Initially, +3.3 V sourced from the FPGA output is directed to the input of two level-shifter ICs, each equipped with 8 output ports to control a total of 16 meta-elements. Subsequently, the output of the level shifter ICs is maintained at +1.33V (for diode-on case), serving as the supply to activate the PIN diodes. At L4, the path of each pair of PIN diodes is then serially connected to an LED, specifically designed for debugging and providing a clear visualization of the on/off states of the PIN diodes during the application of any digital coding sequence from the FPGA. Some more details of PCB layer stackup are provided in Appendix D.

5.7.2 Multi-Beam Generation From DMA

This section describes the basis behind the multiple beam generation from the DMA using specific coding combiantions. The complex behavior of DMA manifests itself in a variety of ways for different coding sequences and offers remarkable features through wave manipulation by binary coding. From Figure 5.18(b):

$$cos\,(90° - \theta) = sin(\theta) = \frac{\Delta\phi}{\beta d} \tag{5.10}$$

$$\theta = \sin^{-1}\frac{\Delta\phi}{\beta d} \tag{5.11}$$

where $\Delta\phi$ is the phase difference (electrical length) between two consecutive CELC elements ($\Delta\phi = \beta d sin(\theta)$), and θ shows the beam direction. The domain of $\sin\theta$ is the set of real

numbers and its range varies between +1 and -1. Therefore, the inverse sine function ($\sin^{-1}$) only produces real solutions for the arguments bound within +1 and -1. Outside this domain of inverse sine function, the solution is not real. As the phase in a waveguide medium is periodic and repeats after every 2π rotations, thus in general, we can generalize Δϕ with Δϕ+2nπ, where n=0, ±1, ±2, ±3... Hence,

$$\theta = \sin^{-1}\frac{\Delta\phi + 2n\pi}{\beta d} = \sin^{-1}\left[\frac{\Delta\phi + 2n\pi}{2\pi} \times \frac{\lambda_g}{d}\right] \quad (5.12)$$

From (5.12), the grating lobe suppression theory of phased array antenna governs that if the modulus of $(\frac{\Delta\phi+2n\times\pi}{2\pi} \times \frac{\lambda_g}{d})$ is greater than 1 for all n≥1, the solution will be non-real values which can be ignored, and the grating lobes can be avoided. This will happen if $\lambda_g/d > 1$ which implies $d < \lambda_g$, or most commonly $d < \lambda_g/2$ to avoid grating lobes. However, if $\lambda_g/d < 1$, (the case when $d > \lambda_g$), then (5.12) gives multiple real solutions for some n > 0 which translates into grating lobes (multi-beam scenario). Moreover, at higher frequency points such as 62 GHz, the electrical inter-element distance (λ_g) appears greater than that of 60 GHz, therefore multi-beams tend to be more pronounced at higher frequency ends, such as for code 3.

To put the above mathematical explanation of multiple beams into coontext, consider that in conventional phased array antennas, the physical distance between the antenna elements *d* can not be changed once the array is designed (as every element is always in a radiation state and contributes to effective antenna aperture). This can be noted from the arrays designed in Chapter 3 and 4 above. Contrary to this, the hallmark effect of the DMA is that we can dynamically control the radiation state of individual meta-elements and meta-element can either be radiating or non-radiating. For non-radiating state it becomes the part of SIW aperture. Thus, we can manipulate the inter-element distance in real-time using a particular digital coding sequence. Exploiting this effect, we applied code 7 and code 8 to purposely increase the inter-CELC distance *d*. Note that the notion of multiple beams from a metasurface antenna's perspective is usually different from the grating lobe perception of conventional phased array antennas. Therefore, thigh gain multiple beams (from grating lobes) are predicted as a blessing, rather than a curse. The multi-beam scenario of the proposed mmWave DMA can be employed in indoor IIoT applications or multi-user scenarios such as in smart factories where the network is usually highly secured and multiple users can be connected simultaneously through a single

antenna. The plots for multiple beams are presented later in in Figure 5.26 (simulated) and 5.37 and 5.38 (measured) of section 5.8.2.

5.7.3 Bandwidth of the Proposed DMA Array

It is worth mentioning here that the characteristics of DMA such as input impedance, pattern, gain, side lobe level (SLL), etc., are critically influenced by the coding sequence as well as the operating frequency. Therefore, in addition to -10 dB input impedance bandwidth, the "pattern bandwidth" (i.e., gain, SLL) should also be considered from a wireless communication point of view. A visualization of the simulated radiation state of the DMA for different coding sequences at the corresponding operating frequency of a maximum number of elements' excitation is demonstrated in Figure 5.19. Note that 2^{16}=65536 different combinations are possible from the coding space, however, to verify the prototype we present 11 different coding sequences as shown in Figure 5.19.

While a single DMA element sets a distinct resonance frequency with a high Q-factor, the utilization of different coding combinations within a DMA is expected to broaden the bandwidth by decreasing the quality factor. This phenomenon is primarily attributed to the relatively wider impedance matching level at the input port of the DMA across a specific frequency range due to the superposition of different radiation states of meta-elements for dynamic coding sequences. As a result, a typically wider operational bandwidth is achieved. The simulated |S11|, |S21| and radiated power of a fully radiating DMA (i.e., when all elements are in a radiation state) are shown in Figure 5.20. This state of DMA has a maximum radiation power at 61 GHz, where |S11| < -10 dB and |S21| is around -16.4 dB. When all PIN diodes are on, the DMA is non-radiating. As expected, it manifests high |S21| and low |S11| with negligible radiated power, as shown in Figure 5.21. However, this would be a trivial case where the radiation effect (antenna effect) of the DMA is lost.

To further elucidate the concept of the operating bandwidth of the DMA, consider the input impedance and radiation profile for code 1, as shown in Figure 5.22. The optimum operating region for code 1 spans from 60.7 GHz to 63 GHz, where |S11| < -8.5 dB, SLL is below -11 dB, realized gain is above 10 dBi with a peak gain of 12.82 dBi at 62 GHz, and peak radiation efficiency is 67.42% at 61 GHz. Note that around 58.5 GHz, although |S11| is < -10 dB and gain is about 10 dBi, however SLL increases to -7 dB.

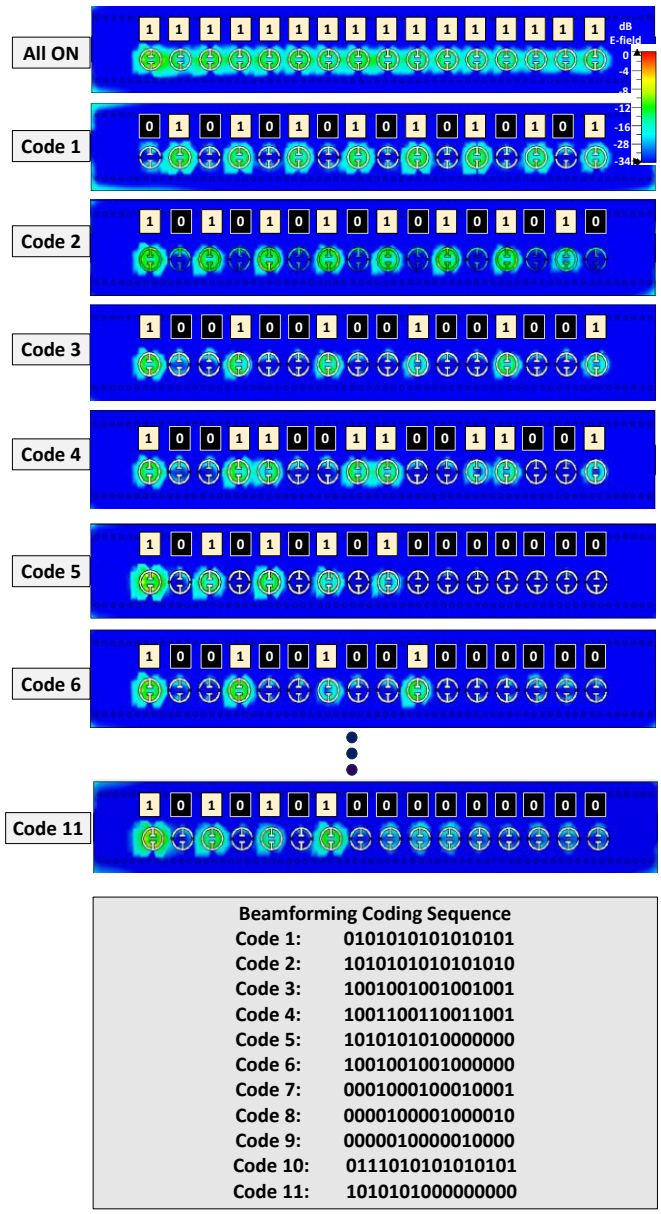

Figure 5.19. Radiation state of the proposed DMA for different coding sequences at the respective frequency of maximum excitation of meta-elements. 11 different applied coding sequences are revealed here. 1's and 0's are w.r.t CELC element states, whereas inverting the same code will depict the state of PIN diodes.

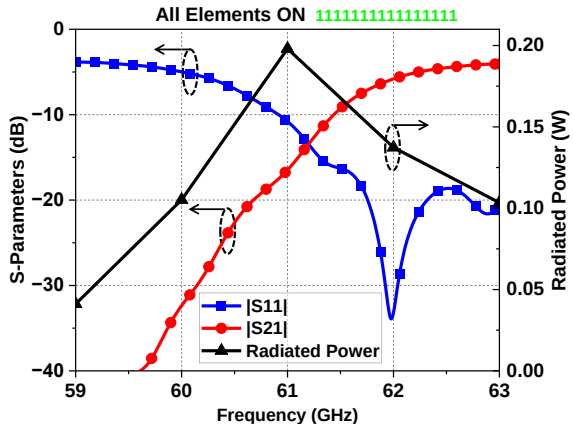

Figure 5.20. |S11|, |S21|, and radiated power of DMA array when all elements are in a radiation state (i.e., all PIN diodes are reverse biased).

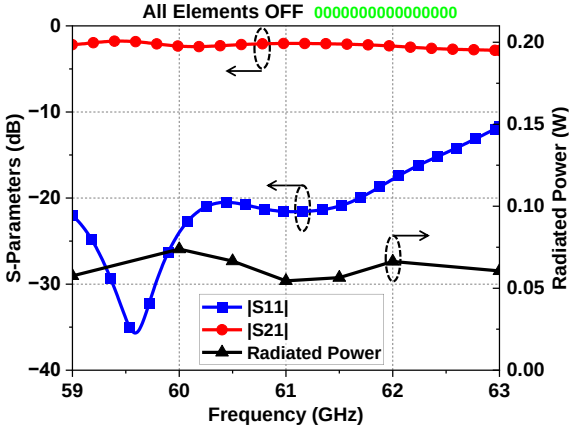

Figure 5.21. |S11|, |S21|, and radiated power of DMA array when all elements are in a non-radiation state (i.e., all PIN diodes are forward-biased).

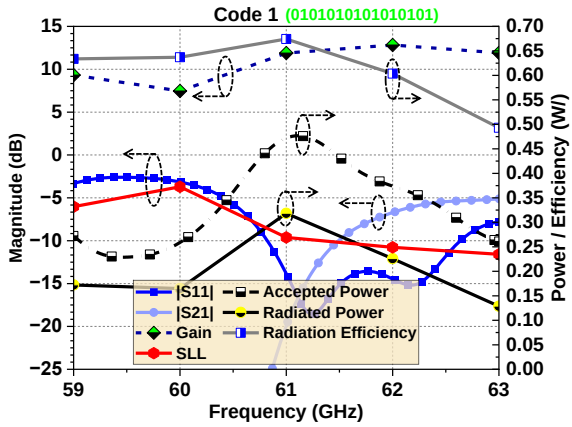

Figure 5.22. S-parameters, radiated power, and gain of DMA for code 1.

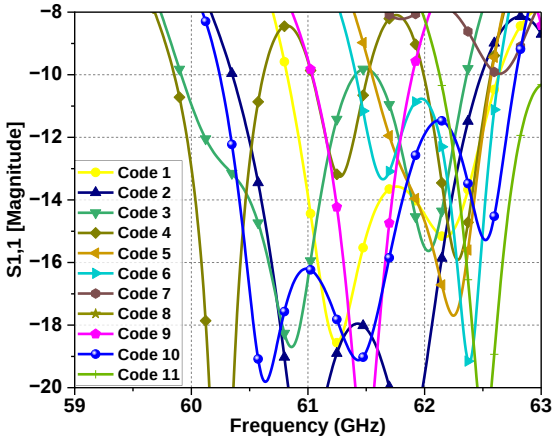

Figure 5.23. Reflection coefficient of various coding sequences from 58 to 64 GHz.

At 60 GHz, the reflection coefficient, SLL, and total efficiency degrade, however, the radiation efficiency is above 63%. Similarly, between 63 GHz and 64 GHz, |S11| < -10 dB, gain is above 10.5 dBi and SLL is at -11 dB, however, the radiation efficiency drops below 50% in this region (because radiated power is low). Therefore, these performance tradeoffs decide the choice of operating bandwidth depending on required application scenarios. For mmWave holographic imaging applications, code 1 might perform quite well from 59 GHz to 63 GHz, because in DMA-based imaging SLL and radiation efficiency are not of main concern, rather various random radiation patterns are of interest [210]. However, the requirements of wireless communication domain are usually stringent regarding SLL, impedance matching, and

radiation efficiency, therefore optimum bandwidth should be considered in a different way considering these metrics.

The reflection coefficient of various selected codes with maximum selected |S11| < -8 dB level is shown in Figure 5.23. Although, some coding sequences show quite good gain, SLL, and efficiency performance at 59 GHz and lower the performance as the operating frequency increases beyond 62 GHz, nevertheless, the high-performance operating range for the proposed DMA lies between 60 GHz and 63 GHz, showcasing a bandwidth exceeding 2.5 GHz. This surpasses the 2.16 GHz bandwidth of a single channel at the 60 GHz ISM band under IEEE 802.11ad and IEEE 802.11ay protocols.

5.7.4 Programmable Electronic Beam-Steering with Digital Coding

Owing to linear array topology, the proposed DMA offers fan-shaped beams with relatively narrow beams in the x-z plane. The 3-D radiation patterns for various codes along with heatmaps are shown in Figure 5.24. For the sake of completion, 2-D radiation patterns in the y-z plane at 60, 61, and 62 GHz for some coding combinbations are presented in Figure 5.25. The radiation patterns are wider and mostly directed towards 0° in the y-z plane. Nevertheless, the principal plane for beam-steering (and thus the plane of interest) is the x-z plane, along the arrangement of CELC meta-elements, as elucidated by beamsteering plots in Figure 5.26.

As illustrated in Figure 5.26, different coding combinations produce different effective radiation apertures of the DMA and form dynamic beam shapes. We can categorize the radiation patterns into three different types for different coding sequences at each operating frequency, such as (a) beams with narrow HPBW, (b) beams with relatively wider HPBW, and (c) multiple beams. Code 2, code 4, and code 10 produce narrow directed beams with an average HPBW of about 10° at 60 GHz, 61 GHz, and 62 GHz. Code 5, code 9, and code 11 produce beams with relatively wider HPBW of around 33° at these three frequency points. Code 7 and code 8 produce multiple beams at 60 GHz, 61 GHz, and 62 GHz. The radiation pattern with code 1 produces wider HPBW of 38° at 60 GHz, whereas at 61 and 62 GHz, it shows relatively narrow HPBW of 12.2° and 8.9° with SLL of -10.35 dB and -11.20 dB respectively. Code 5 provides a broadside beam at 60 GHz whereas all-elements-on case provides a broadside beam at 62 GHz. The beam-steering range for the 11 tested codes varies within ±45°. The versatile beam synthesis of DMA is further explained in the next section.

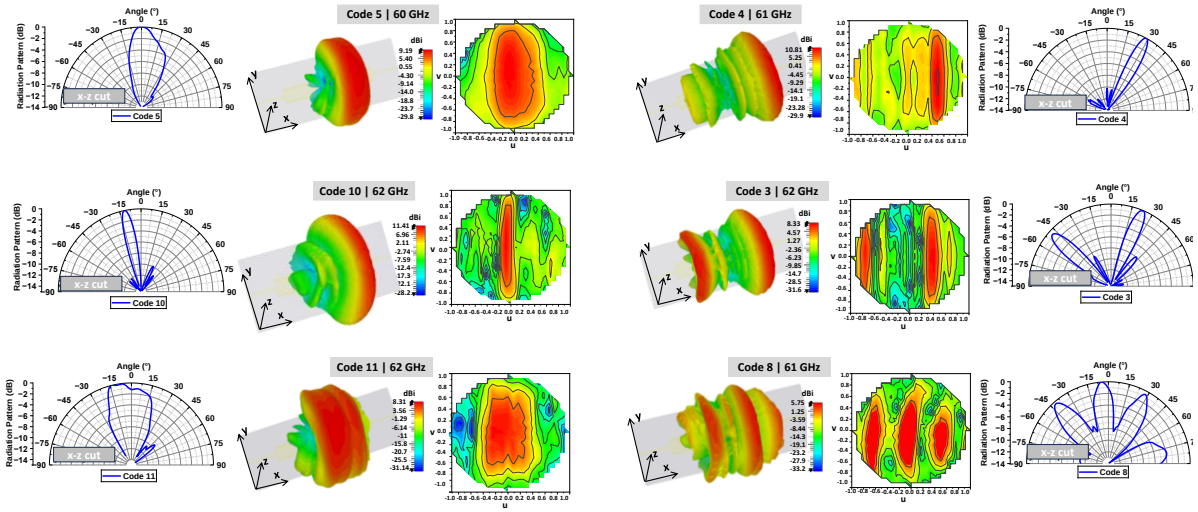

Figure 5.24. Illustration of various types of simulated 3-D radiation patterns along with corresponding u-v orthographic heat maps and x-z cuts produced from different digital coding combinations.

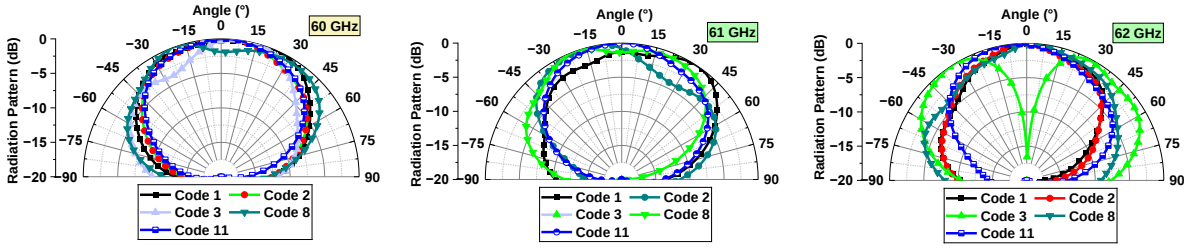

Figure 5.25. Simulated radiation pattern of the proposed DMA in y-z plane at 60 GHz, 61 GHz, and 62 GHz for different coding combinations.

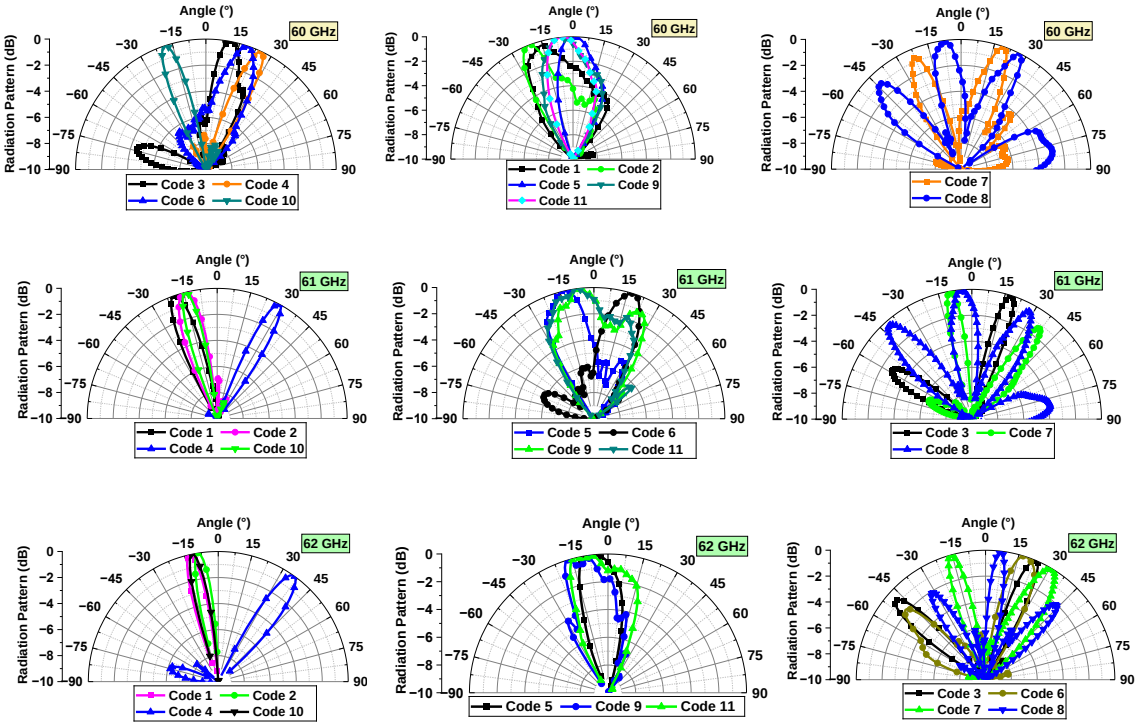

Figure 5.26. Simulated beam-steering plots of DMA at 60 GHz, 61 GHz, and 62 GHz using different coding sequences in the x-z plane. (a, d and g) show directed beams with narrow HPBW. (b, e, h) show beams with relatively wider HPBW.(c, f, i) show multiple beams.

The gain of the DMA for different coding combinations within 60 to 62 GHz is provided in Figure 5.28. For code 1, code 2, code 4, and code 10, the gain is above 10 dBi at 61 GHz with SLL less than -10 dB. For multi-beam codes such as code 8 and code 9, each lobe has a minimum gain of 5 dBi. Moreover, the radiation efficiency is above 60% for most of the coding sequences as shown in Figure 5.29.

5.7.5 Beamwidth Synthesis and Versatility of DMA

The proposed CELC meta-element exhibits interesting behavior when stimulated in a multitude of array topologies in a waveguide aperture. Because the polarizability of the CELC meta-elements is greatly contingent on the resonance frequency as governed by (5.6), their superposition manifests a dynamic behavior at different frequencies corresponding to different digital coding sequences. Consequently, this leads to the formation of versatile beam morphologies. To elucidate this, consider Figure 5.27, where the radiation states and beamforming are demonstrated for code 1 at 60 GHz, 61 GHz, and 62 GHz.

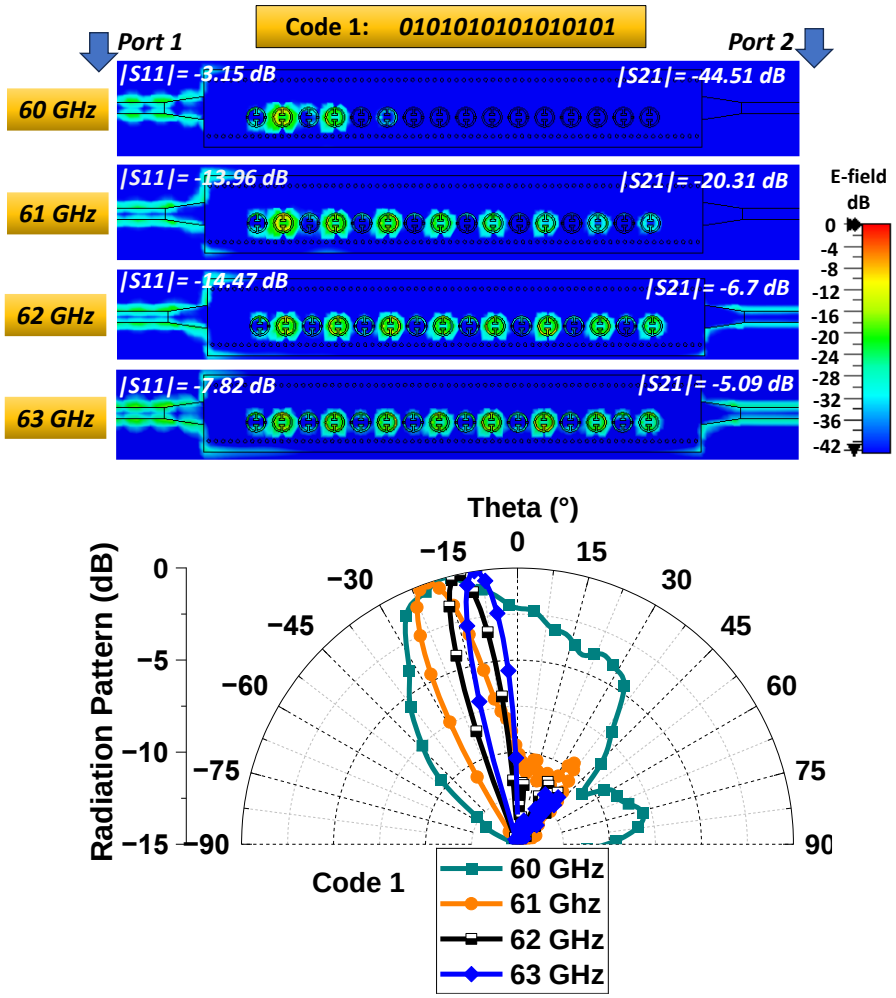

Figure 5.27. DMA response for code 1 leading to radiation pattern with varying HPBW.

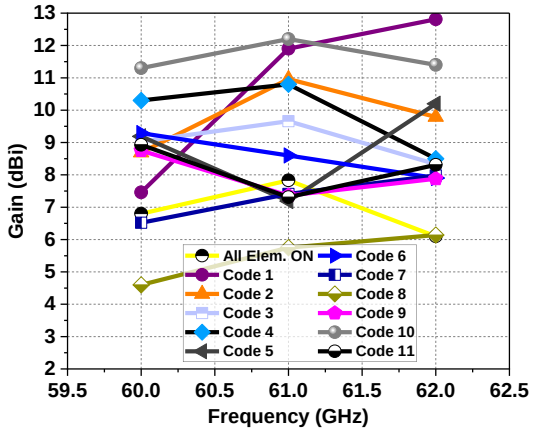

Figure 5.28. Simulated realized gain of the DMA for various beamforming codes.

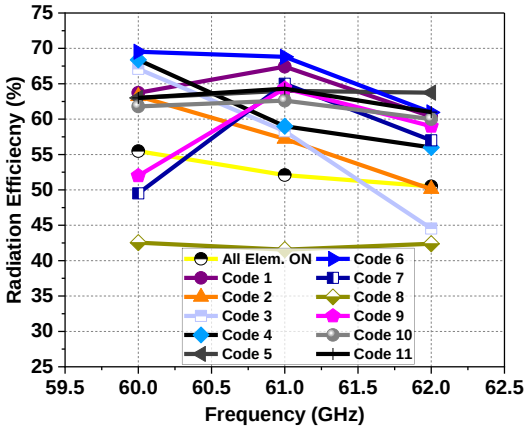

Figure 5.29. Simulated radiation efficiency of the DMA for various beamforming codes.

Since a resonating CELC element behaves as an open circuit at its resonance frequency, hence for code 1, CELC 2 and 4 appear to be strongly resonating while leading to reduced wave transmission towards the output port (|S21 ≈ -41.5 dB) and presenting high impedance mismatch towards the input port (|S11| ≈ 3.15 dB). In this way, other expected on-state elements do not find enough coupling and therefore the effective radiating aperture ($L_{effective}$) of the DMA is reduced. The beamwidth of a uniform linear array antenna is inversely related to the effective radiation aperture of the antenna array and can be estimated as [118]:

$$\mathrm{HPBW} = \frac{0.866\lambda}{\mathrm{L_{effective}}} \tag{5.13}$$

From ((5.13), it can be intuitively deduced that as the effective length of DMA aperture at 60 GHz is reduced, the HPBW is substantially broadened. From 61 GHz to 63 GHz, the CELC elements couple relatively weakly being a function of resonant frequency from ((5.6), and in turn more energy travels towards the outport port. In this way, a greater number of on-state CELC meta-elements tend to radiate as illustrated in Figure 5.27. Therefore, the effective radiating aperture is increased at these operating frequencies, leading to beams with narrow HPBW. Narrow beams are applicable for fine grain resolution whereas the wider beams are applicable for wide area coverage.

5.8 Prototype Fabrication and Measurement Results

The fabricated prototype of the 16-element DMA along with the integrated FPGA is shown in Figure 5.30(a). The size of the fabricated DMA array is 43.6 mm × 36 mm × 1.54 mm. Since the DC biasing path of each CELC meta-element is equipped with an LED at L4, therefore the correct response of the digital coding sequence generated through FPGA is readily noticeable through the on and off states of LEDs (corresponding to on and off states of PIN diodes), as demonstrated in Figure 5.30(c). A graphical user interface (GUI) is exclusively designed to generate any of the desired binary coded combinations and a software program is pre-loaded in the FPGA to reconfigure the DMA, as shown in Figure 5.30(d). The bias voltage applied to each PIN diode can be changed by controlling the FPGA, such that the ON/OFF state of the PIN diode together with the radiation state of each CELC element can be controlled. We used Arty S7 FPGA board from Digilent. Further details of FPGA board are presented in Appendix

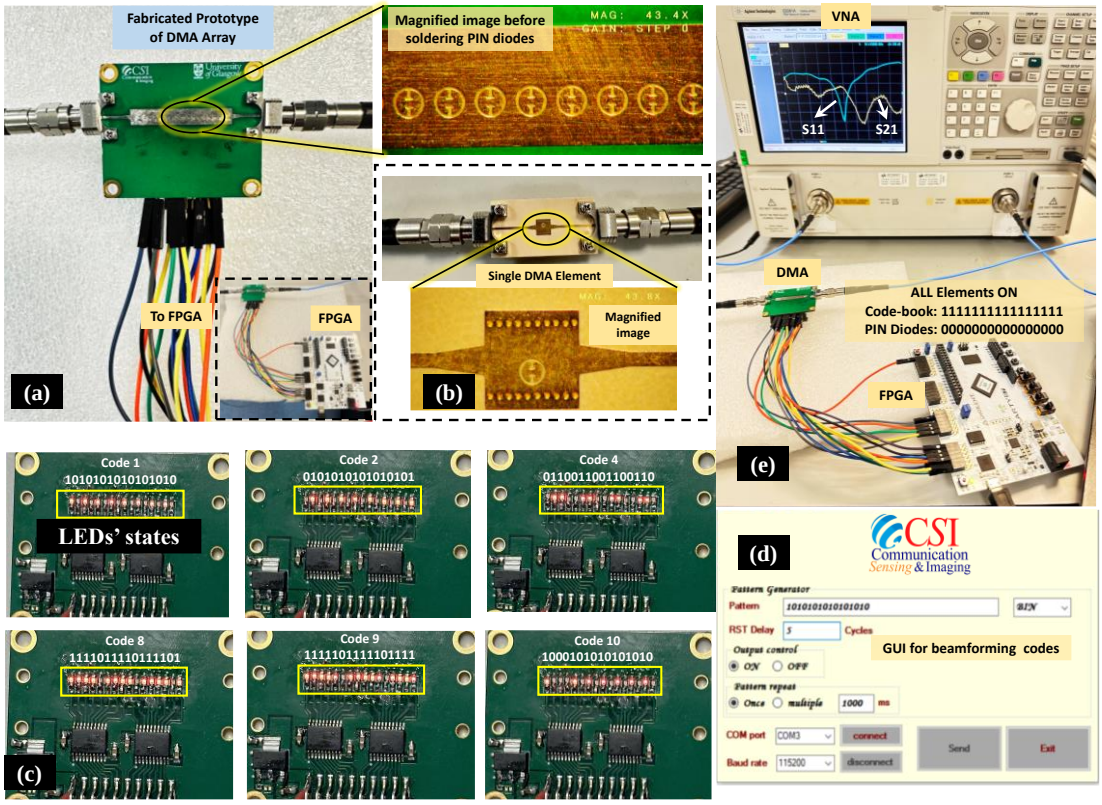

Figure 5.30. (a) Fabricated prototype of DMA integrated with FPGA along with a magnified image of the top layer. (b) fabricated single DMA element prototype and its magnified image. (c) Practical visualization of different on/off states of LEDs corresponding to different coding combinations. The coding 1's and 0's shown in this image correspond to the on and off states of PIN diodes respectively (i.e., inverted to the codebook sequence of Figure 5.19). (d) Developed GUI to generate any of the desired beamforming coding sequences for FPGA towards DMA. (e) Measurement setup for S-parameters on VNA.

E. For ease of measurement and rapid prototype verification of the designed CELC meta-element, a separate prototype of the single DMA element was also fabricated without a biasing network as shown in Figure 5.30(b). This depicts a radiating DMA element state (being an open circuit CELC element). The off-state (non-radiation) performance was instantly accomplished by merely shorting the capacitive gap between CELC and SIW aperture (analogous to PIN diode switching on) through soldering.

5.8.1 S-Parameter Measurements

The S-parameters of the single DMA element as well as the DMA array for various beamforming codes were measured using Agilent E8361A vector network analyzer (VNA) after 2-port calibration, as demonstrated in Figure 5.30(e). The measurement setup of resonance frequency, S21 phase, and group delay of the single DMA element is shown in Figure 5.31. The measured S-parameters are presented in Figure 5.32(a), which reveals that the resonance frequency of the CELC element is around 61.6 GHz. Note that the resonance trend (curve

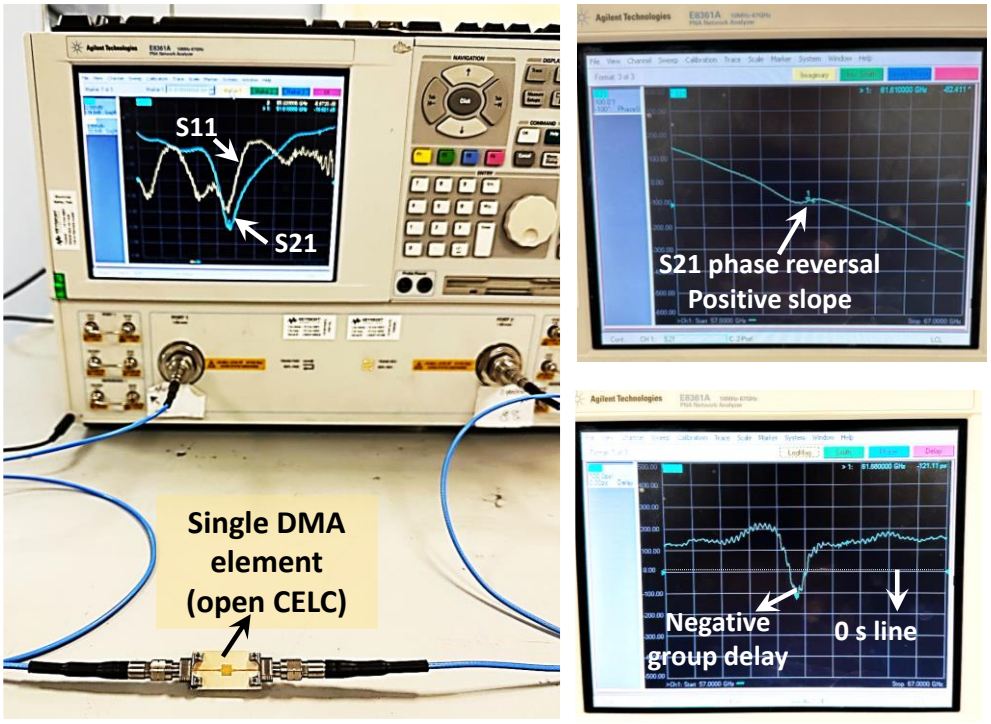

Figure 5.31. Measurement setup for S-parameters of single DMA element on VNA.

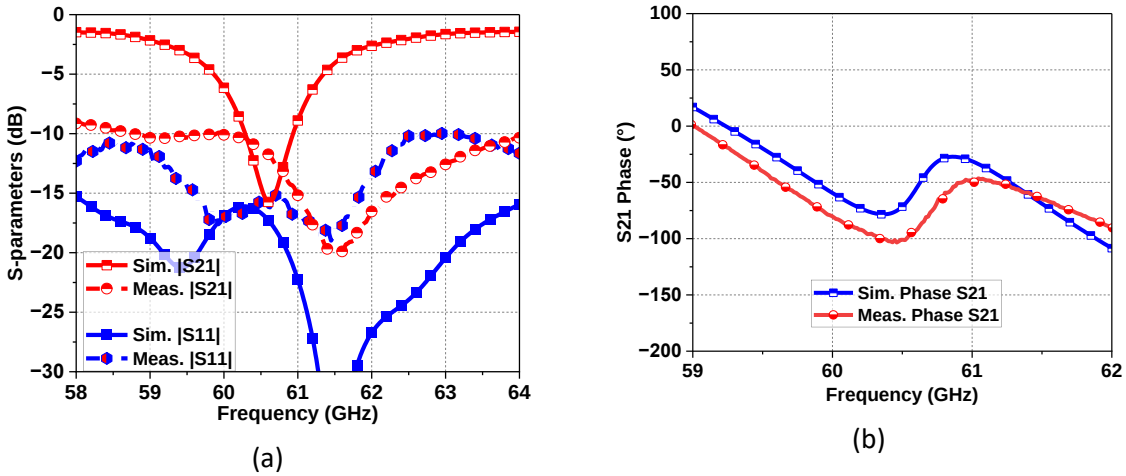

Figure 5.32. (a) Measured reflection and transmission coefficient of single DMA element in radiating state. (b) Measured transmission phase of the single DMA element in radiating state confirming negative group delay.

behavior) is quite similar to the simulated results, however, the measured resonance frequency is blue-shifted due to practical fabrication tolerances. The measured group delay is negative around 61.6 GHz as shown in Figure 5.32(b). The measured S21 phase shows a positive slope around the resonance frequency and therefore is a confirmation of the negative group delay, thereby revealing ENG left-handed metamaterial properties as described in Section 5.4.

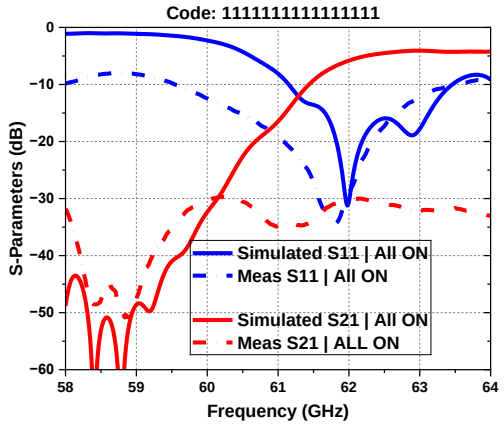

Figure 5.33. Measured reflection and transmission coefficients of the DMA array when all elements are in radiation state (i.e., all PIN diodes are OFF).

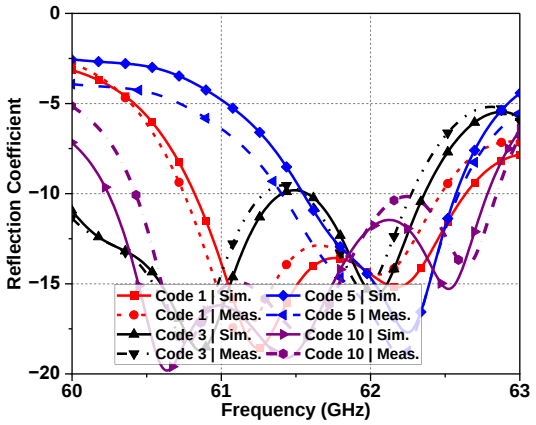

Figure 5.34. Measured reflection coefficient of DMA array for various coding sequences.

Before measuring the reflection and transmission coefficients of the DMA array, the DC test was conducted to ensure the correct operation of the DC biasing network with FPGA. Measured S-parameters for fully radiating DMA are shown in Figure 5.33.

The measured S-parameters are stable during prototype movement and match quite well with the simulations, thereby confirming the robust response of the fabricated prototype. For various coding combinations, the reflection coefficients were measured and shown in Figure 5.34. Minimal deviations in measured S-parameters are mainly due to the practical response of diodes at the 60 GHz band, soldering effects, fabrication tolerance of PCB, and practical losses in the conductor and dielectric. Nevertheless, the resonance behavior of the measured results is in great agreement with the simulation results in general.

5.8.2 Radiation Pattern and Gain Measurements

The measurement setup for the radiation pattern is shown in Figure 5.35. A standard gain V-band horn antenna was used as a transmitter and was mounted on a turntable capable of rotating 360°. The gain was measured using the relative gain comparison method as discussed in Chapter 3, Figure 3.23. The trend of gain variation for different beamforming sequences across the frequency band of interest matches well with the simulated gain result, as shown in Figure 5.36. The peak measured gain is 11.63 dBi at 62 GHz for code 1.

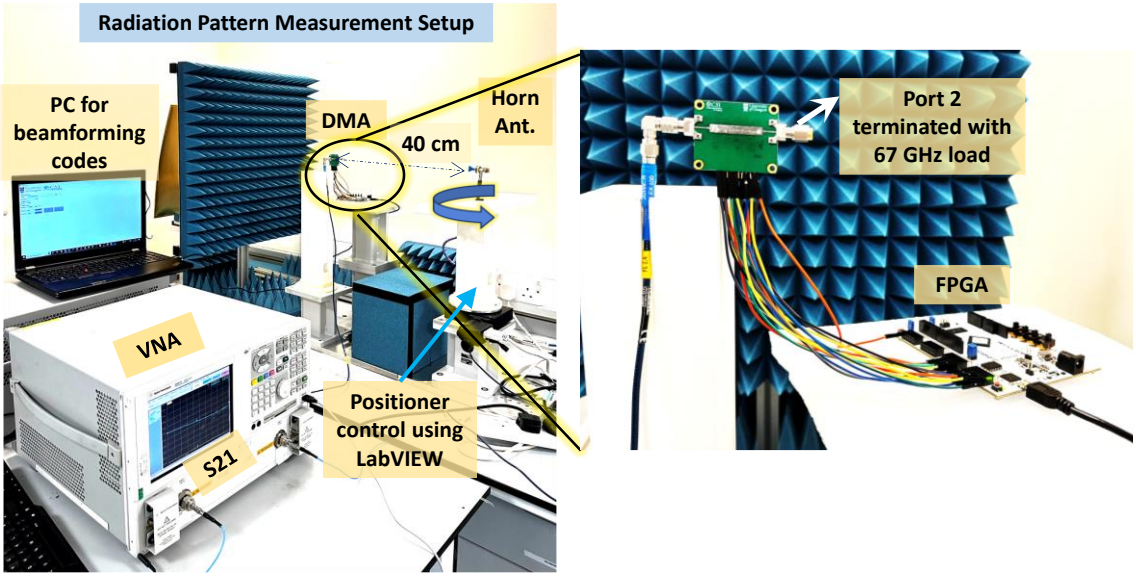

Figure 5.35. Over-the-air experimental setup to measure radiation pattern and gain.

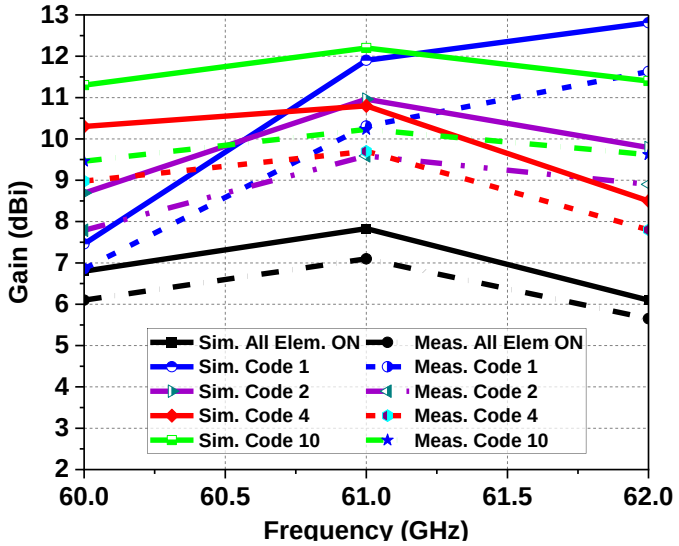

Figure 5.36. Measured gain across frequency for different beamforming coding combinations.

The difference between simulated and measured gain is mainly due to practical conductor losses, PIN diodes, and RF connector effects. The turntable is equipped with a programmable motor which is automated and controlled through LabView. The horn antenna was rotated over a span of 180° (-90° to +90°) with 1° angular steps. The DMA was fixed at a far-field distance of 40 cm ($>2D^2/\lambda$, where D is the largest dimension of DMA) from the horn antenna. A single-tone continuous-wave (CW) frequency signal was produced at each desired operating frequency of 60 GHz and 62 GHz to record the radiation pattern through VNA over a span of 180°.

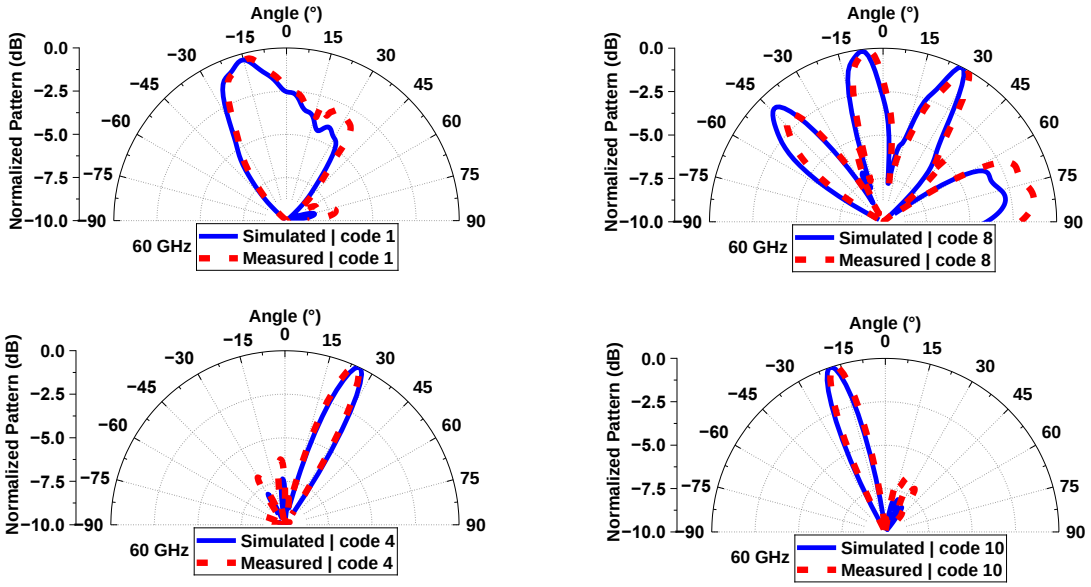

Figure 5.37. Measured radiation patterns for different beamforming coding combinations at 60 GHz in the azimuth (x-z) plane.

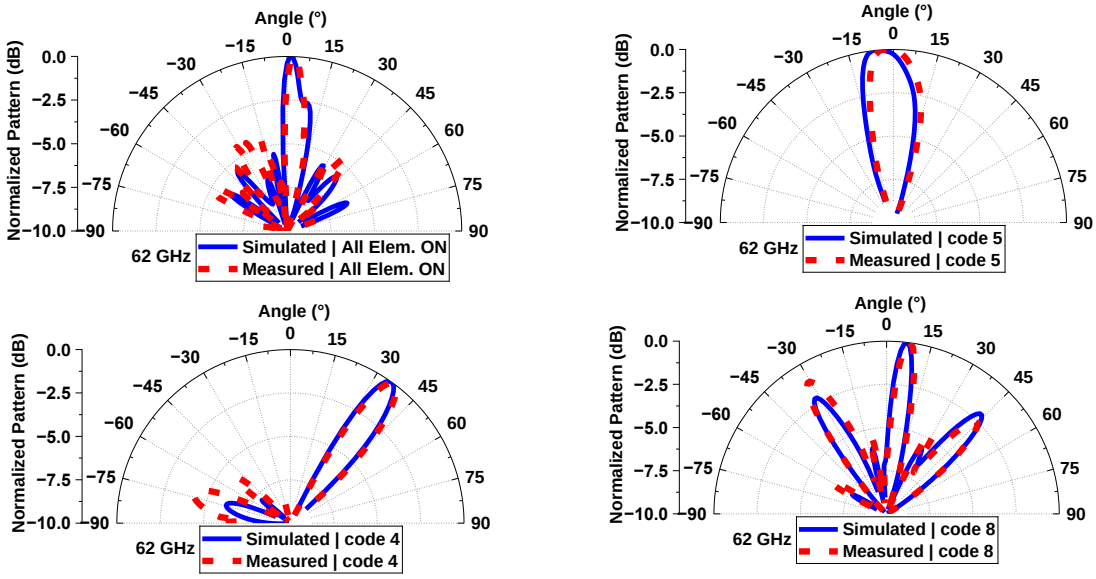

Figure 5.38. Measured radiation patterns for different beamforming coding combinations at 62 GHz in the azimuth (x-z) plane.

The measured radiation patterns for different beamforming codes in the azimuth plane (x-z plane) at 60 GHz and 62GHz are shown in Figure 5.37 and Figure 5.38, respectively. The measured patterns show good agreement with the simulated results, while the measured SLL and null depths are within 1.5 dB as compared to the simulated ones. Due to linear geometry, the radiation patterns in the elevation plane possess wide beamwidth and are symmetrical mostly towards the broadside, they are not of interest for measurements (presented above in simulated results of Figure 5.25).

5.8.3 Beamforming Response Time and Agility Measurement

The DC output of FPGA is +3.3 V which was converted to +1.33 V using an on-board voltage regulator IC to switch on the PIN diodes (element off state), whereas 0V is used to switch off the PIN diodes (element on state). The control signal from FPGA was operated at 250 MHz clock frequency with parallel LVCMOS (Low Voltage Complementary Metal-Oxide-Semiconductor) 3.3 IO standard and achieved a high beam-switching update rate.

All PIN diodes are parallelized to simultaneously provide the digital code to all elements which significantly reduces the beamforming switching time and offers agile beam-steering. Therefore, the overall agility (hardware latency) of the beam-switching between any two coded combinations (for pattern reconfigurability) is around 5 ns. The DMA electronically switches the beam from one direction to a specific scan angle through FPGA, and a mixed signal oscilloscope (TBS1072B) was used to observe the signal level under switching conditions from code 1 to code 2. The time between two steady states is considered as the beam-switching time, which was measured to be less than 5 ns as experimentally demonstrated in Figure 5.39.

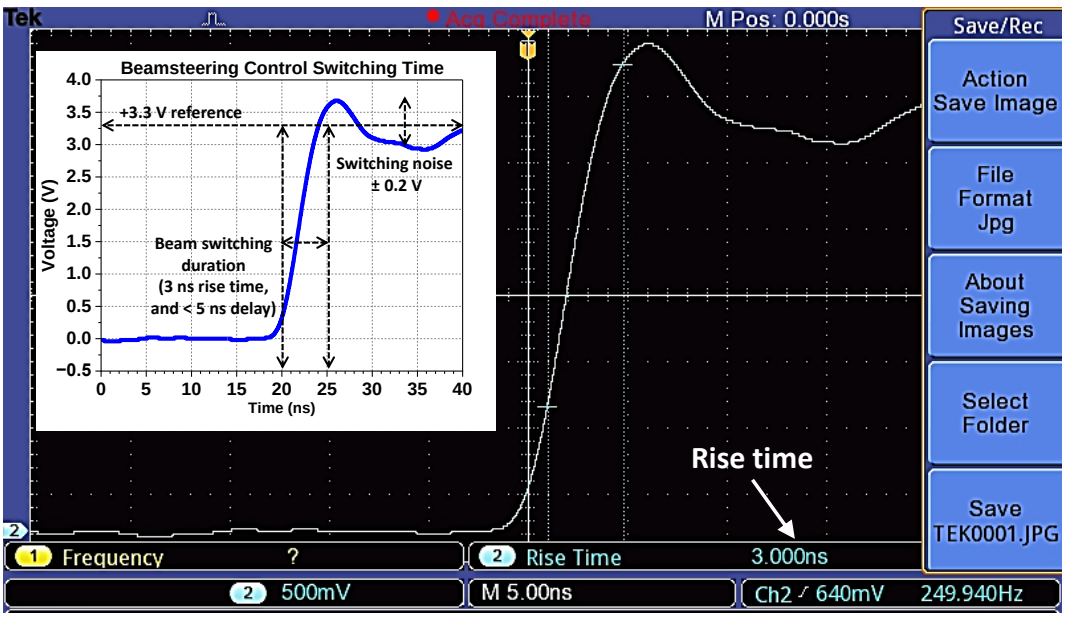

Figure 5.39. Measured response time of switching beams (e.g., from code 1 to code 2) from FPGA.

5.9 Comparative Analysis of DMA

A comparison summary of the proposed DMA design with a few of the available DMA prototypes in the literature is presented in Table 5.1. The proposed DMA offers more than 2.16 GHz of -10 dB impedance bandwidth around 60 GHz, above 8 dBi gain for various beamforming codes, and high radiation efficiency of above 60%.

Table 5.1. Comparison summary of the proposed DMA hardware with the available state-of-the-art DMAs in the literature.

Ref.	Operating Frequency Region (GHz)	DMA Geometry	Electronic Switching Component	DMA Aperture Size (L: mm × W: mm)	Observed Peak Gain (dBi)	Observed Peak Radiation Efficiency (%)
[185], [32]	11.8	4 × 16 planar	PIN Diode	152 × 60.5	10	Not available
[147]	12	1 × 16 linear	PIN Diode	124 × 15	11.02	68.36
[148]	10	8 × 12 planar	Varactor Diode	229 × 120	10	11
[149]	23.5	1 × 41 linear	PIN Diode	Not available	9.3	41.7
[150]	26	8 × 16 planar	Varactor Diode	100 × 89.4	7	Not available
[210]	21	Planar random aperture	PIN Diode	114.24 × 114.24	7.72	40.55
This Work [179]	**60**	**1 × 16 linear**	**PIN Diode**	**27.36 × 4.2**	**11.63**	**69.52**

5.10 A Subtle Difference Between Conventional SIW-based Slotted LWAs and DMAs

It is worth mentioning here that although the excitation mechanism of DMA might seem similar to that of slotted SIW LW antennas, however, in contrast to them a DMA does not always rely on the formation of a specific leaky mode. This distinction stems from the fact that the radiation mechanism of a DMA is based on carefully designed resonant metamaterial elements (an d not the slots) which do not rely on a gradual change in the geometry or periodic

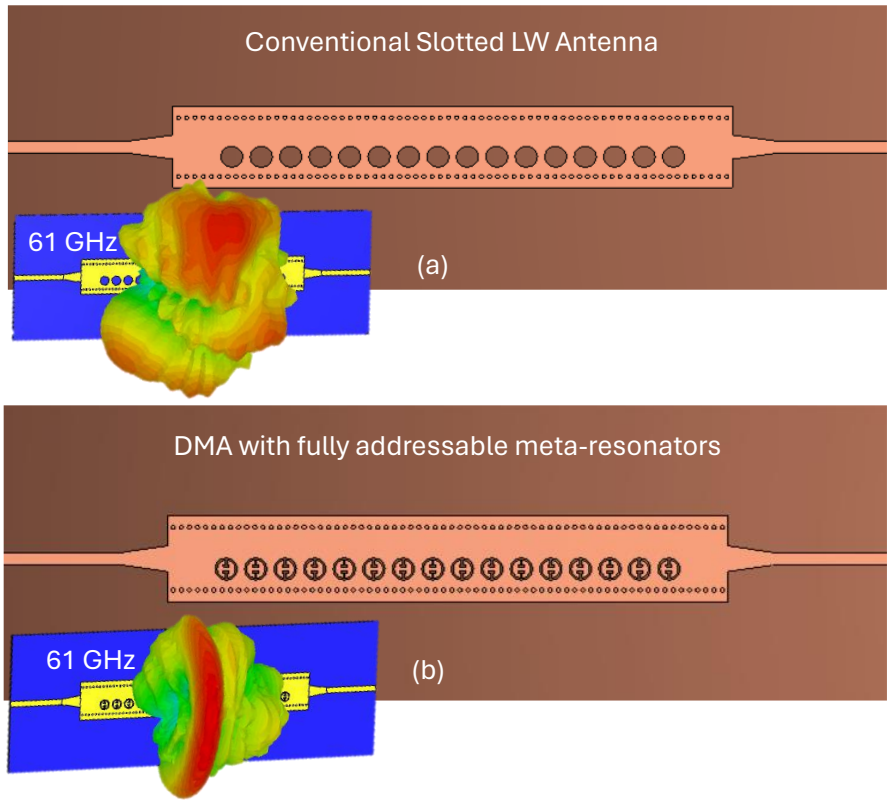

Figure 5.40. (a) Geometry of a conventional slotted LW antenna. (b) Geometry of a DMA comprising CELC resonators.

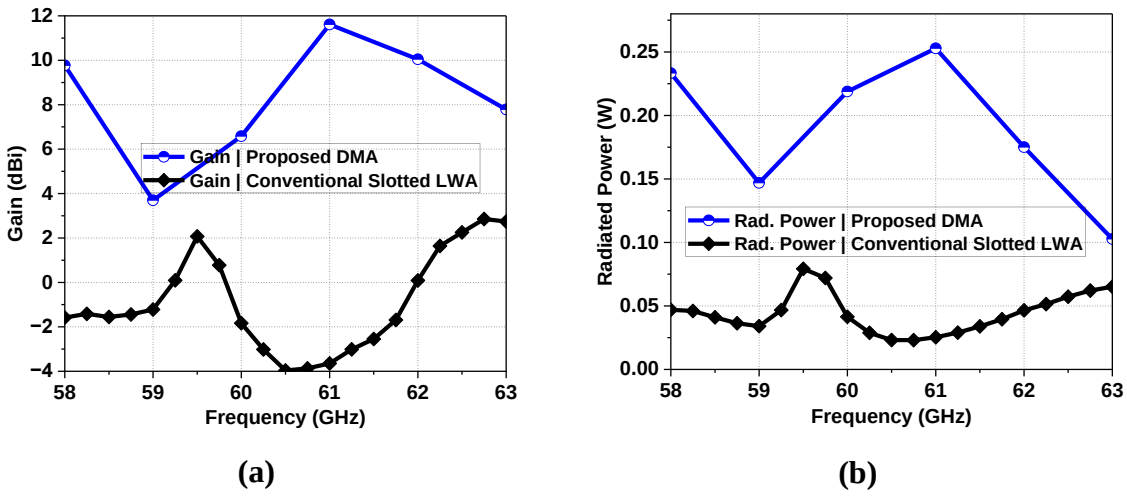

Figure 5.41. Performance comparison between proposed DMA and conventional slotted LWA. (a) simulated gain. (b) simulated radiated power.

arrangement of the elements. This topology offers access to the exotic electromagnetic responses for independent control over the wavefront to achieve fixed frequency beamsteering. On the other hand, LWAs are often employed as frequency-dependent beamscanning antennas

due to the phase change at each operating frequency across the arrangements of slots [41]–[43]. Such beam-squint effect limits their applicability in various scenarios where frequency of operation is fixed, however the inherent squint effect is usually reported as a blessing (in form of frequency-dependent scanning) rather than an impairment in SIW-based slotted LW antena regime.

Although some design techniques can be applied to achieve fixed frequency beamsteering in LW-SWAs [211], [212], however, generally the radiation pattern reconfigurability with such antennas is quite hard to achieve and is not straightforward. This is because a simple slot can not simply provide integration of biasing mechanism of a PIN/varactor diode while isolating RF and DC signals. Instead, it requires the design of additional mechanisms to integrate electronic components with antenna aperture, making the design of LW antennas more complex. The DMA on the other hand offers an extremely easily addressable platform with independent control on the radiation state of each CELC meta-resonator for fixed-frequency beamsteering. Moreover, it is instructive to mention here that a CELC based DMA is not like loading the slot of a LWA aperture with any arbitrary shape, rather the CELC resonator retains and manifests its own properties and thereby governs the overall performance of a DMA.

To elucidate this, a DMA array (same design as presented above) with hollow circular slots, and the one loaded with proposed open circuit CELC elements is simulated for performance comparison as shown in Figure 5.40. The gain and radiatred power for both cases are shown in Figure 5.41(a) and (b) respectively. It can be noted that the LW structure with simple slots does not radiate at the desired band of interest. Similarly, its gain is very low and remains below 2 dBi, whereas the gain of DMA is 12 dBi at 61 GHz. The radiation performance can also be visualized from the 3D radiation patterns at 61 GHz as shown in Figure 5.40.

5.11 Research Contribution and Novelty of the Proposed 60 GHz mmWave DMA

In this thesis, the fundamental design and analysis of a low-profile fully programmable DMA at 60 GHz mmWave band is thoroughly presented. To the best of the authors' knowledge, this is the first reported radiative DMA prototype at 60 GHz band to date. The complete design philosophy, construction, and working principle of a programmable mmWave DMA is elucidated from concept to prototype. The main contributions of this work are summarized are as follows:

- First, the design of a novel circular CELC meta-element (as opposed to the commonly used rectangular CELC element) is proposed at 60 GHz mmWave band. The complete design philosophy of the proposed CELC meta-element is elucidated. The dispersive characteristics and ENG left-handed metamaterial properties of the proposed CELC meta-element are thoroughly investigated and presented through numerical simulations and verified through experiments.
- A fully addressable and dynamically tunable DMA element is designed based on the proposed CELC-meta element. Realistic simulations were carried out including the complete biasing network and PIN diodes which reveal the minimal effect on RF performance. A low-loss substrate integrated waveguide (SIW) structure is designed, and the CELC element is edge-fed using a microstrip line for ease of measurement and ease of integration with RF circuitry.
- A 4-layer PCB of DMA prototype comprising 16 CELC meta-elements is meticulously designed ensuring high gain, low side lobes, high radiation efficiency, and compact profile with more than 2.16 GHz of -10 dB impedance bandwidth. The array is integrated with high-speed FPGA for dynamic control of the radiation state of each meta-element in real-time. All the PIN diodes (and thus all meta-elements) are parallelized, therefore agile beam-switching is achieved by having a latency level within 5 ns, paving the way towards extremely low latency mmWave communication.
- The DMA is fully controllable through software programming and can produce fixed-frequency electronic beam-steering. Our proposed DMA is capable of synthesizing various steerable radiation patterns including narrow beams, wide beams as well as multi-beams based on different digital coding sequences using a single antenna aperture. This immensely reduces the hardware and signal processing complexity by avoiding the use of multiple antennas for imaging and sensing applications.
- With a notion of adaptability to dynamic reconfigurability of EM environment beyond 5G/6G technologies, the DMA prototype is designed in an extremely flexible and programmable manner to work with various beamforming algorithms in the communication domain, as well as signal processing algorithms in the sensing and imaging domain.

- The versatility of our 60 GHz DMA prototype provides a readily accessible and off-the-shelf solution to explore and investigate a diverse range of next-generation mmWave applications.

5.12 Potential Use-Cases and Future Work Using the Proposed 60 GHz DMA

The real-time agile beam tailoring and signal processing capabilities of DMAs with simplified transceiver hardware render them a potential enabler for next-generation mmWave communication, sensing, and imaging (CSI) applications. Furthermore, since the 60 GHz band is an unlicensed spectral region, it offers applicability to a wide range of industrial and healthcare applications. In this section, we briefly highlight the potential use cases of the proposed mmWave DMA in CSI avenues, offering new opportunities for innovative applications due to its flexibility, dynamic reconfigurability, and license-free mmWave operating band.

5.12.1 Communication

DMAs offer an innovative programmable wireless communication paradigm through software-controlled antenna aperture [213]. Owing to the small size of meta-elements involved in the mmWave DMA, a multitude of meta-elements in linear (1-D) topology form a subarray that behaves as a single antenna, and its corresponding planar topology can thus be employed for hybrid analog-digital beamforming. The 2-D planar arrays are envisioned to be utilized in massive-MIMO (multiple-input-multiple-output) base stations and access point communication networks [141], [143]. With simple signal processing algorithms, a massive MIMO system with a multitude of meta-elements can yield significant gains in spectral efficiency, which is one of the key technologies of 6G and beyond [214].

The power consumption of a DMA-based system can be substantially lower as DMAs do not require as many RF chains or traditional active phase shifters to operate . Moreover, the electronic beamsteering and multi-beam synthesis capability of the proposed DMA envisions to support large-scale 60 GHz indoor IoT networks encompassing high transmission rates and massive data throughput. An antenna system equipped with beam scanning capabilities mitigates interference by selectively targeting the radiation pattern in a specific direction, enhancing the stability of data transmission and simultaneously optimizing spatial power allocation based on the node's communication data volume [193]. This optimization presents

an opportunity to decrease the data collision rate, average energy consumption, and packet transmission delays. Nodes equipped with beamsteering antennas exhibit an 88% reduction in energy usage and a 24% decrease in data collision when compared to solutions using omnidirectional antennas [215].

Another potential application of DMAs is looming towards next-generation near-field beam focusing and near-field communication (NFC), which is a prospective research area [216]. Moreover, besides wireless communication, the wireless power transfer (WPT) through energy beamforming for IoT networks using DMAs has also been presented to be an efficient solution in the form of hybrid beamforming, as compared to fully digital beamforming networks [217]. Further experimental investigations are required to explore this area at mmWave bands.

The proposed 60 GHz mmWave DMA prototype with reduced substrate losses, high gain beams, and above 65% radiation efficiency can be a potential candidate to explore and verify its applicability for the enhanced energy beamforming optimization scenarios as compared to expensive high-frequency fully digital beamforming solutions. This is certainly a potential research area that requires further experimental verification.

5.12.2 Sensing

DMAs are greatly envisioned to boost RF sensing accuracy in sensing and localization applications by employing antenna pattern diversity [189]. The object wave and reference propagating wave upon a DMA render it a reconfigurable holographic surface to synthesize a wide range of antenna patterns through externa programming. This adaptability is a key enabler in selecting specific patterns matched to the desired sensing scenarios [192], [218]. Machine learning-based intelligent algorithms can be devised to work with the proposed DMA prototype to identify the required set of antenna patterns for specific activities and then configure the DMA to synthesize those patterns.

Furthermore, the 60 GHz band is a potential mmWave Wi-Fi band with various working protocols such as IEEE 802.11ad/IEEE 802.11ay [113]. The proposed 60 GHz DMA prototype is fully compatible to work with these protocols to achieve mm-level fine-grained resolution for accurate sensing. The real-time electronic beamsteering property of the proposed DMA can be utilized for beamforming training using various algorithms to assess the Channel Impulse Response (CIR) for each direction of beamforming. to enable indoor mmWave Wi-Fi-based radar sensing. Recent studies have indicated the feasibility of employing sector-level sweeping

procedures for opportunistic 60 GHz radar sensing in indoor environments, with a focus on smart IoT applications [219].

5.12.3 Imaging

The CELC-based dynamic apertures have been widely utilized for microwave imaging applications [139], [191], [220]–[225]. Usually, such imaging techniques involve frequency-swept signals, however, the proposed DMA can be employed as fixed frequency beamscanning with simple and efficient programmable hardware [190]. A DMA can illuminate a scene with dynamic radiation patterns (where each DMA configuration is called as a "*mask*") that can be altered based on the dynamic coding sequences. It is instructive to mention here that for imaging applications, random placement of meta-elements can also be utilized in DMA design [210], [226], because SLL is not of the main concern (as opposed to communication regime where Nyquist limit of $\lambda_0/2$ is desirable for element placement). Thus, a sequence of pseudorandom radiation patterns interrogates a scene and the measurements of the return signal against each coding sequence can be acquired. Eventually, the scene can be reconstructed using computational imaging methods [210], [227].

For more fine-grained and high-resolution mmWave holographic computational imaging, the proposed 60 GHz DMA prototype is envisaged to hold a significant potential due to its versatility and control over beam-shaping features.

Chapter 6

Conclusion and Future Directions

6.1 Conclusion

This dissertation focused on the high-performance antenna designs for next-generation industrial wireless applications and technologies such as 6G. The lower ISM band around 2.4 GHz and 5 GHz suffers from some serious impediments such as low available bandwidth, high spectral congestion and high spectral interference. Hence, a thorough exploration of the potential within the 60 GHz mmWave ISM band has been conducted to design low-cost, high-performance and compact mmWave antenna solutions suitable for mmWave industrial wireless applications. Moreover, an in-depth review has been presented on intelligent and software-reconfigurable smart beamforming antenna solutions for advanced wireless technologies (such as B5G/6G) and emrging Industry 4.0 and beyond applciations. Following the investigations of diverse design intricacies of mmWave antennas around 60 GHz and the necessity for innovative beamforming solutions tailored to dynamic wireless environments, the major contributions of this thesis are summarized as following.

- Design of a wideband, high gain, and low-cost frequency-selective beamforming antenna array with a compact footprint of (length) 20 mm × (width) 28 mm × (thickness) 0.25 mm using the simplest microstrip radiators. First, a wideband 8-element microstrip linear array is designed with fan-shaped radiation pattern for P2MP mmWave connectivity. Then combining 8 such sub-arrays with an 8-channel corporate feed network, a compact 64-element hybrid corporate-series fed array is designed with above 19 dBi gain in the entire measured band of 57–67 GHz. Directional narrow beams are produced in both elevation and azimuth planes, suitable for P2P mmWave connectivity\. The proposed array provides frequency selective beamscanning with a scan range of 40° (from -10° to +30° across 57–71 GHz band) with less than 1 dB scan loss.
- Design, fabrication, and prototype testing of a fixed beam16-element wideband microstrip antenna array having dimensions of (length) 15 mm × (width) 33 mm × (thickness) 0.2 mm. The antenna provides a -10 dB impedance bandwidth of 7 GHz

(57–64 GHz), with a high gain of 16.3 dBi at 60.7 GHz and more than 14 dBi gain in the achieved band of interest. Highly directional fixed broadside beams without beam squint effect are produced. The narrow directional beams in the azimuth plane have a half-power beamwidth (HPBW) varying between 7° to 12.9° within 57–64 GHz. The proposed antenna is a low-cost solution to provide mGbps mmWave wireless communication. Moreover, the above two proposed planar antenna arrays can be directly connected to the 1.85 mm RF standard equipment, thereby offering an exceptionally cost-effective solution for testing various 60 GHz use cases, and thereby circumventing the need for expensive mmWave horn antennas.

- First ever design, fabrication, and prototype testing of a Dynamic Metasurfcae Antenna (DMA) hardware at 60 GHz mmWave band, to date. First, a fully addressable novel circular-shaped digital CELC meta-element is designed whose radiation state can be switched by controlling the switching state of the embedded PIN diode. The proposed meta-element manifests left-handed metamaterial properties such as negative group delay, effective negative permittivity, and negative group around the resonance frequency during its radiation state. Then, based on 16 such CELC elements, a 1-D DMA hardware prototype is meticulously designed using a 4-layer PCB. The radiation pattern can be dynamically controlled in real time through binary digital coding combinations generated through a high speed field-programmable gate array (FPGA). The proposed DMA can synthesize narrow beams, wider beams as well as multiple beams based on user-defined digital coding sequences. The proposed DMA offers a cost-effective and advanced beamforming platform to test a diverse range of mmWave communication, sensing, and imaging applications. The beamswitching between any two beam directions is measured to be within 5 ns, thus paving the way towards the neXt generation URLLC (xURLLC).

6.2 Future Directions and Research Opportunities

The antenna design challenges and opportunities are ever-green, with the growing spectrum and emerging next-generation wireless applications. Typically at high frequencies such as 60 GHz or THz bands, antenna design challenges become more pronounced, which brings more future research opportunities.

For instance, the concept of MIMO (and mMIMO) requires a large number of antenna elements within a confined aperture area, which is highly plausible at 60 GHz and above

frequencies due to small wavelengths. Therefore, in the realm of planar microstrip patch antennas, enhanced antenna performance features with digital and hybrid beamforming can be achieved using MIMO antenna arrays. State-of-the-art advancements in MIMO antenna design involve innovations in compact, phased-array configurations, beamforming techniques, and integration with advanced signal processing algorithms to achieve spatial multiplexing and adaptive beamforming as the prime benefits, which lead to high data rate, reliability, and traffic demands. As such, each of the proposed sub-arrays in Chapter 3 can be integrated with an individual phase-shifting mechanism to devise a planar MIMO array with individual beam control. Although at sub-6 GHz, MIMO and digital beamforming are mature, however at 60 GHz and sub-THz bands, they have immense potential in developing PHY hardware.

Vast research opportunities are looming within the field of high-frequency DMA hardware for novel and efficient beamforming capabilities. At 60 GHz and above, the design of a DMA hardware prototype is immensely challenging and requires careful antenna design considerations due to the very small area of metamaterial elements and the integration of tiny PIN diodes/varactor diodes in a very confined area. Moreover, as the geometry of DMA shifts from linear to planar, the design complexities increase manifold which necessitates further exploration of PHY technologies.

The DMA prototype in this work (as well as a few other available low-frequency DMA prototypes) comprises of two ports, where the second port is terminated with a matched load. Instead of making the 2nd port redundant, if RF feed is also provided at the 2nd port with controllable phase shifts, then more wonders can be done through DMA in terms of high flexibility and radiation pattern control, as well as beam synthesis. These features would greatly help in futuristic ISAC applications and mmWave imaging.

MIMO DMA arrays and multi-feed DMAs for digital and hybrid beamforming are not available in the literature yet and offer open research challenges in the advanced beamforming antenna design domain. Furthermore, the exploration of circularly polarized DMAs remains an untapped avenue in antenna design research, offering potential for novel antenna traits.

As highlighted in Chapter 5, RIS is a groundbreaking technique for reconfiguring the wireless propagation environment through software-controlled reflections to achieve enhanced spectral and energy efficiency cost-effectively. In the same way, DMA is a complementary concept based on software software-controlled radiation reconfigurability. At mmWave bands, highly directional antenna beams are used to overcome path loss, however, LOS can easily be blocked by various objects at mmWave band. In that scenario, the coexistence of RIS and DMA

in a software-controlled manner is envisaged as a novel research area for advanced beam steering and seamless connectivity. Especially, around 60 GHz and THz bands, practical hardware designs and prototype evaluation are in their infancy and can be explored further. Therefore, a coherent and intelligent communication framework along with a channel estimation technique needs to be developed and utilized to make this happen practically.

The novel beamforming potential offered by a DMA (as well as RIS) can be further improved by using the potential AI and ML algorithms. A large number of coding combinations exist in a DMA design, as the number of meta-elements increase. For instance, for a 16-element linear DMA array, 2^{16} = 65536 different binary coded combinations are possible. Consequently, it is impossible to test each coding sequence manually in antenna design software and analyze its beam direction. As such, a physics-inspired neural network is used in [228] to predict the beamforming codes and radiation pattern from a dynamic metasurface antenna aperture. Such types of ML-assisted reconfigurable antennas possess huge potential for the next generation of wireless technologies, where the smart antenna system is required to reconfigure its radiation pattern in real-time based on the blockage, jamming, and NLOS scenarios.

Bibliography

[1] Z. Pang, M. Luvisotto, and D. Dzung, "Wireless high-performance communications: The challenges and opportunities of a new target," *IEEE Industrial Electronics Magazine*, vol. 11, no. 3, pp. 20–25, 2017.

[2] L. Da Xu, W. He, and S. Li, "Internet of things in industries: A survey," *IEEE Transactions on Industrial Informatics*, vol. 10, no. 4, pp. 2233–2243, 2014.

[3] T. Kalsoom *et al.*, "Impact of IOT on Manufacturing Industry 4.0: A new triangular systematic review," *Sustainability*, vol. 13, no. 22, p. 12506, 2021.

[4] A. Mahmood *et al.*, "Industrial IoT in 5G-and-beyond networks: Vision, architecture, and design trends," *IEEE Transactions on Industrial Informatics*, vol. 18, no. 6, pp. 4122–4137, 2021.

[5] E. Sisinni, A. Saifullah, S. Han, U. Jennehag, and M. Gidlund, "Industrial internet of things: Challenges, opportunities, and directions," *IEEE Transactions on Industrial Informatics*, vol. 14, no. 11, pp. 4724–4734, 2018.

[6] X. Xu, Y. Lu, B. Vogel-Heuser, and L. Wang, "Industry 4.0 and Industry 5.0—Inception, conception and perception," *Journal of Manufacturing Systems*, vol. 61, pp. 530–535, 2021.

[7] J. Jiang, H. Wang, X. Mu, and S. Guan, "Logistics industry monitoring system based on wireless sensor network platform," *Computer Communications*, vol. 155, pp. 58–65, 2020.

[8] M. Javaid, A. Haleem, R. P. Singh, and R. Suman, "Enabling flexible manufacturing system (FMS) through the applications of industry 4.0 technologies," *Internet of Things and Cyber-Physical Systems*, vol. 2, pp. 49–62, 2022.

[9] A. Angelopoulos *et al.*, "Tackling faults in the industry 4.0 era—a survey of machine-learning solutions and key aspects," *Sensors*, vol. 20, no. 1, p. 109, 2019.

[10] M. Cheffena, "Industrial wireless communications over the millimeter wave spectrum: opportunities and challenges," *IEEE Communications Magazine*, vol. 54, no. 9, pp. 66–72, 2016.

[11] C. Pielli, T. Ropitault, and M. Zorzi, "The potential of mmwaves in smart industry: Manufacturing at 60 ghz," in *International Conference on Ad-Hoc Networks and Wireless*, Springer International Publishing, 2018, pp. 64–76. doi: 10.1007/978-3-030-00247-3_6.

[12] D. Gorecky, M. Schmitt, M. Loskyll, and D. Zühlke, “Human-machine-interaction in the industry 4.0 era,” in *2014 12th IEEE international conference on industrial informatics (INDIN)*, 2014, pp. 289–294.

[13] Y. Wang, H.-S. Ma, J.-H. Yang, and K.-S. Wang, “Industry 4.0: a way from mass customization to mass personalization production,” *Advances in manufacturing*, vol. 5, pp. 311–320, 2017.

[14] Q. Qi and F. Tao, “Digital twin and big data towards smart manufacturing and industry 4.0: 360 degree comparison,” *IEEE Access*, vol. 6, pp. 3585–3593, 2018.

[15] F. Tao, H. Zhang, A. Liu, and A. Y. C. Nee, “Digital twin in industry: State-of-the-art,” *IEEE Transactions on Industrial Informatics*, vol. 15, no. 4, pp. 2405–2415, 2018.

[16] G. N. Schroeder, C. Steinmetz, R. N. Rodrigues, R. V. B. Henriques, A. Rettberg, and C. E. Pereira, “A methodology for digital twin modeling and deployment for industry 4.0,” *Proceedings of the IEEE*, vol. 109, no. 4, pp. 556–567, 2020.

[17] F. Tao, Q. Qi, L. Wang, and A. Y. C. Nee, “Digital twins and cyber--physical systems toward smart manufacturing and industry 4.0: Correlation and comparison,” *Engineering*, vol. 5, no. 4, pp. 653–661, 2019.

[18] F. Pires, A. Cachada, J. Barbosa, A. P. Moreira, and P. Leitão, “Digital twin in industry 4.0: Technologies, applications and challenges,” in *2019 IEEE 17th international conference on industrial informatics (INDIN)*, 2019, pp. 721–726.

[19] A. Ustundag and E. Cevikcan, *Managing The Digital Transformation*, no. September 2018. 2020. doi: 10.1007/978-3-319-57870-5.

[20] P. K. Malik *et al.*, “Industrial Internet of Things and its applications in industry 4.0: State of the art,” *Computer Communications*, vol. 166, no. October 2020, pp. 125–139, 2021, doi: 10.1016/j.comcom.2020.11.016.

[21] J. Yang *et al.*, “Ultra-reliable communications for industrial internet of things: Design considerations and channel modeling,” *IEEE Network*, vol. 33, no. 4, pp. 104–111, 2019.

[22] H. Ren, K. Wang, and C. Pan, “Intelligent Reflecting Surface-aided URLLC in a Factory Automation Scenario,” *IEEE Transactions on Communications*, vol. 70, no. 1, pp. 707–723, 2021, doi: 10.1109/TCOMM.2021.3125057.

[23] M. Wollschlaeger, T. Sauter, and J. Jasperneite, “The future of industrial communication: Automation networks in the era of the internet of things and industry 4.0,” *IEEE Industrial Electronics Magazine*, vol. 11, no. 1, pp. 17–27, 2017.

[24] S. Saponara, F. Giannetti, B. Neri, and G. Anastasi, “Exploiting mm-wave

communications to boost the performance of industrial wireless networks," *IEEE Transactions on Industrial Informatics*, vol. 13, no. 3, pp. 1460–1470, 2017.

[25] A. Jabbar *et al.*, "Millimeter-Wave Smart Antenna Solutions for URLLC in Industry 4.0 and Beyond," *Sensors*, vol. 22, no. 7, p. 2688, 2022, doi: 10.3390/s22072688.

[26] M. Matthaiou, O. Yurduseven, H. Q. Ngo, D. Morales-Jimenez, S. L. Cotton, and V. F. Fusco, "The road to 6G: Ten physical layer challenges for communications engineers," *IEEE Communications Magazine*, vol. 59, no. 1, pp. 64–69, 2021.

[27] B. Ji *et al.*, "Several key technologies for 6G: challenges and opportunities," *IEEE Communications Standards Magazine*, vol. 5, no. 2, pp. 44–51, 2021.

[28] C. De Alwis *et al.*, "Survey on 6G frontiers: Trends, applications, requirements, technologies and future research," *IEEE Open Journal of the Communications Society*, vol. 2, pp. 836–886, 2021.

[29] B. Hassan, S. Baig, and M. Asif, "Key Technologies for Ultra-Reliable and Low-Latency Communication in 6G," *IEEE Communications Standards Magazine*, vol. 5, no. 2, pp. 106–113, 2021.

[30] M. Giordani, M. Polese, M. Mezzavilla, S. Rangan, and M. Zorzi, "Toward 6G networks: Use cases and technologies," *IEEE Communications Magazine*, vol. 58, no. 3, pp. 55–61, 2020.

[31] R. Deng, B. Di, H. Zhang, Y. Tan, and L. Song, "Reconfigurable Holographic Surface: Holographic Beamforming for Metasurface-Aided Wireless Communications," *IEEE Transactions on Vehicular Technology*, vol. 70, no. 6, pp. 6255–6259, 2021, doi: 10.1109/TVT.2021.3079465.

[32] R. Deng *et al.*, "Reconfigurable Holographic Surfaces for Ultra-Massive MIMO in 6G: Practical Design, Optimization and Implementation," *IEEE Journal on Selected Areas in Communications*, 2023.

[33] R. Deng *et al.*, "Reconfigurable Holographic Surfaces for Future Wireless Communications," *IEEE Wireless Communications*, vol. 28, no. 6, pp. 126–131, 2021, doi: 10.1109/MWC.001.2100204.

[34] C. Huang *et al.*, "Holographic MIMO Surfaces for 6G Wireless Networks: Opportunities, Challenges, and Trends," *IEEE Wireless Communications*, vol. 27, no. 5, pp. 118–125, 2020, doi: 10.1109/MWC.001.1900534.

[35] A. Jabbar *et al.*, "Millimeter-Wave Smart Antenna Solutions for URLLC in Industry 4.0 and Beyond," *Sensors*, vol. 22, no. 7, p. 2688, 2022.

[36] T. S. Rappaport, J. N. Murdock, and F. Gutierrez, “State of the art in 60-GHz integrated circuits and systems for wireless communications,” *Proceedings of the IEEE*, vol. 99, no. 8, pp. 1390–1436, 2011, doi: 10.1109/JPROC.2011.2143650.

[37] M. Nandakumar and T. Shanmuganantham, “SIW flower shaped fractal antenna backed with cavity for 60GHz frequency applications,” in *2018 International Conference on Computer, Communication, and Signal Processing (ICCCSP)*, 2018, pp. 1–4.

[38] M. Nanda Kumar and T. Shanmuganantham, “SIW-based slot antenna fed by microstrip for 60/79 GHz applications,” in *Microelectronics, Electromagnetics and Telecommunications*, Springer, 2019, pp. 741–748.

[39] J. U. R. Kazim, A. Abohmra, M. U. Rehman, M. A. Imran, and Q. H. Abbasi, “A Corrugated SIW Based Slot Antenna for Terahertz Application,” in *2020 IEEE International Symposium on Antennas and Propagation and North American Radio Science Meeting*, 2020, pp. 1407–1408.

[40] H. Vettikalladi, W. T. Sethi, M. Himdi, and M. Alkanhal, “60 GHz beam-tilting coplanar slotted SIW antenna array,” *Frequenz*, 2021.

[41] J. Liu, D. R. Jackson, and Y. Long, “Substrate integrated waveguide (SIW) leaky-wave antenna with transverse slots,” *IEEE Transactions on Antennas and Propagation*, vol. 60, no. 1, pp. 20–29, 2011.

[42] A. Sarkar and S. Lim, “60 GHz compact larger beam scanning range PCB leaky-wave antenna using HMSIW for millimeter-wave applications,” *IEEE Transactions on Antennas and Propagation*, vol. 68, no. 8, pp. 5816–5826, 2020.

[43] J. Liu, X. Tang, Y. Li, and Y. Long, “Substrate integrated waveguide leaky-wave antenna with H-shaped slots,” *IEEE transactions on antennas and propagation*, vol. 60, no. 8, pp. 3962–3967, 2012.

[44] Q.-D. Cao, X.-X. Yang, F. Yu, and S. Gao, “High Scanning Rate Millimeter Wave Circularly Polarized CTS Leaky-Wave Antenna,” *IEEE Transactions on Antennas and Propagation*, 2024.

[45] A. T. Almutawa, A. Hosseini, D. R. Jackson, and F. Capolino, “Leaky-wave analysis of wideband planar fabry-pérot cavity antennas formed by a thick prs,” *IEEE Transactions on Antennas and Propagation*, vol. 67, no. 8, pp. 5163–5175, 2019, doi: 10.1109/TAP.2019.2911349.

[46] F. Yavari and N. Pilevari, “Industry Revolutions Development from Industry 1.0 to Industry 5.0 in Manufacturing,” *Journal of Industrial Strategic Management*, vol. 5, no.

2, pp. 44–63, 2020.

[47] Y. Yin, K. E. Stecke, and D. Li, “The evolution of production systems from Industry 2.0 through Industry 4.0,” *International Journal of Production Research*, vol. 56, no. 1–2, pp. 848–861, 2018.

[48] RGBSI, “Industry 4.0 Building a connected manufacturing environment through digitalization,” *Engineering Solutions IT Solutions (White Paper)*, [Online]. Available: www.rgbsi.com

[49] B. Meindl, N. F. Ayala, J. Mendonça, and A. G. Frank, “The four smarts of Industry 4.0: Evolution of ten years of research and future perspectives,” *Technological Forecasting and Social Change*, vol. 168, no. March, p. 120784, 2021, doi: 10.1016/j.techfore.2021.120784.

[50] T. Kalsoom, N. Ramzan, S. Ahmed, and M. Ur-Rehman, “Advances in sensor technologies in the era of smart factory and industry 4.0,” *Sensors*, vol. 20, no. 23, p. 6783, 2020.

[51] D. G. S. Pivoto, L. F. F. de Almeida, R. da Rosa Righi, J. J. P. C. Rodrigues, A. B. Lugli, and A. M. Alberti, “Cyber-physical systems architectures for industrial internet of things applications in Industry 4.0: A literature review,” *Journal of Manufacturing Systems*, vol. 58, pp. 176–192, 2021.

[52] G. Aceto, V. Persico, and A. Pescapé, “Industry 4.0 and health: Internet of things, big data, and cloud computing for healthcare 4.0,” *Journal of Industrial Information Integration*, vol. 18, p. 100129, 2020.

[53] H. Singh, “Big data, industry 4.0 and cyber-physical systems integration: A smart industry context,” *Materials Today: Proceedings*, vol. 46, pp. 157–162, 2021.

[54] R. S. Peres, X. Jia, J. Lee, K. Sun, A. W. Colombo, and J. Barata, “Industrial artificial intelligence in industry 4.0-systematic review, challenges and outlook,” *IEEE Access*, vol. 8, pp. 220121–220139, 2020.

[55] M. Javaid, A. Haleem, R. P. Singh, and R. Suman, “Artificial intelligence applications for industry 4.0: a literature-based study,” *Journal of Industrial Integration and Management*, pp. 1–29, 2021.

[56] D. Mhlanga, “Artificial intelligence in the industry 4.0, and its impact on poverty, innovation, infrastructure development, and the sustainable development goals: Lessons from emerging economies?,” *Sustainability*, vol. 13, no. 11, p. 5788, 2021.

[57] M. Dopico, A. Gómez, D. la Fuente, N. Garc\’\ia, R. Rosillo, and J. Puche, “A vision of

industry 4.0 from an artificial intelligence point of view," in *Proceedings on the international Conference on Artificial intelligence (ICAI)*, 2016, p. 407.

[58] B. Alhayani *et al.*, "5G standards for the Industry 4.0 enabled communication systems using artificial intelligence: perspective of smart healthcare system," *Applied Nanoscience*, pp. 1–11, 2022.

[59] K. Schwab, *The fourth industrial revolution*. Currency, 2017.

[60] S. Vaidya, P. Ambad, and S. Bhosle, "Industry 4.0--a glimpse," *Procedia manufacturing*, vol. 20, pp. 233–238, 2018.

[61] L. Da Xu, E. L. Xu, and L. Li, "Industry 4.0: state of the art and future trends," *International Journal of Production Research*, vol. 56, no. 8, pp. 2941–2962, 2018.

[62] L. Haghnegahdar, S. S. Joshi, and N. B. Dahotre, "From IoT-based cloud manufacturing approach to intelligent additive manufacturing: Industrial Internet of Things—An overview," *The International Journal of Advanced Manufacturing Technology*, pp. 1–18, 2022.

[63] U. M. Dilberoglu, B. Gharehpapagh, U. Yaman, and M. Dolen, "The role of additive manufacturing in the era of industry 4.0," *Procedia Manufacturing*, vol. 11, pp. 545–554, 2017.

[64] S. Pfeiffer, "Robots, Industry 4.0 and humans, or why assembly work is more than routine work," *Societies*, vol. 6, no. 2, p. 16, 2016.

[65] D. Van Huynh, S. R. Khosravirad, L. D. Nguyen, and T. Q. Duong, "Multiple relay robots-assisted URLLC for industrial automation with deep neural networks," in *2021 IEEE Global Communications Conference (GLOBECOM)*, 2021, pp. 1–5.

[66] A. Ranjha, G. Kaddoum, and K. Dev, "Facilitating URLLC in UAV-assisted relay systems with multiple-mobile robots for 6G Networks: A prospective of agriculture 4.0," *IEEE Transactions on Industrial Informatics*, 2021.

[67] E. H. Østergaard, "Welcome to industry 5.0," *Retrieved on February*, vol. 5, p. 2020, 2018.

[68] P. K. R. Maddikunta *et al.*, "Industry 5.0: A survey on enabling technologies and potential applications," *Journal of Industrial Information Integration*, vol. 26, p. 100257, 2022.

[69] F. Firyaguna *et al.*, "Towards Industry 5.0: Intelligent Reflecting Surface (IRS) in Smart Manufacturing," *arXiv preprint arXiv:2201.02214*, 2022.

[70] Y. H. Chai, G. Y. Yew, S. Yusup, and P. L. Show, "Technologies in Industry 5.0," *The*

Prospect of Industry 5.0 in Biomanufacturing, p. 257, 2021.

[71] S. Nahavandi, "Industry 5.0—A human-centric solution," *Sustainability*, vol. 11, no. 16, p. 4371, 2019.

[72] A. S. Duggal *et al.*, "A sequential roadmap to Industry 6.0: Exploring future manufacturing trends," *IET Communications*, vol. 16, no. 5, pp. 521–531, 2022, doi: 10.1049/cmu2.12284.

[73] B. F. Oy, "From industry x to industry 6.0".

[74] S. Vitturi, C. Zunino, and T. Sauter, "Industrial communication systems and their future challenges: Next-generation Ethernet, IIoT, and 5G," *Proceedings of the IEEE*, vol. 107, no. 6, pp. 944–961, 2019.

[75] F. De Pellegrini, D. Miorandi, S. Vitturi, and A. Zanella, "On the use of wireless networks at low level of factory automation systems," *IEEE Transactions on Industrial Informatics*, vol. 2, no. 2, pp. 129–143, 2006.

[76] M. A. Imran, S. Hussain, and Q. H. Abbasi, *Wireless Automation as an Enabler for the Next Industrial Revolution*. John Wiley \& Sons, 2020.

[77] M. Noor-A-Rahim *et al.*, "Wireless Communications for Smart Manufacturing and Industrial IoT: Existing Technologies, 5G and Beyond," *Sensors*, vol. 23, no. 1, p. 73, 2022.

[78] Q. Wang and J. Jiang, "Comparative examination on architecture and protocol of industrial wireless sensor network standards," *IEEE Communications Surveys & Tutorials*, vol. 18, no. 3, pp. 2197–2219, 2016.

[79] X. Li, D. Li, J. Wan, A. V Vasilakos, C.-F. Lai, and S. Wang, "A review of industrial wireless networks in the context of industry 4.0," *Wireless Networks*, vol. 23, no. 1, pp. 23–41, 2017.

[80] R. Candell and M. Kashef, "Industrial wireless: Problem space, success considerations, technologies, and future direction," in *2017 Resilience Week (RWS)*, 2017, pp. 133–139.

[81] D. Mourtzis, *Design and operation of production networks for mass personalization in the era of cloud technology*. Elsevier, 2021.

[82] B. Sokolov, D. Ivanov, and A. Dolgui, *Scheduling in industry 4.0 and cloud manufacturing*, vol. 289. Springer, 2020.

[83] M. Noor-A-Rahim *et al.*, "Wireless Communications for Smart Manufacturing and Industrial IoT: Existing Technologies, 5G and Beyond," *Sensors*, vol. 23, no. 1, p. 73, 2022.

[84] R. Y. Zhong, X. Xu, E. Klotz, and S. T. Newman, “Intelligent manufacturing in the context of industry 4.0: a review,” *Engineering*, vol. 3, no. 5, pp. 616–630, 2017.

[85] E. Negri, L. Fumagalli, and M. Macchi, “A review of the roles of digital twin in CPS-based production systems,” *Procedia manufacturing*, vol. 11, pp. 939–948, 2017.

[86] K. Montgomery, R. Candell, Y. Liu, and M. Hany, *Wireless user requirements for the factory workcell*. Department of Commerce, National Institute of Standards and Technology, 2020.

[87] A. Jabbar, M. A. Jamshed, Q. Abbasi, M. A. Imran, and M. Ur-rehman, “Leveraging the Role of Dynamic Reconfigurable Antennas in Viewpoint of Industry 4 . 0 and Beyond,” pp. 1–22, doi: 10.34133/research.0110.

[88] B. Babakhani, S. K. Sharma, and N. R. Labadie, “A frequency agile microstrip patch phased array antenna with polarization reconfiguration,” *IEEE Transactions on Antennas and Propagation*, vol. 64, no. 10, pp. 4316–4327, 2016.

[89] J. Wu, X. Lu, W. Wang, J. Han, G. Xu, and Z. Huang, “Design of a Compact Polarization Agile and Frequency Tailored Array Antenna with Digital-Controllable Radiation Beams,” *IEEE Transactions on Antennas and Propagation*, 2021.

[90] X. G. Zhang, W. X. Jiang, H. W. Tian, Z. X. Wang, Q. Wang, and T. J. Cui, “Pattern-reconfigurable planar array antenna characterized by digital coding method,” *IEEE Transactions on Antennas and Propagation*, vol. 68, no. 2, pp. 1170–1175, 2019.

[91] Y. Tu, Y. I. A. Al-Yasir, N. Ojaroudi Parchin, A. M. Abdulkhaleq, and R. A. Abd-Alhameed, “A Survey on Reconfigurable Microstrip Filter--Antenna Integration: Recent Developments and Challenges,” *Electronics*, vol. 9, no. 8, p. 1249, 2020.

[92] B. Mohamadzade, R. B. V. B. Simorangkir, S. Maric, A. Lalbakhsh, K. P. Esselle, and R. M. Hashmi, “Recent developments and state of the art in flexible and conformal reconfigurable antennas,” *Electronics*, vol. 9, no. 9, p. 1375, 2020.

[93] D. Christin, P. S. Mogre, and M. Hollick, “Survey on wireless sensor network technologies for industrial automation: The security and quality of service perspectives,” *Future Internet*, vol. 2, no. 2, pp. 96–125, 2010.

[94] E. Mozaffariahrar, F. Theoleyre, and M. Menth, “A Survey of Wi-Fi 6: Technologies, Advances, and Challenges,” *Future Internet*, vol. 14, no. 10, p. 293, 2022.

[95] E. J. Oughton, W. Lehr, K. Katsaros, I. Selinis, D. Bubley, and J. Kusuma, “Revisiting wireless internet connectivity: 5G vs Wi-Fi 6,” *Telecommunications Policy*, vol. 45, no. 5, p. 102127, 2021.

[96] G. Naik, J.-M. Park, J. Ashdown, and W. Lehr, “Next generation Wi-Fi and 5G NR-U in the 6 GHz bands: Opportunities and challenges,” *IEEE Access*, vol. 8, pp. 153027–153056, 2020.

[97] W.-F. Alliance, “Wi-Fi Alliance Introduces Wi-Fi 6.” Accessed: Apr, 2020.

[98] A. Garcia-Rodriguez, D. Lopez-Perez, L. Galati-Giordano, and G. Geraci, “IEEE 802.11 be: Wi-Fi 7 strikes back,” *IEEE Communications Magazine*, vol. 59, no. 4, pp. 102–108, 2021.

[99] L. Fanari, E. Iradier, I. Bilbao, R. Cabrera, J. Montalban, and P. Angueira, “Comparison between Different Channel Coding Techniques for IEEE 802.11 be within Factory Automation Scenarios,” *Sensors*, vol. 21, no. 21, p. 7209, 2021.

[100] V. Frascolla, D. Cavalcanti, and R. Shah, “Wi-Fi Evolution: The Path Towards Wi-Fi 7 and Its Impact on IIoT,” *Journal of Mobile Multimedia*, pp. 263–276, 2023.

[101] G. Naik, D. Ogbe, and J.-M. J. Park, “Can Wi-Fi 7 support real-time applications? On the impact of multi link aggregation on latency,” in *ICC 2021-IEEE International Conference on Communications*, 2021, pp. 1–6.

[102] M. Carrascosa-Zamacois, G. Geraci, L. Galati-Giordano, A. Jonsson, and B. Bellalta, “Understanding Multi-link Operation in Wi-Fi 7: Performance, Anomalies, and Solutions,” *arXiv preprint arXiv:2210.07695*, 2022.

[103] T. Adame, M. Carrascosa-Zamacois, and B. Bellalta, “Time-sensitive networking in IEEE 802.11 be: On the way to low-latency WiFi 7,” *Sensors*, vol. 21, no. 15, p. 4954, 2021.

[104] L. G. Giordano, G. Geraci, M. Carrascosa, and B. Bellalta, “What will Wi-Fi 8 be? A primer on IEEE 802.11 bn ultra high reliability,” *arXiv preprint arXiv:2303.10442*, 2023.

[105] A. A. Abdalhafid, S. K. Subramaniam, Z. A. Zukarnain, and F. H. Ayob, “Multi-Link Operation in IEEE802. 11be Extremely High Throughput: A Survey,” *IEEE Access*, 2024.

[106] C. Deng, G. S. Member, X. Fang, and S. Member, “IEEE 802.11be Wi-Fi 7: New Challenges and Opportunities,” vol. 22, no. 4, pp. 2136–2166, 2020.

[107] D. Lopez-Perez, A. Garcia-Rodriguez, L. Galati-Giordano, M. Kasslin, and K. Doppler, “IEEE 802.11be Extremely High Throughput: The Next Generation of Wi-Fi Technology beyond 802.11ax,” *IEEE Communications Magazine*, vol. 57, no. 9, pp. 113–119, 2019, doi: 10.1109/MCOM.001.1900338.

[108] L. Ward, “Rohde_Schwarz_IEEE-802-11be-technology-introduction_wp_en_3683-4026-52_v0100,” pp. 1–32.

[109] A. Jabbar, M. A. Jamshed, Q. Abbasi, M. A. Imran, and M. Ur-Rehman, “Leveraging the Role of Dynamic Reconfigurable Antennas in Viewpoint of Industry 4.0 and Beyond,” *Research*, vol. 6, p. 110, 2023.

[110] A. Hottinen, M. Kuusela, K. Hugl, J. Zhang, and B. Raghothaman, “Industrial embrace of smart antennas and MIMO,” *IEEE Wireless Communications*, vol. 13, no. 4, pp. 8–16, 2006.

[111] T. Baykas *et al.*, “IEEE 802.15. 3c: The first IEEE wireless standard for data rates over 1 Gb/s,” *IEEE Communications Magazine*, vol. 49, no. 7, pp. 114–121, 2011.

[112] I. 802. 1. W. Group and others, “IEEE 802.11 ad, amendment 3: Enhancements for very high throughput in the 60 GHz band,” *IEEE Standard*, vol. 802, 2012.

[113] Y. Ghasempour, C. R. C. M. C. M. Da Silva, C. Cordeiro, and E. W. Knightly, “IEEE 802.11ay: Next-Generation 60 GHz Communication for 100 Gb/s Wi-Fi,” *IEEE Communications Magazine*, vol. 55, no. 12, pp. 186–192, 2017, doi: 10.1109/MCOM.2017.1700393.

[114] P. Zhou *et al.*, “IEEE 802.11 ay-based mmWave WLANs: Design challenges and solutions,” *IEEE Communications Surveys & Tutorials*, vol. 20, no. 3, pp. 1654–1681, 2018.

[115] A. Jabbar, M. A. Jamshed, M. A. Shawky, Q. H. Abbasi, M. A. Imran, and M. U. Rehman, “Multi-Gigabit Millimeter-Wave Industrial Communication: A Solution for Industry 4.0 and Beyond,” in *IEEE Global Communications Conference*, 2022, pp. 5001–5006.

[116] Y. Banday, G. M. Rather, and G. R. Begh, “Effect of atmospheric absorption on millimetre wave frequencies for 5G cellular networks,” *IET Communications*, vol. 13, no. 3, pp. 265–270, 2019.

[117] S. Rangan, T. S. Rappaport, and E. Erkip, “Millimeter-wave cellular wireless networks: Potentials and challenges,” *Proceedings of the IEEE*, vol. 102, no. 3, pp. 366–385, 2014.

[118] C. A. Balanis, *Antenna theory: analysis and design*. John wiley & sons, 2016.

[119] R. C. Daniels, J. N. Murdock, T. S. Rappaport, and R. W. Heath, “60 GHz wireless: Up close and personal,” *IEEE Microwave magazine*, vol. 11, no. 7, pp. 44–50, 2010.

[120] H. M. Cheema and A. Shamim, “The last barrier: on-chip antennas,” *IEEE Microwave Magazine*, vol. 14, no. 1, pp. 79–91, 2013.

[121] U. Ullah, N. Mahyuddin, Z. Arifin, M. Z. Abdullah, and A. Marzuki, “Antenna in LTCC technologies: a review and the current state of the art,” *IEEE Antennas and Propagation Magazine*, vol. 57, no. 2, pp. 241–260, 2015.

[122] X.-P. Chen, K. Wu, L. Han, and F. He, “Low-cost high gain planar antenna array for 60-GHz band applications,” *IEEE Transactions on Antennas and Propagation*, vol. 58, no. 6, pp. 2126–2129, 2010.

[123] H. Sun, Y.-X. Guo, and Z. Wang, “60-GHz circularly polarized U-slot patch antenna array on LTCC,” *IEEE Transactions on Antennas and Propagation*, vol. 61, no. 1, pp. 430–435, 2012.

[124] W. Yang, K. Ma, K. S. Yeo, and W. M. Lim, “A compact high-performance patch antenna array for 60-GHz applications,” *IEEE Antennas and Wireless Propagation Letters*, vol. 15, pp. 313–316, 2015, doi: 10.1109/LAWP.2015.2443054.

[125] H. Chu, J.-X. Chen, and Y.-X. Guo, “An efficient gain enhancement approach for 60-GHz antenna using fully integrated vertical metallic walls in LTCC,” *IEEE Transactions on Antennas and Propagation*, vol. 64, no. 10, pp. 4513–4518, 2016.

[126] T. S. Mneesy, R. K. Hamad, A. I. Zaki, and W. A. E. Ali, “A novel high gain monopole antenna array for 60 GHz millimeter-wave communications,” *Applied Sciences*, vol. 10, no. 13, p. 4546, 2020.

[127] Y. Al-Alem and A. A. Kishk, “Low-profile low-cost high gain 60 GHz antenna,” *IEEE Access*, vol. 6, pp. 13376–13384, 2018.

[128] B. Biglarbegian, M. Fakharzadeh, D. Busuioc, M.-R. R. Nezhad-Ahmadi, and S. Safavi-Naeini, “Optimized microstrip antenna arrays for emerging millimeter-wave wireless applications,” *IEEE Transactions on Antennas and Propagation*, vol. 59, no. 5, pp. 1742–1747, 2011, doi: 10.1109/TAP.2011.2123058.

[129] Y. Al-Alem and A. A. Kishk, “Efficient millimeter-wave antenna based on the exploitation of microstrip line discontinuity radiation,” *IEEE Transactions on Antennas and Propagation*, vol. 66, no. 6, pp. 2844–2852, 2018.

[130] A. Jabbar, Q. H. Abbasi, M. Ali Imran, M. U. Rehman, M. A. Imran, and M. U. Rehman, “Design of a 60 GHz Antenna for Multi-Gigabit WiGig Communication in Industry 4.0,” in *IEEE International Symposium on Antennas and Propagation and USNC-URSI Radio Science Meeting (AP-S/URSI)*, 2022, pp. 325–326. doi: 10.1109/AP-S/USNC-URSI47032.2022.9886405.

[131] Y. P. Zhang, M. Sun, and L. H. Guo, “On-chip antennas for 60-GHz radios in silicon

technology," *IEEE Transactions on Electron Devices*, vol. 52, no. 7, pp. 1664–1668, 2005.

[132] A. Nähring, "Demystifying over-the-air (OTA) testing – important antenna parameters , test system setup and calibration White paper," 2018. [Online]. Available: Rohde & Schwarz

[133] H. Yang *et al.*, "A programmable metasurface with dynamic polarization, scattering and focusing control," *Scientific Reports*, vol. 6, no. October, pp. 1–11, 2016, doi: 10.1038/srep35692.

[134] C. Pfeiffer and A. Grbic, "Metamaterial Huygens' surfaces: tailoring wave fronts with reflectionless sheets," *Physical review letters*, vol. 110, no. 19, p. 197401, 2013.

[135] L. Zhang and T. J. Cui, "Space-time-coding digital metasurfaces: Principles and applications," *Research*, 2021.

[136] H.-X. Xu *et al.*, "Tunable microwave metasurfaces for high-performance operations: dispersion compensation and dynamical switch," *Scientific reports*, vol. 6, no. 1, p. 38255, 2016.

[137] L. Zhang *et al.*, "Space-time-coding digital metasurfaces," *Nature Communications*, vol. 9, no. 1, pp. 1–11, 2018, doi: 10.1038/s41467-018-06802-0.

[138] T. J. Cui, M. Q. Qi, X. Wan, J. Zhao, and Q. Cheng, "Coding metamaterials, digital metamaterials and programmable metamaterials," *Light: Science & Applications*, vol. 3, no. 10, pp. e218–e218, 2014, doi: 10.1038/lsa.2014.99.

[139] J. Hunt *et al.*, "Metamaterial apertures for computational imaging," *Science*, vol. 339, no. 6117, pp. 310–313, 2013.

[140] M. Noor-A-Rahim *et al.*, "Toward Industry 5.0: Intelligent Reflecting Surface in Smart Manufacturing," *IEEE Communications Magazine*, vol. 60, no. 10, pp. 72–78, 2022.

[141] N. Shlezinger, O. Dicker, Y. C. Eldar, I. Yoo, M. F. Imani, and D. R. Smith, "Dynamic Metasurface Antennas for Uplink Massive MIMO Systems," *IEEE Transactions on Communications*, vol. 67, no. 10, pp. 6829–6843, 2019, doi: 10.1109/TCOMM.2019.2927213.

[142] P. Del Hougne *et al.*, "Dynamic Metasurface Aperture as Smart Around-the-Corner Motion Detector," *Scientific Reports*, vol. 8, no. 1, pp. 1–10, 2018, doi: 10.1038/s41598-018-24681-9.

[143] N. Shlezinger, G. C. Alexandropoulos, M. F. Imani, Y. C. Eldar, and D. R. Smith, "Dynamic Metasurface Antennas for 6G Extreme Massive MIMO Communications,"

IEEE Wireless Communications, vol. 28, no. 2, pp. 106–113, 2021, doi: 10.1109/MWC.001.2000267.

[144] T. Sleasman, M. F. Imani, A. V. Diebold, M. Boyarsky, K. P. Trofatter, and D. R. Smith, "Computational Imaging With Dynamic Metasurfaces: A Recipe for Simple and Low-Cost Microwave Imaging," *IEEE Antennas and Propagation Magazine*, vol. 64, no. 4, pp. 123–134, 2022, doi: 10.1109/MAP.2022.3169395.

[145] R. Deng *et al.*, "Reconfigurable holographic surfaces for future wireless communications," *IEEE Wireless Communications*, vol. 28, no. 6, pp. 126–131, 2021.

[146] M. Lin *et al.*, "A high-efficiency reconfigurable element for dynamic metasurface antenna," *IEEE Access*, vol. 8, pp. 87446–87455, 2020.

[147] S. Li, F. Xu, X. Wan, T. J. Cui, and Y. Q. Jin, "Programmable Metasurface Based on Substrate-Integrated Waveguide for Compact Dynamic-Pattern Antenna," *IEEE Transactions on Antennas and Propagation*, vol. 69, no. 5, pp. 2958–2962, 2021, doi: 10.1109/TAP.2020.3023581.

[148] M. Boyarsky, T. Sleasman, M. F. Imani, J. N. Gollub, and D. R. Smith, "Electronically steered metasurface antenna," *Scientific reports*, vol. 11, no. 1, pp. 1–10, 2021.

[149] G.-B. Wu *et al.*, "A universal metasurface antenna to manipulate all fundamental characteristics of electromagnetic waves," *Nature Communications*, vol. 14, no. 1, p. 5155, 2023.

[150] "Adv Eng Mater - 2023 - Yang - An End-Fed Programmable Metasurface Based on Substrate Integrated Waveguide for Novel Phased.pdf."

[151] A. Jabbar, Z. Pang, G. A. Safdar, Q. Abbasi, M. A. Imran, and M. Ur-Rehman, "A Compact Wideband Millimeter-Wave Beam-Scanning Antenna Array for Industry 4.0 and Beyond Applications," *2023 IEEE International Workshop on Antenna Technology (iWAT)*, pp. 1–4, 2023.

[152] A. Jabbar *et al.*, "A Wideband Frequency Beam-Scanning Antenna Array for Millimeter-Wave Industrial Applications," *Authorea Preprints*, 2023.

[153] B. Thakur and A. Kunte, "Improved design of CELC meta-resonators for bandwidth improvement and miniaturization of patch antenna," *Applied Physics A: Materials Science and Processing*, vol. 124, no. 12, pp. 1–8, 2018, doi: 10.1007/s00339-018-2273-2.

[154] C. Arora, S. S. Pattnaik, and R. N. Baral, "Metamaterial inspired DNG superstrate for performance improvement of microstrip patch antenna array," *International Journal of*

Microwave and Wireless Technologies, vol. 10, no. 3, pp. 318–327, 2018.

[155] M. S. Islam, M. T. Islam, M. D. A. Ullah, G. K. Beng, N. Amin, and N. Misran, "A modified meander line microstrip patch antenna with enhanced bandwidth for 2.4 GHz ISM-band Internet of Things (IoT) applications," *IEEE Access*, vol. 7, pp. 127850–127861, 2019.

[156] C. A. Balanis, *Antenna theory: analysis and design*. John wiley & sons, 2015.

[157] Y. Liu *et al.*, "Design and fabrication of two-port three-beam switched beam antenna array for 60 GHz communication," *IET Microwaves, Antennas \& Propagation*, vol. 13, no. 9, pp. 1438–1442, 2019.

[158] E. A. Ball, "Investigation into Series-Fed Microstrip Patch Arrays at 26 GHz, 28 GHz and 48 GHz--Design, Simulation and Prototype Tests," in *2021 IEEE Texas Symposium on Wireless and Microwave Circuits and Systems (WMCS)*, 2021, pp. 1–6.

[159] K. Z. Ghafoor *et al.*, "Millimeter-wave communication for internet of vehicles: status, challenges, and perspectives," *IEEE Internet of Things Journal*, vol. 7, no. 9, pp. 8525–8546, 2020.

[160] L. Lu, X. Ma, Y. Liang, Z. Liu, X. Fan, and L. Li, "A 60-GHz Hybrid FMCW-Doppler Radar for Vibration Detection With a Robust I/Q Calibration Method," *IEEE Sensors Journal*, vol. 22, no. 21, pp. 20464–20474, 2022.

[161] Z. Briqech, S. Gupta, A.-A. Beltay, A. Elboushi, A.-R. Sebak, and T. A. Denidni, "57--64 GHz imaging/detection sensor—Part II: Experiments on concealed weapons and threatening materials detection," *IEEE Sensors Journal*, vol. 20, no. 18, pp. 10833–10840, 2020.

[162] M. Rameez, M. I. Pettersson, and M. Dahl, "Interference Compression and Mitigation for Automotive FMCW Radar Systems," *IEEE Sensors Journal*, vol. 22, no. 20, pp. 19739–19749, 2022.

[163] H. Li, K. Ota, M. Dong, and H.-H. Chen, "Efficient energy transport in 60 GHz for wireless industrial sensor networks," *IEEE Wireless Communications*, vol. 24, no. 5, pp. 143–149, 2017.

[164] S. Pan, M. Lin, M. Xu, S. Zhu, L.-A. Bian, and G. Li, "A low-profile programmable beam scanning holographic array antenna without phase shifters," *IEEE Internet of Things Journal*, 2021.

[165] J. Zhang, X. Zhang, and A. A. Kishk, "Broadband 60 GHz antennas fed by substrate integrated gap waveguides," *IEEE Transactions on Antennas and Propagation*, vol. 66,

no. 7, pp. 3261–3270, 2018.

[166] J. Säily, A. Lamminen, and J. Francey, “Low cost high gain antenna arrays for 60 GHz millimetre wave identification (MMID),” in *Sixth ESA Workshop on Millimetre-Wave Technology and Applications-Fourth Global Symposium Millimetre Waves, Espoo, Finland*, 2011.

[167] A. Jabbar *et al.*, “A Wideband Frequency Beam-Scanning Antenna Array for Millimeter-Wave Industrial Wireless Sensing Applications,” *IEEE Sensors Journal*, 2024, [Online]. Available: doi: 10.1109/JSEN.2024.3370135

[168] Y. Wang, Z. Zhang, and H. Li, “Universal quickest sensing of spectrum change in millimeter wave communications: a data driven approach,” in *IEEE Global Communications Conference*, 2017, pp. 1–6.

[169] Z. Zhang, L. Li, Y. Fan, and H. Li, “Object tracking via blocking in millimeter wave communications: A blessing misfortune,” in *IEEE International Conference on Communications (ICC)*, 2018, pp. 1–6.

[170] L. K. Mathew, S. C. Nagavarapu, and A. Abraham, “Design and implementation of a Joint Sensing & Communication System for Connected Autonomous Vehicles,” in *17th International Conference on Control, Automation, Robotics and Vision (ICARCV)*, 2022, pp. 392–396.

[171] P. Zetterberg and R. Fardi, “Open source SDR frontend and measurements for 60-GHz wireless experimentation,” *IEEE Access*, vol. 3, pp. 445–456, 2015.

[172] A. Jabbar, Q. Abbasi, Z. Pang, M. A. Imran, and M. Ur-Rehman, “High Performance 60 GHz Beamforming Antenna Array For 5G and Beyond Industrial Applications,” in *17th European Conference on Antennas and Propagation (EuCAP)*, 2023, pp. 1–5.

[173] R. Hosono, R. Sugiura, N. Tomimizu, M. Sono, and S. Abe, “A 60 GHz Wide-Band Communication Module that also Supports the New 5G Band,” *Fujikura Technical Review, No. 51*, pp. 31–34, 2022.

[174] T. Sowlati *et al.*, “A 60-GHz 144-element phased-array transceiver for backhaul application,” *IEEE Journal of Solid-State Circuits*, vol. 53, no. 12, pp. 3640–3659, 2018.

[175] K. Koslowski, F. Baum, L. Buhler, M. Peter, and W. Keusgen, “Enhancing mmWave Devices with Custom Lenses,” *2022 16th European Conference on Antennas and Propagation, EuCAP 2022*, 2022, doi: 10.23919/eucap53622.2022.9769338.

[176] J. John *et al.*, “Wireless Communications for Smart Manufacturing and Industrial IoT: Existing Technologies, 5G, and Beyond,” *arXiv preprint arXiv:2208.06697*, 2022.

[177] M. Luvisotto, Z. Pang, and D. Dzung, “High-performance wireless networks for industrial control applications: New targets and feasibility,” *Proceedings of the IEEE*, vol. 107, no. 6, pp. 1074–1093, 2019.

[178] A. Jabbar, Q. Abbasi, M. A. Imran, and M. Ur-Rehman, “Impact of Dielectric Substrate, Feed Connector, and Fabrication Tolerances on the Performance of Planar Millimeter-Wave Antenna Arrays,” in *18th European Conference on Antennas and Propagation (EuCAP)*, 2024.

[179] A. Jabbar *et al.*, “60 GHz Programmable Dynamic Metasurface Antenna (DMA) for Next-Generation Communication, Sensing and Imaging Applications: From Concept to Prototype,” *IEEE Open Journal of Antennas and Propagation*, 2024, [Online]. Available: doi: 10.1109/OJAP.2024.3386452

[180] A. Jabbar, M. Ali, Q. Abbasi, and M. Ur-Rehman, “60 GHz Programmable Dynamic Metasurface Antenna (DMA) for 6G Avenues, Contactless HealthCare, and Smart Factories,” *2024 IEEE International Symposium on Antennas and Propagation and USNC-URSI Radio Science Meeting (AP-S/URSI)*, 2024.

[181] M. Di Renzo *et al.*, “Smart radio environments empowered by reconfigurable intelligent surfaces: How it works, state of research, and the road ahead,” *IEEE Journal on Selected Areas in Communications*, vol. 38, no. 11, pp. 2450–2525, 2020.

[182] J. Y. Dai *et al.*, “Wireless communications through a simplified architecture based on time-domain digital coding metasurface,” *Advanced materials technologies*, vol. 4, no. 7, p. 1900044, 2019.

[183] Y. Zheng *et al.*, “Metasurface-Assisted Wireless Communication with Physical Level Information Encryption,” *Advanced Science*, vol. 9, no. 34, p. 2204558, 2022.

[184] L. Zhang *et al.*, “A wireless communication scheme based on space-and frequency-division multiplexing using digital metasurfaces,” *Nature electronics*, vol. 4, no. 3, pp. 218–227, 2021.

[185] R. Deng, Y. Zhang, H. Zhang, B. Di, H. Zhang, and L. Song, “Reconfigurable Holographic Surface: A New Paradigm to Implement Holographic Radio,” *IEEE Vehicular Technology Magazine*, vol. 18, no. 1, pp. 20–28, 2023, doi: 10.1109/MVT.2022.3233157.

[186] T. Sleasman *et al.*, “Waveguide-Fed Tunable Metamaterial Element for Dynamic Apertures,” *IEEE Antennas and Wireless Propagation Letters*, vol. 15, pp. 606–609, 2016, doi: 10.1109/LAWP.2015.2462818.

[187] T. H. Hand, J. Gollub, S. Sajuyigbe, D. R. Smith, and S. A. Cummer, “Characterization of complementary electric field coupled resonant surfaces,” *Applied Physics Letters*, vol. 93, no. 21, 2008.

[188] D. R. Smith, O. Yurduseven, L. P. Mancera, P. Bowen, and N. B. Kundtz, “Analysis of a waveguide-fed metasurface antenna,” *Physical Review Applied*, vol. 8, no. 5, p. 54048, 2017.

[189] G. Lan *et al.*, “MetaSense: Boosting RF Sensing Accuracy Using Dynamic Metasurface Antenna,” *IEEE Internet of Things Journal*, vol. 8, no. 18, pp. 14110–14126, 2021, doi: 10.1109/JIOT.2021.3070225.

[190] V. Skouroliakou, A. M. Molaei, and O. Yurduseven, “Towards Real-Time Three-Dimensional (3D) Imaging using Dynamic Metasurface Antennas,” *IEEE European Conference on Antennas and Propagation, EuCAP 2023*, pp. 1–5, 2023.

[191] O. Yurduseven, J. N. Gollub, A. Rose, D. L. Marks, and D. R. Smith, “Design and Simulation of a Frequency-Diverse Aperture for Imaging of Human-Scale Targets,” *IEEE Access*, vol. 4, no. 2016, pp. 5436–5451, 2016, doi: 10.1109/ACCESS.2016.2604823.

[192] G. Lan, M. F. Imani, P. Del Hougne, W. Hu, D. R. Smith, and M. Gorlatova, “Wireless sensing using dynamic metasurface antennas: Challenges and opportunities,” *IEEE Communications Magazine*, vol. 58, no. 6, pp. 66–71, 2020.

[193] M. Lin *et al.*, “Single sensor to estimate DOA with programmable metasurface,” *IEEE Internet of Things Journal*, vol. 8, no. 12, pp. 10187–10197, 2021.

[194] M. Rezvani and R. Adve, “Channel Estimation for Dynamic Metasurface Antennas,” *IEEE Transactions on Wireless Communications*, 2023.

[195] R. J. Williams, P. Ram\’\irez-Espinosa, J. Yuan, and E. De Carvalho, “Electromagnetic based communication model for dynamic metasurface antennas,” *IEEE Transactions on Wireless Communications*, vol. 21, no. 10, pp. 8616–8630, 2022.

[196] I. Yoo, D. R. Smith, and M. Boyarsky, “Experimental Characterization of a Waveguide-Fed Varactor-Tuned Metamaterial Element Using the Coupled Dipole Framework,” *IEEE Antennas and Wireless Propagation Letters*, vol. 22, no. 2, pp. 387–391, 2022, doi: 10.1109/LAWP.2022.3213668.

[197] D. Deslandes and K. Wu, “Accurate modeling, wave mechanisms, and design considerations of a substrate integrated waveguide,” *IEEE Transactions on microwave theory and techniques*, vol. 54, no. 6, pp. 2516–2526, 2006.

[198] D. Deslandes, “Design equations for tapered microstrip-to-Substrate Integrated Waveguide transitions,” *IEEE MTT-S International Microwave Symposium Digest*, pp. 704–707, 2010, doi: 10.1109/MWSYM.2010.5517884.

[199] F. Falcone *et al.*, “Babinet principle applied to the design of metasurfaces and metamaterials,” *Physical review letters*, vol. 93, no. 19, p. 197401, 2004.

[200] Y. L. Loo, H. G. Wang, H. Zhang, and C. K. Ong, “Miniaturized power limiter metasurface based on Fano-type resonance and Babinet principle,” *Optics Express*, vol. 24, no. 18, p. 20816, 2016, doi: 10.1364/oe.24.020816.

[201] “https://www.macom.com/products/product-detail/MADP-000907-14020P.”

[202] V. G. Veselago, “Electrodynamics of substances with simultaneously negative ε and μ,” *Usp. fiz. nauk*, vol. 92, no. 7, p. 517, 1967.

[203] A. Lai, T. Itoh, and C. Caloz, “Composite right/left-handed transmission line metamaterials,” *IEEE microwave magazine*, vol. 5, no. 3, pp. 34–50, 2004.

[204] R. A. Shelby, D. R. Smith, and S. Schultz, “Experimental verification of a negative index of refraction,” *science*, vol. 292, no. 5514, pp. 77–79, 2001.

[205] O. F. Siddiqui, M. Mojahedi, and G. V Eleftheriades, “Periodically loaded transmission line with effective negative refractive index and negative group velocity,” *IEEE Transactions on Antennas and Propagation*, vol. 51, no. 10, pp. 2619–2625, 2003.

[206] M. F. Imani *et al.*, “Review of Metasurface Antennas for Computational Microwave Imaging,” *IEEE Transactions on Antennas and Propagation*, vol. 68, no. 3, pp. 1860–1875, 2020, doi: 10.1109/TAP.2020.2968795.

[207] S. Li, F. Xu, X. Wan, T. J. Cui, and Y.-Q. Jin, “Programmable Metasurface Based on Substrate-Integrated Waveguide for Compact Dynamic-Pattern Antenna,” *IEEE Transactions on Antennas and Propagation*, vol. 69, no. 5, pp. 2958–2962, 2020.

[208] Y. Zou, R. Zhu, L. Shen, and B. Zheng, “Reconfigurable Metasurface Hologram of Dynamic Distance via Deep Learning,” *Frontiers in Materials*, vol. 9, p. 907672, 2022.

[209] L. Pulido-Mancera, P. T. Bowen, M. F. Imani, N. Kundtz, and D. Smith, “Polarizability extraction of complementary metamaterial elements in waveguides for aperture modeling,” *Physical Review B*, vol. 96, no. 23, p. 235402, 2017.

[210] T. V. Hoang, V. Fusco, T. Fromenteze, and O. Yurduseven, “Computational polarimetric imaging using two-dimensional dynamic metasurface apertures,” *IEEE Open Journal of Antennas and Propagation*, vol. 2, pp. 488–497, 2021.

[211] D. K. Karmokar, K. P. Esselle, and S. G. Hay, “Fixed-frequency beam steering of

microstrip leaky-wave antennas using binary switches," *IEEE transactions on antennas and propagation*, vol. 64, no. 6, pp. 2146–2154, 2016.

[212] R. Shaw and M. K. Mandal, "Broadside scanning fixed frequency LWA with simultaneous electronic control of beam angle and beamwidth," *IEEE Transactions on Antennas and Propagation*, vol. 68, no. 5, pp. 3504–3514, 2020.

[213] C. Liaskos, S. Nie, A. Tsioliaridou, A. Pitsillides, S. Ioannidis, and I. Akyildiz, "A new wireless communication paradigm through software-controlled metasurfaces," *IEEE Communications Magazine*, vol. 56, no. 9, pp. 162–169, 2018.

[214] E. Björnson, L. Sanguinetti, H. Wymeersch, J. Hoydis, and T. L. Marzetta, "Massive MIMO is a reality—What is next?: Five promising research directions for antenna arrays," *Digital Signal Processing*, vol. 94, pp. 3–20, 2019.

[215] T. N. Le, A. Pegatoquet, T. Le Huy, L. Lizzi, and F. Ferrero, "Improving energy efficiency of mobile WSN using reconfigurable directional antennas," *IEEE Communications Letters*, vol. 20, no. 6, pp. 1243–1246, 2016.

[216] Y. Liu, C. Ouyang, Z. Wang, J. Xu, X. Mu, and A. L. Swindlehurst, "Near-Field Communications: A Comprehensive Survey," *arXiv preprint arXiv:2401.05900*, 2024.

[217] A. Azarbahram, O. L. A. López, R. D. Souza, R. Zhang, and M. Latva-Aho, "Energy Beamforming for RF Wireless Power Transfer with Dynamic Metasurface Antennas," *IEEE Wireless Communications Letters*, 2023.

[218] A. X. Oesterling, M. F. Imani, O. S. Mizrahi, J. N. Gollub, and D. R. Smith, "Detecting motion in a room using a dynamic metasurface antenna," *IEEE Access*, vol. 8, pp. 222496–222505, 2020.

[219] J. Wang, J. Chuang, S. Berweger, C. Gentile, and N. Golmie, "Towards Opportunistic Radar Sensing Using Millimeter-wave Wi-Fi," *IEEE Internet of Things Journal*, vol. 11, no. 1, pp. 188–200, 2023.

[220] L. Pulido-Mancera *et al.*, "Application of range migration algorithms to imaging with a dynamic metasurface antenna," *JOSA B*, vol. 33, no. 10, pp. 2082–2092, 2016.

[221] J. N. Gollub *et al.*, "Large metasurface aperture for millimeter wave computational imaging at the human-scale," *Scientific reports*, vol. 7, no. 1, p. 42650, 2017.

[222] T. Sleasman, M. Boyarsky, M. F. Imani, J. N. Gollub, and D. R. Smith, "Design considerations for a dynamic metamaterial aperture for computational imaging at microwave frequencies," *JOSA B*, vol. 33, no. 6, pp. 1098–1111, 2016.

[223] G. Lipworth *et al.*, "Metamaterial apertures for coherent computational imaging on the

physical layer," *JOSA A*, vol. 30, no. 8, pp. 1603–1612, 2013.

[224] J. Hunt *et al.*, "Metamaterial microwave holographic imaging system," *JOSA A*, vol. 31, no. 10, pp. 2109–2119, 2014.

[225] O. Yurduseven *et al.*, "Resolution of the frequency diverse metamaterial aperture imager," *Progress In Electromagnetics Research*, vol. 150, pp. 97–107, 2015.

[226] T. V. Hoang, V. Fusco, M. A. B. Abbasi, and O. Yurduseven, "Single-pixel polarimetric direction of arrival estimation using programmable coding metasurface aperture," *Scientific Reports*, vol. 11, no. 1, pp. 1–17, 2021.

[227] M. Boyarsky, T. Sleasman, L. Pulido-Mancera, A. V Diebold, M. F. Imani, and D. R. Smith, "Single-frequency 3D synthetic aperture imaging with dynamic metasurface antennas," *Applied optics*, vol. 57, no. 15, pp. 4123–4134, 2018.

[228] S. Li, Z. Liu, S. Fu, Y. Wang, and F. Xu, "Intelligent Beamforming via Physics-Inspired Neural Networks on Programmable Metasurface," *IEEE Transactions on Antennas and Propagation*, 2022.

Appendix A: Gain and Radiation Pattern Measurement Setup of 1 × 8 Linear Antenna Array

Extensive knowledge through hands-on mmWave antenna measurements was acquired during Ph.D. journey. Moreover, we have established an in-house measurement setup for 60 GHz antennas, expanding our antenna measurement capabilities from 24 GHz to 67 GHz. This is demonstrated in the accompanying appendices.

The setup for gain measurement of 1 × 8 linear array is shown here. The linear array has the largest dimension of 25 mm, for which far-filed distance was kept at 29 cm, which satisfies both extreme measurable frequencies of 57 GHz and 67 GHz. The description of gain and radiation pattern measurements is given in Chapter 3, sections 3.8.2 and 3.8.3 respectively.

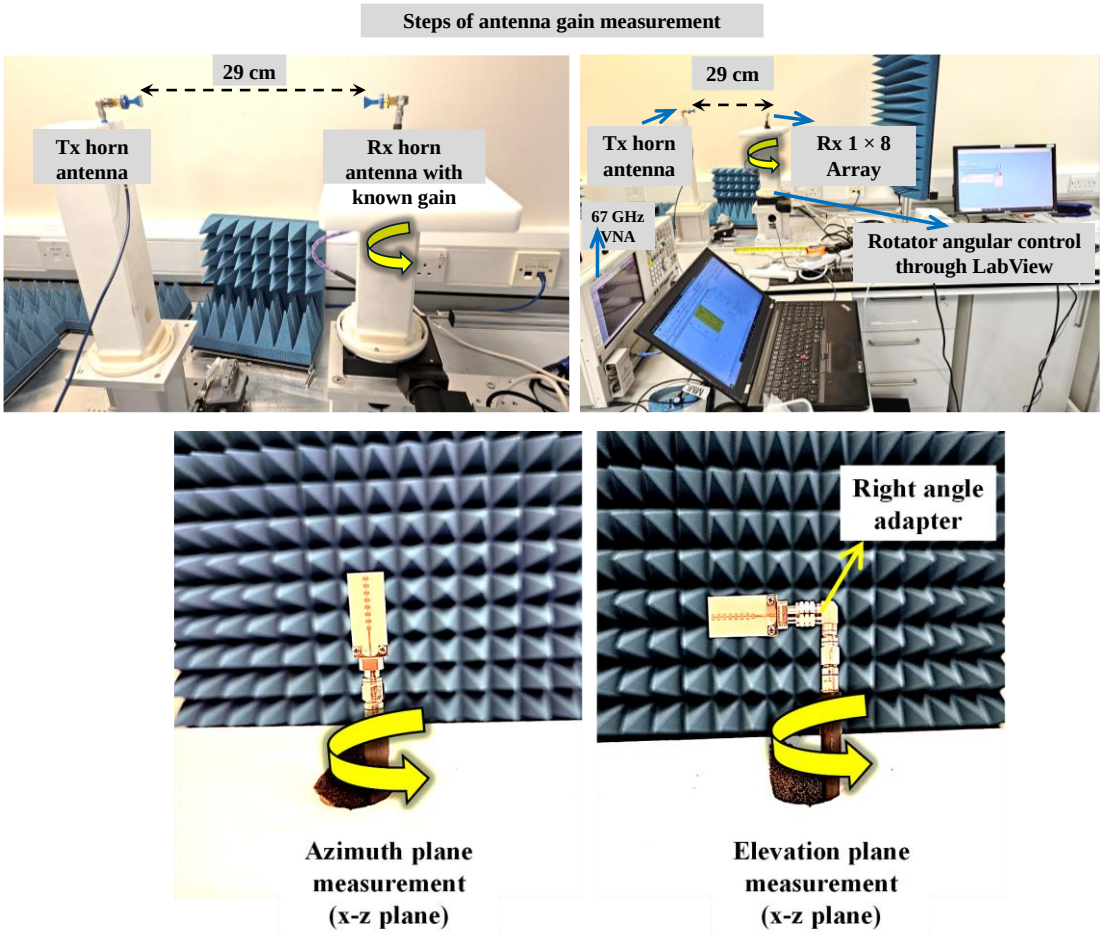

Appendix B: FR-2 mmWave Antenna Measurement Setup | ATS800B OTA Becnchtop CATR System

A compact antenna test range (CATR) system (ATS800B©) from R&S was set up for FR-2 mmWave antenna measurements. This setup eliminates the need for larger chamber space for mmWave antenna arrays where the device size dominates. At a fixed location on the turntable (called a quiet zone), the antenna under test (AUT) of any size can be mounted for radiation pattern and gain measurements between 26 to 50 GHz.

We designed a custom-made LabVIEW program to carry out instrument control using SCPI commands (Standard Commands for Programmable Instruments) communicated through VISA (Virtual Instrument Software Architecture) controller protocol. A standard NI GPIB-USB cable interface is used to connect the VNA to the PC, while the PI motor controller was connected to the PC using a USB interface. A continuous wave (CW) signal is generated (using the LabVIEW program) at each desired operating frequency and the radiation pattern measurement (S21) is automatically recorded at precise angular positions over 180° with a 1° step size (from -90° to +90°). A mmWave array was designed for n257 band (26.5–29.5 GHz band) based on the proposed design philosophy of Chapter 3, to test the radiation pattern on CATR setup. Measured results match quite well with the simulated results as shown below.

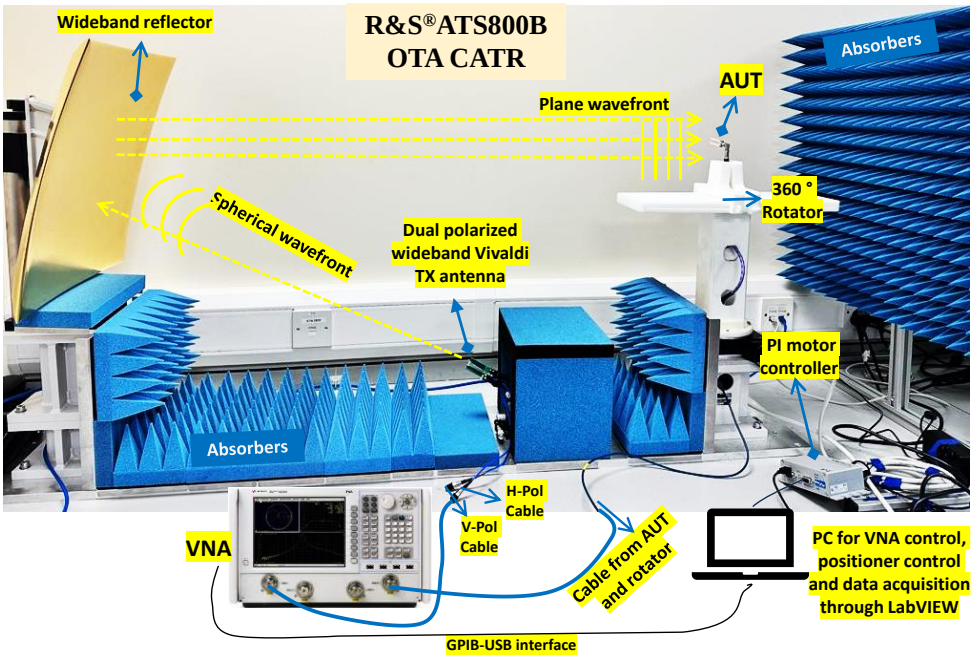

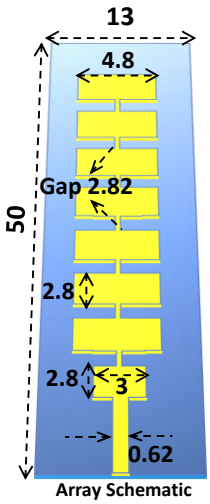

Array Schematic

Fabricated Prototype

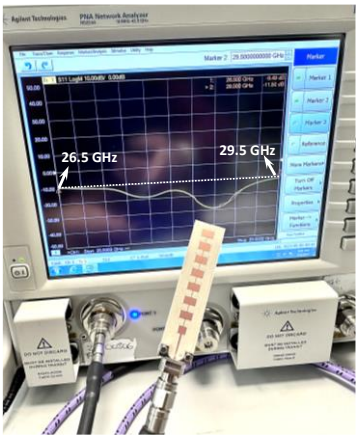

S11 Measurement on VNA

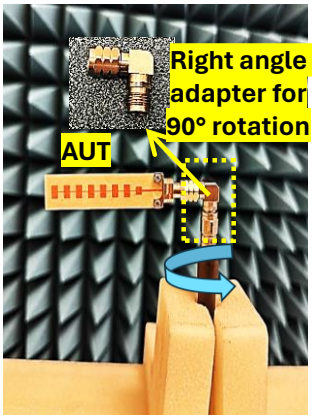

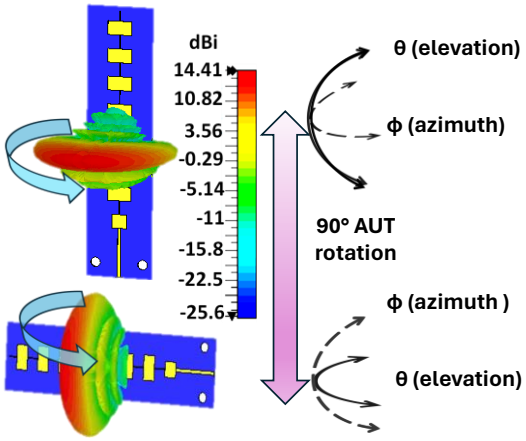

Pattern measurement in the elevational plane

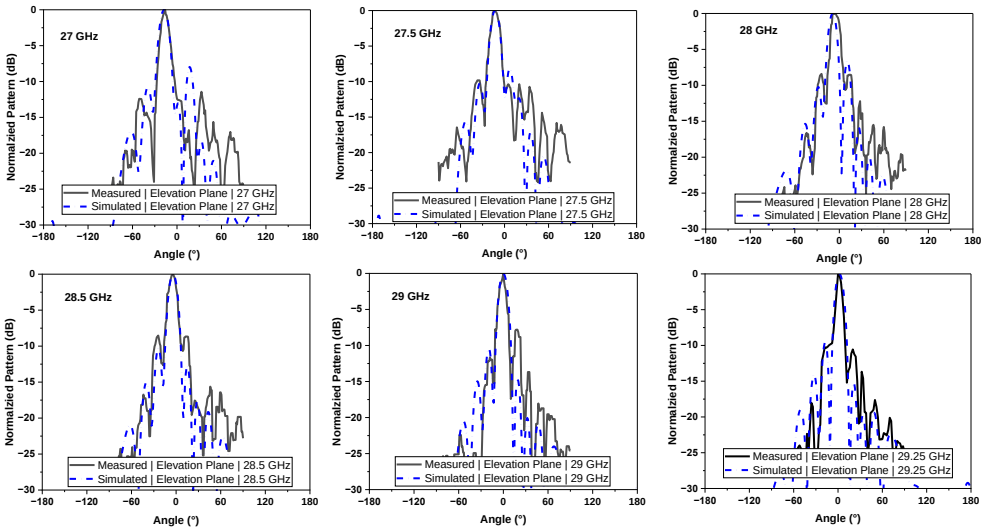

Appendix C: 1.85 mm Solderless V-Connector Layout

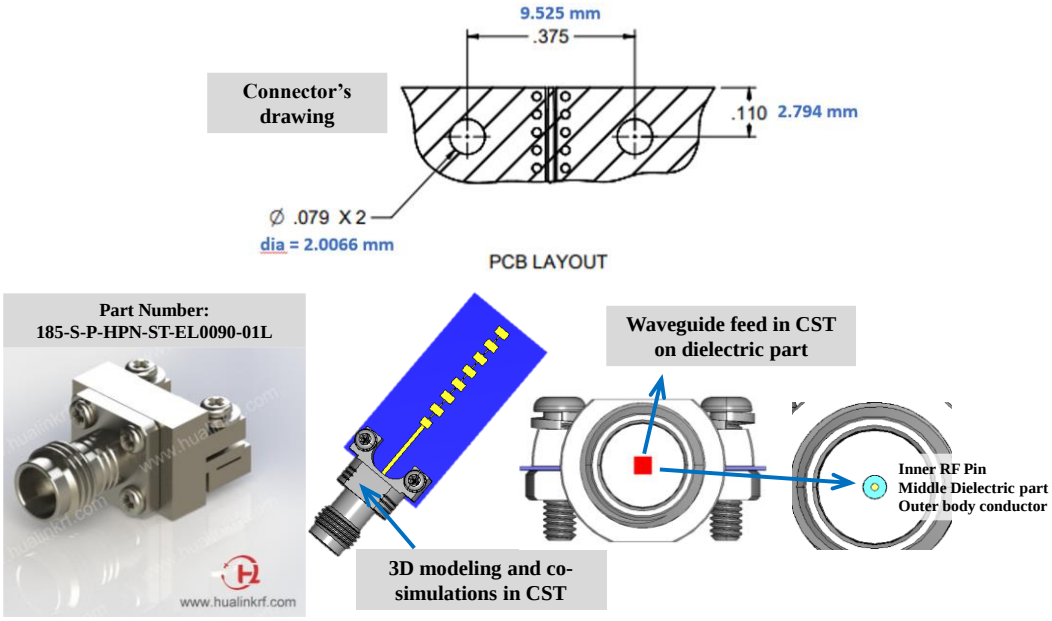

Drawing and 3D model of 1.85 mm solderless V-connector.

Appendix D: Supplement of DMA PCB Hardware Design

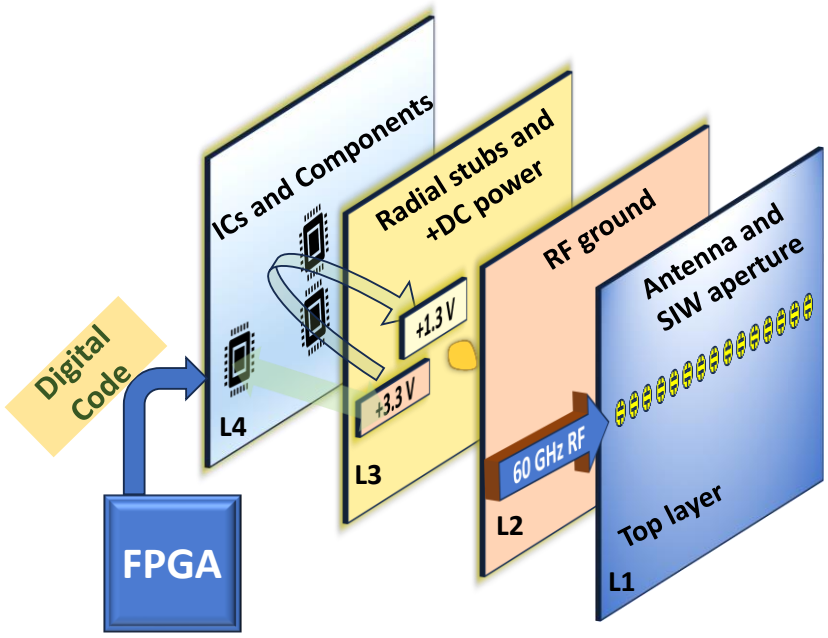

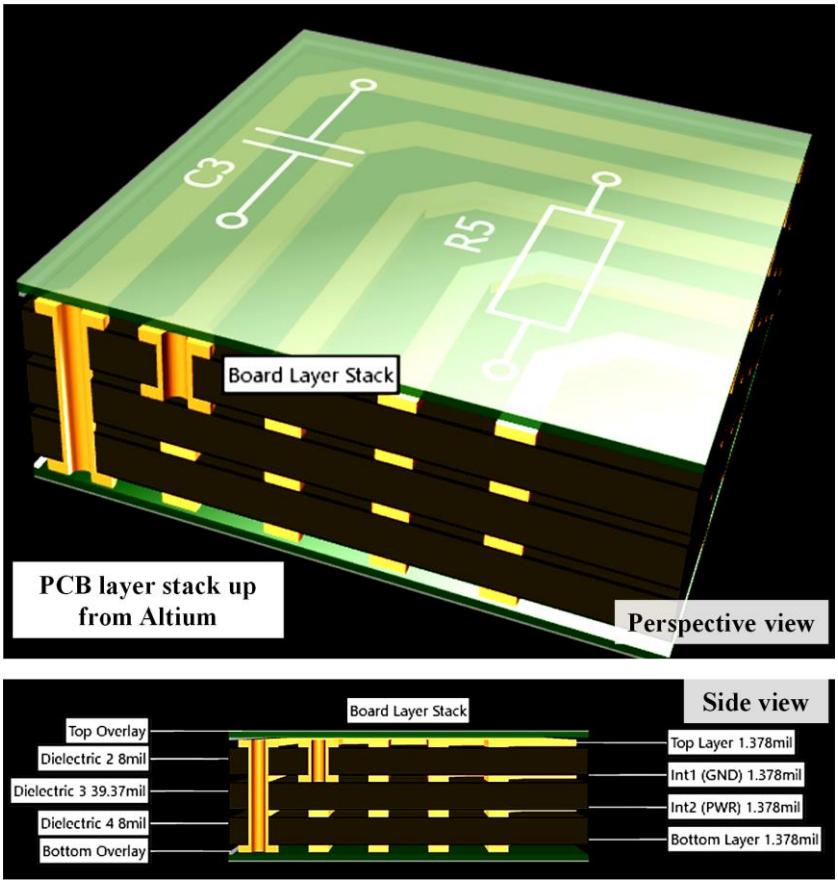

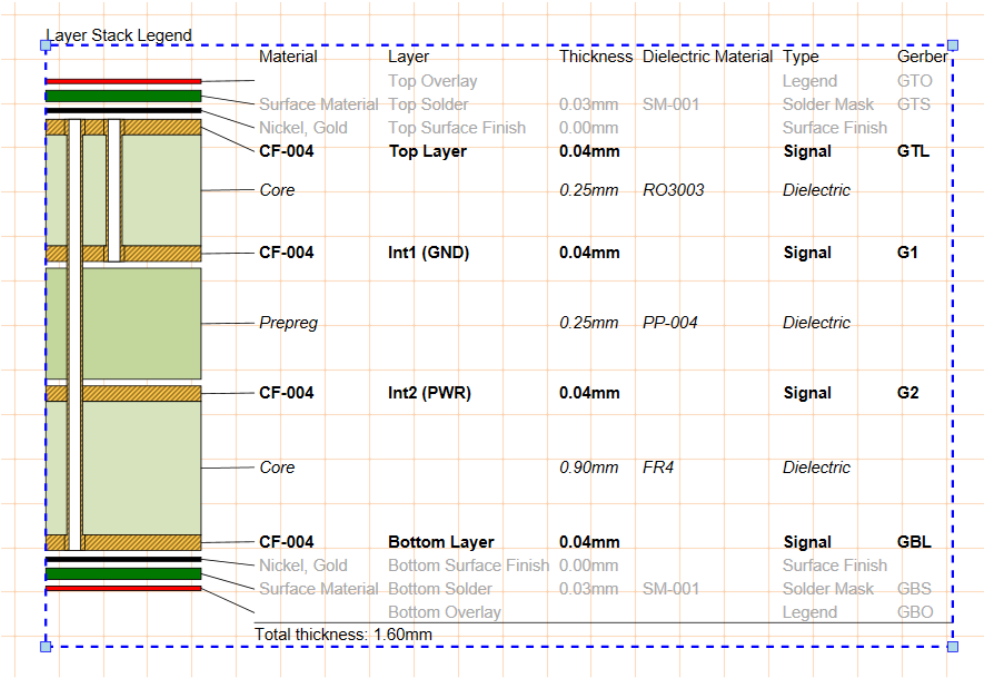

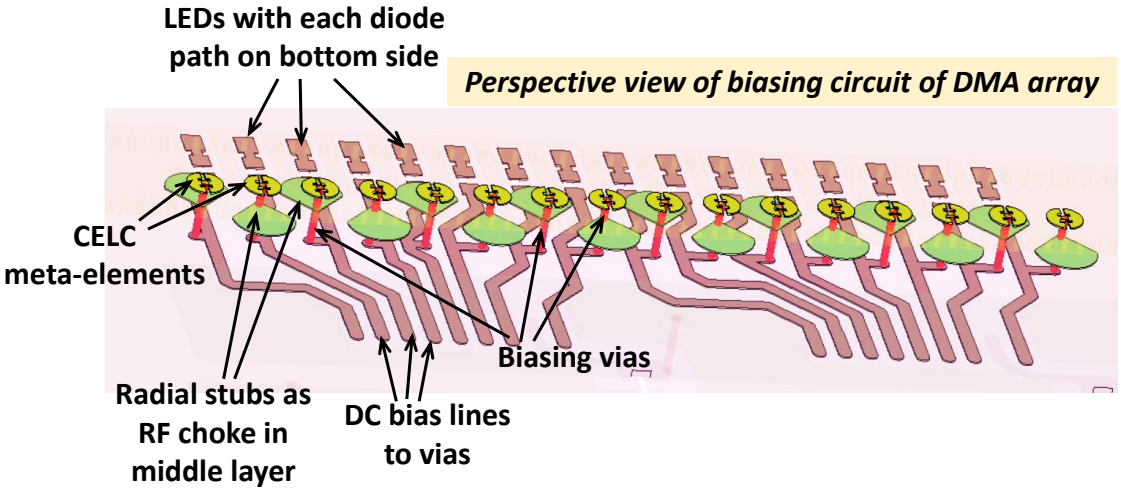

DMA Object Files from Altium

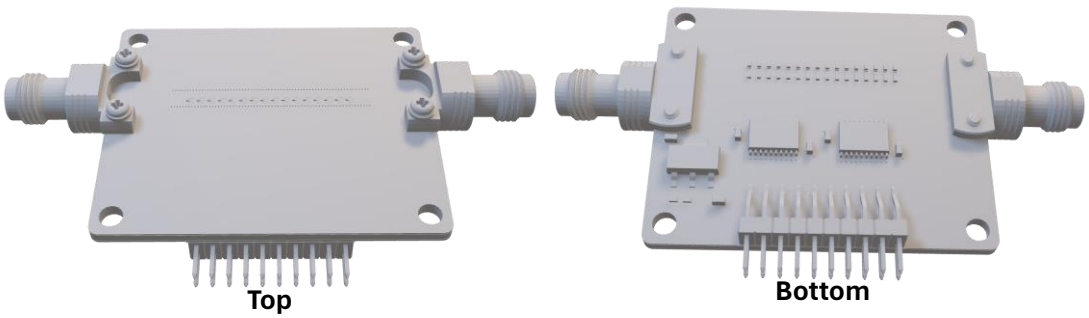

Appendix E: FPGA Board

To generate 16-bit binary coding combinations, we used Arty S7 FPGA from Digilent.

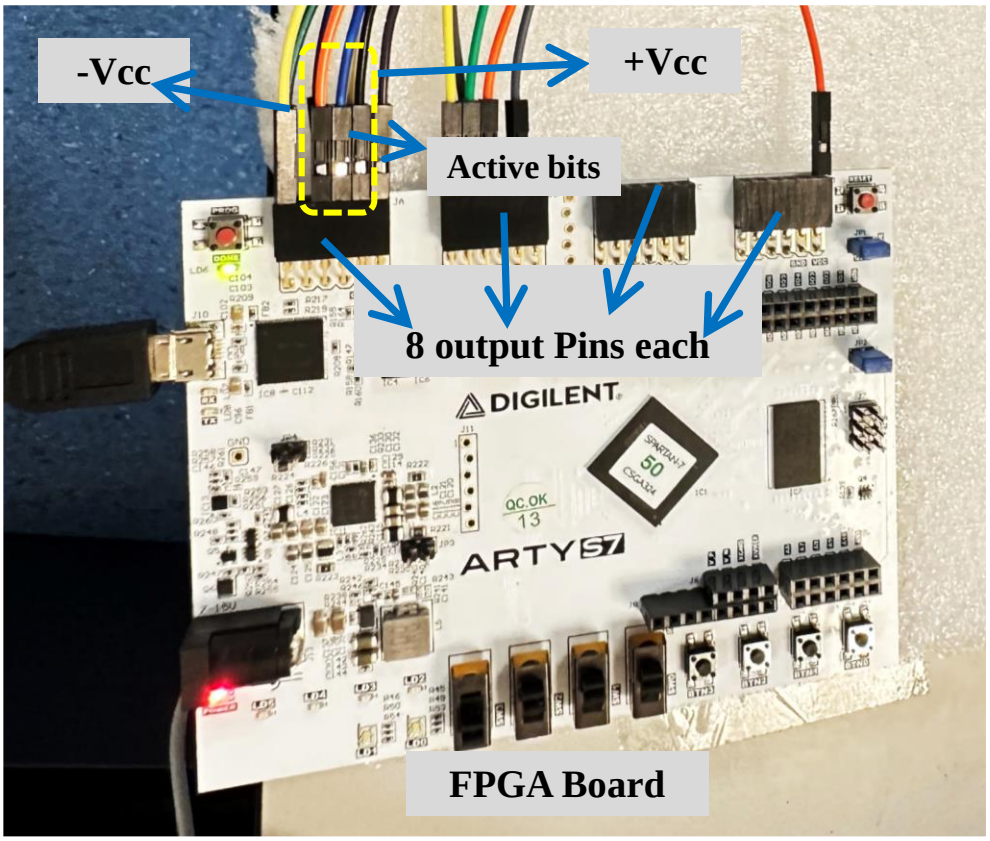

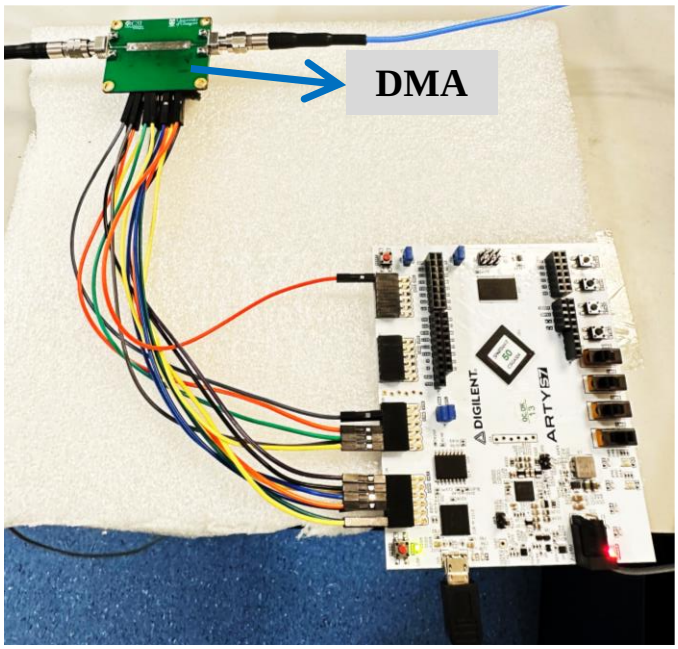

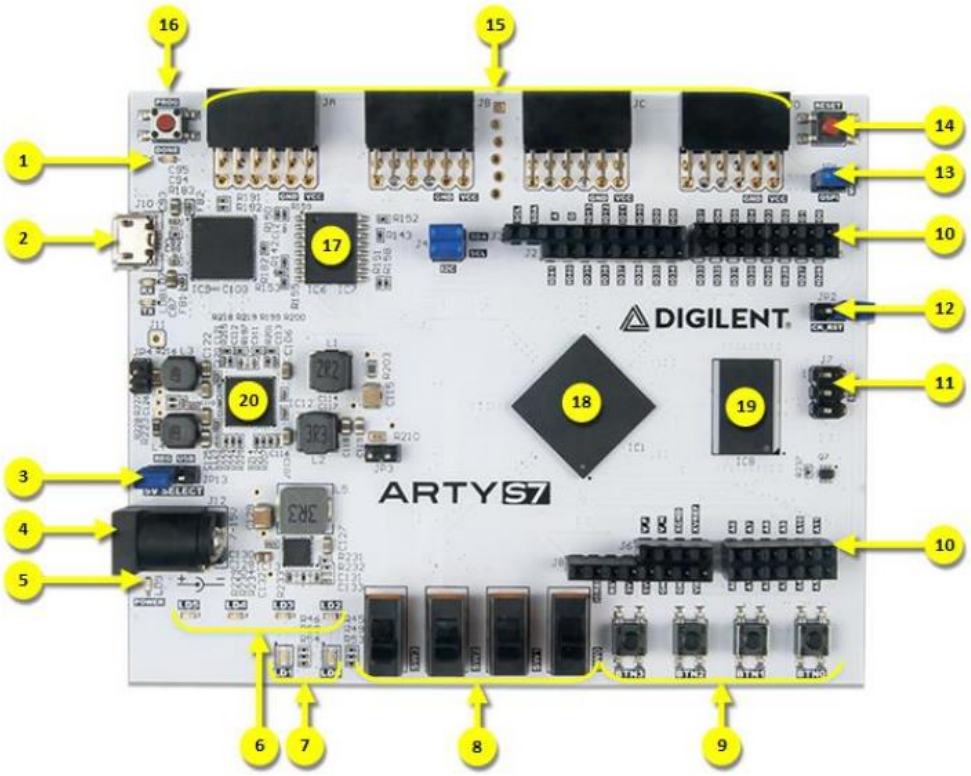

Callout	Description	Callout	Description
1	FPGA programming DONE LED	11	SPI header (Arduino/ChipKIT compatible)
2	Shared USB JTAG / UART port	12	Arduino IDE reset jumper
3	Power select jumper (Ext. supply / USB)	13	FPGA programming mode (JTAG/ Flash)
4	Power jack (for optional ext. supply)	14	Processor reset
5	Power good LED	15	Pmod headers
6	User LEDs	16	FPGA programming reset button
7	User Tri color LEDs	17	SPI Flash
8	User slide switches	18	Spartan-7 FPGA
9	User push buttons	19	DDR3L memory
10	Arduino/ChipKIT shield connectors	20	Analog devices ADP 5052 power supply

Ref: https://digilent.com/reference/_media/reference/programmable-logic/arty-s7/arty-s7_rm.pdf)

Appendix F: Data Sheet of PIN Diode

MADP-000907-14020x

Solderable AlGaAs Flip Chip PIN

Rev. V8

Features

- Low Series Resistance
- Ultra Low Capacitance
- Millimeter Wave Switching & Cutoff Frequency
- Useable up to 70 GHz
- 2 Nanosecond Switching Speed
- Can be Driven by a Buffered TTL
- Silicon Nitride Passivation
- Polyimide Scratch Protection
- RoHS Compliant

Description

The MADP-000907-14020 is a solderable, flip-chip Aluminum Gallium Arsenide (AlGaAs) PIN diode. It is fabricated with MOCVD grown epitaxy using a process and design that optimizes device to device uniformity and produces extremely low parasitics. The diode exhibits an exceptionally low RC product (0.1 ps) and a 2-3 ns switching speed. The chips are fully passivated with silicon nitride and have an added BCB polymer layer for scratch protection. The BCB protective coating prevents damage to the diode junction area and anode air-bridge during handling and assembly.

The ultra low capacitance of the MADP-000907-14020 allows for operation at millimeter wave frequencies for RF switches and phase shifter applications. The diode is designed to be used in pulsed or CW applications, where single digit ns switching speed is required. The low capacitance of

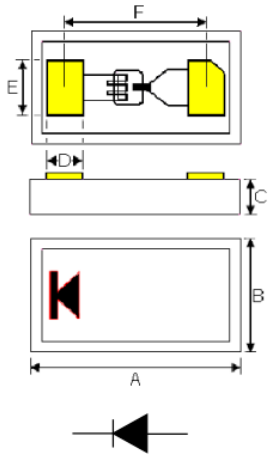

1. Backside metal: 0.2 µm gold over 4 µm nickel.
2. Yellow hatched areas indicate backside ohmic gold contacts.

Outline Dimension

https://www.macom.com/products/product-detail/MADP-000907-14020P